University of Cyprus

DEPARTMENT OF PHYSICS

MOLECULAR CHARGE-TRANSFER AND EXCITONIC PROCESSES: FROM BRIDGE-MEDIATED ELECTRON TRANSFER AND TRANSPORT TO BRIDGE-MEDIATED SINGLET FISSION

DOCTOR OF PHILOSOPHY DISSERTATION

STEFANI VALIANTI

2021

DEPARTMENT OF PHYSICS

MOLECULAR CHARGE-TRANSFER AND EXCITONIC PROCESSES: FROM BRIDGE-MEDIATED ELECTRON TRANSFER AND TRANSPORT TO BRIDGE-MEDIATED SINGLET FISSION

STEFANI VALIANTI

A Dissertation Submitted to the University of Cyprus in Partial Fulfillment of the Requirements for the Degree of Doctor of Philosophy

December 2021

VALIDATION PAGE

Doctoral Candidate: Stefani Valianti

Doctoral Thesis Title: Molecular Charge-transfer and Excitonic Processes: from Bridge-mediated Electron Transfer and Transport to Bridge-mediated Singlet Fission

The present Doctoral Dissertation was submitted in partial fulfillment of the requirements for the degree of Doctor of Philosophy at the ***Department of Physics*** *and was approved on the 20/12/2021 by the members of the* ***Examination Committee***.

Examination Committee:

Research Supervisor: Spiros Skourtis, Assoc. Prof., Dep. of Physics, UCY

Committee Member: Ferdinand Grozema, Prof., Dep. of Chemical Engineering, Delft University of Technology, Netherlands

Committee Member: Grigorios Itskos, Assoc. Prof., Dep. of Physics, UCY

Committee Member: Theodosis Trypiniotis, Asst. Prof., Dep. of Physics, UCY

Committee Member: Sotirios Christodoulou, Lect., Dep. of Chemistry, UCY

DECLARATION OF DOCTORAL CANDIDATE

The present doctoral dissertation was submitted in partial fulfillment of the requirements for the degree of Doctor of Philosophy of the University of Cyprus. It is a product of original work of my own, unless otherwise mentioned through references, notes, or any other statements.

Stefani Valianti

ΠΕΡΙΛΗΨΗ

Η παρούσα διδακτορική διατριβή περιγράφει έρευνα σχετική με μοριακά φαινόμενα μεταφοράς ηλεκτρονίων (ΜΗΛ) και με μοριακές πολυεξιτονικές διεργασίες Ο βασικός στόχος της έρευνας είναι να διερευνήσει μοριακούς μηχανισμούς ΜΗΛ και μηχανισμούς σχάσης απλής εξιτονικής κατάστασης σε τριπλές (ΣΑΚΣΤ). Μέρος της διατριβής, στο πεδίο της μοριακής ηλεκτρονικής και των μοριακών συνδέσεων, εξηγεί τη συμπεριφορά ρεύματος-τάσης και ρεύματος-θερμοκρασίας σε πειράματα μοριακών συνδέσεων. Επίσης προτείνει πειράματα μοριακών συνδέσεων που επιτρέπουν την παρατήρηση της ανεστραμμένης περιοχής Marcus σε αντιδράσεις ΜΗΛ, η οποία μέχρι σήμερα έχει παρατηρηθεί μόνο σε περιβάλλον διαλύματος. Το άλλο μέρος της διατριβής, που σχετίζεται με την πολυεξιτονική μοριακή φυσική, διερευνά διαδικασίες σχάσης απλής κατάστασης σε μοριακά συστήματα δότη (ΔΟ) – γέφυρας (ΓΕ) – δέκτη (ΔΕ). Αναπτύσσει ένα ημιαναλυτικό/υπολογιστικό πλαίσιο για την ανάλυση φαινομένων ΣΑΚΣΤ και το χρησιμοποιεί για να εξηγήσει πρόσφατες πειραματικές παρατηρήσεις.

Οι μοριακές συνδέσεις είναι ιδανικές για τη διερεύνηση μηχανισμών ΜΗΛ που παίζουν σημαντικό ρόλο στη χημεία και τη βιολογία. Περιγράφουμε τη θεωρητική μοντελοποίηση των μηχανισμών ΜΗΛ σε υβριδικές ετεροσυνδέσεις μετάλλου – πρωτεΐνης ΜΗΛ – μετάλλου. Εστιάζουμε σε ένα μεγάλο αριθμό πειραματικών αποτελεσμάτων που μετρούν τη συμπεριφορά ρεύματος-τάσης και ρεύματος-θερμοκρασίας των συνδέσεων. Τα υπό μελέτη συστήματα περιλαμβάνουν ετεροσυνδέσεις Αζουρίνης Holo-Az (η πρωτεΐνη περιέχει άτομο χαλκού), Apo-Az (χωρίς άτομο μετάλλου), όπως και Αζουρίνης με νικέλιο, ή κοβάλτιο ή ψευδάργυρο. Ο στόχος της μοντελοποίησης είναι να κατανοήσουμε από τα πειράματα πως ο μηχανισμός ΜΗΛ εξαρτάται από το είδος του μετάλλου. Λαμβάνουμε υπόψη διαφορετικά μοντέλα μεταφοράς (συνεκτικά και μη-συνεκτικά). Αυτή η εργασία έχει δημοσιευθεί στο Journal of Physical Chemistry C (Valianti, S.; Cuevas, J. C.; Skourtis, S. S. Charge-Transport Mechanisms in Azurin-Based Monolayer Junctions. *J. Phys. Chem. C.* **2019**, *123 (10)*, 5907-5922).

Το άλλο μέρος της διατριβής που σχετίζεται με μηχανισμούς ΜΗΛ προτείνει μία αρχιτεκτονική μοριακής σύνδεσης ΔΟ-ΓΕ-ΔΕ που λειτουργεί μέσω του μη-συνεκτικού μηχανισμού θερμικής μεταπήδησης (ΜΘΜ). Αυτό το είδος συνδέσμου επιτρέπει τη συσχέτιση ανάμεσα στην ένταση ρεύματος, που μετριέται στο πείραμα μοριακής σύνδεσης, με τον ενδομοριακό ρυθμό ΜΗΛ από το δότη (ΔΟ) στο δέκτη (ΔΕ). Προτείνουμε ότι αυτός ο τύπος σύνδεσης μπορεί να χρησιμοποιηθεί για την παρατήρηση της ανεστραμμένης

περιοχής Marcus του ενδομοριακού ρυθμού ΜΗΛ. Η περιοχή αυτή μέχρι σήμερα έχει παρατηρηθεί μόνο σε αντιδράσεις ΜΗΛ σε διάλυμα. Στην προτεινόμενη σύνδεση η πρόσβαση στην ανεστραμμένη περιοχή γίνεται μεταβάλλοντας τη διαφορά δυναμικού κατά μήκος της σύνδεσης. Η πραγματοποίηση ενός τέτοιου πειράματος θα επέτρεπε ουσιαστικές συγκρίσεις μεταξύ του ρυθμού αντίδρασης ΜΗΛ σε περιβάλλον διαλύματος και του ίδιου ρυθμού στο στεγνό περιβάλλον της μοριακής σύνδεσης. Αυτή η εργασία δημοσιεύτηκε στο Journal of Physical Chemistry B (Valianti, S.; Skourtis, S. S. Observing Donor-to-Acceptor Electron-Transfer Rates and the Marcus Inverted-Parabola in Molecular Junctions. *J. Phys. Chem. B* **2019**, *123 (45)*, 9641-9653).

Το άλλο πεδίο της ερευνητικής μου δραστηριότητας σχετίζεται με διαδικασίες ΣΑΚΣΤ σε μοριακά συστήματα ΔΟ-ΓΕ-ΔΕ. Ο κύριος στόχος είναι να κατανοήσουμε πως μία γέφυρα- που συνδέει το ΔΟ με το ΔΕ μπορεί να χρησιμοποιηθεί για να ελέγξει το ρυθμό αντίδρασης ΣΑΚΣΤ. Στην αντίδραση η απλή εξιτονική κατάσταση που δημιουργείται στο ΔΟ, μέσω φωτοδιέγερσης, μετατρέπεται σε δύο τριπλές εξιτονικές καταστάσεις, μία εντοπισμένη στο ΔΟ και μία στο ΔΕ. Ο έλεγχος του ρυθμού αντίδρασης ΣΑΚΣΤ μπορεί να επιτευχθεί ρυθμίζοντας την ηλεκτρονιακή σύζευξη ΣΑΚΣΤ δότη-δέκτη μέσω της γέφυρας. Για το σκοπό αυτό αναπτύσσουμε ένα ημιαναλυτικό / υπολογιστικό πλαίσιο που επιτρέπει την ανάλυση αντιδράσεων ΣΑΚΣΤ σε μοριακές αρχιτεκτονικές ΔΟ-ΓΕ-ΔΕ. Προσδιορίζουμε διαφορετικές περιοχές φυσικών παραμέτρων που καθορίζουν τη σύζευξη. Μελετούμε την εξάρτηση της σύζευξης από τις ενέργειες των εξιτονικών καταστάσεων κάνοντας υπολογισμούς για διαφορετικά συστήματα ΔΟ-ΓΕ-ΔΕ. Αυτή η ημιαναλυτική μεθοδολογία μπορεί να χρησιμοποιηθεί για να καθοδηγήσει υπολογιστικές και πειραματικές μελέτες αντιδράσεων ΣΑΚΣΤ σε συστήματα ΔΟ-ΓΕ-ΔΕ. Στη διατριβή χρησιμοποιούμε τη μεθοδολογία και για να εξηγήσουμε το φαινόμενο συντονισμού γέφυρας για αντιδράσεις ΣΑΚΣΤ, που έχει παρατηρηθεί σε πρόσφατα πειράματα. Οι προαναφερθείσες ερευνητικές μελέτες έχουν υποβληθεί ως άρθρο στο Journal of Physical Chemistry Letters. Σε αυτή τη φάση το άρθρο είναι υπό εξέταση (Valianti, S.; Skourtis, S. S. The Role of Bridge-state Intermediates in Singlet Fission for Donor-bridge-acceptor Systems: A Semi-analytical Approach to Bridge-tuning of the Donor-acceptor Fission Coupling.).

Το τελευταίο μέρος της διδακτορικής διατριβής περιλαμβάνει ένα άρθρο ανασκόπησης που έγραψα σχετικά με την επίδραση των δονητικών μοριακών καταστάσεων στις μοριακές αντιδράσεις ΜΗΛ. Το άρθρο δημοσιεύτηκε στο περιοδικό Molecular Physics (Valianti, S.; Skourtis, S. S. Vibrational control of molecular electron transfer reactions. *Mol. Phys.* **2019**, *117 (19)*, 2618-2631).

ABSTRACT

This Ph.D. Thesis describes research work on molecular electron transfer (ET) and multi-excitonic processes. The underlying objective of the research is to develop a physical understanding of how to control ET and Singlet Fission (SF) in molecules. Part of the work, on the field of molecular electronics, explains current-voltage and current-temperature behavior in molecular-junction experiments, and proposes novel junction experiments for observing the solution-phase Marcus inverted region in junction environments. The other part, that relates to multi-excitonic molecular physics, investigates SF processes in molecular donor (D) – bridge (B) – acceptor (A) systems through the development of a semi-analytical / computational framework. It also uses this framework to explain experimental observations.

Molecular junctions are ideal systems for the investigation of ET mechanisms that play an important role in chemistry and biology. We describe theoretical modeling of ET in hybrid metal – ET protein (e.g., Azurin (Az)) - metal heterojunctions, focusing on a large set of experimental results that measure the current-voltage and current-temperature behavior of the junctions. The systems under study include heterojunctions with Holo-Az (Cu-substituted), Apo-Az (no metal), and Ni-, Co- and Zn-substituted Azurins. The goal of our analysis is to understand from the experiments how the transport mechanism is determined by the metal substitution. We consider different transport models (coherent and incoherent). This work has been published in the Journal of Physical Chemistry C (Valianti, S.; Cuevas, J. C.; Skourtis, S. S. Charge-Transport Mechanisms in Azurin-Based Monolayer Junctions. *J. Phys. Chem. C.* **2019**, *123 (10),* 5907-5922).

The other work related to ET, proposes a D-B-A molecular junction architecture functioning in the incoherent hopping regime, that is suited for establishing direct correlations between the electrode-to-electrode current and the intra-molecular D-to-A ET rate. We suggest that this type of junction may be used to observe the Marcus-inverted-parabola dependence of the intra-molecular rate on energy gap. The Marcus inverted regime is thought to be only observable in solution-phase ET. In the proposed junction the inverted regime is accessed by varying the bias voltage. The realization of such an experiment would enable meaningful comparisons between solution-phase ET rates and molecular-junction currents for the same molecule. This work was published in the Journal of Physical Chemistry B (Valianti, S.; Skourtis, S. S. Observing Donor-to-Acceptor Electron-Transfer Rates and the Marcus Inverted-Parabola in Molecular Junctions. *J. Phys. Chem. B* **2019**, *123 (45),* 9641-9653).

The other field of my research activity is spin molecular physics and chemistry, in particular photo-induced spin processes. My research focuses on the investigation of the Singlet Fission (SF) process in molecular D-B-A systems. The main goal is to understand how a bridge linker connecting D and A can tune the effective SF coupling that leads to D-A-separated correlated triplet excitons. For this purpose, we develop a semi-analytical / computational framework to explore structure-function relationships for SF in D-B-A molecular architectures. We identify different bridge-mediation regimes for the effective SF coupling in the coherent tunneling limit and derive the dominant fission pathways in each regime. We describe the dependence of these regimes on D-B-A exciton state energetics and on D-B (A-B) interactions. This semi-analytical approach can be used to guide computational and experimental searches for D-B-A systems with tuned SF rates. We use this approach to interpret the bridge-resonance effect of SF that has been observed in recent experiments. This work has been submitted to the Journal of Physical Chemistry Letters and is under review (Valianti, S.; Skourtis, S. S. The Role of Bridge-state Intermediates in Singlet Fission for Donor-bridge-acceptor Systems: A Semi-analytical Approach to Bridge-tuning of the Donor-acceptor Fission Coupling.).

The final part of the Thesis includes a review article I wrote on vibrational control of electron transfer reactions that was published in Molecular Physics (Valianti, S.; Skourtis, S. S. Vibrational control of molecular electron transfer reactions. *Mol. Phys.* **2019**, *117 (19)*, 2618-2631).

Dedicated to Skevi

ACKNOWLEDGEMENTS

First of all, I would like to express my sincere gratitude to my supervisor and my mentor, Prof. Spiros S. Skourtis for the continuous guidance, support and encouragement in this long journey of my MSc and Phd studies. His insightful feedback pushed me to expand my thinking and brought my knowledge and work to a higher level. It was an honour for me to work under his supervision all these years.

I am especially grateful to Profs Juan Carlos Cuevas from Autonomous University of Madrid, David Cahen from Weizmann Institute of Science and his group for many helpful discussions, their feedback on my work and for their substantial contributions to the work presented in this Thesis.

I also wish to acknowledge my committee members: Grigorios Itskos, Theodosis Trypiniotis, Sotirios Christodoulou and my external committee member Ferdinand Grozema, for honoring me with their acceptance to join my Thesis committee. I would like to express my appreciation to my professors at the University of Cyprus for their inspiring lectures and for reinforcing my confidence during my PhD.

I am also grateful for having been financially supported by the University of Cyprus and the Physics Department.

I would also like to express my sincere thanks to all my friends, and especially my fellow students for their support, understanding and encouragement, and for adding an enjoyable note in this long and extremely difficult journey. Without them this journey would be even more difficult.

Last but foremost, I am deeply grateful to my family, my parents, my brothers and my sisters, for their unconditional love and support, especially for their encouragement during this period.

Table of Contents

List of Figures

Figure 3.3. Experimental current-voltage curves via Holo-Az: (a) I versus V ($-1 \leq V \leq 1$), with current plotted as log(I), at different temperatures. (b) Current at 0.1 V and 0.5 V, indicating the same temperature-independent behavior at different bias voltages (exp. II).

Figure 3.4 Comparison of current-voltage behaviors in experiments I and II. Each current is normalized by its value at 1.0 V and the temperature is 200 K.

Figure 3.5 Schematic representation of the layout used for the description of some theoretical models to describe the experiments. M denotes metal dopant (e.g., Cu) and H_L, H_R are the protein-mediated tunneling matrix elements between L and R electrodes.

Figure 3.6 Schematic representation of the basic parameters used in the Landauer models ($\varepsilon_0(V)$, $\Gamma_{L(R)}$).

Figure 3.7 Reorganization energy, λ, distributions W_{ox} and W_{red} at equilibrium (left) and after application of a cathodic overpotential.

Figure 3.8 Experimental ln(J) versus 1000/T of Apo- and Holo-Az junction at +50 mV bias.

Figure 3.9 Experimental ln(J) versus 1000/T of Cu-Az (Holo-Az) for different bias voltages versus theoretical predictions (eqs (3.1)-(3.4)). (a) Bias voltages of -50 mV and -250 mV, (b) bias voltages of +50 mV and +250 mV. Parameter values of eqs (3.1)-(3.4) for all graphs: ε_0=0.03 eV, α=0.75, Γ_L=3.3 10^{-5}eV, and Γ_R/Γ_L=1000.

Figure 3.10 (a) Experimental ln(J) versus voltage of Cu-Az at T = 300 K and theoretical best-fit using the single-channel resonant-tunneling model (eqs (3.1)-(3.4)) with the best fit parameter values of ε_0=0.03 eV, α=0.75 , Γ_L=3.3 10^{-5} eV and Γ_R/Γ_L=1000, as in Fig. 3.9. The fit fails for bias voltages beyond 250 mV. This is because the current of a single resonant tunneling channel will saturate at higher bias voltages. (b) Theoretical resonant tunneling J versus voltage of Cu-Az at T = 300 K showing the saturation of the current at higher voltages for the best fit parameters. Since the resonant tunneling current in this parameter regime is larely temperature-independent for T = 100-400 K the shape of the J-V curve will not be altered within the experimental temperature range.

Figure 3.11 Experimental ln(*J*) versus voltage of Cu-Az at *T* = 300 K and theoretical best-fit using the off-resonant tunneling model (eqs (3.1)-(3.4)) with the best fit parameter values of ε_0=0.8 eV, α=0.5, Γ_L=3.3 10^{-4} eV and Γ_R /Γ_L=1000.

Figure 3.12 Experimental ln(*J*) versus 1000/*T* of Cu-Az (Holo-Az) for different bias voltages versus theoretical best-fit using the one-site hopping model (eqs (3.5)-(3.7)). (a) Bias voltages of -50 mV and -250 mV, (b) bias voltages of +50 mV and +250 mV. The parameter values of eqs (3.5)-(3.7) for all graphs are: λ=0.2 eV, α=0.75, ε_0=0.01 eV, Γ_L=1.0 10^{-4} eV and Γ_R/Γ_L=1000.

Figure 3.13 (a) Experimental ln(*J*) versus voltage of Cu-Az at *T* = 300K and theoretical best-fit using the one-site hopping model (eqs (3.5)-(3.7)) (parameter values: λ=0.2 eV, α=0.75, ε_0=0.01 eV, Γ_L=1.0 10^{-4} eV and Γ_R/Γ_L=1000). (b) Theoretical single-channel resonant hopping *J* versus voltage of Cu-Az at *T* = 300 K for the same parameter values, showing saturation behavior of the current. The behavior does not qualitatively change with temperature as the model predicts temperature independent transport for *T* = 100-400 K (Fig. 3.12).

Figure 3.14 Schematic representation of the Cu-level multi-channel hypothesis.

Figure 3.15 Theoretical *J* versus V of Cu-Az at *T* = 300 K using a range of energy levels, $\varepsilon_{0,k\neq1}$ =0.1-0.5 eV (a) for the coherent resonant tunneling model (parameter values: $\varepsilon_{0,1}$=0.03 eV (best-fit at low bias regime), α=0.75, Γ_L=3.3 10^{-5} eV, Γ_R /Γ_L=1000) and (b) for the incoherent hopping model (parameter values: $\varepsilon_{0,1}$=0.01 eV (best-fit at low bias regime), λ=0.2 eV, α=0.75, Γ_L=1.0 10^{-4} eV, Γ_R /Γ_L=1000).

Figure 3.16 Experimental ln(*J*) versus voltage of Cu-Az at *T* = 300 K and theoretical fits using the multi-channel hypothesis of eq. (3.8) using (a) the incoherent hopping mechanism (coefficients derived from multiple regression analysis: P_1=0.35, P_2=0.50, P_3=3.14, P_4=4.68, P_5=13.01), (b) the coherent tunneling mechanism (coefficients of multiple regression analysis: P_1=0.06, P_2=6.84, P_3=7.77, P_4=3.21, P_5=7.68).

Figure 3.17 Experimental ln(*I*) versus 1000/*T* of Cu-Az at +500 mV and +100 mV bias, versus theoretical fits (eqs (3.1)-(3.4)) using the parameter values: α=0.470, ε_0=0.80 eV, Γ_L=1.15 10^{-5} eV and Γ_R/Γ_L=1000.

Figure 3.18 Experimental ln(*I*) versus voltage of Cu-Az at (a) 275 K and (b) 25 K, versus theoretical fits (eqs (3.1)-(3.4)) using the parameter values: α=0.470, ε_0=0.80 eV, Γ_L=1.15 10^{-5} eV, and Γ_R/Γ_L=1000.

Figure 3.19 (a) Experimental ln(*J*) versus voltage of Apo-Az at T = 128 K and theoretical fits using eqs (3.1)-(3.4). Since for $100 \leq T \leq 200$ K, the current is temperature independent, the fit does not change with temperature. (b) Experimental ln(*J*) versus 1000/*T* of Apo-Az as a function of temperature at V = 0.05 and 0.10 V, and theoretical fits using eqs (3.1)-(3.4). For both (a), (b) the parameter values in eqs (1)-(4) are: α=0.50, ε_0=0.70 eV, Γ_L=1.0 10^{-3} eV, Γ_R/Γ_L=1.

Figure 3.20 (a) Experimental ln(*J*) versus 1000/*T* of Apo-Az as a function of temperature at V = -0.05 V versus theoretical fits (eqs (3.9)-(3.10)). (b) Experimental ln(*J*) versus voltage of Apo-Az at T = 128 K (low temperature regime) and theoretical fits using eqs (3.9)-(3.10). (c) Experimental ln(*J*) versus voltage of Apo-Az at T = 308 K (high temperature regime) and theoretical fits using eqs (3.9)-(3.10). For all graphs the parameter values are: λ=1.1 eV, α=0.50, ε_0=0.60 eV, Γ_L=1.0 10^{-3} eV and Γ_R/Γ_L=1.

Figure 3.21 Schematic representation of the hopping model where a molecular bridge with N=3 incoherent sites coupled to the left (L) and right (R) electrodes.

Figure 3.22 (a) Experimental ln(*J*) versus voltage of Apo-Az at T = 308 K and theoretical fits (eqs (3.11)-(3.14)). (b) Experimental ln(*J*) versus 1000/*T* of Apo-Az at V = 0.50 V over the entire temperature range and theoretical fits (using eqs (3.11)-(3.14) at high temperatures, eqs (3.1)-(3.4) at low temperatures and eq. (3.15) for both temperature regimes). Model parameter values of eqs (3.11)-(3.14): N=3, λ=0.3 eV, α_L=α_R=-0.40, ε_0=0.40 eV, Γ=3.30 10^{-7} eV, Γ_L=3.30 10^{-8} eV and Γ_R/Γ_L=100. Model parameter values of eqs (3.1)-(3.4): α=0.50, ε_0=0.70 eV, Γ_L=1.0 10^{-3} eV and Γ_R/Γ_L=1. Parameter value of eq. (3.15) (red line): p=0.3.

Figure 3.23 Experimental ln(*J*) versus 1000/*T* of Ni-, Co- and Zn-Az at -50 mV bias and theoretical best-fit using the off-resonant tunneling model (eqs (3.1)-(3.4)) with the best fit parameter values of Γ_L=1.0 10^{-3} eV, Γ_R/Γ_L=1, α=0.50 and ε_0=0.20, 0.22, 0.55 eV for Ni-, Co- and Zn-Az heterojunctions respectively.

Figure 3.24 Experimental ln(*J*) versus 1000/*T* of Zn-Az at *V*=-50 mV over the entire temperature range and theoretical fits (using eqs (3.11)-(3.14) at high temperatures, eqs (3.1)-(3.4) at low temperatures and eq. (3.15) for both temperature regimes). Model parameter values of eqs (3.11)-(3.14): *N*=3, λ=0.3eV, $\alpha_L=\alpha_R$=-0.40, ε_0=0.20 eV, Γ=1.0 10^{-12} eV, Γ_L=3.30 10^{-8} eV and Γ_R/Γ_L=1. Model parameter values of eqs (3.1)-(3.4): α=0.50, ε_0=0.55 eV, Γ_L=1.0 10^{-3} eV and Γ_R/Γ_L=1. Parameter value of eq. (3.15) (red line): *p*=0.3.

Figure 4.1 Schematic representation of a linear one-site hopping model with a single hopping site (redox moiety M) connected to left (L) and right (R) electrodes, respectively. The connection to the L electrode is through a molecular bridge that is assumed to act as a high tunneling barrier for the transferring electrons. The M-to-electrode hopping rates are given by Marcus theory rates for heterogeneous ET (eqs (4.2) and (4.3)).

Figure 4.2 Schematic representation of the molecular levels in the junction setup of Fig. 4.1. The diagram shows a positive bias situation, where the backward rates are much larger than the forward rates. The bridge levels B_L and B_R shown to be of much higher energy than the redox level M. M indirectly couples to the L and R electrodes through the bridge levels (electronic couplings are represented by red dotted lines).

Figure 4.3 Left backward rate ($\overleftarrow{k}_L$ eq. (4.2)) versus the bias voltage *V* at T = 100-400 K. The heterogeneous ET rates have a sigmoidal dependence on voltage, increasing in the normal regime and saturating in the inverted regime. Parameter values: $\alpha = 0.65$, $\varepsilon_0 = 0$, $\lambda = 0.2$ eV, $c_L = 0.15 \times 10^2$ $eV^{-1/2}$ ns^{-1} and $c_R/c_L = 1000$.

Figure 4.4 (a) Current *I* versus the bias voltage *V* at T = 300 K. Exact current expression (eq. (4.1) black dots) and approximate expressions for the positive bias voltage regime ($I(V) \approx e\overleftarrow{k}_L$ red dots) and for the negative bias regime ($I(V) \approx -e\overrightarrow{k}_L$ blue dots). (b) Current *I* versus *1000/T* at V = 0.05 V (black dots) indicates the normal Marcus regime, 0.2 V (red

dots) indicates the activationless regime, 0.4 V (blue dots) indicates the inverted Marcus regime. Parameter values: $\alpha = 0.65$, $\varepsilon_0 = 0$, $\lambda = 0.2$ eV, $c_L = 0.15 \times 10^2$ $eV^{-1/2}$ ns^{-1} and $c_R/c_L = 1000$.

Figure 4.5 Schematic representation of the linear redox junction model. Donor (M_L) and acceptor (M_R) redox groups are connected to left (L) and right (R) electrodes, respectively via left (B_L) and right (B_R) bridges and also connected to each other by a middle bridge (B_M). All bridge units are tunneling barriers for the transferring electrons. The model assumes that the ET mechanism between M_L and M_R is incoherent hopping with forward and backward intra-molecular ET rates given by eq. (4.6). ET between M_L (M_R) and the L (R) electrode is also incoherent hopping with forward and backward heterogeneous ET rates given by eqs (4.2) and (4.3).

Figure 4.6 Schematic representation of the levels in the $B_LM_LB_MM_RB_R$ junction of Fig. 4.5. Electronic couplings between the levels are represented by red dotted lines. The diagram shows a positive bias situation with the M_L (M_R) DA energy gap written as a function of the total bias across the junction. In our model this fraction is controlled by the parameters α_L and α_R. The figure shows that the bridge levels act as deep tunneling barriers for the transferring electron such that only M_L and M_R change their oxidation state during transfer. Positive bias leads to a positive L-to-R current (R-to-L electron flow).

Figure 4.7 Current I (eqs (4.8) and (4.9)) versus the bias voltage V at T = 308 K for the partially pinned system of Fig. 4.6. Parameter values: $\alpha_L = \alpha_R = 0.33$, $\varepsilon_0 = 0$, $\lambda_L = \lambda_R = 0.1$ eV, $c_L = c_R = 0.22 \times 10^1$ $eV^{-1/2}$ ns^{-1} and $c = 0.15$ $eV^{1/2}$ ns^{-1}. The current shows a gaussian dependence on the voltage that reflects the energy gap dependence of the intra-molecular ET rates $\overleftarrow{k}_{\text{int}}$ or $\vec{k}_{\text{int}}$.

Figure 4.8 (a) Backward intra-molecular rate $\overleftarrow{k}_{\text{int}}$ versus the bias voltage V and Gibbs free energy ΔG at T = 308 K. (b) Current I versus the bias voltage V and Gibbs free energy ΔG at T = 308 K (covering the positive V region of Fig. 4.7). Exact current expression (eq. (4.9) black dots) and approximate current expression ($I(V) \approx e\overleftarrow{k}_{\text{int}}$ red dots). Parameter values for both graphs: $\alpha_L = \alpha_R = 0.33$, $\varepsilon_0 = 0$, $\lambda_L = \lambda_R = 0.1$ eV, $c_L = c_R = 0.22 \times 10^1$ $eV^{-1/2}$ ns^{-1} and $c = 0.15$ $eV^{1/2}$ ns^{-1}. $V^{\max} = 3\Delta G^*/e = 3(\lambda_L + \lambda_R)/e$ and $\sigma_I = \sigma_{k_{\text{int}}} = 3\sqrt{2(\lambda_L + \lambda_R)k_BT}/e$.

Figure 4.9 (a) Backward intra-molecular rate $\overleftarrow{k}_{\text{int}}$ versus the bias voltage *V* and Gibbs free energy *ΔG* at T = 308 K. (b) Current *I* versus the bias voltage *V* and Gibbs free energy *ΔG* at T = 308 K. Exact current expression (eq. (4.9) black dots) and approximate current expression ($I(V) \approx e\overleftarrow{k}_{\text{int}}$ red dots). Parameter values for both graphs: $\alpha_L = \alpha_R = 0.33$, $\varepsilon_0 = 0$, $\lambda_L = \lambda_R = 0.2$ *eV*, $c_L = c_R = 0.15 \times 10^1$ $eV^{-1/2}$ ns^{-1} and $c = 0.38$ $eV^{1/2}$ ns^{-1}. $V^{\max} = 3\Delta G^*/e = 3(\lambda_L + \lambda_R)/e$ and $\sigma_I = \sigma_{k_{\text{int}}} = 3\sqrt{2(\lambda_L + \lambda_R)k_B T}/e$.

Figure 4.10 Current *I* versus the bias voltage *V* at T = 308 K for a junction with off-resonant M_L and M_R redox levels at zero bias. Parameter values for both graphs: $\alpha_L = \alpha_R = 0.33$, $\varepsilon_0 = 0.1$ *eV*, $\lambda_L = \lambda_R = 0.1$ *eV*, $c_L = c_R = 0.22 \times 10^1$ $eV^{-1/2}$ ns^{-1} and $c = 0.15$ $eV^{1/2}$ ns^{-1}. (a) Exact current expression (eq. (4.9) black dots) and approximate current expressions for the positive bias voltage regime ($I(V) \approx \frac{e\overleftarrow{k}_R \overleftarrow{k}_{\text{int}}}{\overleftarrow{k}_{\text{int}} + \overleftarrow{k}_R + \vec{k}_R}$ red dots) and for the negative bias regime ($I(V) \approx -\frac{e\vec{k}_L \vec{k}_{\text{int}}}{\vec{k}_{\text{int}} + \vec{k}_L + \overleftarrow{k}_L}$ blue dots). (b) Current *I* versus the bias voltage *V* at T = 308 K (covering the positive *V* region). Exact current expression (eq. (4.9) black dots) and rate-limited approximate current expression ($I(V) \approx e\overleftarrow{k}_{\text{int}}$ red dots).

Figure 4.11 (a) Right backward injection rate $\overleftarrow{k}_R$ (black dots) and left forward injection rate $\vec{k}_L$ (red dots) versus the bias voltage *V* at T = 308 K. (b) Current *I* versus the bias voltage *V* at T = 308 K. Exact current expression (eq. (4.9) black dots) and approximate current expressions for the positive bias voltage regime ($I(V) \approx \frac{e\overleftarrow{k}_R k_{\text{int}}}{3k_{\text{int}} + \overleftarrow{k}_R + \vec{k}_R}$ red dots) and for the negative bias regime ($I(V) \approx -\frac{e\vec{k}_L k_{\text{int}}}{3k_{\text{int}} + \overleftarrow{k}_L + \vec{k}_L}$ blue dots). Parameter values for both graphs: $\alpha_L = \alpha_R = 0.50$, $\varepsilon_0 = 0$, $\lambda_L = \lambda_R = 0.1$ *eV*, $c_L = c_R = 0.22 \times 10^1$ $eV^{-1/2}$ ns^{-1} and $c = 0.15$ $eV^{1/2}$ ns^{-1}.

Figure 4.12 Current *I* versus the bias voltage *V* at T = 308 K for a junction with partially pinned M_L and M_R. Parameter values: $\alpha_L = \alpha_R = 0.33$, $\varepsilon_0 = 0$, $\lambda_L = \lambda_R = 0.1$ *eV*, $c_L = c_R = 0.15$ $eV^{-1/2}$ ns^{-1} and $c = 0.15 \times 10^2$ $eV^{1/2}$ ns^{-1}. The timescale of ET between the M_L and M_R sites is

of the order of tens of psec. The ET timescale between the M_i and the leads is of the order of nsec.

Figure 4.13 (a) Current (eq. (4.9)) *I* versus the bias voltage *V* at T = 100-400 K. (b) The natural logarithm of the current versus *1000/T* at V = 0.2 V (black dots) indicates the temperature dependence of the intra-molecular Marcus rate: 0.2 V (black dots) normal Marcus regime (current behavior "A" of main text), 0.6 V (red dots) activationless regime (current behavior "B" of main text), 1.0 V (blue dots) inverted regime (current behavior "A"). Parameter values for both graphs: $\alpha_L = \alpha_R = 0.33$, $\varepsilon_0 = 0$, $\lambda_L = \lambda_R = 0.1$ *eV*, $c_L = c_R = 0.22 \times 10^1$ $eV^{-1/2}$ ns^{-1} and $c = 0.15$ $eV^{1/2}$ ns^{-1}. The current is limited by the intra-molecular M_L-to-M_R rate.

Figure 4.14 (a) Exact current *I* (eq. (4.9)) versus the bias voltage *V* at T = 100-400 K. (b) The natural logarithm of the current versus *1000/T* at V = 0.6 V (black dots) indicates the temperature dependence of the intra-molecular Marcus rate: 0.6 V (black dots) normal Marcus regime (current behavior "A"), 1.2 V (red dots) activationless regime (current behavior "B"), 1.8 V (blue dots) inverted regime (current behavior "A"). Parameter values for both graphs: $\alpha_L = \alpha_R = 0.33$, $\varepsilon_0 = 0$, $\lambda_L = \lambda_R = 0.2$ *eV*, $c_L = c_R = 0.15 \times 10^1$ $eV^{-1/2}$ ns^{-1} and $c = 0.38$ $eV^{1/2}$ ns^{-1}. The current is limited by the intra-molecular M_L-to-M_R rate.

Figure 4.15 Schematic representation of the levels in the $B_LM_LB_MM_RB_R$ junction. The diagram shows a positive bias situation with the M_L (M_R) energy gap written as a function of the total bias across the junction. The bridge levels act as deep tunneling barriers for the transferring electron such that only M_L and M_R change their oxidation state during transfer. The M_L and M_R redox energies are slightly higher than the Fermi levels of the leads at zero bias such that the charge injection rates from the leads are activated and possibly current limiting for a voltage bias range.

Figure 4.16 Current *I* versus the bias voltage *V* and the Gibbs free energy ΔG at T = 308 K for a junction with off-resonant redox levels at zero bias (Fig. 4.15). The energy gap is given by $\Delta G(V) = eV/3$. Parameter values: $\alpha_L = \alpha_R = 0.33$, $\lambda_L = \lambda_R = 0.1$ *eV*, $c_L = c_R = 0.22 \times 10^1$ $eV^{-1/2}$ ns^{-1} (the timescale of ET between the M_i and the leads is in the order of tens of psec), $c = 0.15$ $eV^{1/2}$ ns^{-1} (the timescale of ET between the M_L and M_R sites is in the order of nsec) and $\varepsilon_0 = 0$ (black dots), $\varepsilon_0 = 0.1$ *eV* (red dots), $\varepsilon_0 = 0.2$ *eV* (blue dots), $\varepsilon_0 = 0.25$ *eV* (cyan

dots, could correspond to Ferrocene M_L and M_R redox groups with Au leads), $\varepsilon_0 = 0.3$ *eV* (magenta dots), and $\varepsilon_0 = 0.35$ *eV* (yellow dots, could correspond to Azurin Cu center redox groups with Au leads). The low bias current decreases as the ε_0 value increases (charge injection becomes more activated), but the current has the expected intra-molecular-rate energy gap behavior (inverted and normal).

Figure 4.17 Current I versus bias voltage V at T = 308 K (positive V region). Parameter values: $\alpha_L = \alpha_R = 0.33$, $\varepsilon_0 = 0.35$ *eV*, $\lambda_L = \lambda_R = 0.1$ *eV*, $c_L = c_R = 0.22 \times 10^1$ $eV^{-1/2}$ ns^{-1} and $c = 0.15$ $eV^{1/2}$ ns^{-1}. Exact current expression (eq. (4.9) black line) and approximate current expressions ($I(V) \approx \frac{e\vec{k}_R \vec{k}_{\text{int}}}{\vec{k}_{\text{int}} + \vec{k}_R + \vec{k}_R}$ blue dots, $I(V) \approx e\vec{k}_{\text{int}}$ red dots).

Figure 4.18 Schematic representation of a tight-binding nearest-neighbor model of a $B_L M_L B_M M_R B_R$ junction. The B_L, B_M and B_R linear bridges consist of n_{B_L}, n_{B_M} and n_{B_R} sites, respectively. At zero bias the bridge site-energies are equal, of value ε_0^B (measured with respect to the Fermi level of the electrodes). The redox level $M_{L(R)}$ energies are off-resonant to the bridge energies and resonant to the electrodes. The nearest-neighbor electronic couplings between bridge sites are denoted t (curved red lines). The nearest-neighbor electronic couplings between $M_{L(R)}$ and the bridge sites are denoted $T_{L(R)}$ and those between the last (first) bridge site and the L (R) electrode, are denoted $\bar{T}_{L(R)}$ (red dotted lines). D_{L,M_L}, D_{M_L,M_R} and $D_{M_R,R}$ are the distances of the L-M_L, M_L-M_R and M_R-R segments of the junction. The diagram shows a symmetric junction with $D_{L,M_L} = D_{M_R,R} = D_{M_L,M_R}$. $D_{tot} = D_{L,M_L} + D_{M_L,M_R} + D_{M_R,R}$ is the total length of the junction. The distance between nearest neighbor sites is $a = D_{tot}/(N+1)$.

Figure 4.19 (a) Bias-dependent $H^2_{M_L,M_R}(V)$ (eq. (4.30)) versus the bias voltage V at T = 308 K for the positive bias region, (b) Bias-dependent broadening $\Gamma_{L(R)}(V)$ versus bias voltage V. (c) Current (eqs (4.2)-(4.11)) versus bias voltage V using $H_{M_L,M_R}(V=0)$ and $\Gamma_{L(R)}(V=0)$ (red dots, as in Fig. 4.7), and using the $H_{M_L,M_R}(V)$ and $\Gamma_{L(R)}(V)$ (black dots). Parameter values for all graphs: $n_{B_R} = n_{B_M} = n_{B_L} = 5$, $\varepsilon_0^B = 10.0$ *eV*, $\lambda_L = \lambda_R = 0.1$ *eV*, $t = 4.0$ *eV*, $T_L = T_R = 1.5 \times 10^{-1}$ *eV* and $\bar{T}_L = \bar{T}_R = 1.0 \times 10^{-3} eV$.

Figure 5.1 Schematic illustration of the notation used to describe the many-electron basis states relevant to the SF pathways. (a) Examples of singly-excited (LE and CT) and (b) doubly-excited (LDE and CTDE) states using the minimum set of orbitals per fragment (HOMO and LUMO). The kets denote Slater determinants with the spin distributions shown in the diagrams. The actual basis states used in the calculations (Table 5.1 and Supplement section 5.4.1), are spin-adapted (singlet) states that are linear combinations of Slater determinants.

Figure 5.2 Schematic representation of type-I, type-II and type-III D-B regimes in the independent-electron approximation. Virtual orbitals are shown in red and occupied orbitals in blue. Since we only consider bridge-mediated tunneling case, $y > x$.

Figure 5.3 Reference D-B-A systems. (a) Pi-stacking pentacene trimer, (b) non-pi-stacking pentacene trimer, (c) pentacene-tetracene-pentacene trimer, (d) NC1 system. For (a)-(c) $R_{H\text{-}H} \approx 3.5$ Å.

Figure 5.4 $ln|V_{SF}|$ plot as a function of Y/X and z/X parameters for (a) pi-stacking conformation shown in Fig. 5.3a, (b) the non-pi-stacking conformation shown in Fig. 5.3b, (c) the pentacene-tetracene-pentacene molecular system of Fig. 5.3c and (d) the NC1 molecular system of Fig. 5.3d. The dashed lines outline the three regimes defined in Fig. 5.2. The black contour corresponds to a coupling $|V_{SF}| = 10^{-1} eV$, the blue to $|V_{SF}| = 10^{-2} eV$ and the magenta lines to $|V_{SF}| = 10^{-3} eV$. The colormap scaling is the same for all plots. The circles represent the Y/X, z/X and V_{SF} values of the reference systems in Fig. 5.3. The labels (i) to (iv) refer to the pathway structures discussed in the text.

Figure 5.5 Schematic representation of the energies and the couplings structure of the intermediate states of Table 5.1, for (a) the type-I, (b) the type-II (or -III) energetic regime and (c) the deep-tunneling case with $Y/X \gg 1.0$. V_{2e} (red arrows) denotes coupling dominated by 2e matrix elements, $V_{2e} = \langle \Psi_n | \hat{V}^{2e} | \Psi_m \rangle$, and V_{1e} (black arrows) denotes coupling dominated by 1e matrix elements, $V_{1e} = \langle \Psi_n | \hat{h}^{1e} | \Psi_m \rangle$. The weaker matrix elements are represented by dotted lines and $E_{res} = \left(E_{in} + E_{fi} \right) / 2$. These dominant pathway structures relate to symmetric D-B-A systems for which (D=A) and to non-polar solvents.

Figure A.1 Bridge-mediated donor-to-acceptor electron transfer (ET). The energy difference between donor (D) and acceptor (A) electronic states, ΔE_{DA}, is modulated by vibrations (accepting modes) that bring D and A to resonance. In the diagram one accepting mode R is assumed to modulate the D-state energy. When the B electronic state energy (E_B^{el}) is off-resonant to the donor and acceptor energies (E_D^{el}, E_A^{el}), the bridge acts as a tunnelling barrier for the transferring electron. The bridge-mediated tunnelling matrix element between D and A is denoted V. Bridge vibrations that modulate E_B^{el} cause fluctuations in V (promoting modes). The diagram shows a single promoting mode Q. If $E_B^{el}(Q)$ fluctuations are large enough to bring the B state to D (A) resonance, ET may take place by a flickering resonance or a hopping mechanism, rather than tunnelling.

Figure A.2 The dynamics of the accepting mode R in Fig. A.1 depend on the transferring electron's state. When the electron is initially localized at the donor (D) state, the accepting mode R "sees" the potential energy surface $E_D^{BO}(R)$ (diabatic BO surface) with equilibrium value R_D. When the electron has transferred to the acceptor (A) state the dynamics of R is governed by $E_A^{BO}(R)$ with equilibrium value R_A. With the electron initially at D, and assuming that R is a classical vibration, the oscillations of R around R_D lead to D-A energy gap fluctuations $\Delta E_{DA}(R)$. Whenever crosses R_{res}, D an A states become resonant and ET takes place with high probability due to the coupling V, with a probability equal to the Landau-Zener probability $P_{D\to A}^{LZ}$. In the nonadiabatic limit, the coupling is weak $P_{D\to A}^{LZ} \ll 1$, and many crossings of R_{res} are required to change electronic state from D to A (i.e., for ET to take place). Thus, the diabatic BO surfaces (diagonal part of the Hamiltonian in eq. (A.1)), give the correct electronic-state-dependent dynamics of R.

Figure A.3 In the adiabatic limit (strong D-A coupling V) the dynamics of the promoting mode R is best described by an adiabatic BO surface (lowest eigenstate of the Hamiltonian in eq. (A.1)). Due to the large value of V, D and A states are quasi-resonant in a wider region of R around R_{res}. Assuming that R is a classical coordinate, D-to-A ET takes place with near-unity probability every time R enters this quasi-resonance region, $P_{D\to A}^{LZ} \approx 1$. Thus, as a function of R, the potential energy surface that determines the dynamics in the resonance

region is due to the lowest adiabatic BO state which is a linear combination of diabatic D and A BO states of Fig. A.2.

Figure A.4 Vibronic picture of the nonadiabatic ET rate for a quantum accepting mode. The average rate is a thermally weighted sum of vibronic rates $k^{nad}_{D,n_D \to A,n_A}$ between initial $|D;n_D\rangle = |D\rangle|n_D\rangle$ and final $|A;n_A\rangle = |A\rangle|n_A\rangle$ vibronic states. Each transition is induced by the vibronic coupling $V \times \langle n_D | n_A \rangle$. $|n_D\rangle$ and $|n_A\rangle$ denote harmonic oscillator eigenstates of the $E_D^{BO}(R)$ and $E_A^{BO}(R)$, respectively. Γ_{n_D} and Γ_{n_A} are the vibrational relaxation rates of the initial and final vibrational states ($\Gamma = \Gamma_{n_D} + \Gamma_{n_A}$). The quantum nonadiabatic regime is valid when $|V \times \langle n_D | n_A \rangle| < \hbar\Gamma$. In the quantum adiabatic regime, $|V \times \langle n_D | n_A \rangle| \geq \hbar\Gamma$, and coherent oscillations between quasi-resonant $|D\rangle|n_D\rangle$ and $|A\rangle|n_A\rangle$ vibronic states may be important. The ET transition is not fully described by simple rate equations.

Figure A.5 A D moiety connected via left (L) and right (R) B units to distinct A moieties. Upon photo-excitation of D by UV, irreversible ET is initiated to A_L and to A_R simultaneously (with ET rates k_L and k_R). The IR excitation of one B unit which trasiently affects the corresponding ET rate, can irreversibly affect the the L to R reaction yield of the competing ET reactions and thus tune the directionality of ET.

Figure A.6 UV(pump)–IR(pump)-Vis(probe) experiment on an anthracene/dimethylaniline (DMA-GC-Anth) structure bridged by a guanosine-cytidine (GC) hydrogen-bonded pair. Photoexcitation of anthracene by the UV pump induces an ET reaction from DMA to the photo-excited anthracene on a timescale of tens of picoseconds. The experiment found that the IR pulse exciting bridge hydrogen-bond vibrations causes the ET rate slowing about 67% per excited molecule. A more recent experiment showed that the IR excitation accelerates the recombination rate by 3.5-fold per molecule.

Figure A.7 (a) UV(pump)-IR(pump)-IR(probe) experiments on ET molecules with phenothiazine (PTZ) donors, a naphthalene monoimide (NAP) acceptor, and a platinum(II)-trans-acetylide bridge. A 400nm UV-pump prepares a DB^+A^- charge transfer (CT) state. Following the UV excitation a DB^+A^- to $^3D^+BA^-$ ET reaction takes place on timescales of up to tens of picoseconds. The IR excitation of the acetylide bridge -C≡C- stretching modes can

fully suppress this reaction. (b) Experiments with fac-[$Re^{I}(CO)_3$(DCEB)(3-DMABN)] (ReEBA) complexes where 3DMABN is 3-dimethylaminobenzonitrile and DCEB is 4,4′-(dicarboxyethyl)-2,2-bipyridine. Photo-excitation by UV creates a triplet metal-to-ligand charge transfer (^{3}MLCT) excited state where the electron is localized in 3-DMABN. This state then converts to a triplet ligand-to-ligand charge transfer (^{3}LLCT) state through a ~10 picosecond ET reaction from 3-DMABN to DCEB. The IR (pump) excitation which targets the electron-acceptor (DCEB) ring-stretching modes accelerates the ET rate by ~28%.

Figure B.1 Basis States energies as a function of Y/X and z/X parameters for: (a) the pi-stacking tri-pentacene conformation shown in Fig. 5.3a, (b) the non-pi-stacking tri-pentacene conformation shown in Fig. 5.3b, (c) the pentacene-tetracene-pentacene molecular system of Fig. 5.3c, and (d) the NC1 molecular system of Fig. 5.3d.

List of Tables

states for the D-B-A system as a function of ionization potentials, electron affinities, core terms and two-electron integrals.

Table 5.5 Analytical expressions for Hamiltonian matrix elements between spin-adapted states. 1st column: Coupling Notation, V_{1e} denotes coupling dominated by the 1e matrix element (Fock matrix element), while V_{2e} is a coupling dominated entirely by 2e matrix elements. 2nd column: notation of the states involved in the corresponding coupling. 3rd column: Exact expressions for the off-diagonal matrix elements as a function of Fock matrix elements and 2e integrals ignoring overlap off-diagonal matrix elements.

Table 6.1 Spin eigenfunctions $X(k)$ ($k=1-5$) as linear combinations of primitive spin functions, θ_i (i keeps track of the number of primitive functions from 0 to 20) multiplying with the appropriate coefficients, c.

Table 6.2 Spin-spatial multi-electronic states written as linear combinations of singly- and doubly-excited Slater determinants. 1st column: Names of the different groups of lowest-lying singlet basis states for the D-B-A system. 2nd column: Mathematical notation for the spin-adapted basis states in each group. 3rd column: Spin-spatial multi-electronic states as linear combinations of singly- and doubly-excited Slater determinants. In most cases the grouping is according to the B state, such as B^+, B^- and bridge excitonic (BE) state, while the initial and final CTP states are denoted as (in) and (fi).

Table 7.1 Analytical exact expressions for basis-state energies. 1st column: Names of the different groups of the basis states for the D-B-A system. 2nd column: Mathematical notation of the spin-adapted (SA) many-electron basis states. 3rd column: Exact expressions for the excitation energies of these states of the D-B-A system as a function of ionization potentials, electron affinities, core terms and two-electron integrals.

Table 7.2 Analytical exact coupling expressions. 1st column: Mathematical notation of the Hamiltonian element. 2nd column: Symbolism of the calculated coupling, defining the diabatic states that it consists of. 3rd column: Exact expressions for the off-diagonal matrix elements as a function of Fock matrix elements, and two-electron integrals.

CHAPTER 1

Introduction

Molecular electron transfer (ET) reactions are of great importance in chemistry, biology and energy science. [1-4] Over the past decades, experimental, theoretical and computational studies of ET molecules and ET proteins (ETpr's) have shown that it is possible to tune molecular ET rates and the overall charge flow in biological ET chains by chemical modifications of the donor, acceptor and the bridge units or by modifying the solvent environment. [2,5] Since there is extensive knowledge of how to tune solution-phase through-protein ET mechanisms by chemical modifications, [4,5] an attractive idea is to use ETpr's as the main current-carrying material in molecular electronics devices. Thus, an intensive area of research is molecular electron transport (ETr) in molecular junctions. [1,3,6]

Experimental studies by Prof. David Cahen's research team at the Weizmann Institute of Science suggest that metal-containing ETpr's, may be ideal tunable components in a molecular electronics device. [7,8] This research group measured the current-voltage and current-temperature dependencies of Azurin monolayer heterojunctions as a function of metal-type substitution in the Az active site. The experiments give a rich phenomenology of current dependencies [7,8] for a variety of metal substituents. Using models for coherent and incoherent charge transport, we interpret this phenomenology in terms of underlying transport mechanisms that are specific to the different types of metal substituents (see Chapter 3). [9]

How do solution-phase ET mechanisms in a donor-bridge-acceptor system correlate with junction-phase ETr mechanisms for the same donor-bridge-acceptor system? To address this question, we propose donor-bridge-acceptor architectures and junction experiments for observing the Marcus Inverted regime (see Chapter 4). [10] The Marcus inverted region is a signature of solution-phase nonadiabatic ET and it has never been observed in a junction. Our work derives the necessary conditions for observing the full inverted Marcus parabola as a function of donor-acceptor driving force in the junction current. Metal donors and acceptor moieties such as those encountered in biological ET chains are good candidates for the proposed junction.

Singlet Fission (SF) is a spin-allowed process in which a photo-excited singlet state S_1 in a molecular system is converted into two correlated triplet excited states $2\times T_1$. [12-14] SF offers a promising way to overcome the Shockley-Queisser limit on the efficiency of single-junction photovoltaics. [12-15] An extensive body of work has examined SF in different materials [16-19] due to its potential for photovoltaics applications. Part of my research work is dedicated to developing analytical models and semi-analytical / computational frameworks for exploring SF structure-function relationships in donor-bridge-acceptor molecular architectures. In such systems the donor is photo-excited and one measures the rate for creating donor and acceptor (separated) triplets as a function of bridge structure. The proposed semi-analytical / computational framework is used to explain experimental observations on the role of bridge linkers in SF donor-to-acceptor rates (see Chapters 5-8). [19-21] It is also used to characterized the different types of bridge-mediated SF pathways in different classes of molecular systems.

Further, in Appendix A we present a comprehensive review article on vibrational effects in molecular electron transfer reactions. [22] In the following, we give a brief introduction to the theory of ET in molecular systems and of ETr in junctions, as a background for the third and fourth chapters.

1.1 Electron Transfer in Molecules

This section is a brief overview of some of the basic concepts of molecular electron transfer (ET) reactions. The ET process can be thought as a spontaneous transfer of electrons from an initial state spatially localized in the electron donor part to a final state spatially localized in the acceptor part of the molecular system. The dynamics of the electronic transition are always accompanied by instantaneous nuclear rearrangement and by the interaction between electronic and nuclear dynamics. Next, the theories of electron transfer rates will be discussed, accompanied by presentations of the different regimes of electron transfer rates using the Landau-Zener approach. Finally, we conclude with the classical Marcus ET theory in the nonadiabatic regime introducing the well-known Marcus-rate expression.

1.1.1 The Born-Oppenheimer Approximation

Let us first consider a molecule composed of N electrons and N_{nuc} nuclei atoms. The Cartesian coordinates and momenta will be denoted as $\vec{r}_I$ and $\vec{p}_I$, for electrons and $\vec{R}_n$, $\vec{p}_n$ for the nuclei, respectively. The total Hamiltonian operator has the general form

$$\hat{H}^{mol} = \hat{T}^{el} + \hat{T}^{nuc} + \hat{V}, \tag{1.1}$$

$\hat{T}^{nuc}$ is the nuclear kinetic energy, $\hat{T}^{el}$ is the electron kinetic energy, $\hat{V}$ is the potential energy of the system. The kinetic equations of $\hat{T}^{el}$ and $\hat{T}^{nuc}$ are given by,

$$\hat{T}^{el} = \sum_{I=1}^{N} \frac{p_I^2}{2m_{el}}, \hat{T}^{nuc} = \sum_{n=1}^{N_{nuc}} \frac{p_n^2}{2M_n}, \tag{1.2}$$

where, M_n and m_{el} are the mass of the n^{th} nucleus and electron, respectively.

The potential energy includes Coulomb repulsion interactions between electron-electron and nuclear-nuclear, and Coulomb attractive interactions between electrons and nuclei

$$\hat{V}^{2e} = \frac{1}{2}\sum_{I\neq J}^{N}\sum_{J=1}^{N} \frac{1}{4\pi\varepsilon_0}\frac{e^2}{\left|\vec{r}_I - \vec{r}_J\right|}, \hat{V}^{nuc-nuc} = \frac{1}{2}\sum_{m\neq n}^{N_{nuc}}\sum_{n=1}^{N_{nuc}} \frac{1}{4\pi\varepsilon_0}\frac{Z_m Z_n e^2}{\left|\vec{R}_m - \vec{R}_n\right|}, \hat{V}^{el-nuc} = -\sum_{I}^{N}\sum_{n}^{N_{nuc}} \frac{1}{4\pi\varepsilon_0}\frac{Z_n e^2}{\left|\vec{r}_I - \vec{R}_n\right|} \tag{1.3}$$

where, Z_m, Z_n are the atomic numbers of the m^{th} and n^{th} nucleus.

Thus, the time-dependent Schrödinger equation for this system is,

$$\hat{H}^{mol}\vec{\Psi}\left(\vec{r},\vec{R}\right) = \varepsilon\vec{\Psi}\left(\vec{r},\vec{R}\right), \tag{1.4}$$

where, $\vec{\Psi}\left(\vec{r},\vec{R}\right)$ is the multi-particle wavefunction (system eigenstate), and $\vec{r},\vec{R}$ denote the electronic and nuclear Cartesian coordinates, respectively. ε denotes the total energy of the system (eigenenergy).

Due to the large number of particles, the Schrodinger equation cannot be solved analytically and approximations are required. Since nuclei are much heavier than electrons, they move more slowly. [1,3,23] Hence, a good approximation, one can consider the electrons in a molecule to be moving in the field of fixed nuclei. Within the approximation, the kinetic energy of the nuclei, $\hat{T}^{nuc}$, can be neglected and the Coulomb repulsion interactions between the nuclei, $\hat{V}^{nuc-nuc}$, can be consider to be constant. Any constant added to an operator only adds to the operator eigenvalues and has no effect in the operator eigenfunctions. Thus, the remaining terms in the molecular Hamiltonian, are the electronic Hamiltonian or Hamiltonian describing the motion of N in the field of N_{nuc} point charges,

$$\hat{H}^{el}\left(\vec{r},\vec{R}\right)=\hat{T}^{el}+\hat{V}^{el-nuc}+\hat{V}^{2e}. \tag{1.5}$$

The solution to a Schrodinger equation involving the electronic Hamiltonian,

$$\hat{H}^{el}\Psi^{el}\left(\vec{r},\vec{R}\right)=\varepsilon_{el}\Psi^{el}\left(\vec{r},\vec{R}\right) \tag{1.6}$$

is the electronic wavefunction which describes the motion of the electrons and explicitly depends on the electronic coordinates but depends parametrically on the nuclear coordinates. In order to find the total energy of the system, it needs to add to the electronic energy, ε_{el} and the constant nuclear repulsion,

$$\varepsilon=\varepsilon_{el}+\frac{1}{2}\sum_{m\neq n}^{N_{nuc}}\sum_{n=1}^{N_{nuc}}\frac{1}{4\pi\varepsilon_0}\frac{Z_m Z_n e^2}{\left|\vec{R}_m-\vec{R}_n\right|}. \tag{1.7}$$

This approximation, leads to the definition of the Born-Oppenheimer Hamiltonian,

$$\hat{H}^{BO}\left(\vec{r},\vec{R}\right)=\hat{H}^{el}\left(\vec{r},\vec{R}\right)+\hat{V}^{nuc-nuc}. \tag{1.8}$$

The Born-Oppenheimer Hamiltonian $\hat{H}^{BO}$ is comprised of the electronic Hamiltonian $\hat{H}^{el}$ and the nuclei repulsion interactions $\hat{V}^{nuc-nuc}$. Like $\hat{H}^{el}$, so the $\hat{H}^{BO}$ carry a parametric dependence on the nuclear coordinates, $\vec{R}$. Therefore, instead of solving the Schrodinger equation for the total molecular Hamiltonian, one can solve the respective Schrodinger equation within the Born-Oppenheimer approximation,

$$\hat{H}^{BO}\vec{\Psi}^{BO}\left(\vec{r},\vec{R}\right)=E^{BO}\left(\vec{R}\right)\vec{\Psi}^{BO}\left(\vec{r},\vec{R}\right) \tag{1.9}$$

where, $\vec{\Psi}^{BO}\left(\vec{r},\vec{R}\right)$ and $E^{BO}\left(\vec{R}\right)$ are the eigenstates and eigenenergies of the $\hat{H}^{BO}$, respectively. $E^{BO}\left(\vec{R}\right)$ defines a surface in the space of nuclear coordinates $\vec{R}$, the potential energy surface (PES) for the nuclear motions in a specific state.

1.1.2 Regimes of Electron Transfer - Landau-Zener Theory

In order to characterize Electron Transfer (ET) in a DA (Donor - Acceptor) complex, we will use the widely used classical approach developed by Landau and Zener. [1-4,11,23-36] Initially, Landau considered scattering between two atoms, while Zener focused on the electronic states of a diatomic molecule. The advantage of the approach is that one can draw

an analytical formula for the electron transfer rate that applies to any value of the V_{DA} coupling ranging from adiabatic to nonadiabatic ET.

In order to front the ET reaction in a DA complex, according to Landau and Zener, must be chosen a classic description for a single vibrational coordinate. To ensure the ET rate, we let the vibrational coordinate begin moving to the donor potential energy surface (PES) away from the crossing point R_{res}, to the acceptor potential energy surface. If the coordinate moves through the crossover regime, will be determined the probability with which the electron is transferred to the acceptor's level, as well as the probability of remaining at the donor's level.

The vibrational Hamiltonian $E_m(R)$ $(m = D,A)$ includes the dynamic energy of the D and A, $E_D(R)$ and $E_A(R)$, respectively. Both depend on the vibrational coordinate R and may in principle have an arbitrary shape. The crossing point R_{res} between $E_D(R)$ and $E_A(R)$ plays an important role in the transport, so the two dynamic energies are extended around R_{res},

$$E_m(R) = E_{res} - F_m(R_{res})\Delta R \tag{1.10}$$

where,

$$F_m(R_{res}) = -\frac{\partial E_m(R)}{\partial R}\Big|_{R=R_{res}} \tag{1.11}$$

denotes the force with which the vibrational coordinate stabilizes at R_{res} when the electron is in $m = D,A$. Furthermore, $\Delta R = R - R_{res}$, and $E_{res} = E_D(R_{res}) = E_A(R_{res})$ (see Fig. 1.1 below).

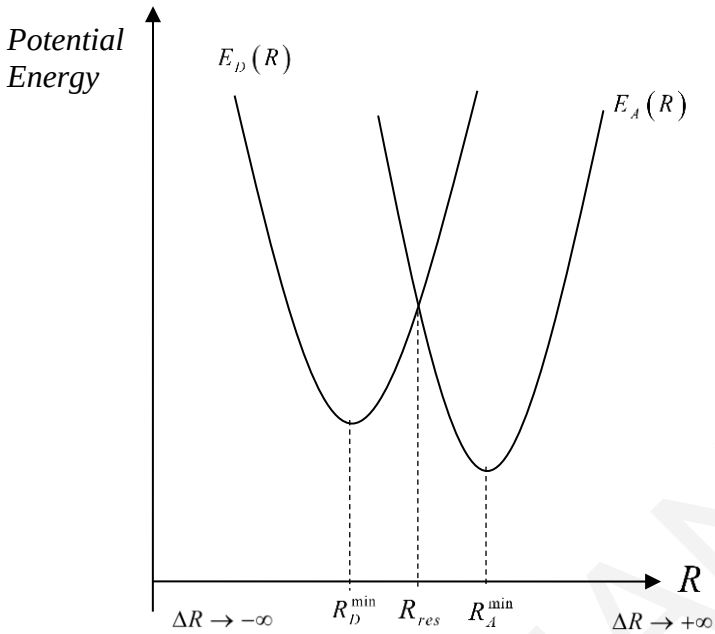

Figure 1.1 The coupled dynamic energy of a DA complex Vs. the coordinate of the reaction. According to Landau-Zener theory, dynamic energies are approached by straight lines around the crossing point. Asymptotic regions $\Delta R \to \pm\infty$ are also indicated.

The time dependence of R (or ΔR) coordinate is unknown. Based on these approaches, Hamiltonian becomes time-dependent,

$$\hat{H}^{DA} = \hat{T}^{vib} + \hat{H}\left(R_{res}\right) + \hat{H}^{el} . \tag{1.12}$$

The classic part $\hat{T}^{vib} + \hat{H}\left(R_{res}\right)$ is less interesting than the following. The time-dependent piece is also written,

$$\hat{H}^{el}(t) = E_D\left(R(t)\right)|D\rangle\langle D| + E_A\left(R(t)\right)|A\rangle\langle A| + V_{DA}\left(|D\rangle\langle A| + |A\rangle\langle D|\right) \tag{1.13}$$

where, $E_D\left(R(t)\right)$, $E_A\left(R(t)\right)$ represents diabatic PES localized at D and A, respectively. At a time window t_{res} the reaction coordinate reaches the resonance region $\left(R\left(t_{res}\right) = R_{res}\right)$ during which the D and A electronic energies cross, such that $E_{res} = E_D\left(R_{res}\right) = E_A\left(R_{res}\right)$.

The D to A transition probability for this crossing event can be estimated adopting the Landau-Zener approach which assumes a linear time dependence of the reaction coordinate around the resonance regime. We perform a Taylor expansion for both PES,

$$E_m\left(R(t)\right) = E_{res} + \left[\left.\frac{dE_m}{dR}\right|_{R_{res}} \times \left.\frac{dR}{dt}\right|_{t_{res}}\right]\left(t - t_{res}\right). \tag{1.14}$$

The D to A Landau-Zener transfer probability is given by,

$$P_{DA} = 1 - exp\left[-\left(2\pi\right)^2 \gamma\right] \tag{1.15}$$

It depends on the so-called Massey parameter which is defined as,

$$\gamma = \tau_{LZ} / \tau_{Rabi} \tag{1.16}$$

and written as a ratio of two times, the Rabi time and the Landau Zener time. The Rabi time is $\tau_{Rabi} = h/\left|V_{DA}\right|$ and is a good estimate for the time required in a time-independent resonant D-A system, i.e., when $\left|E_D - E_A\right| \le \left|V_{DA}\right|$, to induce a complete D to A transition $\left(P_{DA} \approx 1\right)$. Landau-Zener time τ_{LZ} is the spent by the D and A energies in the resonance region in a time-dependent D-A system and given by,

$$\tau_{LZ} = \frac{\left|V_{DA}\right|}{\left|\left\{dR/dt\right|_{t_{res}}\right\}\left\{dE_D/dR - dE_A/dR\right\}\left|_{R_{res}}\right|}. \tag{1.17}$$

In the adiabatic limit $\left(\gamma = \tau_{LZ}/\tau_{Rabi} \gg 1\right)$, the D and A energies remain in resonance for a long time, $\tau_{LZ} > \tau_{Rabi}$ and induce a complete D to A transition. The probability of electron transfer is 100% for each crossing $\left(P_{DA} \approx 1\right)$. The respective adiabatic ET rate can be expressed as a standard Arrhenius $k_{DA} \sim e^{-E_{act}/k_B T}$, where E_{act} is the activation energy to reach the resonance region.

In the nonadiabatic limit, the motion of the reaction coordinate in the resonance region $\left(\left|E_D - E_A\right| \le \left|V_{DA}\right|\right)$ is so fast such that the D and A energies do not remain in resonance for long time, $\tau_{LZ} < \tau_{Rabi}$, in order to induce a complete D to A transition i.e., $\gamma = \tau_{LZ}/\tau_{Rabi} \ll 1$. In the limit, then exponent can be expanded in a Taylor series such that the D to A transition probability becomes promotional to the square of the electronic coupling, $P_{DA} \approx \left(2\pi\right)^2 \gamma \approx \left|V_{DA}\right|^2$, so the corresponding nonadiabatic ET rate is proportional to $\left|V_{DA}\right|^2$. It is obvious, that in the nonadiabatic limit the probability of ET for every crossing is small.

1.1.3 The Nonadiabatic Regime of Electron Transfer and Classical Marcus Theory

The definition of nonadiabatic electron transfer (ET) has already been introduced in the previous section. In molecular ET reactions the observable quantity is often the D to A ET rate and the main model describing ET reactions is the classical Marcus-rate expression. [1-4,11,24-27] "Classical" means that the vibrations of atoms that activate ET are described by classical mechanics. The expression of the rate equation, should be given by a usual Arrhenius form,

$$k_{ET} \propto \left|V_{DA}\right|^2 e^{-E_{act}/k_B T} . \tag{1.18}$$

In the high temperature limit, the energy of a characteristic vibrational quantum $\hbar\omega$ of the reaction coordinate R is much smaller than the thermal energy $k_B T$ $\left(k_B T \gg \hbar\omega\right)$. In this case the vibrational modes of the system can be described using classical physics.

Generally, a collective set of system motions, described by the reaction coordinate R, modulates the energies of D and A electronic states. Then, thermal fluctuations of R, bring the system to a D-A resonance conformation R_{res} for which $E_{res} = E_D\left(R_{res}\right) = E_A\left(R_{res}\right)$ and thus should become ET. The ET from D to A only proceeds if the system is in the resonance regime. In this case, the total energy needed for R to reach R_{res} should be $E^{tot} \geq E_D^{min} + E_{act}$ (see Fig. 1.2 below). For every time t_{res}, R_{res} is reached, the D to A transfer probability will be given by the Landau-Zener transfer probability in the nonadiabatic limit,

$$P_{DA}\left(E^{tot}\right) = \left(2\pi\right)^2 \gamma = \frac{2\pi\left|V_{DA}\right|^2}{\hbar\left|\left\{dR/dt\big|_{t_{res}}\right\}\left\{dE_D/dR - dE_A/dR\right\}\big|_{R_{res}}\right|} \tag{1.19}$$

and the respective ET rate will be given by,

$$k_{DA}\left(E^{tot}\right) = 2\,P_{DA}\left(E^{tot}\right)\frac{\omega}{2\pi} \tag{1.20}$$

As known, for an ensemble of D-A molecules, the ET rate is given by a product of a Boltzmann probability average over the D PES and k_{DA}, for every energy crossing,

$$k_{DA} = \int_{E_D(R_{res})}^{\infty} dE^{tot} k_{DA}\left(E^{tot}\right) P_{Boltz.}\left(E^{tot}\right),$$

$$P_{Boltz.}\left(E^{tot}\right) = \frac{e^{-E^{tot}/k_B T}}{\int_{E_D^{min}}^{\infty} dE^{tot} e^{-E^{tot}/k_B T}}. \tag{1.21}$$

This calculation leads to the Marcus-rate expression,

$$k_{DA} = \frac{2\pi}{\hbar}\left|V_{DA}\right|^2 \rho_{FC} \tag{1.22}$$

where,

$$\rho_{FC} = \frac{1}{\sqrt{4\pi\lambda k_B T}} exp\left(-E_{act}/k_B T\right) \tag{1.23}$$

is the classical Franck-Condon factor (or classical high-temperature Boltzmann probability) for the activation step, [1-4,11,24-27] and

$$E_{act} = \frac{\left(\left|\Delta E\right| + \lambda\right)^2}{4\lambda} \tag{1.24}$$

is the activation energy to reach the resonance conformation R_{res}.

$\left|\Delta E\right| = \left|E_{\mathrm{A}}^{min} - E_D^{min}\right|$ is frequently called as the driving force of the ET reaction, λ denotes the reorganization energy given by, $\lambda = E_{D(A)}\left(R_{A(D)}^{min}\right) - E_{D(A)}\left(R_{D(A)}^{min}\right)$, or $\lambda = m\omega^2\left(R_A - R_D\right)^2/2$. The reorganization energy is defined as the energy required to reorganize the system to the new equilibrium coordinate conformation.

All the parameters we introduced above are shown in the Fig. 1.2 below for the potential energy of the ET system.

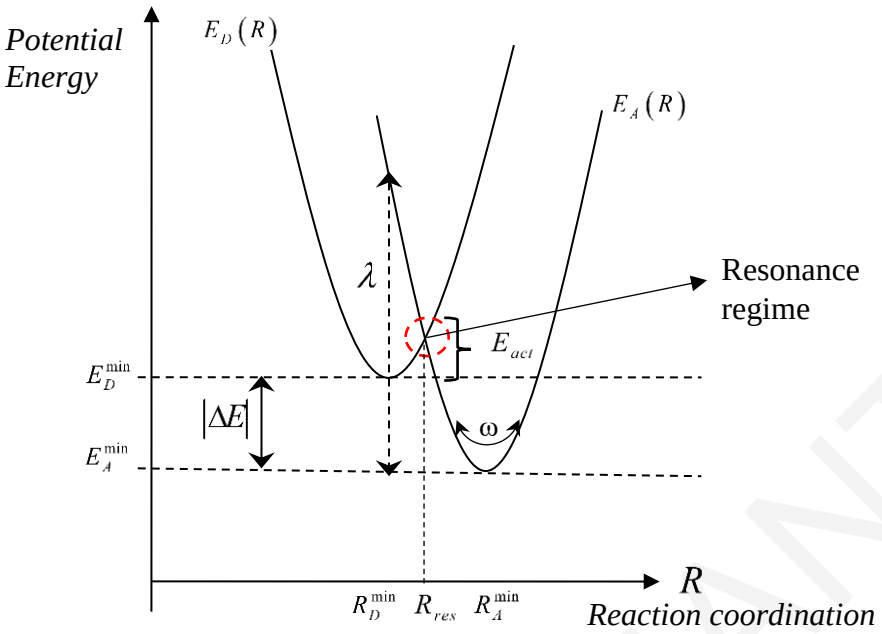

Figure 1.2. Potential energy surfaces of the ET system when the electron is at the D electronic states (initial), E_D and the A electronic states (final), E_A.

Let us examine the ET rate in dependence on the driving force ΔE of the reaction at a given value of V_{DA} and λ. The situation shown in Fig. 1.3a, called the normal regime of the ET. Starting from this regime and increasing the ΔE, move R_{res} to the left until the activation energy $E_{act} = 0$ for $\Delta E = \lambda$ (see Fig. 1.3b). This is an activationless regime. This ET regime is observed in the experiment if the rate becomes temperature-independent. Further increase in ΔE, implies increase in E_{act}. This is the so-called inverted regime.

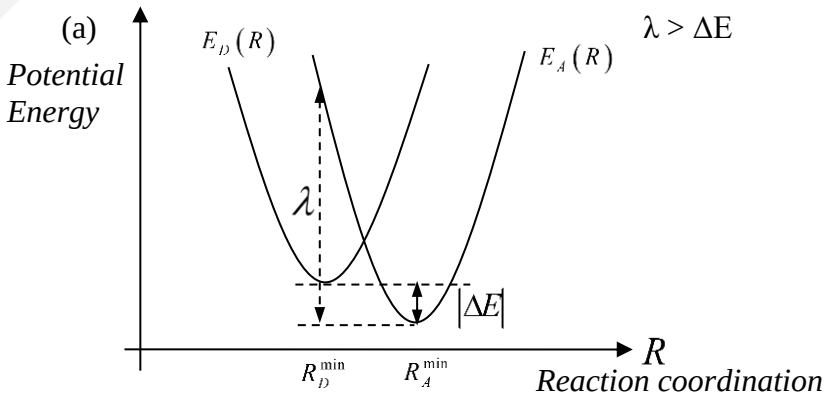

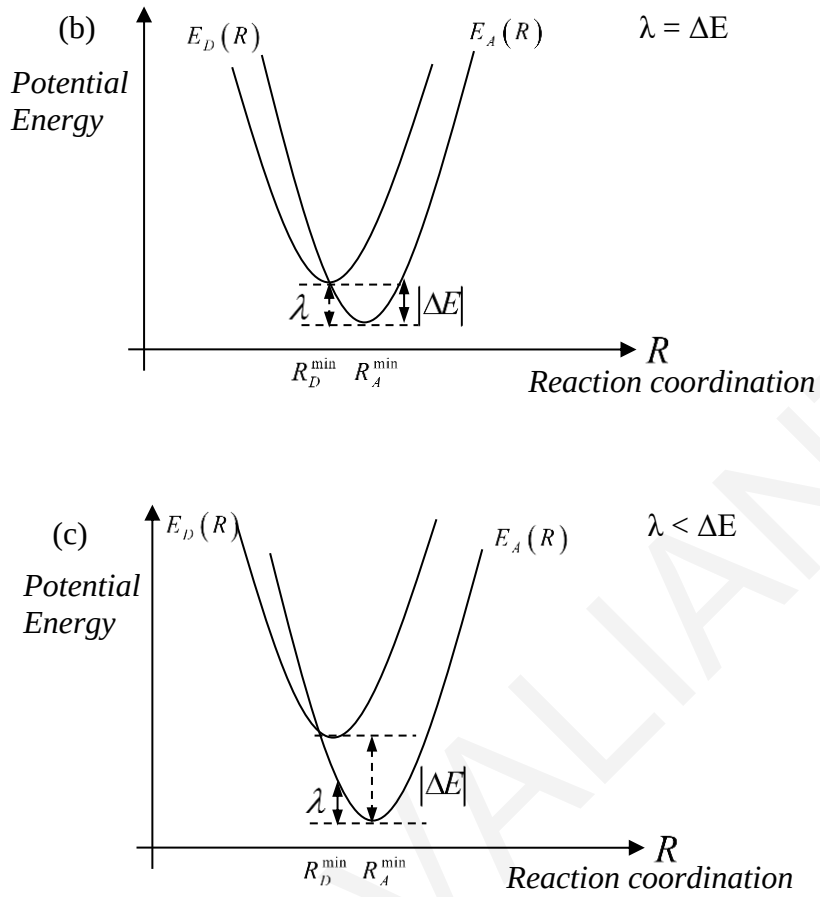

Figure 1.3 ET regimes, (a) normal regime (upper graph), (b) activationless regime (center graph) and (c) inverted regime (lower graph).

1.2 Molecular Electronics

Molecular electronics is the field of science that investigates electronic circuits in which the charge transfer (electrons or holes) takes place in part, through molecules. Obviously, some of the characteristic dimensions of these molecular circuits are of the order of nanometers (or even smaller) and, therefore, molecular electronics should be considered as a subfield of nanosciences and nanotechnology in traditional disciplines such as physics, chemistry, materials science, electrical engineering and biology. [6] From the point of view of basic science, molecular electronics offers the possibility of researching electronic and thermal conductivity on the smallest scale imaginable, where physics is completely dominated by the effects of quantum mechanics. Also, the small dimensions of molecular circuits along with the variety of electrical, mechanical and optical properties of the molecules can lead to countless new natural phenomena. Molecular junctions are also ideal systems where they

can be explored and at the same time shed light on fundamental electron transport mechanisms that play a key role in both chemistry and biology.

1.2.1 Coherent Transfer via Molecular Junctions

The electrical conductivity in macroscopic metal wires is described by Ohm's law, which states that the current I is proportional to the applied voltage V. The constant of proportionality is simply the conductivity, G, which for a given sample increases linearly with transverse region S and is inversely proportional to the length of L, i.e.,

$$G = \sigma \frac{S}{L} \tag{1.25}$$

where σ is the conductivity of the sample. Conductivity will be a key quantity in our analysis, for the transport properties of atomic and molecular nodes. However, concepts such as Ohm's law do not apply on an individual scale. Atomic-sized conductors are a marginal case of a mesoscopic system in which quantum coherence plays a central role in transport properties.

In this chapter we will introduce the scattering (or Landauer) approach, [1,3,6] which is currently the best theoretical formalism to describe coherent transport in nanowires. The central idea of this approach is that if one can ignore inelastic interactions, a transport problem can always be treated as a scattering problem. This, in practice means that transport properties, such as electrical conductivity, are closely linked to the transmission probability of an electron.

1.2.2 Introduction to the Landauer Approach

In a typical transfer experiment in a nanodevices, the sample is connected to macroscopic electrodes from a set of conductors (or electrodes) that allow current to flow from the sample and determine the voltage difference between the electrodes. The electrodes act as ideal electron reservoirs in thermal equilibrium with well-defined temperature and chemical potential. The basic idea of the scattering approach is to correlate transport properties with transmission and reflection probabilities. In this one-electron approach, phase-coherence is supposed to be maintained throughout the samples and non-elastic scattering limited to electron reservoirs only. Instead of dealing with complex processes that take place inside the

reservoirs, one deals only with their description as a set of boundary conditions. Despite its simplicity, this approach has been very successful in explaining many nanowire experiments.

Before dealing with the description of the general scattering formalism, it is useful to understand the relationship between current I and the transmission probability T with a simple argument. Consider a one-dimensional state, as illustrated in Fig. 1.4. Here, the potential simulates the central part of an intersection, where electrons are scattered elastically before reaching one of the electrodes. Assume that when the electrons are in the reservoirs, they are in thermal equilibrium at the temperature of the corresponding electrode. Let us now consider that a plane wave, $\left(1/\sqrt{L}\right)e^{ikx}$ (incident reservoir scattering state) strikes the potential barrier from the left (L represents the length of the system). This wave is partially reflected with probability amplitude R and partially transmitted with probability $T=|t|^2$. We can now calculate the electric current density, J_k, carried by an electron and described by this wavefunction. It will be given by the following expression,

$$J_k = \frac{\hbar}{2mi}\left[\Psi^*(x)\frac{d\Psi}{dx} - \Psi(x)\frac{d\Psi^*}{dx}\right] = \frac{e}{L}u(k)T(k) \tag{1.26}$$

where $u(k)=\hbar k/m$ is the group velocity.

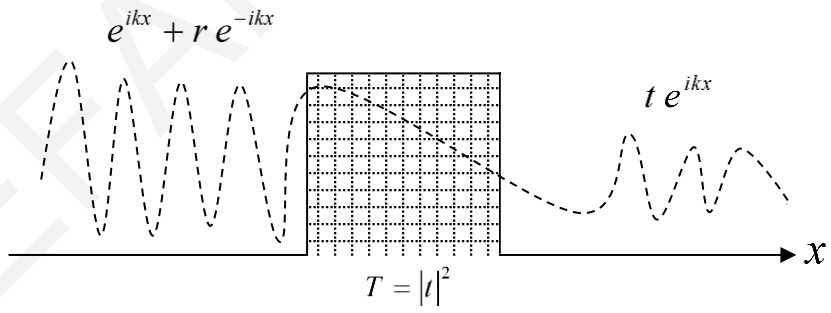

Figure 1.4 Scattering wavefunction (incident wave) colliding with a potential barrier. The wave is partially reflected with probability R and partially transmitted with probability $T=|t|^2$ (where t is the width of the transmission probability). [6]

In a solid-state device there are many electrons that contribute to the value of the current. Therefore, we need to enter a sum with respect to all k. In addition, we must take into account Pauli's principle, which in practice means that we must introduce a factor

$f_L(k)\left(1-f_R(k)\right)$, where $f_{L(R)}(k)$ is the Fermi function of the electron reservoir on the left, L (right, R) of the potential barrier. These Fermi functions also take into account the fact that the corresponding chemical potentials can be changed by an applied polarization voltage, V. The factor $f_L(k)\left(1-f_R(k)\right)$ ensures that only the initially occupied states on the left and unoccupied states on the right contribute to the current flowing from left to right, $J_{L\to R}$,

$$J_{L\to R}=\frac{e}{L}\sum_k u(k)T(k)\,f_L(k)(1-f_R(k)) \tag{1.27}$$

Now, we can convert the sum to an integral with the usual substitution $(1/L)\sum_k g(k)\to\frac{1}{2\pi}\int g(k)dk$. So, we have,

$$J_{L\to R}=\frac{e}{2\pi}\int u(k)T(k)\,f_L(k)(1-f_R(k))\,dk \tag{1.28}$$

Then we can do the conversion from the variable k to the energy E, by entering the density of states, $\frac{dk}{dE}=\left(\frac{dE}{dk}\right)^{-1}=\frac{m}{\hbar^2 k}$, since $E=\frac{\hbar^2k^2}{2m}$. The current flowing from left to right, $J_{L\to R}$, takes the form,

$$J_{L\to R}=\frac{e}{h}\int T(E)\,f_L(E)(1-f_R(E))\,dE \tag{1.29}$$

Now, the total current $I(V)=J_{L\to R}-J_{R\to L}$, can easily be expressed as,

$$I(V)=\frac{2e}{h}\int_{-\infty}^{\infty}T(E)\left[f_L(E)-f_R(E)\right]dE \tag{1.30}$$

This expression is the simplest version of the so-called Landauer formalism and shows the close relation between current and the transmission probability. [1,3,6] At zero temperature, $f_{L(R)}(E)$ are step functions, equal to 1 below $E_F+eV/2$ and $E_F-eV/2$ respectively, and 0 above these energies. If we also assume that we have low voltages (linear region), this expression (eq. 1.30) becomes $I=GV$, where the conductivity is $G=\left(2e^2/h\right)T$, and where T is calculated in the Fermi energy. This expression proves that if the electron transmission between the two electrodes is perfect, then the conductivity is given by the quantity $G_0=2e^2/h\approx\left(12.9\,k\Omega\right)^{-1}$.

1.2.3 Introduction to the Hopping Mechanism

One of the central topics of this chapter is the analysis of charge transfer in situations in which phase coherence is completely lost within the molecular junction. This incoherent limit describes the transition when the tunneling traversal time is significantly longer than the time scale associated with the inelastic interactions. Obviously, this becomes more likely as the length of the molecular junction increases. In the extreme case where the inelastic scattering time is much shorter than the tunneling traversal time, the current is transferred by electrons that successively hop from one part of the molecule (localized state) to another in an incoherent way. This mechanism of transport is also referred to as hopping regime. [1,3,4,26,28-30]

In long molecules, especially biological ones, there are additional issues that need to be considered when exploring electronic transport through them. Thus, for example, the environment (solvent, atmosphere, etc.) in which the experiments are performed plays a decisive role. The hopping regime, however, is characterized by the following two characteristics: the conductivity decreases inversely with the length of the molecular wire and also depends exponentially on temperature as $e^{-\Delta E/k_B T}$, where ΔE is an activation energy that depends on the system under study.

In the following, we will discuss a simple model that shows where these two characteristics come from. The model for a metal-molecule-metal junction is schematically represented in Fig. 1.5. Here, the molecular bridge has N parts (with localized states-levels and electronic couplings between them). The hopping transfer mechanism is described by transfer rates $k_{i,j}$ (from state j to state i). For the sake of simplicity, we assume that all states have the same energy, which differs by ΔE from the Fermi energy (equilibrium energy) of the conductors.

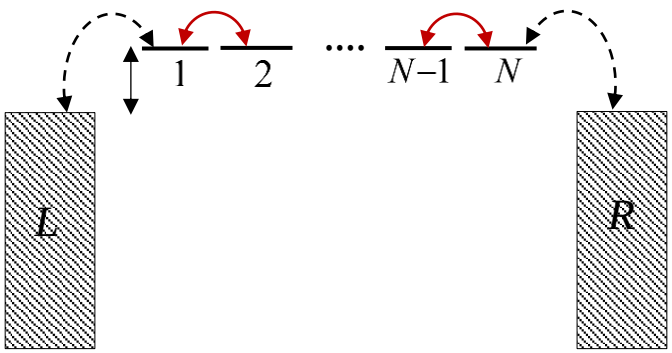

Figure 1.5 Schematic representation of the model described in the hopping mechanism via a molecular junction. Here, each localized electron level j in the j regime of the molecule (straight lines) is connected to the nearest levels with a transfer rate $k_{j,j\pm1}$ (dashed arrow lines). The metallic states of the electrodes are shown on the left and right and ΔE is the activation energy. [6]

In this model the current between the states j and $j+1$ is determined by the rate $k_{j,j+1}$ and the probabilities of finding the charge at the respective levels P_j and P_{j+1},

$$I_j = e\left(k_{j+1,j}P_j - k_{j,j+1}P_{j+1}\right) \tag{1.31}$$

The rates follow the following equations,

$$\begin{aligned}
&\dot{P}_1 = -(k_{0,1}+k_{2,1})P_1 + k_{1,0}P_0 + k_{1,2}P_2 \\
&\vdots \\
&\dot{P}_j = -(k_{j-1,j}+k_{j+1,j})P_j + k_{j,j-1}P_{j-1} + k_{j,j+1}P_{j+1} \\
&\vdots \\
&\dot{P}_N = -(k_{N-1,N}+k_{N+1,N})P_N + k_{N,N-1}P_{N-1} + k_{N,N+1}P_{N+1}
\end{aligned} \tag{1.32}$$

where $\dot{P}_j$ means dP_j/dt, $P_0 = f_L$ and $P_{N+1} = f_R$, $f_{L(R)}$ are the Fermi functions that describe the electron occupations on the left and right electrodes. We are interested in cases of stationary current where $\dot{P}_j = 0$. In this case, the previous kinetic equations are combined into the following algebraic equations,

$$\begin{aligned}
&(k_{0,1}+k_{2,1})P_1 = k_{1,0}P_0 + k_{1,2}P_2 \\
&\vdots \\
&(k_{j-1,j}+k_{j+1,j})P_j = k_{j,j-1}P_{j-1} + k_{j,j+1}P_{j+1} \\
&\vdots \\
&(k_{N-1,N}+k_{N+1,N})P_N = k_{N,N-1}P_{N-1} + k_{N,N+1}P_{N+1}
\end{aligned} \tag{1.33}$$

As a further simplification, we assume that all internal rates in the bridge molecule are equal: $k_{j,j\pm1} = k$. In addition, the state of equilibrium leads to the following rates relations,

$$k_{1,0} = k_L e^{-(\Delta E - eV)/k_B T},\ k_{0,1} = k_L$$
$$k_{N,N+1} = k_R e^{-\Delta E/k_B T},\ k_{N+1,N} = k_R \tag{1.34}$$

Solving the above equations, we end up with the steady state current,

$$I = e \frac{e^{-\Delta E/k_B T}}{\left[1/k_L + 1/k_R + (N-1)/k\right]} \left[e^{eV/k_B T} f_L - f_R \right]. \tag{1.35}$$

Also, the corresponding linear conductivity can be expressed as,

$$G = \frac{e^2}{k_B T} \frac{e^{-\Delta E/k_B T}}{\left[1/k_L + 1/k_R + (N-1)/k\right]}. \tag{1.36}$$

Here, for the sake of simplicity, we have neglected the temperature dependence of the Fermi functions of the conductors. From the previous equation one can observe the two characteristics described at the beginning of this section. First, we observe that the conductivity decreases inversely with respect to the number of states, N and therefore to the length of the molecular bridge. This is nothing but Ohm's classical law, which is a consequence of the loss of quantum coherence. Conductivity, on the other hand, depends exponentially on temperature, T as in any thermal process. In this model, this process takes place at the metal-molecule interfaces, but in general can occur at any point along the junction (i.e., the rates $k_{j,j\pm1} = k$).

1.3 References

[1] May, V.; Kuhn, O. *Charge and Energy Transfer Dynamics in Molecular Systems*; 3rd ed.; Wiley-VCH, Berlin, 2011.

[2] Jortner, J.; Bixon, M.; Prigogine, I.; Rice, S.A. *Electron Transfer - from Isolated Molecules to Biomolecules*; John Wiley & Sons, *New York, 1999.*

[3] Nitzan A. *Chemical Dynamics in Condensed Phases*; Oxford University Press, 2006.

[4] *Balzani, V.; Piotrowiak, P.; Rodgers, M.A.J.; Mattay, J.; Astruc, D.; Gray, H.B.; Wrinkler, J.; Fukuzumi, S.; Mallouk, T.E.; Haas, Y.; et al. Electron Transfer in Chemistry*; I–V ed.; Weinheim:Wiley-VCH, 2001.

[5] Winkler, J.R.; Gray, H.B. Electron Flow through Metalloproteins. *Chem. Rev*. **2014**, *114*, 3369-3380.

[6] Cuevas, J.C.; Scheer, E. *Molecular Electronics: An Introduction to Theory and Experiment*; 2nd ed.; World Scientific, Singapore, 2017.

[7] Amdursky, N.; Sepunaru, L.; Raichlin, S.; Pecht, I.; Sheves, M.; Cahen, D. Electron Transfer Proteins as Electronic Conductors: Significance of the Metal and Its Binding Site in the Blue Cu Protein, Azurin. *Adv Sci (Weinh).* **2015**, *2*, 1400026.

[8] Yu, X.; Lovrincic, R.; Sepunaru, L.; Li, W.; Vilan, A.; Pecht, I.; Sheves, M.; Cahen, D. Insights into Solid-State Electron Transport through Proteins from Inelastic Tunneling Spectroscopy: The Case of Azurin. *ACS Nano*. **2015**, *9*, 9955-9963.

[9] Valianti, S.; Cuevas, J. C.; Skourtis, S. S. Charge-Transport Mechanisms in Azurin-Based Monolayer Junctions. *J. Phys. Chem. C* **2019**, *123 (10)*, 5907−5922.

[10] Valianti, S.; Skourtis, S.S. Observing Donor-to-Acceptor Electron-Transfer Rates and the Marcus Inverted Parabola in Molecular Junctions. *J. Phys. Chem. B* **2019**, *123 (45)*, 9641-9653.

[11] Marcus, R.A; Sutin, N. Electron transfers in chemistry and biology. *Biochim. Biophys. Acta.* **1985**, *811*, 265-322.

[12] Smith, M.B.; Michl, J. Singlet Fission. *Chem. Rev.* **2010**, *110*, 6891-6936.

[13] Smith, M.B.; Michl, J. Recent Advances in Singlet Fission. *Annu. Rev. Phys. Chem.* **2013**, *64*, 361-384.

[14] Casanova, D. Theoretical Modeling of Singlet Fission. *Chem. Rev.* **2018**, *118*, 7164-7207.

[15] Hanna, M. C.; Nozik, A. J. Solar conversion efficiency of photovoltaic and photoelectrolysis cells with carrier multiplication absorbers. *J. Appl. Phys.* **2006**, *100*, 074510.

[16] Burdett, J. J.; Bardeen, C.J. The Dynamics of Singlet Fission in Crystalline Tetracene and Covalent Analogs. *Acc. Chem. Res.* **2013**, *46 (6)*, 1312–1320.

[17] Pensack, R.D. *et al*. Exciton Delocalization Drives Rapid Singlet Fission in Nanoparticles of Acene Derivatives. *J. Am. Chem. Soc.* **2015**, *137 (21)*, 6790–6803.

[18] Zimmerman, P. M.; Zhang, Z.; Musgrave, C. B. Singlet Fission in pentacene through multi-exciton quantum states. *Nat. Chem.* **2010**, *2*, 648-652.

[19] Basel, B. S. *et al*. Evidence for Charge-Transfer Mediation in the Primary Events of Singlet Fission in a Weakly Coupled Pentacene Dimer. *Chem.* **2018**, *4 (5)*, 1092-1111.

[20] Basel, B. S. *et al*. Unified model for singlet fission within a non-conjugated covalent pentacene dimer. *Nat Commun.* **2017**, *8*, 15171.

[21] Papadopoulos, I. *et al*. Varying the Interpentacene Electronic Coupling to Tune Singlet Fission. *J. Am. Chem. Soc.* **2019**, *141*, 6191-6203.

[22] Valianti, S.; Skourtis, S. S. Vibrational control of molecular electron transfer reactions. *Mol. Phys.* **2019**, *117 (19)*, 2618-2631.

[23] Atkins, P.; Friedman, R. *Molecular Quantum Mechanics*; 5th ed.; Oxford Univ. Press, New York, 2011.

[24] Blumberger, J. Recent Advances in the Theory and Molecular Simulation of Biological Electron Transfer Reactions. *Chem. Rev.* **2015**, *115 (20)*, 11191–11238.

[25] Mohseni, M.; Omar, Y.; Engel, G.; Plenio, M.B. *Quantum Effects in Biology*; Cambridge Univ. Press, 2014.

[26] Kuznetsov, A.M.; Ulstrup, J. *Electron Transfer in Chemistry and Biology: An Introduction to the Theory*. John Wiley & Sons, Chichester, 1999.

[27] Skourtis, S.S. Reviewprobing protein electron transfer mechanisms from the molecular to the cellular length scales. *Inc. Biopol. Pept. Sci.* **2013**, *100 (1)*, 82-92.

[28] Zhang, J.; Kuznetsov, A.; Medvedev, I. G.; Chi, Q.; Albrecht, T.; Jensen, P.; Ulstrup, J. Single-Molecule Electron Transfer in Electrochemical Environments. *Chem. Rev.* **2008**, *108*, 2737−2791.

[29] Schmickler, W.; Santos, E. *Interfacial Electrochemistry*, 2nd ed.; Springer: Berlin, 2010.

[30] Migliore, A.; Nitzan, A. Nonlinear Charge Transport in Redox Molecular Junctions: A Marcus Perspective. *ACS Nano* **2011**, *5*, 6669−6685.

CHAPTER 2

Computational Methodologies

The aim of quantum-chemical computational methods is to determine the molecular electronic and vibrational structure. The central approximation used in most methods is the Born-Oppenheimer approximation mentioned in Chapter 1. Ab-initio quantum-chemical methods solve numerically the molecular Schrödinger equation with inputs the values of the fundamental constants, the atomic numbers of the atoms and their coordinates. The computations of electronic and vibrational structure can be performed using a variety of quantum chemistry computer programs. In this chapter we describe basic concepts underlying quantum-chemical computational techniques that are used in this dissertation. I mainly performed ab initio electronic structure calculations using the GAMESS-US and PyQuante package programs. [1-4] These computational approaches were mostly used in the studies of Singlet Fission described in Chapters 5-8.

2.1 Hartree-Fock Theory

In computational physics and chemistry, the Hartree–Fock (HF) method is an approximate method for the determination of the wavefunction and the corresponding energy of a quantum many-body system in a stationary state. [5-8] The HF method often assumes that the exact $N-$ body wavefunction of the system can be approximated by a single Slater determinant [9] (in the case where the particles are fermions) or by a single permanent (in the case of bosons) of N spin-orbitals. By invoking the variational method, one can derive a set of $N-$ coupled equations for the N spin orbitals. A solution of these equations yields the HF wavefunction and energy of the system.

The HF method is the starting point for a plurality of electronic structure computational approaches. The basic idea is to first model the ground state, Ψ_0 and then any multi-electronic state, as a single Slater determinant. Each of these determinants consist of products of N spin orbitals, $\chi(\vec{x})$, each a product of a spatial orbital, $\psi(\vec{r})$, and a spin function (spin up $\alpha(\omega)$ or spin down $\beta(\omega)$). Sometimes it is convenient to use a notation that indicates a spin orbital by its spatial part, using a bar $\left(\overline{\psi}(\vec{r}) \equiv \psi(\vec{r})\beta(\omega)\right)$ or a lack of a bar

$\left(\psi(\vec{r}) \equiv \psi(\vec{r})\alpha(\omega)\right)$ to describe the spin component. The HF $N-$ electrons ground state is the single determinant

$$\Psi_0 = \frac{1}{\sqrt{N!}} \begin{vmatrix} \chi_i(\vec{x}_1) & \chi_j(\vec{x}_1) & \cdots & \chi_k(\vec{x}_1) \\ \chi_i(\vec{x}_2) & \chi_j(\vec{x}_2) & \cdots & \chi_k(\vec{x}_2) \\ \vdots & \vdots & & \vdots \\ \chi_i(\vec{x}_{N_{el}}) & \chi_j(\vec{x}_{N_{el}}) & \cdots & \chi_k(\vec{x}_N) \end{vmatrix}. \tag{2.1}$$

The factor $(N!)^{-1/2}$ is a normalization factor. This Slater determinant has N electrons occupying N spin orbitals $(\chi_i, \chi_j, \ldots, \chi_k)$ without specifying which electron is in which orbital. Slater determinants meet the requirement of the antisymmetric principle since, interchanging the coordinates of any two electrons (corresponding to interchanging two rows of the Slater determinant), changes the sign of the determinant. It would be useful for the rest of the discussion to introduce a short notation for a normalized Slater determinant, which includes the normalization constant,

$$\Psi_0 = \Psi(\vec{x}_1, \vec{x}_2, \ldots, \vec{x}_N) = |\chi_i \chi_j \ldots \chi_k\rangle \tag{2.2}$$

choosing the electron labels to be in the order $x_1, x_2, \ldots, x_N$.

Starting with the Born-Oppenheimer approximation, the molecular Hamiltonian, $\hat{H}^{BO}$ can be written as the sum of the electronic Hamiltonian, $\hat{H}^{el}$ and the repulsive Coulomb interaction between nuclei, $\hat{V}^{nuc-nuc}$

$$\hat{H}^{BO} = \hat{H}^{el} + \hat{V}^{nuc-nuc}, \tag{2.3}$$

$$\hat{H}^{el} = \hat{T}^{el} + \hat{V}^{el-nuc} + \hat{V}^{2e}. \tag{2.4}$$

The first two terms in the electronic Hamiltonian constitute the one-electron operator, $\hat{h}^{1e}$ including the kinetic energy of the N electrons as well as the attractive interactions between the N electrons and the N_{nuc} nuclei. The last term constitutes the two-electron Coulombic operator, $\hat{V}^{2e}$ describing the repulsive interactions between the electrons.

The essence of the HF method is that the Coulombic two-electron interactions, $\hat{V}^{2e}$ are treated in an "average" way, so that each single electron is considered to be embedded in the average electrostatic field of the nuclei and the remaining electrons. [5,6] The repulsive Coulomb interactions between nuclei, $\hat{V}^{nuc-nuc}$ are a constant for the computation of

electronic structure (but become as dynamical variables for the computational of vibrational structure in the Born-Oppenheimer approach operations). The variation principle (on which the computational HF methodology is based) states that the best wavefunction of the form in eq. (2.1) is the one that gives the lowest possible energy,

$$E_0 = \langle \Psi_0 | \hat{H}^{el} | \Psi_0 \rangle \tag{2.5}$$

which is always greater or equal to the real the ground state energy of the Hamiltonian.

The spin orbitals are computed by minimizing E_0 with respect to variations in the orbitals. This variational method leads to a self-consistent field equation, known as the Hartree-Fock equation which determines the optimal spin orbitals, [5,6]

$$\hat{f}(\vec{x}_1)\chi_i(\vec{x}_1) = \varepsilon_i \chi_i(\vec{x}_1). \tag{2.5}$$

ε_i is the energy of the χ_i spin orbital and $\hat{f}$ is an effective one-electron operator (called the Fock operator). The Fock operator is defined as a sum of the core-Hamiltonian $\hat{h}^{1e}$ (one-electron operator), the Coulomb $\hat{J}$, and the exchange operator $\hat{K}$.

$$\hat{f}(\vec{x}_1) = \hat{h}^{1e}(\vec{x}_1) + \sum_b \left[\hat{J}_b(\vec{x}_1) - \hat{K}_b(\vec{x}_1) \right], \tag{2.6}$$

where the sum is over all the occupied orbitals. The Coulomb operator $\hat{J}_b$ acting on spin orbital χ_i represents the average potential of an electron in spin orbital χ_i at position $\vec{x}_1$ due to the charge distribution from an electron in spin orbital χ_b,

$$\hat{J}_b(\vec{x}_1)\chi_i(\vec{x}_1) = \left(\int d\vec{x}_2 \, \chi_b^*(\vec{x}_2) r_{12}^{-1} \chi_b(\vec{x}_2) \right) \chi_i(\vec{x}_1). \tag{2.7}$$

In the same way, we define the exchange operator $\hat{K}_b$ derived from the antisymmetric property of the determinantal wavefunction. This operator is defined as,

$$\hat{K}_b(\vec{x}_1)\chi_i(\vec{x}_1) = \left(\int d\vec{x}_2 \, \chi_b^*(\vec{x}_2) r_{12}^{-1} \chi_i(\vec{x}_2) \right) \chi_b(\vec{x}_1). \tag{2.8}$$

For an electron in spin orbital χ_i the expectation values of the Coulomb and exchange potentials $\hat{J}_b$ and $\hat{K}_b$ are just the well-known Coulomb and exchange integrals, i.e.,

$$\langle \chi_i(\vec{x}_1) | \hat{J}_b(\vec{x}_1) | \chi_i(\vec{x}_1) \rangle = \int d\vec{x}_1 \, d\vec{x}_2 \, \chi_i^*(\vec{x}_1) \chi_i(\vec{x}_1) \, r_{12}^{-1} \, \chi_b^*(\vec{x}_1) \chi_b(\vec{x}_1) = [ii|bb] \tag{2.9}$$

$$\left\langle \chi_i(\vec{x}_1)\middle|\hat{K}_b(\vec{x}_1)\middle|\chi_i(\vec{x}_1)\right\rangle = \int d\vec{x}_1\, d\vec{x}_2\, \chi_i^*(\vec{x}_1)\chi_b(\vec{x}_1)\, r_{12}^{-1}\, \chi_b^*(\vec{x}_1)\chi_i(\vec{x}_1) = \left[ib\middle|bi\right] \quad (2.10)$$

2.1.1 Closed-Shell Hartree-Fock: Restricted Spin Orbitals

The spin orbitals described in the previous section may be of two types: restricted spin orbitals, which are constrained to have the same spatial function for spin functions α (spin up) and β (spin down), and unrestricted spin orbitals, which have different spatial functions for spin up and spin down. In this section we focus on procedures calculating closed-shell restricted HF (RHF) wavefunctions. In other words, the RHF method assumes that each spatial orbital $\psi(\vec{r})$ is doubly occupied by electrons with opposite spins.

A restricted set of N spin orbitals $\chi_i(\vec{x})$ has the form [5]

$$\chi_i(\vec{x}) = \begin{cases} \psi_j(\vec{r})\alpha(\omega) \\ \psi_j(\vec{r})\beta(\omega) \end{cases}, j = 1,\ldots,N/2, \quad (2.11)$$

and the closed-shell restricted ground state is

$$\Psi_0^{RHF} = \left|\psi_1 a\, \psi_1 \beta \ldots \psi_{N/2} a\, \psi_{N/2}\beta\right\rangle = \left|\psi_1 \bar{\psi}_1 \ldots \psi_{N/2}\bar{\psi}_{N/2}\right\rangle. \quad (2.12)$$

By converting the general HF equation (2.5) to a spatial orbital eigenvalue equation, we obtain the Roothan equations. [10] The HF equations for the individual spatial orbital wavefunctions are,

$$\hat{f}(\vec{r}_1)\psi_j(\vec{r}_1) = \varepsilon_j \psi_j(\vec{r}_1). \quad (2.13)$$

The closed-shell Fock operator thus has the form,

$$\hat{f}(\vec{r}_1) = \hat{h}^{1e}(\vec{r}_1) + \sum_b^{N/2}\left[2J_b(\vec{r}_1) - K_b(\vec{r}_1)\right] \quad (2.14)$$

where now the closed-shell Coulomb and exchange operators are defined by

$$J_b(\vec{r}_1) = \int d\vec{r}_2\, \psi_b^*(\vec{r}_2) r_{12}^{-1} \psi_b(\vec{r}_2) \quad (2.15)$$

$$K_b(\vec{r}_1)\psi_j(\vec{r}_1) = \left[\int d\vec{r}_2\, \psi_b^*(\vec{r}_2) r_{12}^{-1} \psi_j(\vec{r}_2)\right]\psi_b(\vec{r}_1). \quad (2.16)$$

These equations are analogous to those for spin orbitals eqs (2.5)-(2.8), except for the "2" factor occurring with the Coulomb operator and the sum in eq. (2.14) which is over the $N/2$ occupied orbitals $\{\psi_b(\vec{r})\}$.

The closed-shell HF energy for the closed-shell determinant Ψ_0^{RHF} (see eq. (2.12)) is

$$E_0^{RHF} = 2\sum_{\alpha} h_{aa} + \sum_{\alpha}\sum_{b}[2J_{\alpha b} - K_{\alpha b}] \tag{2.17}$$

where, h_{aa} is the matrix element $\langle\psi_\alpha|\hat{h}^{1e}|\psi_\alpha\rangle$ and $J_{\alpha b}$ $(K_{\alpha b})$ are the Coulomb (exchange) integrals over the spatial molecular orbitals ψ_α and ψ_b .

2.1.2 The Roothan Equations

To solve the HF equation (2.13) one must introduce a set of K known spatial (atom-centered) basis functions and express each unknown molecular orbital as a linear combination of the basis functions,

$$\psi_j = \sum_{\mu=1}^{K} C_{\mu j}\,\varphi_\mu\,,\ j = 1,2,\ldots,K\,. \tag{2.18}$$

$C_{\mu j}$ are unknown coefficients and $\{\varphi_\mu\}$ is a set of K atomic orbital basis functions. Substituting eq. (2.18) into HF eq. (2.13) and multiplying by $\varphi_\mu^*(\vec{r}_1)$, one can arrive at two matrices, the overlap matrix $\tilde{S}$ and the Fock matrix $\tilde{F}$ which are defined as,

$$S_{\mu\nu} = \int d\vec{r}_1\,\varphi_\mu^*(\vec{r}_1)\,\varphi_\nu(\vec{r}_1) \tag{2.19}$$

$$F_{\mu\nu} = \int d\vec{r}_1\,\varphi_\mu^*(\vec{r}_1)\,\hat{f}(\vec{r}_1)\,\varphi_\nu(\vec{r}_1)\,. \tag{2.20}$$

With these definitions of $\tilde{F}$ and $\tilde{S}$ the integrated HF equation can be written as,

$$\sum_{\nu} F_{\mu\nu}C_{\nu j} = \varepsilon_j \sum_{\nu} S_{\mu\nu}C_{\nu j}\,,\ j = 1,2,\ldots,K \tag{2.21}$$

These are the Roothan equations that can be written in matrix form as,

$$\tilde{F}\,\tilde{C} = \tilde{S}\,\tilde{C}\,\tilde{\varepsilon} \tag{2.22}$$

where, $\tilde{C}$ and $\tilde{F}$ are $K \times K$ square matrices of the coefficients and the Fock elements respectively. $\tilde{\varepsilon}$ is a $K \times K$ diagonal matrix of the orbital energies ε_j.

2.1.3 The Fock Matrix

The Fock matrix is the matrix representation of the Fock operator (see eq. (2.14)) in the $\{\varphi_\mu\}$ basis,

$$\begin{aligned} F_{\mu\nu} &= \int d\vec{r}_1 \, \varphi_\mu^*(\vec{r}_1) \, \hat{f}(\vec{r}_1) \varphi_\nu(\vec{r}_1) \\ &= \int d\vec{r}_1 \, \varphi_\mu^*(\vec{r}_1) \, \hat{h}^{1e}(\vec{r}_1) \, \varphi_\nu(\vec{r}_1) + \sum_b^{N/2} \int d\vec{r}_1 \, \varphi_\mu^*(\vec{r}_1) \left[2\hat{J}_b(\vec{r}_1) - \hat{K}_b(\vec{r}_1) \right] \varphi_\nu(\vec{r}_1). \end{aligned} \tag{2.23}$$

The first term in this relation is defined as the core-Hamiltonian matrix and consists of one-electron integrals (kinetic energy and nuclear attraction integrals) according to eq. (2.4),

$$H_{\mu\nu}^{core} = \int d\vec{r}_1 \, \varphi_\mu^*(\vec{r}_1) \, \hat{h}^{1e}(\vec{r}_1) \, \varphi_\nu(\vec{r}_1) = T_{\mu\nu}^{el} + V_{\mu\nu}^{el-nuc}, \tag{2.24}$$

$$T_{\mu\nu}^{el} = \int d\vec{r}_1 \, \varphi_\mu^*(\vec{r}_1) \, \hat{T}^{el}(\vec{r}_1) \, \varphi_\nu(\vec{r}_1), \tag{2.25}$$

$$V_{\mu\nu}^{el-nuc} = \int d\vec{r}_1 \, \varphi_\mu^*(\vec{r}_1) \, \hat{V}^{el-nuc}(\vec{r}_1) \, \varphi_\nu(\vec{r}_1). \tag{2.26}$$

Returning to eq. (2.23), we can express the Coulomb and exchange integrals according to eqs (2.9) and (2.10) and then insert the linear expansion for the molecular orbitals (eq. (2.18)) to get,

$$F_{\mu\nu} = H_{\mu\nu}^{core} + 2\sum_{\lambda\sigma}\sum_b^{N/2} C_{\lambda b} C_{\sigma b}^* \left[(\mu\nu|\sigma\lambda) - (\mu\lambda|\sigma\nu)/2 \right]. \tag{2.27}$$

It contains a one-electron part H^{core} and a two-electron part which depends on the unknown coefficients of the molecular orbitals and a set of two-electron integrals of the form

$$(\mu\nu|\sigma\lambda) = \int d\vec{r}_1 \, d\vec{r}_2 \, \varphi_\mu^*(\vec{r}_1) \varphi_\nu(\vec{r}_1) \, r_{12}^{-1} \, \varphi_\sigma^*(\vec{r}_2) \varphi_\lambda(\vec{r}_2). \tag{2.28}$$

Because of the large number of the atomic orbitals $\{\varphi_\mu\}$ that form a specific molecular orbital, the evaluation and manipulation of such a two-electron integral is the major difficulty in a HF calculation. For a set of K basis functions $\{\varphi_\mu\}$ the number of two-electron integrals

to evaluate is of the order of K^4. Specialized quantum chemistry package programs contain subroutines to calculate efficiently such integral.

With the background of the HF method, we are now able to describe the computational procedure for obtaining RHF wavefunctions for molecules. The computational solution procedure used is the well-known self-consistent-field (SCF) method that handles and solves HF equations iteratively. According to this procedure, initially we have to choose a set of spatial basis functions $\{\varphi_\mu\}$ (usually atomic orbitals). Subsequently, we calculate all the required molecular integrals, such as the overlap matrix elements $S_{\mu\nu}$, the one-electron core-Hamiltonian elements $H_{\mu\nu}^{core}$ and the two-electron integrals $(\mu\nu|\sigma\lambda)$. Then, using various methods provided by respective program, we guess a set of trial expansion coefficients $\{C_{\mu j}\}$ and construct from them, and from the abovementioned integrals, the Fock and overlap matrices to be diagonalized by solving the Roothan equations (see eq. (2.22)). The diagonalization leads to a new set of expansion coefficients $\{C_{\mu j}\}'$ and consequently a new set of molecular orbitals $\{\psi_j\}'$. With these new molecular orbitals, we calculate the updated matrix elements, $S_{\mu\nu}'$, $H_{\mu\nu}^{core\prime}$ and $(\mu\nu|\sigma\lambda)'$. The procedure is repeated iteratively until the ground state energy converges as a function of iteration, so self-consistency is reached (see Chapter 8).

2.2 Configuration Interaction

The HF ground state wavefunction that we introduced above is an approximation and definitely does not represent the exact wavefunction. The HF ground state energy E_0^{RHF} differ from the exact nonrelativistic energy of the system ε_0. The HF energy is an upper bound to the exact energy, so the correction (or correlation) energy is negative,

$$E_{corr} = \varepsilon_0 - E_0^{RHF} < 0. \tag{2.29}$$

The Configuration Interaction (CI) method [5,6,11-14] is based on the variational method for obtaining the correlation energy. In the CI method the exact $N-$ electron ground state wavefunction may be expressed as a linear combination of $N-$ electron trial determinants. It is convenient to describe these other determinants by stating how they differ from the RHF

$N-$ electron ground state wavefunction Ψ_0^{RHF} (called as the "reference" state). If Ψ_0^{RHF} is a reasonable approximation to exact electronic wavefunction Φ_0, then we know from the variation principle that a better approximation is

$$\left|\Phi_0\right\rangle = c_0\left|\Psi_0^{RHF}\right\rangle + \sum_{i\alpha} c_i^{\alpha}\left|\Psi_i^{\alpha}\right\rangle + \sum_{\substack{i<j \\ \alpha<b}} c_{ij}^{\alpha b}\left|\Psi_{ij}^{\alpha b}\right\rangle + \sum_{\substack{i<j<k \\ \alpha<b<c}} c_{ijk}^{\alpha bc}\left|\Psi_{ijk}^{\alpha bc}\right\rangle + \ldots \tag{2.30}$$

This is the form of the full CI wavefunction. $\left|\Psi_i^{\alpha}\right\rangle$ denotes a singly-excited determinant in which an electron, which occupied χ_i in the HF ground state, has been promoted to a virtual spin orbital χ_α. In the same way, $\left|\Psi_{ij}^{\alpha b}\right\rangle$ denotes a doubly-excited determinant in which two electrons, that occupied χ_i and χ_j in the HF ground state, has been promoted to virtual spin orbitals χ_α and χ_b, respectively. $\left|\Psi_{ijk}^{\alpha bc}\right\rangle$ denotes a triply-excited determinant in which three electrons, that occupied χ_i, χ_j and χ_k in the HF ground state, has been promoted to virtual spin orbitals χ_α, χ_b and χ_c, respectively. The $c's$ are expansion coefficients and restrictions on the summation indices (e.g., $\alpha < b, i < j$).

2.2.1 Configuration Interaction Singles

The Configuration Interaction Singles (CIS) method assumes that only single-excitations are allowed. So, this method describes excitation energies for one-electron transitions (single electron-hole excitations). [5,12,15] Therefore, we must limit the above linear combination (eq. (2.30)) to a basis of singly-excited determinants, i.e., a CIS state is expressed as,

$$\left|\Phi_{0,CIS}\right\rangle = c_0\left|\Psi_0^{RHF}\right\rangle + \sum_{i\alpha} c_i^{\alpha}\left|\Psi_i^{\alpha}\right\rangle. \tag{2.31}$$

The Hamiltonian matrix elements among CIS basis states are

$$\left\langle\Psi_i^{\alpha}\left|\hat{H}^{el}\right|\Psi_j^{b}\right\rangle = E_0^{RHF}\delta_{ij}\,\delta_{\alpha b} + \delta_{ij}\,F_{\alpha b} - \delta_{\alpha b}\,F_{ij} + 2\left(i\alpha\middle|jb\right) - \left(ij\middle|ab\right). \tag{2.32}$$

This Hamiltonian is diagonalized to obtain all CIS eigenstates and eigenenergies. E_0^{RHF} is the RHF ground state energy (see eq. (2.17)), $F_{\alpha b}$ and F_{ij} are Fock matrix elements (see eq. (2.20)), and the last two terms are two-electron integrals as described in eq. (2.28).

Given the above matrix elements and assuming real CI coefficients, the CIS energy for the CIS wavefunction $\Phi_{0,CIS}$ is given by,

$$E_{CIS} = E_0^{RHF} + 2\sum_{i\alpha} c_0 c_i^{\alpha} F_{i\alpha} + \sum_{i\alpha b} c_i^{\alpha} c_i^{b} F_{\alpha b} - \sum_{ij\alpha} c_i^{\alpha} c_j^{\alpha} F_{ij} + \sum_{ij\alpha b} c_i^{\alpha} c_j^{b} \left[\left(i\alpha \middle| jb \right) - \left(ij \middle| ab \right) \right]. \quad (2.33)$$

2.2.2 Configuration Interaction Singles and Doubles

The Configuration Interaction Singles Doubles (CISD) method is similar to CIS but it includes both singly- and doubly-excited determinants. The CISD trial state is

$$\left| \Phi_{0,CISD} \right\rangle = c_0 \left| \Psi_0^{RHF} \right\rangle + \sum_{i\alpha} c_i^{\alpha} \left| \Psi_i^{\alpha} \right\rangle + \sum_{\substack{i<j \\ \alpha<b}} c_{ij}^{\alpha b} \left| \Psi_{ij}^{\alpha b} \right\rangle. \quad (2.34)$$

The widely-employed CISD wavefunction includes only those $N-$ electron basis functions which represent single or double substitutions relative to the reference state and typically accounts for about 95% of the correlation energy for small molecules near their equilibrium geometries. The Hamiltonian matrix elements of CISD are more complex than eq. 2.32. These matrix elements are described in detail in Chapter 7.

2.3 References

[1] Dupuis, M.; Spangler, D.; Wendolowski, J.J. *National Resource for Computations in Chemistry Software Catalog*; University of California, Berkeley, CA, Program QG01, 1980.

[2] Schmidt, M.W.; Baldridge, K.K.; Boatz, J.A.; Elbert, S.T.; Gordon, M.S.; Jensen, J.H.; Koseki, S.; Matsunaga, N.; Nguyen, K.A.; Shujun, S.; et al. General Atomic and Molecular Electronic Structure System. *J. Comput. Chem.* **1983**, *14 (11)*, 1347-1363.

[3] Advances in electronic structure theory: GAMESS a decade later; Gordon, M.S., Schmidt, M.W., Dykstra, C.E., Frenking, G., Kim, K.S., Scuseria, G.E., Eds.; Theory and Applications of Computational Chemistry: the first forty years; Elsevier, Amsterdam, 2005; pp 1167-1189.

[4] Sun, Q.; Berkelbach, T.C.; Blunt, N.S.; Booth, G.H.; Guo, S.; Li, Z.; Liu, J.; McClain, J.; Sayfutyarova, E.R.; Sharma, S.; et al. PySCF: The Python-based Simulations of Chemistry Framework. *Wiley Interdiscip. Rev.: Comput. Mol. Sci.* **2018**, *8*, e1340.

[5] Szabo, A.; Ostlund, N.S. *Modern Quantum Chemistry: Introduction to Advanced Electronic Structure Theory*; Dover, Mineola, New York, 1996.

[6] Atkins, P.; Friedman, R. *Molecular Quantum Mechanics*; 5th ed.; Oxford Univ. Press, New York, 2011.

[7] Cramer, C.J. *Essentials of Computational Chemistry: Theories and Models*; 2nd Ed.; Wiley, Chichester, England, 2002.

[8] Hinchliffe, A. *Molecular Modelling for Beginners*; 2nd Ed.; Wiley, Chichester, U.K., 2003.

[9] Slater, J.C. A Simplification of the Hartree-Fock Method. *Phys. Rev.* **1951**, *81*, 385-390.

[10] Roothan, C.C.J. New Developments in Molecular Orbital Theory. *Rev. Mod. Phys.* **1951**, *23*, 69-89.

[11] Pauncz, R. *The Symmetric Group in Quantum Chemistry*; CRC Press, Florida, 1995.

[12] Maurice, D.; Head-Gordon, M. Configuration interaction with single substitutions for excited states of open-shell molecules. *J. Quantum Chem. Symp.* **1995**, *29*, 361-370.

[13] Sherrill, C.D. *Derivation of the Configuration Interaction Singles (CIS): Method for Various Single Determinant References and Extensions to Include Selected Double Substitutions (XCIS)*; School of Chemistry and Biochemistry, Georgia Institute of Technology, September 1996.

[14] Maurice, D.; Head-Gordon, M. On the Nature of Electronic Transitions in Radicals: An Extended Single Excitation Configuration Interaction Method. *J. Phys. Chem.* **1996**, *100 (15)*, 6131-6137.

[15] Foresman, J.B.; Head-Gordon, M.; Pople, J.A.; Frisch, M.J.; Toward a systematic molecular orbital theory for excited states. *J. Phys. Chem.* **1992**, *96 (1)*, 135-149.

CHAPTER 3

Charge-Transport Mechanisms in Azurin-Based Monolayer Junctions

We study the transport mechanisms of different types of Azurin (Az) monolayer heterojunctions with a variety of metal substituents. The systems include Holo-Az (Cu-substituted), Apo-Az (no metal) and Ni-, Co- and Zn-substituted Azurins. Our theoretical analysis is based on measurements of the voltage and temperature dependencies of the current and attempts to reproduce both dependencies using a common mechanism and corresponding set of parameters. Our results strongly suggest that for Holo-Az the transport mechanism depends on the protein monolayer/heterojunction setup. In one type of heterojunction, transport is dominated by resonant incoherent hopping through the Cu redox site, whereas in the other it is mediated by off-resonant tunneling. For the unsubstituted (Apo-Az) and other metal substituted Azurins the dominant transport mechanism at low temperatures is off-resonant tunneling, with an average tunneling barrier that depends on the type of metal dopant, and at the highest temperatures it is through-amino acid hopping.

Biomolecular electron-transfer (ET) reactions participate in many biological functions such as biological energy conversion processes, biological signalling pathways and disease-repair mechanisms. [1-10] Biomolecular ET reactions are often components of ET chains which are hopping networks of donor-to-acceptor charge-transfer rates. [3] The electron/hole donor (D) and acceptor (A) moieties in these chains are atom or molecule dopants embedded in protein or DNA matrices which act as the bridge (B) connecting donors to acceptors. [5-7] Each D-to-A hopping step of the network involves through-protein or through-DNA electron tunneling. The D-to-A electronic couplings and D-to-A activation energies of each step determine the magnitude of the corresponding D-to-A ET hopping rate (k_{ET}). [11-14] Biological ET chains can operate over a variety of length scales (from nanometer to over micrometer distances). [8,9]

Over the past decades, experimental, theoretical and computational studies of ET molecules and ET proteins (ETpr's) have shown that it is possible to tune molecular ET rates and the charge flow in biological ET chains by chemical modifications of the donor, acceptor and the bridge, by changing the locations of donor and acceptor, or by modifying the solvent environment. [4,7,11-18]

ETpr's are also of interest in molecular electronics. [19,20] Since there is extensive knowledge of how to tune solution-phase through-protein ET mechanisms by chemical modifications, [7,11] an attractive idea is to use ETpr's as the main current-carrying material in hybrid electronic devices. Chemical modifications of the ETpr's in the device may enable tuning the through-protein current and thus the functionality of the device. [21,22]

Solution-phase ET reactions mediated by blue Copper proteins, (containing a Cu ion as the redox center), and in particular Azurin, have been studied thoroughly both experimentally and computationally (e.g., ref. [7, 16, 17, 23, 24] and references therein). In addition to the solution-phase ET studies, there are several experiments that measure transport (current) through Azurin in different types of molecular junction setups, e.g., refs [25-28] for early works.

This work focuses on two experiments, [29,30] that measure current-voltage and current-temperature characteristics of Az monolayer heterojunctions. Ref. [29] (also denoted exp. I) reported current measurements for heterojunctions comprised of oriented Az monolayers, sandwiched between an Si-oxide substrate and a gold (Au) or mercury (Hg) macroscopic LOFO (lift-off, float-on) contact [31] with an area of 0.2 mm^2. In the present study, we focused on the experiments conducted with the Au LOFO contact, for comparison purposes with the results of ref. [30] (see below). The experiments in ref. [29] observed temperature-independent transport across the Az monolayer (transport distance is about 3.5 nm) for a wide range of temperatures $\left(T = 100 - 400K\right)$ for Az molecules containing Cu (Holo-Az). When the Cu atom is removed from Az (Apo-Az) the current $\left(I\right)$ through the monolayers is reduced by more than two orders of magnitude as compared to Holo-Az for $T < 200K$. Also, for Apo-Az the current becomes temperature-dependent for $T > 200K$. We summarize the experimental results of exp. I in Fig. 3.1.

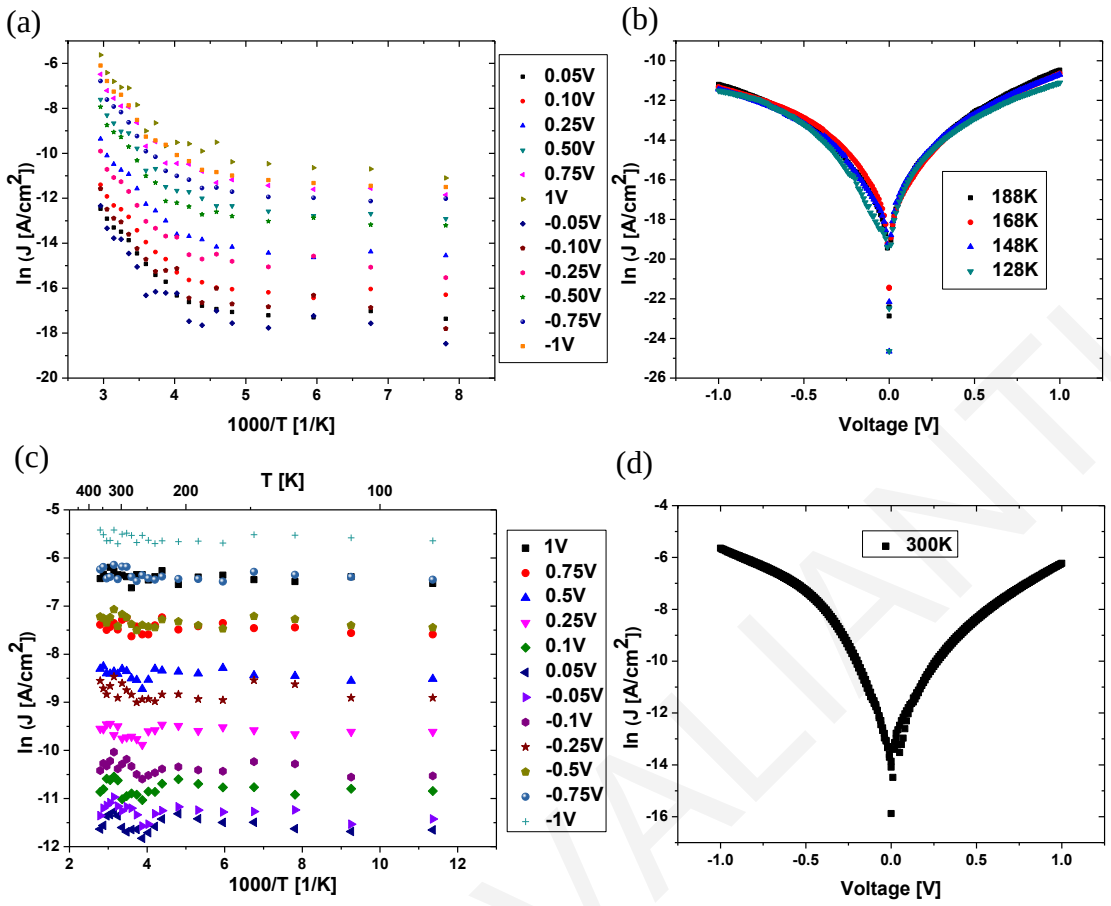

Figure 3.1 (a) Experimental current density (current per unit area) versus temperature (ln(*J*) versus 1000/*T*) for Apo-Az at different bias voltages. (b) Experimental ln(*J*) versus *V* for Apo-Az at *T* = 128, 148, 168, 188 K. (c) Experimental ln(*J*) versus 1000/*T* of Holo-Az at different bias voltages. (d) Experimental ln(*J*) versus *V* of Holo-Az junction at room temperature (exp. I). [29]

An interesting observation in ref. [29] is that substitutions of Apo-Az with metals other than Cu, show temperature dependencies that are intermediate between Apo-Az and Holo-Az (see Fig. 3.2 below).

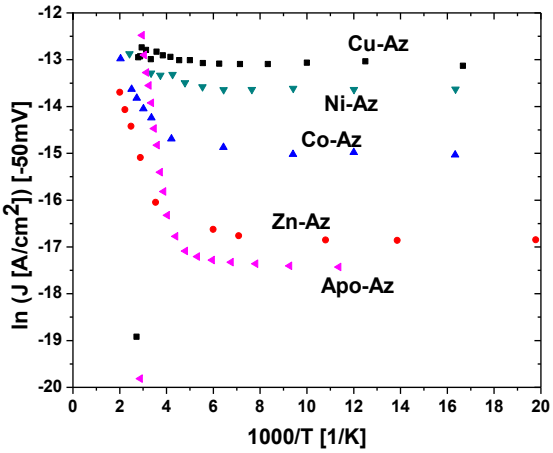

Figure 3.2 Experimental ln(*J*) versus 1000/*T* of Holo-, Ni-, Co-, Zn- and Apo-Az junction at -50 mV bias (exp. I). [29]

Ref. [30] (also denoted exp. II) reported experiments on oriented Holo-Az monolayers sandwiched between soft Au microelectrodes using the "suspended-wire" technique. [32,33] The currents measured in ref. [30] are temperature-independent [34] for a range of temperatures from 25 to 275 K (see Fig. 3.3).

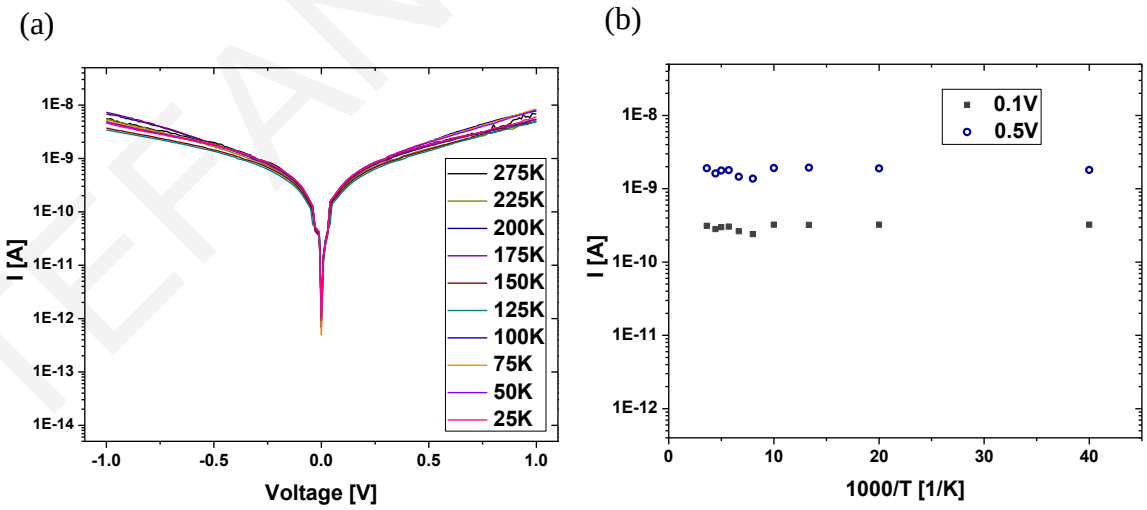

Figure 3.3. Experimental current-voltage curves via Holo-Az: (a) *I* versus *V* (-1 ≤ *V* ≤ 1), with current plotted as log(*I*), at different temperatures. (b) Current at 0.1 V and 0.5 V, indicating the same temperature-independent behavior at different bias voltages (exp. II). [30]

The abovementioned experiments involve different numbers of proteins in the monolayer ($N_{contact} \approx 10^{7} - 10^{9}$ for ref. 29 and $N_{contact} \approx 50 - 200$ for ref. [30]). Further, in the first experiment, [29] the proteins in the monolayer are covalently bound to the P^{++} Si/oxide Si substrate via the exposed cysteine residue (Cys3 or Cys26) which binds to a (≈ 6 Å) 3-MPTMS linker molecule. The other side of the monolayer is physisorbed to the Au/Hg LOFO. In the second experiment, [30] the proteins in the monolayer are covalently bound to both Au substrates by an S-Au bond between the Au and one of the relatively exposed Az cysteine thiolates.

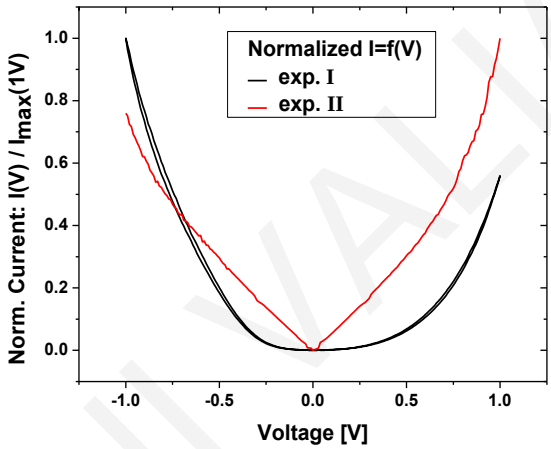

Figure 3.4 Comparison of current-voltage behaviors in experiments I [29] and II [30]. Each current is normalized by its value at 1.0 V and the temperature is 200 K.

Figure 3.4 is an example of the normalized current, in linear scale, as a function of voltage for the two experiments [29,30] (the normalization is with respect to the current value at 1.0 V). Note that the normalized current in ref. [29] grows slowly around $V = 0$, while in ref. [30] it grows more rapidly and almost linearly. Comparing the two graphs (Fig. 3.4), the $I - V's$ have very different shapes, especially in the low voltage $(V < 0.5V)$ regime. Also, the current per molecule, $I = I_{total} / N_{contact}$, at a constant voltage value seems to be very different in the two experiments. For example, for $V = 0.1V$ and using the abovementioned and approximate coverages, $I = 6.0\ 10^{-19} - 6.0\ 10^{-17}\ A$ in ref. [29] and $I = 1.5\ 10^{-12} - 6.0\ 10^{-12}\ A$ in ref. [30]. This difference is probably due to the insulating layer added by the SiOx and a linker in the setup of ref. [29], which lowers the current by some

orders of magnitude, since $I \sim e^{-\beta R}$, where β is the tunneling decay parameter for Az at the average injection energy and R is the molecular bridge's length. [34] Therefore, even though the protein transport medium in both experiments is the same (Az monolayers), the transport mechanisms in the two systems seem to be different.

In the present work, we will study the $I-V$ and $I-T$ behaviors reported in the experiments using different phenomenological models which describe possible transport mechanisms (see below). We will also attempt to explain the changes in current behavior seen when the Cu ion is removed from Az (see Figs 3.1a, 3.1b). To our knowledge, there is still no comprehensive theoretical modeling of both experiments. Our modeling results are relevant to the analysis of the current behavior over a range of temperatures for any molecular-heterojunction device.

3.1 Theoretical Methods

We will present and discuss results for current-voltage and current-temperature measurements as reported in both experiments [29,30] using different basic models that relate to different transport mechanisms. These include the one-site hopping model, [13,14,20,35,36] the Landauer off-resonant tunneling and resonant tunneling models, [13,14,19] multi-site extensions of these models, the extended fully adiabatic Newns-Anderson model [37-40] and the two-step ET model (2sETm). [41,42] These models are motivated by the experiments [29,30] and are described in full detail below.

For all models, in the schematic representation (Fig. 3.5), $L(R)$ denote the left (right) electrodes, where the protein Azurin and the binding ligands are placed between them. For the experimental setup of ref. [29], R represents the LOFO (Au or Hg) and L represents the substrate (Si / oxide Si). It is believed that on average, Cu is closer to the R electrode. However, in our modeling we do not make any assumptions about orientation. For the experiments of ref. [30], R and L represent Au electrodes.

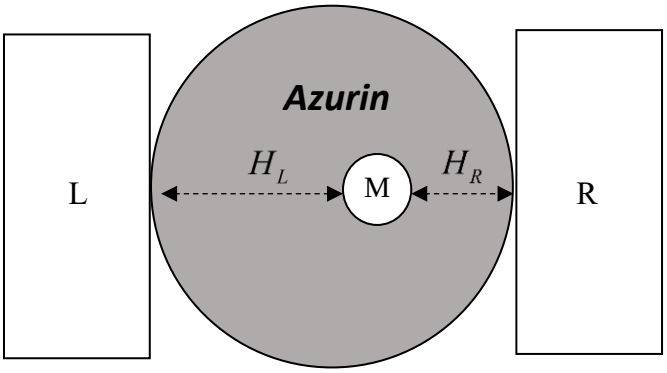

Figure 3.5 Schematic representation of the layout used for the description of some theoretical models to describe the experiments. M denotes metal dopant (e.g., Cu) and H_L, H_R are the protein-mediated tunneling matrix elements between L and R electrodes.

For an Az monolayer of $N_{contact}$ molecules, the total current is approximated by $I_{total} = N_{contact} I$ and below we describe several models for I. The experiments measure a current density $J = I_{total}/A$, where A is the total contact area. It should be noted that the effective number of contacts (molecules) in these experiments is to some extent an uncertain variable due to the complexity of the heterojunctions. Also, the effective number of contacts will depend on the extent of intermolecular interactions which is also unknown. [43] Thus, in our fitting, we probe a range of $N_{contact}$ values and we place more importance on modeling the experimental temperature and voltage dependencies rather than absolute current values.

The first set of models used, describe coherent transport and are based on the Landauer formalism. [13,14,19] The current per molecule is given by

$$I(V) = -e\int dE \ \frac{1}{\pi\hbar} T(E,V) \left[f\left(E + eV/2\right) - f\left(E - eV/2\right)\right], \tag{3.1}$$

where

$$T(E,V) = \frac{4\Gamma_L \Gamma_R}{\left[E - \varepsilon_0(V)\right]^2 + \left[\Gamma_L + \Gamma_R\right]^2} \tag{3.2}$$

is the transmission probability, V is the voltage bias across the junction, $-eV/2 = \mu_L$ (the Fermi energy of L electrode), $+eV/2 = \mu_R$ (the fermi energy of R electrode) (see Fig. 3.6). Here, $\varepsilon_0(V)$ is a molecular level energy, which acts as a transmission channel,

$$\varepsilon_0(V) = \varepsilon_0 + (\alpha - 1/2)eV\,. \tag{3.3}$$

The dependence of the level energy on bias enters via a parameter α. For example, if $\alpha = 0.5$, the level energy is independent of voltage. For $\varepsilon_0 = 0$ and $\alpha = 0$, it is pinned to μ_L and for $\varepsilon_0 = 0$ and $\alpha = 1$, it is pinned to μ_R. Moreover, $\Gamma_{L(R)}$ are the level broadenings associated with the level couplings $H_{L(R)}$ to the $L(R)$ leads (see Fig. 3.5),

$$\Gamma_{L(R)} = \pi H_{L(R)}^2 \rho_{L(R)}\,, \tag{3.4}$$

where $\rho_{L(R)}$ are the electronic densities of states of the $L(R)$ leads. These broadenings are related to the Fermi Golden rule rates, $\gamma_{L(R)}$, for electron transfer from the level to the leads $\gamma_{L(R)} = (2/\hbar)\Gamma_{L(R)}$. The main parameters of this model are, $\varepsilon_0(V)$ and $\Gamma_{L(R)}$ (see Fig. 3.6).

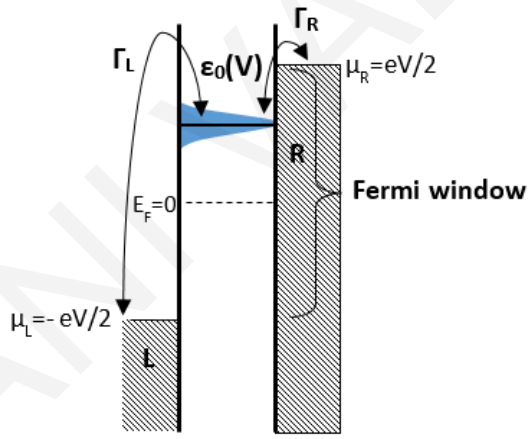

Figure 3.6 Schematic representation of the basic parameters used in the Landauer models ($\varepsilon_0(V)$, $\Gamma_{L(R)}$).

The Landauer model, summarized in eqs (3.1)-(3.4), is used in two ways. Ref. [29] observed that upon extraction of the Cu atom from Az (Holo→Apo), the current is reduced by two orders of magnitude for a large range of temperatures (see Fig. 3.1). Thus, for Holo-Az, Cu seems to provide the most important transmission channel. For this reason, when modeling Holo-Az via eqs (3.1) and (3.2), the level energy $\varepsilon_0(V)$ will be interpreted as a Cu state energy. $H_{L(R)}$ will be interpreted as the through-Az tunneling matrix elements between the

Cu level and the $L(R)$ electrodes. In this case, eqs (3.1) and (3.2) describe an (off-) resonant tunneling model (through Cu).

For the case of Apo-Az, the Az/ligand supra-molecule seems to be a deep tunneling barrier for a wide range of temperatures (thus, the current reduction in Figs 3.1a, 3.1b). Since Apo-Az contains many amino acids with several levels providing tunneling transmission channels, $\varepsilon_0(V)$ cannot be interpreted as a single Az protein (amino acids) electronic level. Therefore, in eq. (3.3), $\varepsilon_0(V)$ is taken to be an effective parameter that modulates the overall tunneling barrier provided by the molecule. When $\varepsilon_0(V) \gg \mu_{L(R)}$ the model describes an off-resonant tunneling mechanism through the Az amino acids. When $\varepsilon_0(V) \approx \mu_{L(R)}$ the model describes a resonant tunneling mechanism through the Az amino acids. We will also consider generalizations of the Landauer model which incorporate single and multiple fluctuating resonances. These more general models may be collectively described as descriptions of thermally modulated coherent tunneling. [44-46] They will be used to explore mostly the high temperature regime of the Apo-Az experiments. [29]

Since for Holo-Az the Cu atom plays a central role for the transmission, we also need to consider the possibility that Cu provides a fully incoherent transmission channel. The length of the molecular bridge (30 Å) gives us the right to consider the ET as a hopping process, involving reversible transitions between the two oxidation states of bridge (oxidized and reduced Cu' s electronic states) (see Fig. 3.7) and the $L(R)$ electrodes. Thus, an alternative model used for Holo-Az is the one-site hopping model (incoherent model), where the hopping site is a Cu level. For the case of the hopping model, Cu acts as a redox site with reorganization energy λ (see Fig. 3.7). This means that when the electron reaches the Cu atom, it remains there for sufficient time to reorganize the Cu-Az ligands. The steady state current per molecule is given by

$$I(V) = -e\frac{k_L^{\rightarrow}(V)k_R^{\rightarrow}(V) - k_L^{\leftarrow}(V)k_R^{\leftarrow}(V)}{k_L^{\rightarrow}(V) + k_L^{\leftarrow}(V) + k_R^{\rightarrow}(V) + k_R^{\leftarrow}(V)}, \tag{3.5}$$

where $\vec{k}_{L(R)}$ and $\overleftarrow{k}_{L(R)}$ are hopping rates to Cu from $L(R)$ leads and from Cu to $L(R)$ leads. When the Az - electrodes couplings are weak, so that the time scale for ET is long relative to that of thermal relaxation, each hopping step is associated with a rate obtained with the framework of the Marcus heterogeneous ET theory, [13,14,20,35,36]

$$\vec{k}_L(V) = 2\frac{\Gamma_L}{\hbar}\int dE\, f(E-\mu_L) W_{ox}\left(\varepsilon_0(V),\mu_L\right),$$

$$\vec{k}_R(V) = 2\frac{\Gamma_R}{\hbar}\int dE\, f(E-\mu_R) W_{ox}\left(\varepsilon_0(V),\mu_R\right),$$

$$\overleftarrow{k}_L(V) = 2\frac{\Gamma_L}{\hbar}\int dE\left[1-f(E-\mu_L)\right] W_{red}\left(\varepsilon_0(V),\mu_L\right), \tag{3.6}$$

$$\vec{k}_R(V) = 2\frac{\Gamma_R}{\hbar}\int dE\left[1-f(E-\mu_R)\right] W_{red}\left(\varepsilon_0(V),\mu_R\right).$$

In the equations above, $W_{ox}\left(\varepsilon_0(V),\mu_{L(R)}\right)$ and $W_{red}\left(\varepsilon_0(V),\mu_{L(R)}\right)$ are distribution functions [35] for Cu oxidation and reduction respectively (see Fig. 3.7) and are given by

$$W_{ox}\left(\varepsilon_0(V),\mu_{L(R)}\right) = \frac{1}{\sqrt{4\pi\lambda k_B T}} e^{-\frac{\left(\lambda-\left(\mu_{L(R)}+E\right)+\varepsilon_0(V)\right)^2}{4\lambda k_B T}}$$

$$W_{red}\left(\varepsilon_0(V),\mu_{L(R)}\right) = \frac{1}{\sqrt{4\pi\lambda k_B T}} e^{-\frac{\left(\lambda+\left(\mu_{L(R)}+E\right)-\varepsilon_0(V)\right)^2}{4\lambda k_B T}}. \tag{3.7}$$

The chemical potentials of the $L(R)$ electrode are set to $\mu_L = -eV/2$ $\left(\mu_R = +eV/2\right)$.

The main parameters used in this model are: the Cu's site energy, $\varepsilon_0(V)$, the reorganization energy, λ, for oxidation / reduction of Cu and $\Gamma_{L(R)}$ arising from the electrodes to Cu tunneling couplings through Az amino acids (see Fig. 3.7).

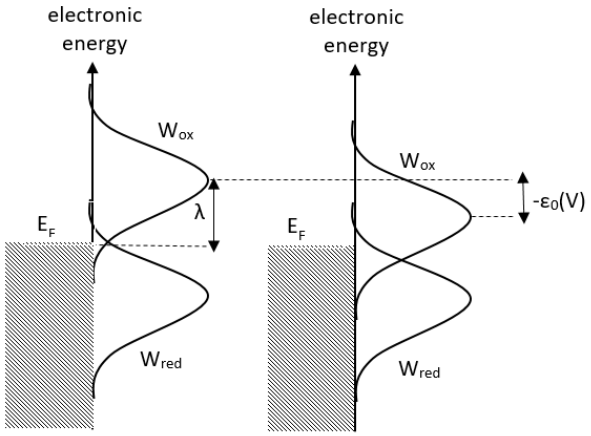

Figure 3.7 Reorganization energy, λ, distributions W_{ox} and W_{red} at equilibrium (left) and after application of a cathodic overpotential.

We will also consider generalizations of the above incoherent hopping model, to multi-site hopping through the Az monolayer. This generalization will be necessary for describing the temperature dependence of Apo-Az in the $T > 200K$ region (see Fig. 3.1a and Fig. 3.8 below). In addition to the above simplest models that represent the extremes of coherent and incoherent transport we have also tested models describing intermediate regimes and containing relatively few parameters. These are the extended – fully adiabatic Newns-Anderson model [37-40] and the two-step vibrationally coherent ET model (2sETm) [41,42] and are described in the Supplement section.

3.2. Modeling of Holo-Az heterojunctions in experiments I and II

3.2.1 Experiment on Si-oxide substrate – Az – Au LOFO heterojunctions (exp. I)

Figures 3.1a and 3.1c show the temperature dependence of $\ln(J)$ $(J = I_{total}/A)$ for Apo-Az (Fig. 3.1a) and Holo-Az (Fig. 3.1c) for a wide range of bias voltages. In the case of Apo-Az, the current decreases with decreasing temperature for $T > T_c$ $(T_c = 200K)$ and then becomes temperature-independent. T_c remains the same for all voltages. Transport via Holo-Az is orders of magnitude greater than Apo-Az (apart from the highest temperatures, when the Holo- and Apo-Az currents are similar). Further, the Holo-Az current is temperature-independent for all temperatures $(T = 100 - 400K)$ and all voltages $(|V| = 0.05 - 1.0V)$.

Figure 3.8 is an example comparison of the Holo- and Apo-Az currents, as a function of temperature, for a specific voltage value $(V = +50mV)$. This figure shows the switch at $T > 200K$ from temperature independence to temperature dependence (activated transport) in the case of Apo-Az. The activation energy for thermally activated transport is $E_a \approx 250 - 255meV$.

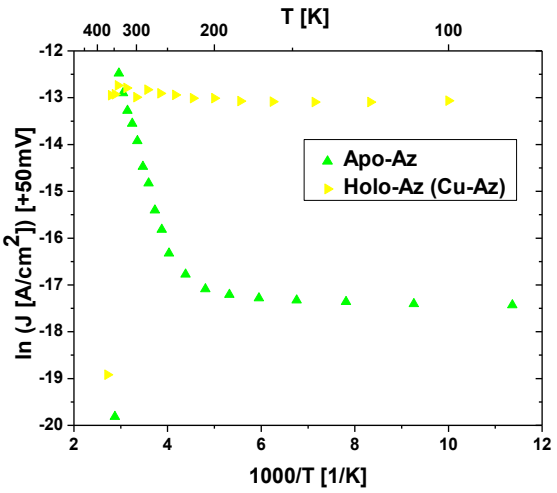

Figure 3.8 Experimental ln(*J*) versus 1000/*T* of Apo- and Holo-Az junction at +50 mV bias. [29]

The large enhancement of the current due to the addition of Cu (Apo → Holo) observed in ref. [29] (Fig. 3.8), indicates that Cu is the most important transmission channel for Holo-Az. Thus, for Holo-Az, Cu is likely to act as a near-resonant/resonant tunneling or incoherent hopping site. In the following, we attempt to fit the temperature and voltage dependencies of the Holo-Az current using the simplest one-level coherent model (eqs (3.1)-(3.4)) and the one-level incoherent hopping model (eqs (3.5)-(3.7)). The best-fit parameters for both models are derived from the low bias regime for which we do not expect the electric field to perturb the structures of the proteins in the monolayer.

Figures 3.9 and 3.10 show representative simultaneous fits of the temperature and voltage dependencies of the current measured in ref. [29], using the coherent tunneling model, (eqs (3.1)-(3.4)) with a common set of parameter values. Figure 3.9 shows $ln(J)-T$ fitting for $V=\pm 50,250mV$ and Fig. 3.10a shows $ln(J)-V$ fitting at $T=300K$. The common parameter values derived from these fits are: $\varepsilon_0=0.03eV$, $\alpha=0.75$, $\Gamma_L=3.3\,10^{-5}eV$ and $\Gamma_R/\Gamma_L=10-1000$ (the Fermi level at zero bias is 0 eV). We find that there is no much flexibility in the ε_0 value which affects both the voltage and temperature dependence. There is more flexibility in the $\Gamma_{L(R)}$ values due to the uncertainty about the exact number of proteins in the system, $N_{contact}$. Thus, the best-fit of the coherent tunneling model predicts a very low tunneling barrier at zero bias, as expected by the large enhancement seen in the current for Holo-Az as compared to Apo-Az.

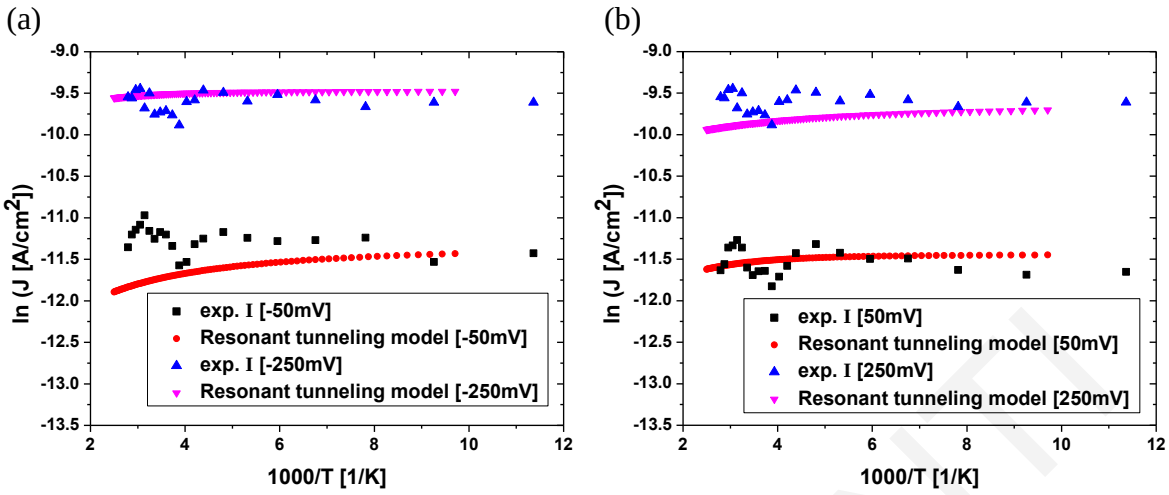

Figure 3.9 Experimental ln(J) versus 1000/T of Cu-Az (Holo-Az) [29] for different bias voltages versus theoretical predictions (eqs (3.1)-(3.4)). (a) Bias voltages of -50 mV and -250 mV, (b) bias voltages of +50 mV and +250 mV. Parameter values of eqs (3.1)-(3.4) for all graphs: ε_0=0.03 eV, α=0.75, Γ_L=3.3 10^{-5}eV, and Γ_R/Γ_L=1000.

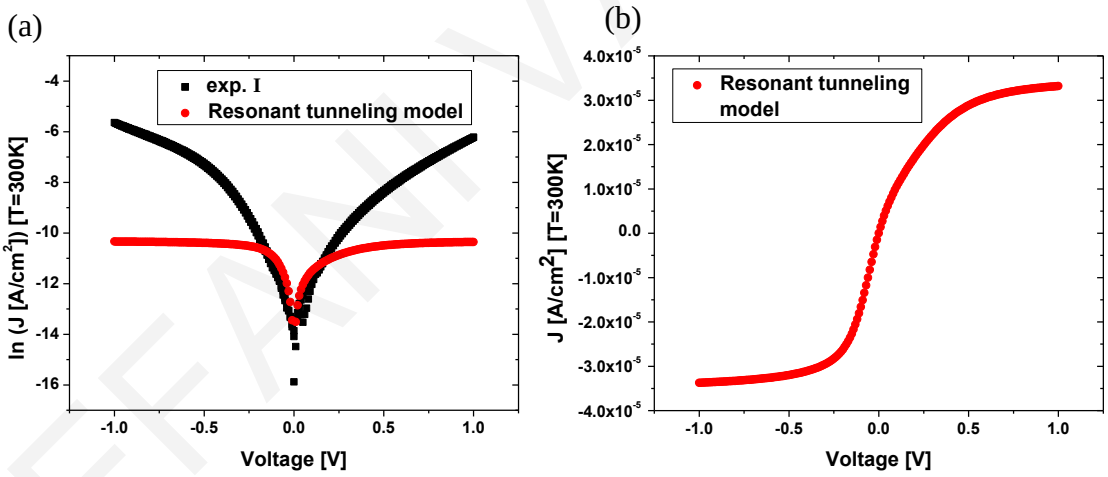

Figure 3.10 (a) Experimental ln(J) versus voltage of Cu-Az [29] at T = 300 K and theoretical best-fit using the single-channel resonant-tunneling model (eqs (3.1)-(3.4)) with the best fit parameter values of ε_0=0.03 eV, α=0.75 , Γ_L=3.3 10^{-5} eV and Γ_R/Γ_L=1000, as in Fig. 3.9. The fit fails for bias voltages beyond 250 mV. This is because the current of a single resonant tunneling channel will saturate at higher bias voltages. (b) Theoretical resonant tunneling J versus voltage of Cu-Az at T = 300 K showing the saturation of the current at higher voltages for the best fit parameters. Since the resonant tunneling current in this parameter regime is larely temperature-independent for T = 100-400 K the shape of the J-V curve will not be altered within the experimental temperature range.

Figure 3.9 shows that the current can be near temperature independent for the resonant tunneling regime. This is an expected feature of this regime, [19] only if $k_B T \le \Gamma_L + \Gamma_R$, $\varepsilon_0(V)$ which turns out to be the case for the experimental temperature range and for the abovementioned best fit parameters. Figure 3.10a shows that the resonant tunneling channel that reproduces the low bias experimental results cannot reproduce the high bias current. This feature is expected for a single-channel resonant tunneling current which tends to saturate at high enough voltages.

Although it is tempting to adopt an off-resonant tunneling model (high ε_0 in eq. (3.3)) which is known to give temperature independence, [19] such a model completely fails to predict the low bias voltage profile of the experiments in ref. [29]. A representative example is shown in Fig. 3.11, which shows a typical $ln(J)-V$ best-fit for an one-level coherent tunneling model, where the level energy is high $(\varepsilon_0 = 0.8eV)$, such that the current is temperature independent at all voltages. Figure 3.11 clearly demonstrates that such a model can only reproduce the experimental results at very low voltages.

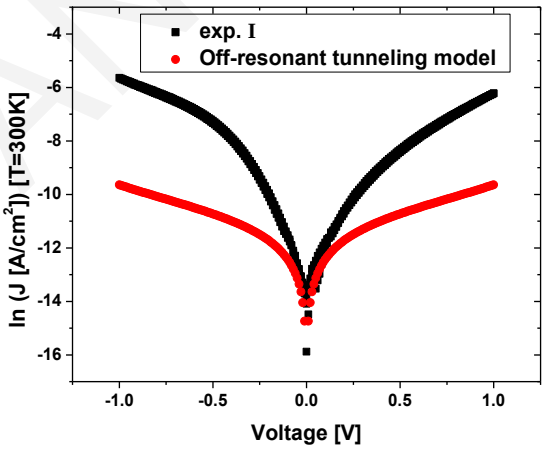

Figure 3.11 Experimental ln(*J*) versus voltage of Cu-Az [29] at *T* = 300 K and theoretical best-fit using the off-resonant tunneling model (eqs (3.1)-(3.4)) with the best fit parameter values of ε_0=0.8 eV, α=0.5, Γ_L=3.3 10^{-4} eV and Γ_R/Γ_L=1000.

Figures 3.12 and 3.13 are representative simultaneous fits of the temperature and voltage dependencies of the current measured in ref. [29], using the incoherent one-site hopping

model (eqs (3.5)-(3.7)) with a common set of parameter values given by: $\lambda = 0.2eV$, $\alpha = 0.75$, $\varepsilon_0 = 0.01 - 0.03eV$, $\Gamma_L = 1.0\ 10^{-5} - 1.0\ 10^{-3} eV$ and $\Gamma_R/\Gamma_L = 10 - 1000$. Figure 3.12 shows $ln(J) - T$ fits for $V = \pm 50, 250mV$ and Fig. 3.13a shows $ln(J) - V$ fitting at $T = 300K$. The range of values of our fit parameters, is due to the uncertainty about the exact number of proteins in the system, $N_{contact}$. The one-site hopping model thus predicts a near resonant Cu level at zero bias that enters the Fermi window at non-zero bias. It also predicts a low reorganization energy for the Cu redox site which is consistent with inner sphere redox reorganization energies in Azurin. [47] Both of these features are necessary to give a near temperature-independent current at the various voltages (Fig. 3.12). [36] The model simultaneously reproduces the $ln(J) - V$ behavior for bias values up to $\pm 250mV$ (Fig. 3.13a). Beyond the $\pm 250mV$ bias the one-level hopping current saturates (Fig. 3.13b), as expected.

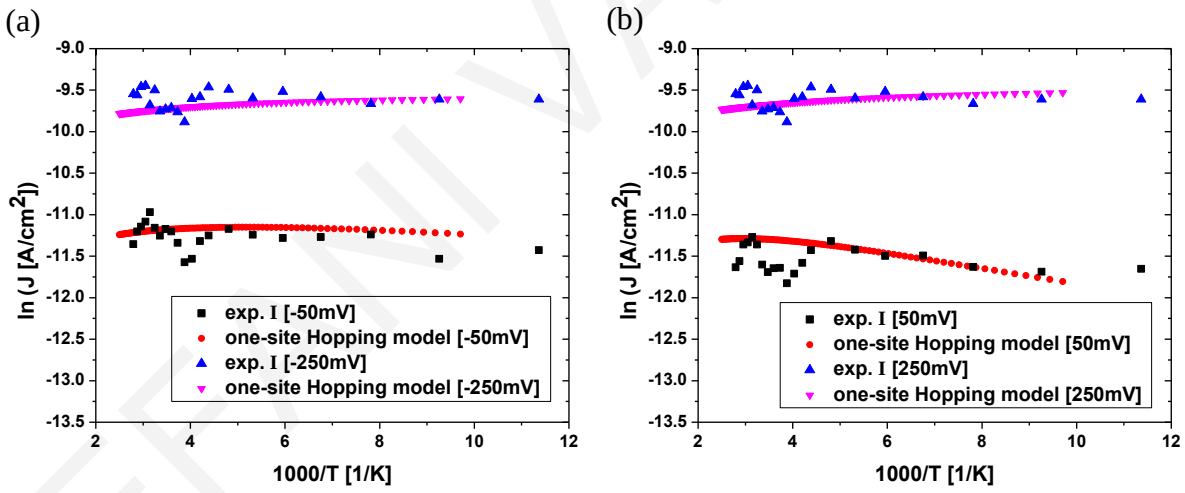

Figure 3.12 Experimental ln(J) versus 1000/T of Cu-Az (Holo-Az) [29] for different bias voltages versus theoretical best-fit using the one-site hopping model (eqs (3.5)-(3.7)). (a) Bias voltages of -50 mV and -250 mV, (b) bias voltages of +50 mV and +250 mV. The parameter values of eqs (3.5)-(3.7) for all graphs are: λ=0.2 eV, α=0.75, ε_0=0.01 eV, Γ_L=1.0 10^{-4} eV and Γ_R/Γ_L=1000.

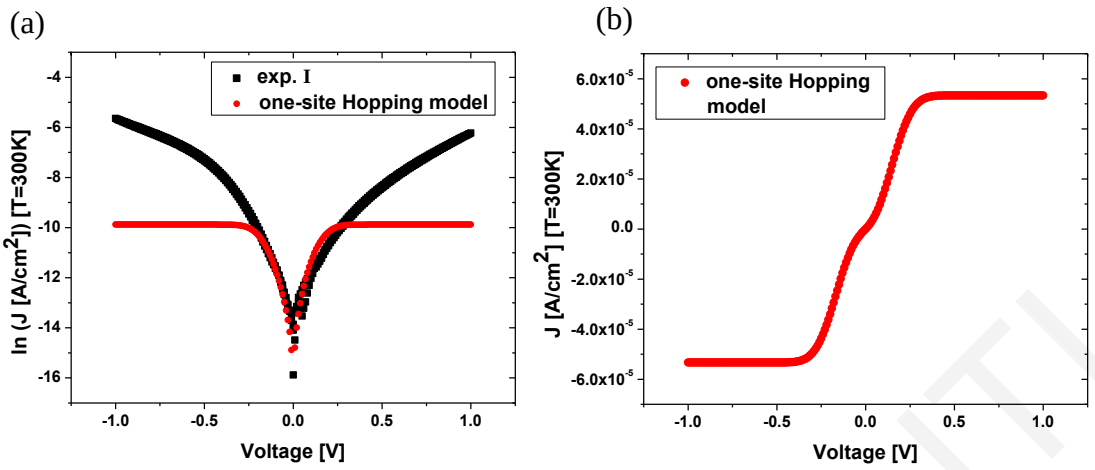

Figure 3.13 (a) Experimental ln(*J*) versus voltage of Cu-Az [29] at T = 300K and theoretical best-fit using the one-site hopping model (eqs (3.5)-(3.7)) (parameter values: λ=0.2 eV, α=0.75, ε_0=0.01 eV, Γ_L=1.0 10^{-4} eV and Γ_R/Γ_L=1000). (b) Theoretical single-channel resonant hopping *J* versus voltage of Cu-Az at T = 300 K for the same parameter values, showing saturation behavior of the current. The behavior does not qualitatively change with temperature as the model predicts temperature independent transport for T = 100-400 K (Fig. 3.12).

A comparison of the $ln(J)-V$ fits obtained using the coherent resonant tunneling (Fig. 3.10a) to the fits obtained from the resonant single-channel hopping model (Fig. 3.13a), shows that the one-site hopping model gives a better fit for a wider range of bias voltages. However, both models fail to reproduce the high bias currents since both predict current saturation. We were also not able to reproduce the experimental results by global fitting using more complex models such as Newns-Anderson [37-40] or 2sETm [41,42] (see Supplement section for a description of these models).

The conclusion that a through-Cu resonant hopping model (with a low reorganization energy of 0.1-0.2 eV) can reproduce the low-bias Holo-Az currents of ref. [29] is consistent with previous modeling of EC-STM experiments on Holo-Az molecular junctions. [28] Further, the reorganization energy values predicted by our fitting using the through-Cu hopping model are consistent with ab-initio and molecular dynamics computations of inner-sphere reorganization energies for the Cu ion in blue copper proteins [17,47,48] (the systems we study are not in aqueous environment, so we expect the reorganization energy to be inner-sphere). Recent experiments on small molecule systems [49] clearly demonstrate transport via a

hopping mechanism. A very recent experimental work on Azurin-based molecular junctions, [50] showed that by weakening the coupling between the protein and the gold electrodes, the amount of inelastic current increases. This trend clearly suggests that in experiments like those of ref. [29], which involve linkers that weaken the Cu-electrode couplings, the current may well proceed incoherently through the molecules.

The analysis in Figs 3.9 - 3.13 shows that the high-bias current observed in ref. [29] cannot be due to a single resonant $\varepsilon_0(V)$ transport channel. Since the current does not saturate, additional resonant $\varepsilon_0(V)$ channels in the protein monolayer must come into resonance at higher voltages. [36] In the monolayer, different proteins are expected to have slightly different orientations, conformations and local environments. Therefore, the Cu energy levels of the different Holo-Az proteins at zero bias will have a range of values (which are expected to be closer to the Fermi level as compared to the amino acids, see Table 3.1). Figure 3.14a illustrates this idea, where $\varepsilon_{0,k}$ refers to the zero-bias Cu level energy of protein k in the monolayer. Given the fact that we were able to fit the voltage dependence of the current for the lower bias voltages with single channel (single ε_0 value) models (Figs 3.9, 3.10 and 3.12, 3.13), a fraction of the energies $\{\varepsilon_{0,k}\}$ should be quasi-resonant with the Fermi level at zero bias. However, since $\varepsilon_{0,k}(V) = \varepsilon_{0,k} + (\alpha - 1/2)eV$, for high-enough bias more Cu levels in the monolayer ensemble will enter the Fermi window (Fig. 3.14b), providing the monolayer with additional transport channels and avoiding a saturation of the monolayer current at high voltages (Fig. 3.14b).

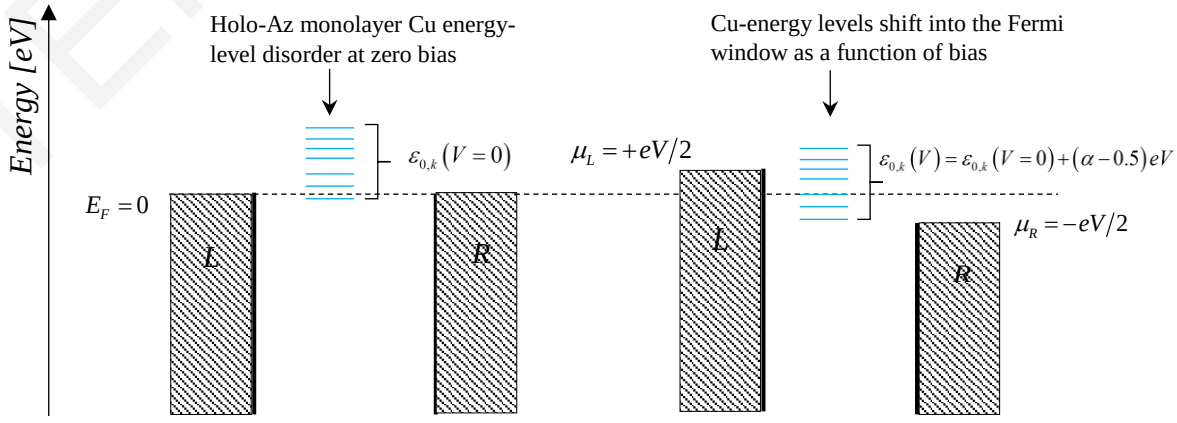

Figure 3.14 Schematic representation of the Cu-level multi-channel hypothesis.

To test in the simplest manner this multi-channel hypothesis for both, the resonant tunneling and hopping mechanisms, we describe the monolayer (ensemble) current in terms of the following formula,

$$J_{multi} = \underbrace{J\left(\varepsilon_{0,1}(V)\right)}_{low\ bias\ channel} + \sum_{k\neq 1} P_k\, J\left(\varepsilon_{0,k}(V)\right),\quad \varepsilon_{0,k\neq 1} > \varepsilon_{0,1}\ . \tag{3.8}$$

On the right-hand side of this equation the J's are current densities that are either computed by eqs (3.1)-(3.4) (coherent tunneling) or (3.5)-(3.7) (incoherent hopping). The subscript "multi" means multi- $\varepsilon_0(V)$ sum. The first J ($\varepsilon_{0,1}(V)$) is computed using the zero-bias ε_0 value and the other parameter values that produce the low-bias fits in Figs 3.9, 3.10 (for the coherent model) or Figs 3.12, 3.13 (for the incoherent model). The remaining J's are computed by using a range of higher zero bias level energies $\varepsilon_{0,k\neq 1} = 0.1 - 0.5eV$ with all other parameters fixed to the values of the low bias channel. The prefactors P_k are calculated from fitting to the experimental $\ln(J) - V$ for the whole range of experimental voltages using multiple regression analysis. P_k can be interpreted as the zero-bias ratio of population of proteins in the ensemble with a given $\varepsilon_{0,k\neq 1}$ to the population of proteins with $\varepsilon_{0,1}$.

Figure 3.15 below shows the individual J's in eq. (3.8) for the coherent (Fig. 3.15a) and the incoherent hopping (Fig. 3.15b) models for a similar range of $\varepsilon_{0,k}$ values. The bias saturation behaviors of the current in the two mechanisms are very different. Figure 3.16 shows the monolayer (ensemble) current obtaining from eq. (3.8) for both mechanisms using the identical zero bias level energies, $\varepsilon_{0,k\neq 1}$. Figure 16a is a representative fit of the $\ln(J) - V$ dependence measured in ref. [29], using the incoherent multi-channel hopping model and Fig. 3.16b shows the fit results using the coherent multi-channel tunneling model. The hopping model of eq. (3.8) gives a much better fit for a wider range of bias voltages, up to $V = \pm 0.75V$, after which starts to saturate (to avoid saturation, more $\varepsilon_{0,k\neq 1}$ should be added).

On the other hand, the tunneling model of eq. (3.8) begins to saturate at much lower voltages and also shows an asymmetry when reversing the voltage, not consistent with the experimental results. Both models give approximate temperature independence of the multi-channel current (similar to Figs 3.9 and 3.12). We conclude that the dominant mechanism of Holo-Az transport in ref. [29], for the whole range of bias voltages probed in the experiments, is resonant through-Cu hopping.

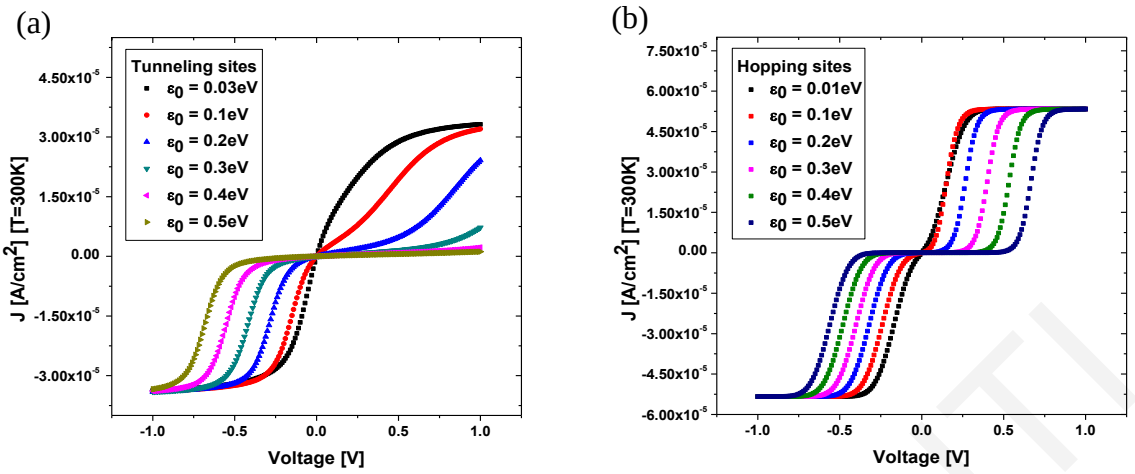

Figure 3.15 Theoretical J versus V of Cu-Az at T = 300 K using a range of energy levels, $\varepsilon_{0,k\neq1}$ =0.1-0.5 eV (a) for the coherent resonant tunneling model (parameter values: $\varepsilon_{0,1}$=0.03 eV (best-fit at low bias regime), α=0.75, Γ_L=3.3 10^{-5} eV, Γ_R /Γ_L=1000) and (b) for the incoherent hopping model (parameter values: $\varepsilon_{0,1}$=0.01 eV (best-fit at low bias regime), λ=0.2 eV, α=0.75, Γ_L=1.0 10^{-4} eV, Γ_R /Γ_L=1000).

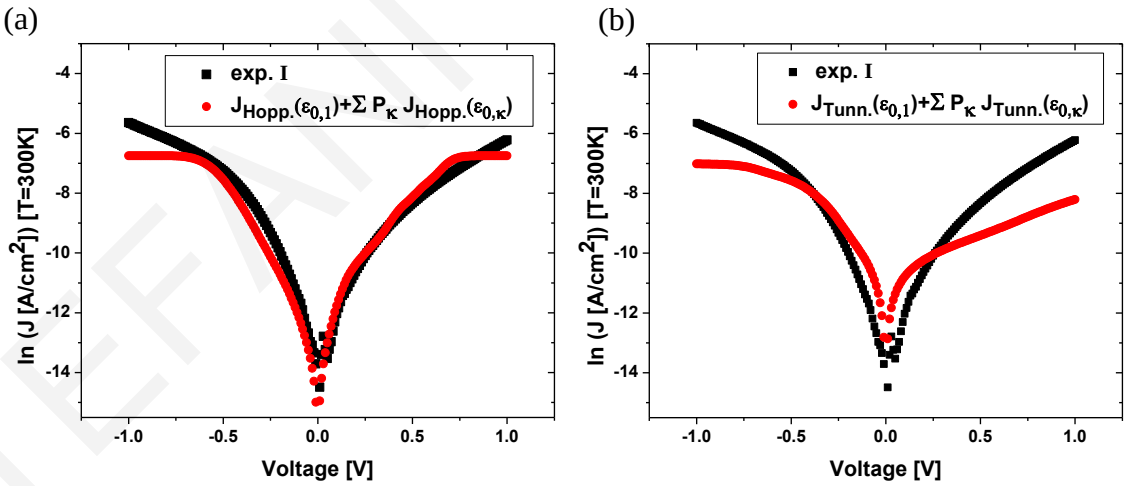

Figure 3.16 Experimental ln(J) versus voltage of Cu-Az [29] at T = 300 K and theoretical fits using the multi-channel hypothesis of eq. (3.8) using (a) the incoherent hopping mechanism (coefficients derived from multiple regression analysis: P_1=0.35, P_2=0.50, P_3=3.14, P_4=4.68, P_5=13.01), (b) the coherent tunneling mechanism (coefficients of multiple regression analysis: P_1=0.06, P_2=6.84, P_3=7.77, P_4=3.21, P_5=7.68).

3.2.2 Experiment on Au microelectrode – Az – Au microelectrode heterojunctions (exp. II)

Ref. [30] reported temperature-dependent current-voltage $(I-V)$ measurements on Au(substrate) – Holo Az – Au (nanowire) junctions with a small number of proteins (nominally ≈ 50). The currents were approximately temperature-independent (Figs 3.3a, 3.3b). The $I-V$ curves are symmetric in contrast to the $J-V$ curves in ref. [29].

We find that the $I-V$ experimental results of ref. [30] can be reproduced by a single-channel coherent tunneling model (eqs (3.1)-(3.4)), where the level energy is off-resonant to the Fermi level, ε_0 at zero bias. Typical $ln(I)-T$ and $ln(I)-V$ experimental and modeling plots are shown in Figs 3.17 and 3.18. The coherent tunneling model (eqs (3.1)-(3.4)) parameter values that reproduce the experimental results are: $\alpha = 0.470$, $\varepsilon_0 = 0.70 - 0.80eV$, $\Gamma_L = 1.1\ 10^{-5} - 2.5\ 10^{-5} eV$ and $\Gamma_R/\Gamma_L = 100 - 1000$.

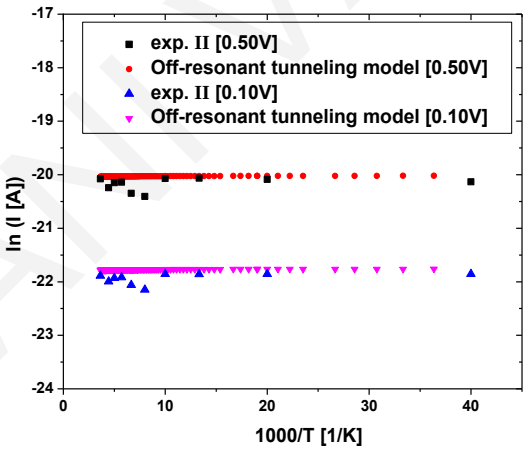

Figure 3.17 Experimental ln(*I*) versus 1000/*T* of Cu-Az [30] at +500 mV and +100 mV bias, versus theoretical fits (eqs (3.1)-(3.4)) using the parameter values: α=0.470, ε_0=0.80 eV, Γ_L=1.15 10^{-5} eV and Γ_R/Γ_L=1000.

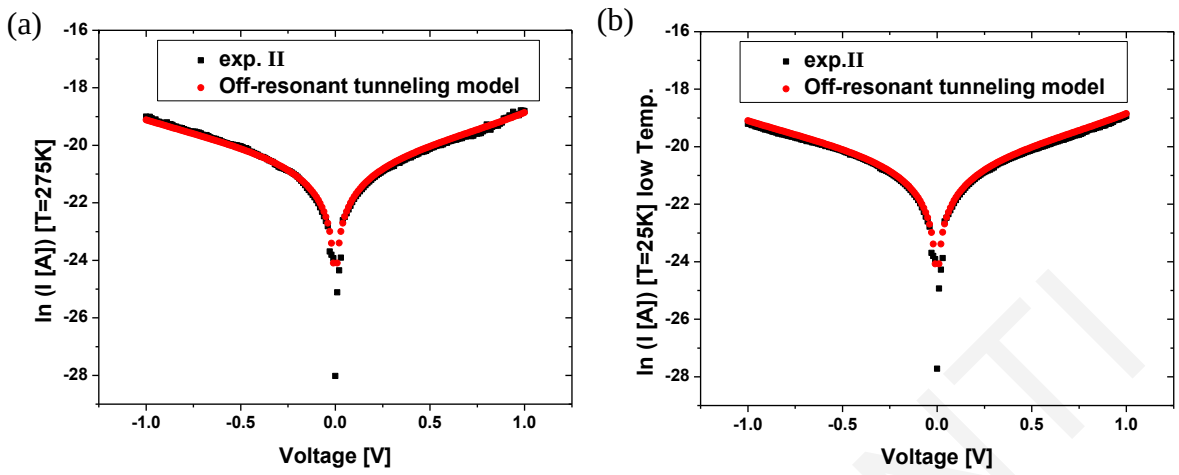

Figure 3.18 Experimental ln(*I*) versus voltage of Cu-Az [30] at (a) 275 K and (b) 25 K, versus theoretical fits (eqs (3.1)-(3.4)) using the parameter values: α=0.470, ε_0=0.80 eV, Γ_L=1.15 10^{-5} eV, and Γ_R/Γ_L=1000.

In conclusion, the Holo-Az transport mechanisms differ in the two experiments [29,30] as suggested by Fig. 3.4. For the Holo-Az heterojunction in ref. [29], the best low bias fits to experiment are obtained by an one-channel resonant hopping model. To reproduce the high bias currents multiple resonant Cu-hopping channels must be introduced. For ref. [30] a single-channel off-resonant tunneling model adequately describes the experimental results. These results are not that surprising given the structural differences between the heterojunctions in the two experiments. In the experiment of ref. [30], the proteins in the monolayer are covalently bound to both leads. In the experiment of ref. [29] the proteins in the monolayer are only covalently bound via a linker molecule to the substrate and are physisorbed to the Au LOFO. Thus, in the latter heterojunctions, there is much more disorder and weaker coupling of the metal to the leads (as compared to ref. [30]), both due to the physisorption and due to the linker molecule, which increases by approximately 6 Å the molecular bridge.

3.3 Modeling of Apo-Az heterojunction experiments (exp. I)

The modeling of Apo-Az experiments [29] is more involved. This is because two behaviors of the current as a function of temperature are observed. For $T < 200K$ the temperature dependence of the current is largely flat and for $T > 200K$, the dependence is activated. It

is notable that for the highest temperatures in the experiments (i.e. $T = 400K$), the current for Apo-Az approaches the current for Holo-Az.

3.3.1 Low Temperatures ($T < T_c$)

We find that the experimental results for the Apo-Az heterojunction in the temperature-independent regime $(T < 200K)$ can only be described via eqs (3.1)-(3.4) using an off-resonant tunneling model. Example comparisons of experiment and theory are shown in Fig. 3.19. The parameter values employed for the fit are: $\alpha = 0.50$, $\varepsilon_0 = 0.60 - 0.70eV$, $\Gamma_L = 1.0\ 10^{-3} - 2.5\ 10^{-3} eV$ and $\Gamma_R/\Gamma_L = 1$. The off-resonant tunneling behavior may be interpreted as a consequence of the fact that the proteins are missing the metal ion capable to localize the charge (in a locally stable state).

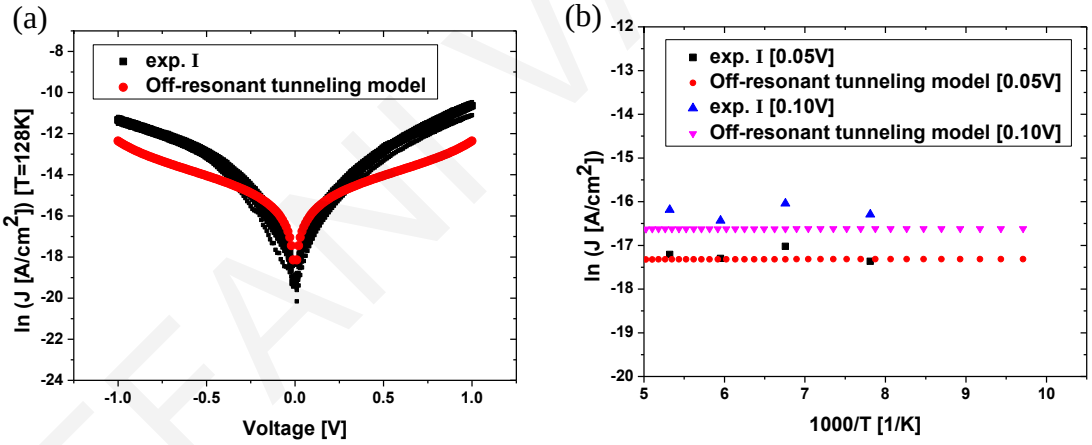

Figure 3.19 (a) Experimental ln(J) versus voltage of Apo-Az [29] at T = 128 K and theoretical fits using eqs (3.1)-(3.4). Since for 100 ≤ T ≤ 200 K, the current is temperature independent, the fit does not change with temperature. (b) Experimental ln(J) versus 1000/T of Apo-Az as a function of temperature at V = 0.05 and 0.10 V, and theoretical fits using eqs (3.1)-(3.4). For both (a), (b) the parameter values in eqs (1)-(4) are: α=0.50, ε_0=0.70 eV, Γ_L=1.0 10^{-3} eV, Γ_R/Γ_L=1.

In contrast to the case of Holo-Az, where ε_0 in eqs (3.2), (3.3) was interpreted as a Cu-level energy, in the case of Apo-Az ε_0 should be interpreted as an average amino acid tunneling barrier.

3.3.2 High Temperatures ($T > T_c$)

In order to reproduce the experimental results for the Apo-Az heterojunctions (ref. [29], Figs 3.1a, 3.1b, 3.2) in the thermally activated transport regime $(T > 200K)$, we need a mechanism that shows activated current behavior and produces Apo-Az current for the highest temperatures that approach the Holo-Az currents (see Fig. 3.8). This last observation implies that at the highest temperatures the protein (amino acids) provides channels (resonances) that are either within the Fermi window or that can easily be accessed thermally. These resonances will either be accessed by transferring charge coherently or incoherently.

We find that the simple coherent transport model of eqs (3.1)-(3.4) cannot reproduce both the flat and the activated dependence of the Apo-Az current. The simplest generalization of this coherent model which incorporates a fluctuating resonance is a thermally modulated tunneling model. [44-46] In this model the level energy ε_0 in eqs (3.2)-(3.3) is a stochastic variable with a Gaussian probability density,

$$\rho(\varepsilon_0) = \frac{1}{\sqrt{2\pi}\sigma(T)} e^{-(\varepsilon_0 - \bar{\varepsilon}_0)^2 / 2\sigma(T)^2}, \tag{3.9}$$

where $\sigma(T) = \sqrt{\lambda_{eff} k_B T}$ (λ_{eff} is an effective reorganization energy that characterizes the dependence of ε_0 level fluctuations as a function of temperature). The measured mean current is an average over level fluctuations,

$$\langle I(V) \rangle = \int_{-\infty}^{+\infty} d\varepsilon_0 \, \rho(\varepsilon_0) \mathrm{I}(V, \varepsilon_0), \tag{3.10}$$

where $\mathrm{I}(V, \varepsilon_0)$ is the current per molecule based on the Landauer Formalism (eqs (3.1)–(3.4)). This model can partially reproduce the temperature dependence of the current in the thermally activated and the thermally-independent regions for $\lambda_{eff} \sim 1.1eV$ and $\varepsilon_0 = 0.60eV$ and only for low voltage values $(V \leq 0.250V)$ (see Fig. 3.20a). However, the parameters

that give the temperature-dependence in Fig. 3.20a cannot reproduce the experimental voltage dependence in the different temperature regimes (Figs 3.20b for $T = 128K$ and 3.20c for $T = 308K$).

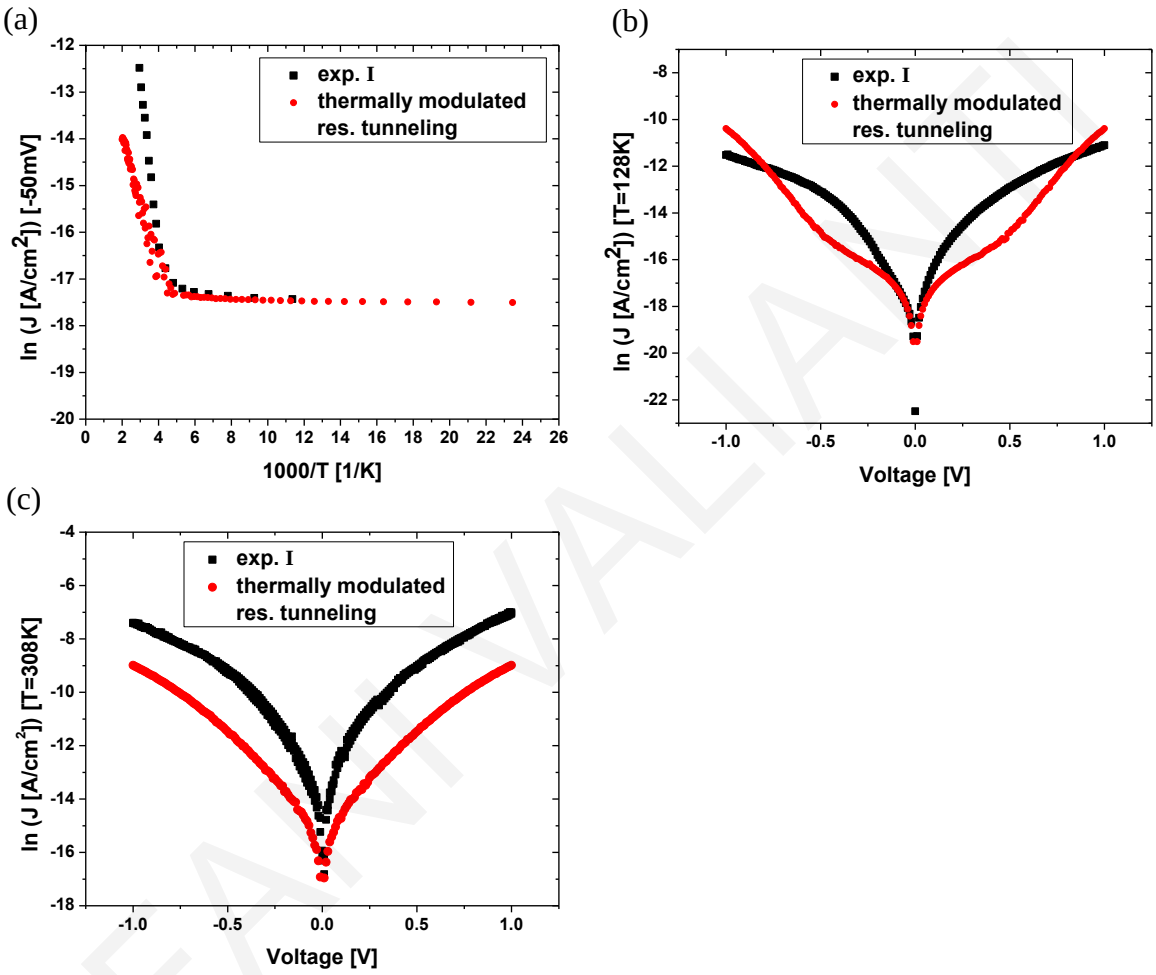

Figure 3.20 (a) Experimental ln(J) versus 1000/T of Apo-Az [29] as a function of temperature at V = -0.05 V versus theoretical fits (eqs (3.9)-(3.10)). (b) Experimental ln(J) versus voltage of Apo-Az at T = 128 K (low temperature regime) and theoretical fits using eqs (3.9)-(3.10). (c) Experimental ln(J) versus voltage of Apo-Az at T = 308 K (high temperature regime) and theoretical fits using eqs (3.9)-(3.10). For all graphs the parameter values are: λ=1.1 eV, α=0.50, ε_0=0.60 eV, Γ_L=1.0 10^{-3} eV and Γ_R/Γ_L=1.

As an alternative to the above model for the behavior of the Apo-Az currents at high T , we have also tested a multi-site incoherent hopping model. To describe incoherent transport through the amino acids we use a generalization of the one-site hopping model to N sites,

where N is a parameter to be determined by fitting. This model [51,52] is schematically represented in Fig. 3.21, where $L(R)$ denote the left (right) electron reservoirs (electrodes) and the B_i correspond to the different incoherent sites each of which should be interpreted as an electronic level of energy $\varepsilon_i(V)$, delocalized over one or more amino acids. The different $k_{i\to j}$ in this figure correspond to the different (forward and backward) electron transfer rates between these levels.

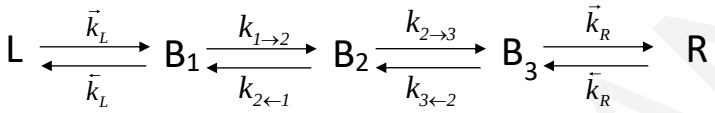

Figure 3.21 Schematic representation of the hopping model where a molecular bridge with *N*=3 incoherent sites coupled to the left (L) and right (R) electrodes.

To determine the steady state current in this model, we need to compute the stationary occupations $\left(\dot{P}_i^{(ss)}=0\right)$ in the different sites (e.g., $N=3$ below) by solving the corresponding kinetic equations:

$$\begin{aligned}
&-\left(\overleftarrow{k}_L + k_{1\to 2}\right)P_1^{(ss)} + k_{2\leftarrow 1}P_2^{(ss)} + \vec{k}_L P_{L,R}^{(ss)} = 0 \\
&k_{1\to 2}P_1^{(ss)} - \left(k_{2\leftarrow 1} + k_{2\to 3}\right)P_2^{(ss)} + k_{3\leftarrow 2}P_3^{(ss)} = 0 \\
&k_{2\to 3}P_2^{(ss)} - \left(k_{3\leftarrow 2} + \vec{k}_R\right)P_3^{(ss)} + \overleftarrow{k}_R P_{L,R}^{(ss)} = 0
\end{aligned} \tag{3.11}$$

The steady state current per molecule (evaluated at the left interface) is simply given by:

$$I(V) = -e\left(\vec{k}_L P_{L,R}^{(ss)} - \overleftarrow{k}_L P_1^{(ss)}\right). \tag{3.12}$$

In order to specify the voltage dependence of the molecular levels $\left(\varepsilon_i(V)\right)$, we will assume that a portion $\alpha_{L,R}$ of the bias voltage drops at the left and the right metal-molecule interfaces, and a portion a_M drops along the molecule such that: $a_L + a_M + a_R = 1$.

For simplicity, we will assume that all the forward rates are equal, $k_{i\to i+1} = k_f$. The same is true for the backward intra-molecular rates, $k_{i\leftarrow i-1} = k_b$. The rates are given by:

$$k_{i\to j} = k\, e^{-\left(\varepsilon_i(V)-\varepsilon_j(V)+\lambda_i+\lambda_j\right)^2 \Big/ 4k_BT\left(\lambda_i+\lambda_j\right)} \tag{3.13}$$

and they satisfy the detailed balance equation below:

$$k_{i\to i+1}/k_{i\leftarrow i-1} = e^{-\Delta G_{i\to i+1}/k_BT}\,. \tag{3.14}$$

For the voltage-dependent rates involving charge transfer to the electrodes, we shall use the typical expressions taken from heterogeneous electron transfer theory, [13] in eqs (3.6)-(3.7). For hopping rates from/to the $L(R)$ electrode we use the molecular level coupled to the $L(R)$ electrode, $\varepsilon_{1(\mathrm{N})}(V)$.

The main parameters used in this model are: N (number of incoherent hopping sites), λ (reorganization energy), ε (the one-site energy of the molecular level at zero bias, assumed to be equal for all of them), k (zero-bias intra-molecular transfer rate), $\alpha_{L,R}$ (parameters describing the voltage drop at the metal-molecule interfaces) and $\gamma_{L(R)} = (2/\hbar)\Gamma_{L(R)}$ (golden rule rates).

We find that to reproduce the activated behavior of the Apo-Az current for $T > 200K$ we need at least $N = 3$ incoherent sites in the molecular bridge (amino acid centers). An example comparison of experiment and $N-$ site hopping theory is shown in Fig. 3.22. Figure 3.22a compares the experimental $ln(J)-V$ curve (black square) to a theoretical fit using the $N = 3$ hopping-site model (red circle). Figure 3.22b compares the experimental $ln(J)-T$ curve to a theoretical fit using the same model (magenta triangle). The hopping model parameter values are: $\lambda = 0.3eV$ (typical for amino acids [53]), $\alpha_L = \alpha_R = -0.40$, $\varepsilon_0 = 0.40eV$, $\Gamma_L = 1.0\ 10^{-8} - 3.30\ 10^{-8} eV$, $\Gamma_R/\Gamma_L = 100$ and $\Gamma = 1.0\ 10^{-7} - 3.30\ 10^{-7} eV$.

Since the $N = 3$ hopping-site model is not relevant to the low temperature behavior, Fig. 3.22b also shows a theoretical fit of the low temperature regime using the off-resonant tunneling model (eqs (3.1)-(3.4)) (blue triangle).

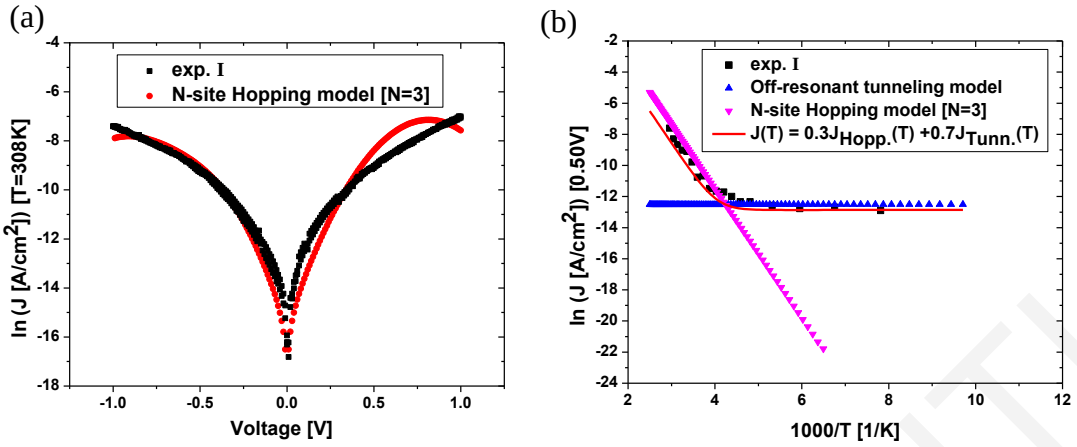

Figure 3.22 (a) Experimental ln(J) versus voltage of Apo-Az [29] at T = 308 K and theoretical fits (eqs (3.11)-(3.14)). (b) Experimental ln(J) versus 1000/T of Apo-Az at V = 0.50 V over the entire temperature range and theoretical fits (using eqs (3.11)-(3.14) at high temperatures, eqs (3.1)-(3.4) at low temperatures and eq. (3.15) for both temperature regimes). Model parameter values of eqs (3.11)-(3.14): N=3, λ=0.3 eV, α_L=α_R=-0.40, ε_0=0.40 eV, Γ=3.30 10^{-7} eV, Γ_L=3.30 10^{-8} eV and Γ_R/Γ_L=100. Model parameter values of eqs (3.1)-(3.4): α=0.50, ε_0=0.70 eV, Γ_L=1.0 10^{-3} eV and Γ_R/Γ_L=1. Parameter value of eq. (3.15) (red line): p=0.3.

The fitting results suggest that the Apo-Az current at low temperatures is mediated by tunneling and at high temperatures by through-amino acid hopping. The simplest interpretation of the above is that, the ensemble (monolayer) current density is described by the following simple relationship

$$J_{total} = pJ_{Hopp.}(T) + (1-p)J_{Tunn.}(T) \qquad (3.15)$$

where $J_{Hopp.}(T)$ is the current density through the $N=3$ hopping sites at the high temperature regime and $J_{Tunn.}(T)$ is the off-resonant tunneling current density. A good fit of eq. (3.15) to the experimental temperature dependence for the whole range of temperatures is also shown in Fig. 3.22b (red line).

If we consider that every protein in the ensemble may transport charge via two dominant channels, hopping and tunneling, then the prefactor p could be interpreted as the probability of hopping and $1-p$ as the probability of tunneling. However, this probabilistic interpretation of the parameter may be an oversimplified picture given the approximate nature of the models. Equation (3.15) could also be interpreted as a result emerging from a

more complete, rigorous theory, which reduces to the two limiting cases (tunneling, hopping) at different (low, high) temperatures.

3.4 Modeling heterojunction experiments of Zinc-, Cobalt- and Nickel-substituted Azurins (exp. I)

In addition to the Apo- and Holo-Az heterojunction experiments, ref. [29] reports the temperature and voltage dependencies of the current for Zn-, Ni- and Co- substituted Azurin heterojunctions. Figure 3.2 compares the current temperature dependencies of Apo-Az and Holo-Az to those of Zn-, Co- and Ni-Az at a voltage of -50 mV. The current temperature dependencies all exhibit a temperature independent region $\left(T < T_c\right)$ and temperature-dependent (activated) region $\left(T > T_c\right)$. The shapes of the $ln\left(J\right)$ versus $1/T$ plots for Zn-, Co- and Ni-Az are intermediates between those of Apo-Az and Holo-Az. The Zn-Az and Apo-Az heterojunctions have similar current temperature dependencies and so do the Holo-Az and Ni-Az heterojunctions. The Co-Az current temperature dependence is approximately intermediate between the Apo-Az and Holo-Az extremes.

As the medium is changed from Apo-Az to Zn-, Co-, Ni- and Cu-substituted Az, the trend in the temperature dependence of the current is a reduction of the total current enhancement in the thermally-activated region, i.e., a reduction of $\Delta J^{act} = \ln\left(J_{\max}\right) - \ln\left(J_{\min}\right) \approx \ln\left(J\left(T_{\max}\right)\right) - \ln\left(J\left(T_{\min}\right)\right)$, with a simultaneous increase of the minimum current, $\ln\left(J_{\min}\right) \approx \ln\left(J\left(T_{\min}\right)\right)$, in the temperature-independent region. This trend seems to be correlated with the reduction potentials Vs. SHE of the substituted metals and of some common amino acids (Table 3.1). The last column in Table 3.1 converts the reduction potentials Vs. SHE to an absolute energy scale (in eV) with respect to vacuum, [50,54-58] to be compared to the Au fermi level of -5.1 eV. [59] It is obvious from the table that the barrier ΔG_X^0 for reduction of a metal or of an amino acid (AA) X from Au follows the same trend as ΔJ_X^{act}, i.e., $\Delta G_{Cu}^0 < \Delta G_{Ni}^0 < \Delta G_{Co}^0 < \Delta G_{Zn}^0 < \Delta G_{AA}^0$ and $\Delta J_{Cu-Az}^{act} < \Delta J_{Ni-Az}^{act} < \Delta J_{Co-Az}^{act} < \Delta J_{Zn-Az}^{act} < \Delta J_{Apo-Az}^{act}$.

Reactions	Reduction Potential ΔG_X^0 Vs. SHE [mV]	Reduction Potential ΔG_X^0 with respect to vaccum [eV]
Cu^{2+}/Cu^{+} (Azurin)	310	-4.75
Cu^{2+}/Cu^{+}	160	-4.6
Ni^{2+}/Ni	-257	-4.18
Co^{2+}/Co	-277	-4.16
Zn^{2+}/Zn	-760	-3.68
Amino acids [at pH=7]		
Gly	1225	-3.215
Trp	1250	-3.19
Cys	1300	-3.14
Tyr	1350	-3.09

Table 3.1 Conversion of reduction potentials vs. SHE (mV) into electronic energies with respect to vacuum (eV) for metals relevant to experiments I and II and for some amino acids. [50,54-58]

Therefore, we expect that in going from Zn to Ni the ensemble-averaged barrier for tunneling through Az is progressively lowered if the metal participates in transport. Figure 3.23 shows fits of the experimental results for the cases of Ni-, Co- and Zn-Az heterojunctions in the temperature-independent regime $(T < 200K)$ using the tunneling model (eqs (3.1)-(3.4)) with different values of ε_0 that follow the trend of ΔG_X^0 in Table 3.1. An example comparison of experiment and theory is shown in Fig. 3.23. The parameter values employed for the fit are: $\Gamma_L = 1.0\ 10^{-3} - 2.5\ 10^{-3} eV$, $\Gamma_R/\Gamma_L = 1$, $\alpha = 0.50$ and $\varepsilon_0 = 0.2, 0.22, 0.55 eV$ for Ni-, Co- and Zn-Az heterojunctions respectively (eqs (3.1)-(3.4)).

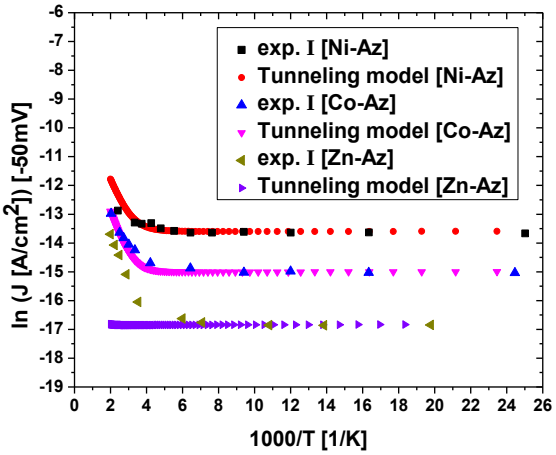

Figure 3.23 Experimental ln(J) versus 1000/T of Ni-, Co- and Zn-Az [29] at -50 mV bias and theoretical best-fit using the off-resonant tunneling model (eqs (3.1)-(3.4)) with the best fit parameter values of Γ_L=1.0 10^{-3} eV, Γ_R/Γ_L=1, α=0.50 and ε_0=0.20, 0.22, 0.55 eV for Ni-, Co- and Zn-Az heterojunctions respectively.

In the cases of Ni-Az and Co-Az heterojunctions, we can reproduce the experimental results both in the temperature-independent $(T < 200K)$ and thermally activated regimes $(T > 200K)$ using the Landauer model (eqs (3.1)-(3.4)) with $\varepsilon_0 = 0.2\ eV$ (Ni) and $\varepsilon_0 = 0.22\ eV$ (Co). In the case of the Zn-Az heterojunction the current-temperature dependence resembles very much that of Apo-Az. This is reasonable since the reduction potential of Zn ($E^0 = -760mV$ Vs. SHE) [54] is relatively close to that amino acid redox potentials (e.g. Tyr, Cys, Trp, Gly) (see Table 3.1). Therefore, Zn does not provide a much better transport channel than the amino acids in Azurin, and to explain the temperature behavior we can adopt the same modeling as in Apo-Az. Figure 3.23 shows that the Zn-Az current in the temperature-independent region $(T < 200K)$ is reproduced by a tunneling model with $\varepsilon_0 = 0.55eV$, but this model cannot reproduce the current in the thermally activated region $(T > 200K)$. For this region, we use the $N-$ site hopping model, and as in the Apo-Az case we can reproduce the current for $N \geq 3$ (Fig. 3.24).

As in the case of Apo-Az, the hopping and tunneling currents can be combined to reproduce the Zn-Az current in the whole temperature range via eq. (3.15). Figure 3.24 (red line) shows the monolayer Zn-Az current computed from eq. (3.15) and compared to the experimental results of ref. [29].

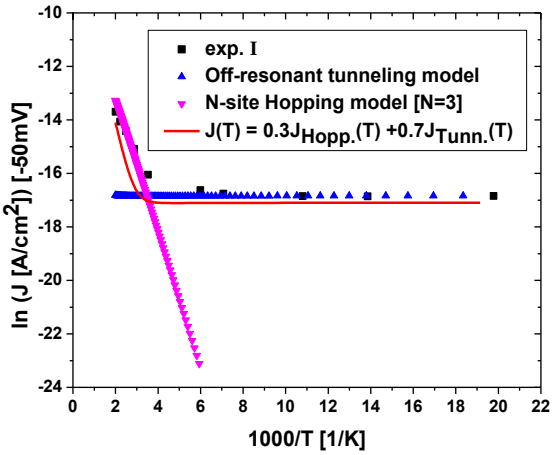

Figure 3.24 Experimental ln(*J*) versus 1000/*T* of Zn-Az [29] at *V*=-50 mV over the entire temperature range and theoretical fits (using eqs (3.11)-(3.14) at high temperatures, eqs (3.1)-(3.4) at low temperatures and eq. (3.15) for both temperature regimes). Model parameter values of eqs (3.11)-(3.14): N=3, λ=0.3eV, $\alpha_L=\alpha_R$=-0.40, ε_0=0.20 eV, Γ=1.0 10^{-12} eV, Γ_L=3.30 10^{-8} eV and Γ_R/Γ_L=1. Model parameter values of eqs (3.1)-(3.4): α=0.50, ε_0=0.55 eV, Γ_L=1.0 10^{-3} eV and Γ_R/Γ_L=1. Parameter value of eq. (3.15) (red line): p=0.3.

It should be noted that the temperature dependencies of the activated currents in Fig. 3.2 for Ni-Az and Co-Az can also be reproduced by a through – amino acid hopping model, as is the case of Apo- and Zn-Az. Given the fact that at the highest temperatures all currents in Fig. 3.2 converge to similar values, the best interpretation of the activated region is that the current is dominated by through amino acid hopping in all cases.

3.5 Conclusions

The present theoretical investigation is motivated by experiments [29,30] which measure the current-voltage and current-temperature dependencies of ETpr Azurin monolayer heterojunctions. The experiments in ref. [29] (exp. I) involve Si-oxide substrate – Az – Au or Hg LOFO heterojunctions and compare the voltage and temperature dependencies of Holo-Az (with Cu as the redox site) and Apo-Az (with Cu removed). They also measure the temperature dependencies of other metal-substituted Azurins (Ni, Co, and Zn). The experiments in ref. [30] (exp. II) involve Au microelectrode – Az – Au microelectrode heterojunctions and measure the current-voltage and current-temperature dependencies of Holo-Az. The experimental results are very interesting because they enable the analysis of

transport through the same protein monolayer medium as a function of the metal substitution, temperature and voltage.

In both types of heterojunctions [29,30] the Holo-Az current is approximately temperature independent but the bias voltage dependence of the Holo-Az current in ref. [29] differs considerably from ref. [30]. Further, in contrast to the temperature-independent Holo-Az, the Apo-Az current in ref. [29] shows activationless behavior at lower temperatures $(T < 200K)$ and activated behavior at higher temperatures $(T > 200K)$. The temperature dependencies of the current for the other metal substituted Azurin monolayers interpolate between the Holo-Az behavior and the Apo-Az behavior. In the temperature-independent regime, the magnitude of the current is the highest for Holo-Az and the lowest for Apo-Az with the other metal-substituted Azurins showing intermediate current values between the two extremes (Cu-Az > Ni-Az > Co-Az > Zn-Az > Apo-Az). At the highest temperatures the current magnitudes of all Azurin types are similar.

The richness of the above phenomenology offers an opportunity to explore transport mechanisms through the Azurin monolayers and to gain insight into the competition between metal- and amino acid-mediated transport in these systems. In our work we have attempted to fit the experimental results using several standard models of coherent and incoherent transport mechanisms. Importantly, for each mechanism we fit simultaneously both the voltage and temperature dependencies of the logarithm of the current, using a common set of parameters. This approach turns out to limit to a large extent both the type of transport mechanism and its corresponding parameter set compatible with experiment. Our results do not exclude the possibility that the systems studied may operate in more complex, in intermediate regimes between the extremes of fully coherent and fully incoherent transport. However, given the information we have about the systems, it is impossible to determine more precisely those regimes. Our results are summarized in Table 3.2.

Holo-Az experiments [29,30]	**Zn- and Apo-Az experiments** [29]	**Ni- and Co-Az experiments** [29]
Temp. independent current	Temp. dependent current: $T > T_c$ Temp. independent current: $T < T_c$	Current temp. dependence is intermediate between the Holo- and Apo-Az behaviors

Exp. I [29] through-Cu incoherent resonant hopping (high disorder)	$T < T_c$ off-resonant tunneling	$T < T_c$ near-resonant tunneling
Exp. II [30] off-resonant tunneling	$T > T_c$ through-amino acid hopping	$T > T_c$ both near-resonant tunneling and through-amino acid hopping are consistent with experiment

Table 3.2 Transport mechanisms for the Azurin heterojunctions [29,30] in the different temperature regimes. $T_c \approx 200K$ remains the same for all Azurin heterojunctions.

We find that in the Holo-Az heterojunctions of ref. [29] transport is mediated by through-Cu incoherent resonant hopping with the possibility of through-Cu coherent resonant tunneling also contributing for low bias voltages. In contrast, for the Holo-Az heterojunctions in ref. [30], transport is mediated by off-resonant tunneling. Our analysis also shows that the Cu-level energies of the Holo-Az monolayers in ref. [29] are much more disordered compared to the monolayers in ref. [30]. These results explain the large differences in the low bias voltage dependencies of the current per Azurin molecule observed in the two experiments (Fig. 3.4) and also are consistent with the structural differences between the two types of heterojunctions. The proteins in ref. [29] are covalently bound via a linker molecule to one lead and physisorbed to the other. The proteins in ref. [30] are covalently bound by S-Au bonds to both leads. Thus, each Cu metal in the heterojunctions of ref. [29] is on average much more weakly coupled to the leads as compared to ref. [30], and the protein monolayer is much more disordered.

For the Apo-Az experiments, [29] we find that the removal of the Cu atom changes the transport mechanism to through-amino acid off-resonant tunneling in the lower temperature (temperature-independent) regime and to through-amino acid hopping in the higher temperature, activated regime. For the other metal substituted Azurins (Zn, Ni, Co), the off-resonant tunneling model reproduces the currents in the temperature-independent regime with average tunneling barriers that follow the same magnitude trend as the redox potentials of the metals, indicating that the metal type plays a role in influencing the average tunneling

barrier in these systems. For the high-temperature, activated regime, through-amino acid hopping can reproduce the current behavior for all three metal substitutions, although the off-resonant tunneling model can also reproduce the activated region for Ni- and Co-substituted Azurins. The best self-consistent interpretation of the currents' temperature dependence at the highest temperatures in Apo-, Zn- Co-, and Ni-Az monolayers is a through-amino acid hopping mechanism.

The variability and mixing of transport mechanisms in the protein heterojunctions (see Table 3.2) is consistent with our current understanding of biomolecular ET. Even at the single molecule level, protein structural fluctuations can lead to fluctuating molecular and metal electronic-level energies and intra-level couplings, giving rise to a spread of ET rates and to ET mechanism switches. [8,16,18,24,46,60] At the monolayer level there is also additional static disorder. Further, the dominance of the through-Cu hopping mechanism for the Holo-Az heterojunctions with weak metal-lead couplings is not surprising given the recent theoretical and experimental results on redox molecular junctions. [49,61,62] Our results show that when the redox hopping site is near-resonant to or within the Fermi window, and the reorganization is small, (as is the case of the Cu level in the heterojunctions of ref. [29]), the hopping current can be near temperature-independent for finite bias voltages. Therefore, a temperature-independent current does not necessarily imply a coherent tunneling mechanism nor does it exclude a hopping mechanism. This conclusion is consistent with other theoretical working on hopping transport. [36]

3.6 Supplement

In addition to the models described in detail in the main text which were partially successful in reproducing all of the experiments, we also tried to fit the experimental data using two more-complex models that often appear in the literature. These models failed to reproduce the experimental results of both experiments. [29,30] For the sake of completeness, we describe the models in the following. The first is the extended – fully adiabatic Newns-Anderson model. [37-40] According to the Newns-Anderson model the current is modulated by a collective coordinate Q (solvent or molecule coordinate). The instantaneous current [37] $\tilde{I}$ for a fixed value of Q is given by

$$\tilde{I}(V;\eta,Q)=\frac{2e}{h}\Gamma_a\left(\arctan\frac{\varepsilon_0(V)+eV}{\Gamma}-\arctan\frac{\varepsilon_0(V)}{\Gamma}\right), \qquad (3.16)$$

where

$$\Gamma = \Gamma_L + \Gamma_R \text{ and } \frac{4}{\Gamma_a} = \frac{1}{\Gamma_L} + \frac{1}{\Gamma_R} \tag{3.17}$$

are the arithmetic and harmonic averages of the broadening functions $\Gamma_{L(R)}$. The energy offset from the substrate's Fermi energy at fixed molecular configuration Q, can be expressed as

$$\varepsilon_0(Q,\eta,V) = -e\xi\eta - e\delta V + \lambda(1-2Q), \tag{3.18}$$

where λ is the reorganization energy, ξ is a gating efficiency, $0 \le \xi \le 1$, η is the overpotential, $\eta = V_{eq} - \frac{\mu_L}{e}$ $\left(V_{eq} = (\mu_L + \mu_R)/2e\right)$, and δ is a voltage division factor $0 \le \delta \le 1$.

The theoretical (total) current to be compared with the experimental current should be computed as a temporal average within a time $\sim \tau_{meas}$. Because τ_{meas} is long compared to τ_{fluct} instead of temporal averaging, one can perform ensemble averaging

$$\left\langle \tilde{I}(V;\eta,Q)_Q \right\rangle_Q = \frac{\int_{-\infty}^{\infty} \tilde{I}(V;\eta,Q) P(Q;\eta,V)\, dQ}{\int_{-\infty}^{\infty} P(Q;\eta,V)\, dQ}, \tag{3.19}$$

where $P(Q;\eta,V)$ is the thermal weight and can be expressed as $P(Q;\eta;V) = \exp\left[-U_{ad}/k_B T\right]$, where $U_{ad}(Q;\eta;V)$ is the adiabatic Gibbs free energy. In this model the site $\varepsilon_0(Q,\eta,V)$ is interpreted as the redox Cu state energy which depends on a molecular conformation Q.

The other model is a vibrationally coherent two-step ET model (2sETm). [41,42] The formula which gives the current and describes molecular transport in the adiabatic limit and for $V > 0$ is the following:

$$I = \frac{2AV}{\exp\left[\frac{1}{4\lambda k_B T}\left(\lambda - e\xi\eta - e\delta V\right)^2\right] + \exp\left[\frac{1}{4\lambda k_B T}\left(\lambda + e\xi\eta - (1-\delta)eV\right)^2\right]}, \tag{3.20}$$

where

$$A = \frac{e^2}{4\pi} w_{ph} k_{L(R)} \rho_{L(R)} \tag{3.21}$$

is a prefactor, $k_{L(R)}$ are the microscopic transmission rates, $\rho_{L(R)}$ are the densities of states and w_{ph} is an average of the (solvent) phonon frequency.

The specific research work presented in this chapter has been published during the doctoral program (see ref. [63]).

3.7 References

[1] Marcus, R.A.; Sutin, N. Electron Transfers in Chemistry and Biology. *Biochim. Biophys. Acta*. **1985**, *811*, 265–322.

[2] Bendall, D.S. *Protein Electron Transfer*; Bios Scientific Publishers, Oxford, U.K., 1996.

[3] Canters, G.W.; Vijgenboom, E. *Biological Electron Transfer Chains: Genetics, Composition and Mode of Operation*; Springer, Dordrecht, 1998.

[4] Jortner, J.; Bixon, M.; Prigogine, I.; Rice, S.A. *Electron Transfer - from Isolated Molecules to Biomolecules*; John Wiley & Sons, *New York, 1999.*

[5] Schuster, *G.B. Long-Range Charge Transfer in DNA I and II;* Top Curr. Chem, vol. 236-237, Springer, Berlin, 2004.

[6] Beratan, D.N.; Skourtis, S.S. Electron Transfer through Proteins. *Encyclopedia of Biophysics*. **2012**, 625-630.

[7] Winkler, J.R.; Gray, H.B. Electron Flow through Metalloproteins. *Chem. Rev*. **2014**, *114*, 3369-3380.

[8] Skourtis, S.S. Probing Protein Electron Transfer Mechanisms From the Molecular to the Cellular Length Scales. *Biopolymers*. **2013**, *100*, 82-92.

[9] Beratan, D.N.; Skourtis, S.S.; Erb, T.J.; Gerlt, J.A. Energy/Mechanistic Biology. Curr *Opin Chem Biol*. **2018**, *47*, A1-A6, 1-142.

[10] Teo, R.D.; Rousseau, B.J.G.; Di Felice, R.; Beratan, D.N.; Migliore, A. Charge Transfer between [4Fe4S] Proteins and DNA Is Unidirectional: Implications for Biomolecular Signaling. *Chem*. **2019**, *5*, 122-137.

[11] *Balzani, V.; Piotrowiak, P.; Rodgers, M.A.J.; Mattay, J.; Astruc, D.; Gray, H.B.; Wrinkler, J.; Fukuzumi, S.; Mallouk, T.E.; Haas, Y.; et al. Electron Transfer in Chemistry*; I–V ed.; Weinheim:Wiley-VCH, 2001.

[12] Kuznetsov, A. M.; Ulstrup, J. *Electron Transfer in Chemistry and Biology: An Introduction to Theory*; John Wiley & Sons Ltd, Chichester, UK, 1999.

[13] May, V.; Kuhn, O. *Charge and Energy Transfer Dynamics in Molecular Systems*; 3rd ed.; Wiley-VCH, Berlin, 2011.

[14] Nitzan A. *Chemical Dynamics in Condensed Phases*; Oxford University Press, 2006.

[15] Beratan, D.N.; Skourtis, S.S.; Balabin, I.A.; Balaeff, A.; Keinan, S.; Venkatramani, R.; Xiao, D. Steering Electrons on Moving Pathways. *Acc. Chem. Res*. **2009**, *42*, 1669-1678.

[16] Skourtis, S.S.; Waldeck, D.H.; Beratan, D.N. Fluctuations in Biological and Bioinspired Electron-Transfer Reactions. *Annu. Rev. Phys. Chem*. **2010**, *61*, 461-485.

[17] Blumberger, J. Recent Advances in the Theory and Molecular Simulation of Biological Electron Transfer Reactions. *Chem. Rev*. **2015**, *115*, 11191-11238.

[18] Beratan, D.N.; Liu, C.; Migliore, A.; Polizzi, N.F.; Skourtis, S.S.; Zhang, P.; Zhang, Y. Charge Transfer in Dynamical Biosystems, or The Treachery of (Static) Images. *Acc Chem Res*. **2015**, *48*, 474-481.

[19] Cuevas, J.C.; Scheer, E. *Molecular Electronics: An Introduction to Theory and Experiment*; 2nd ed.; World Scientific, Singapore, 2017.

[20] Zhang, J.; Kuznetsov, A.; Medvedev, I.G; Chi, Q.; Albrecht, T.; Jensen, P.; Ulstrup, J. Single-Molecule Electron Transfer in Electrochemical Environments. *Chem. Rev*. **2008**, *108*, 2737-2791.

[21] Amdursky, N.; Marchak, D.; Sepunaru, L.; Pecht, I.; Sheves, M.; Cahen, D. Electronic Transport via Proteins. *Adv. Mater*. **2014**, *26*, 7142-7161.

[22] Ruiz. M.P.; Aragonès, A.C.; Camarero, N.; Vilhena, J.G.; Ortega, M.; Zotti, L.A.; Pérez, R.; Cuevas, J.C.; Gorostiza, P.; Díez-Pérez, I. Bioengineering a Single-Protein Junction. *J. Am. Chem. Soc*. **2017**, 139, 15337-15346.

[23] Skourtis, S.S; Balabin, I.A.; Kawatsu, T. Beratan, D.N. Protein Dynamics and Electron Transfer: Electronic Decoherence and Non-Condon Effects. *Proc. Natl. Acad. Sci. USA*. **2005**, *102*, 3552-3557.

[24] Balabin, I.A.; Beratan, D.N.; Skourtis, S.S. Persistence of Structure Over Fluctuations in Biological Electron-Transfer Reactions. *Phys. Rev Lett*. **2008**, *101*, 158102.

[25] Chi, Q.; Zhang, J.; Andersen, J.; Ulstrup, J. Ordered Assembly and Controlled Electron Transfer of the Blue Copper Protein Azurin at Gold (111) Single-Crystal Substrates. *J. Phys. Chem. B.* **2001**, *105*, 4669-4679.

[26] Chi, Q.; Farver, O.; Ulstrup, J. Long-Range Protein Electron Transfer Observed at the Single-Molecule Level: In Situ Mapping of Redox-Gated Tunneling Resonance. *Proc. Natl. Acad. Sci. USA*. **2005**, *102*, 16203-16208.

[27] Alessandrini, A.; Salerno, M.; Frabboni, S.; Facci, P. Single-Metalloprotein Wet Biotransistor. *Appl. Phys. Lett*. **2005**, *86*, 133902.

[28] Alessandrini, A.; Corni, S.; Facci, P. Unravelling Single Metalloprotein Electron Transfer by Scanning Probe Techniques. *Phys. Chem. Chem. Phys*. **2006**, *8*, 4383-4397.

[29] Amdursky, N.; Sepunaru, L.; Raichlin, S.; Pecht, I.; Sheves, M.; Cahen, D. Electron Transfer Proteins as Electronic Conductors: Significance of the Metal and Its Binding Site in the Blue Cu Protein, Azurin. *Adv Sci (Weinh)*. **2015**, *2*, 1400026.

[30] Yu, X.; Lovrincic, R.; Sepunaru, L.; Li, W.; Vilan, A.; Pecht, I.; Sheves, M.; Cahen, D. Insights into Solid-State Electron Transport through Proteins from Inelastic Tunneling Spectroscopy: The Case of Azurin. *ACS Nano*. **2015**, *9*, 9955-9963.

[31] Vilan, A.; Cahen, D. Soft Contact Deposition onto Molecularly Modified GaAs. Thin Metal Film Flotation: Principles and Electrical Effects. *Adv. Funct. Mater*. **2002**, *12*, 795-807.

[32] Smith, P.; Nordquist, C.; Jackson, T.; Mayer, T.; Martin, B.; Mbindyo, J.; Mallouk, T. Electric-Field Assisted Assembly and Alignment of Metallic Nanowires. *Appl. Phys. Lett*. **2000**, *77*, 1399-1401.

[33] Freer, E.; Grachev, O.; Duan, X.; Martin, S.; Stumbo, D. High-Yield Self-Limiting Single-Nanowire Assembly with Dielectrophoresis. *Nat. Nanotechnol*. **2010**, *5*, 525-530.

[34] Garg, K.; Ghosh, M.; Eliash, T.; van Wonderen, J.; Butt, J.; Shi, L.; Jiang, X.; Zdenek, F.; Blumberger, J.; Pecht, I.; et al. Direct Evidence for Heme-Assisted Solid-State Electronic Conduction in Multi-Heme c-Type Cytochromes. *Chem. Sci*. **2018**, *9*, 7304-7310.

[35] Schmickler, W.; Santos, E. *Interfacial Electrochemistry*; 2nd ed.; Springer, Berlin, 2010.

[36] Migliore, A.; Nitzan, A. Nonlinear Charge Transport in Redox Molecular Junctions: A Marcus Perspective. *Acs Nano*. **2011**, *5*, 6669-6685.

[37] Schmickler, W. A Theory of Adiabatic Electron-Transfer Reactions. *J. Electroanal. Chem*. **1986**, *204*, 31-43.

[38] Baldea, I. Important Insight into Electron Transfer in Single-Molecule Junctions Based on Redox Metalloproteins from Transition Voltage Spectroscopy. *J. Phys. Chem. C*. **2013**, *117*, 25798-25804.

[39] Medvedev, I.G. Tunnel Current through a Redox Molecule Coupled to Classical Phonon Modes in the Strong Tunneling Limit. *Phys. Rev. B*. **2007**, *76*, 125312.

[40] Baldea, I. Ambipolar Transition Voltage Spectroscopy: Analytical Results and Experimental Agreement. *Phys. Rev. B*. **2012**, *85*, 035442.

[41] Kuznetsov, A. Mechanisms of in Situ Scanning Tunneling Microscopy of Organized Redox Molecular Assemblies. *J. Phys. Chem. A*. **2000**, *104*, 11531-11540.

[42] Artes, J.; Martinez, M.; Giraudet, A.; Perez, I.; Sanz, F.; Gorostiza, P. Current-Voltage Characteristics and Transition Voltage Spectroscopy of Individual Redox Proteins. *J. Am. Chem. Soc*. **2012**, *134*, 20218-20221.

[43] Landau, A.; Kronik, L.; Nitzan, A. Cooperative Effects in Molecular Conduction. *J. Comput. Theor. Nanosci*. **2008**, *5*, 535-544.

[44] Williams, P.D.; Reuter, M.G. Level Alignments and Coupling Strengths in Conductance Histograms: The Information Content of a Single Channel Peak. *J. Phys. Chem. C*. **2013**, *117*, 5937-5942.

[45] Frisenda, R.; Perrin, M.L.; Valkenier, H.; Hummelen, J.C.; van der Zant, H.S.J. Statistical Analysis of Single-Molecule Breaking Traces. *Phys. Status Solidi B*. **2013**, *250*, 2431-2436.

[46] Zhang, Y.; Liu, C.; Balaeff, A.; Skourtis, S.S.; Beratan, D. Biological Charge Transfer via Flickering Resonance. *PNAS*. **2014**, *111*, 10049-10054.

[47] Cascella, M.; Magistrato, A.; Tavernelli, I.; Carloni, P.; Rothlisberger, U. Role of Protein Frame and Solvent for the Redox Properties of Azurin from *Pseudomonas aeruginosa*. *PNAS*. **2006**, *103*, 19641-19646.

[48] Sigfridsson, E.; Olsson, M.H.M.; Ryde, U. A Comparison of the Inner-Sphere Reorganization Energies of Cytochromes, Iron-Sulfur Clusters, and Blue Copper Proteins. *J. Phys. Chem. B*. **2001**, *105*, 5546-5552.

[49] Yuan, L.; Wang, L.; Garrigues, A.R.; Annadata, H.V.; Antonana, M.A.; Barco, E.; Nijhuis, C.A. Transition from Direct to Inverted Charge Transport Marcus Regions in Molecular Junctions via Molecular Orbital Gating. *Nat. Nanotechnol*. **2018**, *13*, 322-329.

[50] Fereiro, J.; Yu, X.; Pecht, I.; Sheves, M.; Cuevas, J.C.; Cahen, D. Tunneling Explains Efficient Electron Transport via Protein Junctions. *PNAS*. **2018**, *115*, E4577-E4583.

[51] Livshits, G.; Sterm, A.; Rotem, D.; Borovok, N.; Eidelshtein, G.; Migliore, A.; Penzo, E.; Wind, S.; Felice, R.; Skourtis, S.S.; et al. Long-Range Charge Transport in Single G-quadruplex DNA Molecules. *Nat. Nanotechnol*. **2014**, *9*, 1040-1046.

[52] Lechmann, L.; Ingold, G.-L.; Hanggi, P. Incoherent Charge Transport through Molecular Wires: Interplay of Coulomb Interaction and Wire Population. *Chemical Physics*. **2002**, *281*, 199-209.

[53] Milan-Garces, E.; Kaptan, S.; Puranik, M. Mode-Specific Reorganization Energies and Ultrafast Solvation Dynamics of Tryptophan from Raman Line-Shape Analysis. *Biophys. J.* **2013**, *105*, 211-221.

[54] Bard, A.J.; Faulkner, L.R. *Electrochemical Methods. Fundamentals and Applications*; 2nd ed.; John Wiley & Sons, Inc., USA, 2000.

[55] Trasatti, S. The Absolute Electrode Potential: An Explanation Note. *Pure & Appl. Chem*. **1986**, *58*, 955-966.

[56] Pascher, T.; Karlsson, B.; Nordling, M.; Makmstrom, B.; Vanngard, T. Reduction Potentials and Their pH Dependence in Site-Directed-Mutant Forms of Azurin from Pseudomas Aeruginosa. *Eur. J. Biochem*. **1993**, *212*, 289-296.

[57] Khoshtariya, D.E.; Dolidze, T.D.; Tretyakova, T.; Waldeck, D.H.; van Eldik, R. Electron Transfer with Azurin at Au-SAM Junctions in Contact with a Protic Ionic Melt: Impact of Glassy Dynamics. *Phys. Chem. Chem. Phys*. **2013**, *15*, 16515-16526.

[58] Matelkova, K.; Ossberger, K.; Hudak, J.; Vatral, J.; Boca, R.; Linert, W. Redox activity of some non-innocent amino acids. *Monatsh Chem*. **2013**, *144*, 937-949.

[59] Sachtler, W.M.H.; Dorgelo, G.J.H.; Holscher, A.A. The work function of gold. *Surf. Sci*. **1966**, *5*, 221-229.

[60] Troisi, A.; Nitzan, A.; Ratner, M.A. A Rate Constant Expression for Charge Transfer through Fluctuating Bridges. *J. Chem. Phys*. **2003**, *119*, 5782-5788.

[61] Migliore, A.; Nitzan, A. Irreversibility and Hysteresis in Redox Molecular Conduction Junctions. *J. Am. Chem. Soc*. **2013**, *135*, 9420-9432.

[62] White, A.J.; Migliore, A.; Galperin, M.; Nitzan, A. Quantum Transport with Two Interacting Conduction Channels. *J. Chem. Phys*. **2013**, *138*, 174111.

[63] Valianti, S.; Cuevas, J. C.; Skourtis, S. S. Charge-Transport Mechanisms in Azurin-Based Monolayer Junctions. *J. Phys. Chem. C* **2019**, *123 (10)*, 10, 5907–5922.

CHAPTER 4

Observing Donor-to-Acceptor Electron-Transfer Rates and the Marcus Inverted Parabola in Molecular Junctions

A recurring theme in molecular electronics is the relationship between the intra-molecular electron transfer rate in a donor-bridge-acceptor system and the conductance at low bias in the corresponding electrode-bridge-electrode junction. The similarities between through-bridge donor-to-acceptor electron tunneling and through-bridge electrode-to-electrode Landauer transport led to the suggestion of an approximate linear relationship between the rate and the conductance for any given bridge. A large body of work indicates that the two quantities are not necessarily linearly related, showing different behaviors as a function of temperature, voltage and bridge length. Apart from Landauer tunneling, incoherent hopping can be an important mechanism in molecular junctions. We propose a donor-bridge-acceptor molecular junction, functioning in the incoherent hopping regime, that is suited for establishing direct correlations between the electrode-to-electrode current and the intra-molecular donor-to-acceptor electron transfer rate. We suggest that this type of junction may be used to observe the Marcus-inverted-parabola dependence of the intra-molecular rate on energy gap by varying the bias voltage. The realization of such an experiment would enable meaningful comparisons between solution-phase electron transfer rates and molecular-junction currents for the same molecule.

A recurring theme in molecular electron transfer (ET) and transport (ETr) is understanding the role of the molecular bridge in transferring electrons, whether in the context of a donor-bridge-acceptor ET reaction or in the context of an electrode-bridge-electrode ETr experiment. What features of the bridge's structure tune the rate of an ET reaction and the conductance of a molecular-junction ETr experiment? Is it possible to correlate a donor-to-acceptor ET rate to the electrode-to-electrode conductance for the same molecular bridge? These questions were posed in refs [1,2] where it was argued that an approximately linear relationship between the ET rate and the low-bias Landauer conductance exists in the simplest cases.

References [1,2] inspired theoretical and experimental studies that explored correlations between ET rates and conductances. [3-8] The general conclusion is that the relationship

between the two quantities is not linear. There are several differences between an intra-molecular ET experiment and a molecular ETr experiment, even when comparing a donor-bridge-acceptor system to an electrode-bridge-electrode junction comprised of the same bridging molecule. For example, the molecular electron donor and acceptor states are localized, with discrete energies, in contrast to the electrode-donor and electrode-acceptor states which are more delocalized with a continuous or quasi-continuous energy spectrum. The donor-bridge and acceptor-bridge energy gaps and couplings in the ET experiment will generally differ from the electrode-bridge energy gaps and couplings in ETr. The solvent environment, much "dryer" in a molecular junction as compared to solution-phase ET, is also likely to influence the role of the bridge by perturbing the bridge's conformation and its electronic states, and by altering the time scale of dephasing and vibrational relaxation. The electric field applied across a molecular junction induces additional types of perturbation to the bridge which are absent in the (zero-field) molecular donor-bridge-acceptor experiment. In addition to all of the above, differences in experimental probes (e.g., current versus time resolved absorption measurements), and other experiment-specific differences such as bridge-electrode contact disorder, are likely to make simple correlation between ET rates and ETr conductances.

In spite of the above complications there are common bridge-dependence trends among ET and ETr experiments. For example, saturated bridges are less conductive than unsaturated ones and bridges that act as tunneling barriers show exponential dependence of the rate and the conductance on bridge length. In both ET and ETr communities one talks about through-bridge off-resonant tunneling, resonant-tunneling and hopping mechanisms, and there are efforts to incorporate biological ET molecules (proteins and DNA) in molecular junctions or self-assembled monolayer heterojunctions with the aim of using some of the molecular ET properties to tune the corresponding currents in the junctions. [9,10]

The most common ET mechanism in chemical and biological systems is incoherent hopping. [12-18] The hopping centers (sites) are redox moieties connected by molecular bridges that most often act as tunneling barriers. The electron moves from the donor site (D) to the acceptor site (A) via a through-bridge coherent tunneling step. The closest analogy in a junction is through-bridge electrode-to-electrode coherent tunneling at low bias, described by the Landauer theory. However, it is possible, in the regime of weak electrode-bridge coupling, that a part of the molecular bridge between the electrodes acts as an incoherent site that accepts (donates) a transferring electron. Simple rate models for such incoherent transport mechanisms are abundant. [2,3,19-21] For example, the introduction of a redox moiety inside the

molecular bridge can create an additional incoherent channel that involves switching between the redox moiety's oxidation states. Indeed, recent theoretical work considered junctions containing a redox moiety with multiple fast and slow channels. [22-24] Such junctions (denoted "redox") have very rich voltammetric phenomenology such as negative differential resistance and hysteresis because the switching charge state of the redox moiety can gate the molecular electronic level energies. In general, there is strong experimental evidence of incoherent hopping in junctions where a bridge contains a redox center. [24-26]

Motivated by these advances and by ref. [2] that compared the low-bias conductance to a D-to-A ET rate, we propose a molecular junction setup containing two redox centers connected to each other by a linear bridge and also to the electrodes by linear bridges. "Linear" is an approximate term, e.g., a planar bridge with one dimension much larger than the other two is also considered linear if the redox center/electrode is connected at the end of the larger bridge dimension. The two redox centers of the junction may be chosen from solution-phase ET systems for which they are the DA pair in bridge-mediated D-to-A ET reactions operating in the limit of nonadiabatic Marcus theory. We discuss junction parameters that enable the direct observation of a nonadiabatic bridge-mediated ET rate between these redox centers by measuring the junction current under a bias voltage.

4.1 Theoretical methods

Prior to discussing the proposed junction setup, we review a simple (single-site) hopping model that is often used to describe the incoherent hopping mechanism (Fig. 4.1). [19,20,25,26] A redox center (incoherent hopping site) is connected to a left (L) electrode and to a right (R) electrode via bridges (linkers). The bridges are not necessarily of the same length and both act as tunneling barriers for electron transfer between the hopping site and the electrodes (Fig. 4.2). There is only one (hopping) channel that supports the current and it involves a single electronic level of M.

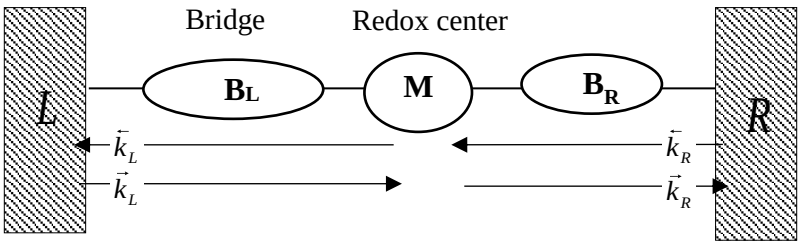

Figure 4.1 Schematic representation of a linear one-site hopping model with a single hopping site (redox moiety M) connected to left (L) and right (R) electrodes, respectively. The connection to the L electrode is through a molecular bridge that is assumed to act as a high tunneling barrier for the transferring electrons. The M-to-electrode hopping rates are given by Marcus theory rates for heterogeneous ET (eqs (4.2) and (4.3)).

In the fully incoherent limit (weak M-electrode coupling) the bias-voltage and temperature dependence of the current can be interpreted in terms of a hopping model that involves heterogeneous ET between the level of M and the right (R) or left (L) electrode. Figure 4.2 shows the energetics assuming a positive bias. The left and right bridge levels B_L (B_R) are shown to be of much higher energy than both M level energy and the L (R) Fermi levels. This depiction implies that the bridge levels act as tunneling barriers, providing only virtual intermediates for the transferring electrons. For example, assuming that the current is carried by holes, the accessible charge states of the junction are $LB_LM^+B_RR$ and LB_LMB_RR (with $LB_L^+MB_RR$ and $LB_LMB_R^+R$ energetically inaccessible).

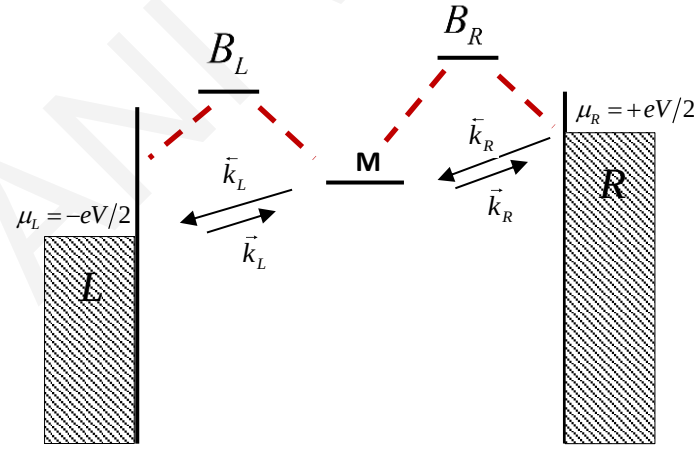

Figure 4.2 Schematic representation of the molecular levels in the junction setup of Fig. 4.1. The diagram shows a positive bias situation, where the backward rates are much larger than the forward rates. The bridge levels B_L and B_R shown to be of much higher energy than the redox level M. M indirectly couples to the L and R electrodes through the bridge levels (electronic couplings are represented by red dotted lines).

The steady-state current given the above assumptions is

$$I(V) = -e\frac{k_L^{\rightarrow}(V)k_R^{\rightarrow}(V) - k_L^{\leftarrow}(V)k_R^{\leftarrow}(V)}{k_L^{\rightarrow}(V) + k_L^{\leftarrow}(V) + k_R^{\rightarrow}(V) + k_R^{\leftarrow}(V)}, \tag{4.1}$$

where the rates are described by Marcus theory for heterogeneous ET, [19,21,22,27,28]

$$\begin{aligned}\vec{k}_L(V) &= 2\frac{\Gamma_L}{\hbar}\int dE\, f(E-\mu_L)W_{ox}\left(E,\varepsilon_M(V),\mu_L\right),\\ \overleftarrow{k}_L(V) &= 2\frac{\Gamma_L}{\hbar}\int dE\left[1-f(E-\mu_L)\right]W_{red}\left(E,\varepsilon_M(V),\mu_L\right),\end{aligned} \tag{4.2}$$

and

$$\begin{aligned}\vec{k}_R(V) &= 2\frac{\Gamma_R}{\hbar}\int dE\left[1-f(E-\mu_R)\right]W_{red}\left(E,\varepsilon_M(V),\mu_R\right),\\ \overleftarrow{k}_R(V) &= 2\frac{\Gamma_R}{\hbar}\int dE\, f(E-\mu_R)W_{ox}\left(E,\varepsilon_M(V),\mu_R\right).\end{aligned} \tag{4.3}$$

In the equations above, $\vec{k}_i\left(\overleftarrow{k}_i\right)$ are reduction (oxidation) rates of M by the i^{th} electrode (i = L, R). $W_{ox}\left(E,\varepsilon_M(V),\mu_{L(R)}\right)$ and $W_{red}\left(E,\varepsilon_M(V),\mu_{L(R)}\right)$ are distribution functions [27] for the oxidation and reduction of M, and are given by

$$\begin{aligned}W_{ox}\left(E,\varepsilon_M(V),\mu_{L(R)}\right) &= \frac{1}{\sqrt{4\pi\lambda k_B T}}e^{-\frac{\left(\lambda-\left(\mu_{L(R)}+E\right)+\varepsilon_M(V)\right)^2}{4\lambda k_B T}},\\ W_{red}\left(E,\varepsilon_M(V),\mu_{L(R)}\right) &= \frac{1}{\sqrt{4\pi\lambda k_B T}}e^{-\frac{\left(\lambda+\left(\mu_{L(R)}+E\right)-\varepsilon_M(V)\right)^2}{4\lambda k_B T}}.\end{aligned} \tag{4.4}$$

$\mu_L = -eV/2$ $\left(\mu_R = +eV/2\right)$ are the chemical potentials of the L (R) electrode and $\varepsilon_M(V)$ the redox-level energy, given by $\varepsilon_M(V) = \varepsilon_0 + (\alpha - 1/2)\times eV$, where ε_0 is the zero-bias energy of the M level and α determines the voltage dependence of the level, e.g., a value of $\alpha = 0.5$ leads to $\varepsilon_M(V) = \varepsilon_0$, whereas $\alpha > 0.50$ would give a voltage dependence of the M level energy that is more pinned to the right electrode. λ is the reorganization energy for oxidation / reduction of the redox moiety, and $\Gamma_{L(R)}$ are the level broadenings associated with the bridge-mediated couplings $H_{L(R)}$ between M and the L (R) leads,

$$\Gamma_{L(R)} = \pi H_{L(R)}^2 \rho_{L(R)}, \tag{4.5}$$

where $\rho_{L(R)}$ are the electronic densities of states of the L (R) leads. $H_{L(R)}$ should be interpreted as a through-bridge ($B_{L(R)}$) tunneling matrix elements. In the following we denote the prefactors for the heterogeneous ET rates as $c_{L(R)} = \frac{2\Gamma_{L(R)}}{\hbar}\frac{1}{\sqrt{4\pi\lambda_{L(R)}}}$. These prefactors can be approximated from voltammetric studies of nonadiabatic heterogeneous ET for a variety of redox center-bridge-electrode systems. [29,30]

If H_L is much weaker than H_R, we expect to encounter regimes for which the $\vec{k}_L(V)$ $\left(\overleftarrow{k}_L(V)\right)$ is current limiting, depending on the sign of the bias voltage (much smaller than the $\vec{k}_R(V)\left(\overleftarrow{k}_R(V)\right)$. For example, in a situation when the $\overleftarrow{k}_L(V)$ is current limiting, the current in eq. (4.1) is directly proportional to $k_L(V)$, i.e., $I(V) \approx e\overleftarrow{k}_L(V)$ for $V > 0$ and $I(V) \approx -e\vec{k}_L(V)$ for $V < 0$. In this situation, the voltage and temperature dependence of the current reflects the voltage and temperature dependence of the heterogeneous ET rate. Figs 4.3 and 4.4 are examples of this situation for a system with $\varepsilon_M(V) = +(0.15)\times eV$, $\lambda = 0.2eV$ and $c_L << c_R$. Figure 4.3 is a plot of $\overleftarrow{k}_L(V)$ as a function of voltage at different temperatures. The behavior is typical of a heterogeneous ET rate which has a sigmoidal dependence on overpotential, increasing in the normal region and saturating in the inverted region (the former showing activated temperature dependence and the latter temperature independence, see Fig. 4.4b). Figure 4.4a shows the exact and approximate (rate-limited) current expression as a function of voltage, indicating that $I(V) \approx e\overleftarrow{k}_L(V)$ for $V > 0$ and $I(V) \approx -e\vec{k}_L(V)$ for $V < 0$. Figure 4.4b shows the temperature dependence of the current at three different voltages, corresponding to the normal (thermally activated), inverted and activationless regimes of the heterogeneous ET rate in Fig. 4.3 and the approximate current. The signatures of Marcus heterogeneous ET rates have recently been observed in ref. [24], which probed the bias-voltage dependence of the current in a more complex (redox) molecular junction, and in ref. [26].

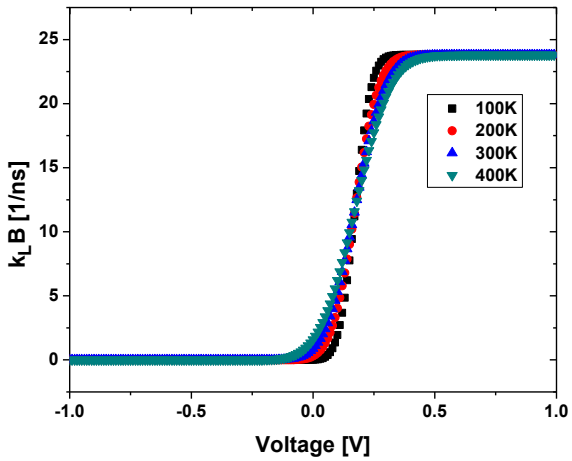

Figure 4.3 Left backward rate ($\overleftarrow{k}_L$ eq. (4.2)) versus the bias voltage *V* at T = 100-400 K. The heterogeneous ET rates have a sigmoidal dependence on voltage, increasing in the normal regime and saturating in the inverted regime. Parameter values: $\alpha = 0.65$, $\varepsilon_0 = 0$, $\lambda = 0.2$ *eV*, $c_L = 0.15 \times 10^2$ $eV^{-1/2}$ ns^{-1} and $c_R/c_L = 1000$. [29]

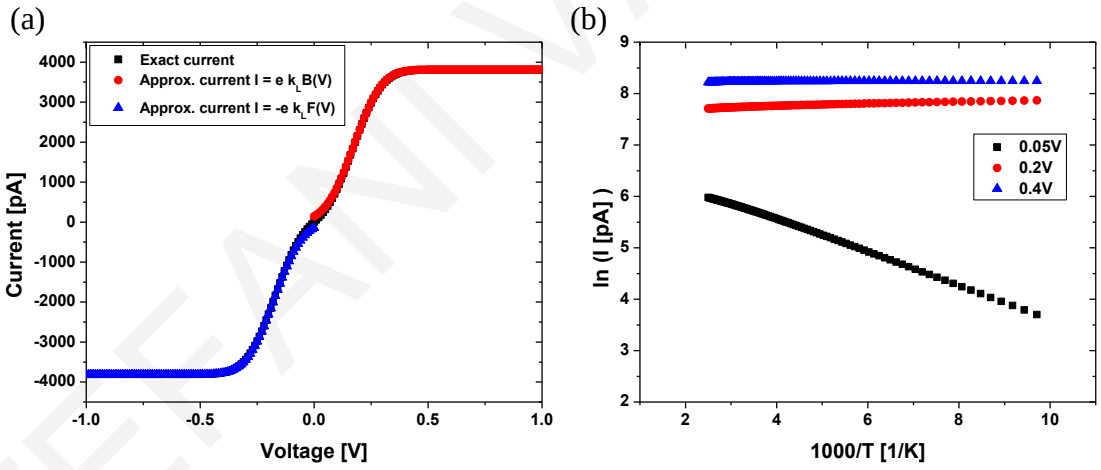

Figure 4.4 (a) Current *I* versus the bias voltage *V* at T = 300 K. Exact current expression (eq (4.1) black dots) and approximate expressions for the positive bias voltage regime ($I(V) \approx e\overleftarrow{k}_L$ red dots) and for the negative bias regime ($I(V) \approx -e\overrightarrow{k}_L$ blue dots). (b) Current *I* versus *1000/T* at V = 0.05 V (black dots) indicates the normal Marcus regime, 0.2 V (red dots) indicates the activationless regime, 0.4 V (blue dots) indicates the inverted Marcus regime. Parameter values: $\alpha = 0.65$, $\varepsilon_0 = 0$, $\lambda = 0.2$ *eV*, $c_L = 0.15 \times 10^2$ $eV^{-1/2}$ ns^{-1} and $c_R/c_L = 1000$.

In contrast to the Marcus heterogeneous ET rate between a redox center and an electrode (eqs (4.2)-(4.5)) the intra-molecular Marcus ET rate between two redox centers (D and A) in a DBA system shows an inverted-parabola behavior (for the natural logarithm of the rate) as a function of DA energy gap. [31,32] As the energy gap is changed from positive to negative values, the rate increases (in the normal activated region) reaches a maximum (in the activationless region) and then decreases again (in the inverted activated region). We propose a molecular junction setup suited to observe directly an intra-molecular ground-state D-to-A ET rate in the current measurement. The ultimate proof of success for the junction experiment would be to demonstrate that the natural logarithm of the current under bias shows the inverted-parabola behavior of the rate's energy gap dependence. We discuss conditions under which this observation would be possible.

The simplest setup (model) is a linear junction with two groups M_L and M_R that act as incoherent D and A hopping sites, and that are connected by a central molecular bridge (B_M). B_M acts as a tunneling barrier for electron transfer between M_L and M_R (Fig. 4.5). The M_L group is also connected to a left electrode (L) via a bridge B_L and the M_R group to a right electrode (R) via a bridge B_R (both acting as tunneling barriers). Applying a bias voltage V across the junction induces a current that involves electron tunneling between M_L and M_R. The rate of M_L-M_R electron transfer is nonadiabatic, described by Marcus theory. Due to the quasi-linearity of the junction there are no other parallel transport channels that avoid M_L-M_R electron transfer. Under what conditions is the current proportional to bridge-mediated M_L-to-M_R ET rates (backward or forward), similar to the intra-molecular D-to-A ET rates that would be observed in a solution-phase ground-state ET experiment of the DBA system where M_L and M_R act as D and A?

A critical condition is that M_L and M_R redox levels be weakly coupled to each other by the bridge, such that ET between M_L and M_R within the junction is the slowest rate process (thus current limiting). Using the notation of Figure 5, the M_L-to-M_R ET rates, $\vec{k}_{\text{int}}$ and $\overleftarrow{k}_{\text{int}}$, [31] are given by,

$$\vec{k}_{\text{int}} = \frac{2\pi}{\hbar}\frac{1}{\sqrt{4\pi\left(\lambda_L+\lambda_R\right)k_BT}}H^2_{M_L,M_R}\,e^{-\frac{\left(\Delta G(V)+(\lambda_L+\lambda_R)\right)^2}{4(\lambda_L+\lambda_R)k_BT}},$$

$$\overleftarrow{k}_{\text{int}} = \frac{2\pi}{\hbar}\frac{1}{\sqrt{4\pi\left(\lambda_L+\lambda_R\right)k_BT}}H^2_{M_L,M_R}\,e^{-\frac{\left(\Delta G(V)-(\lambda_L+\lambda_R)\right)^2}{4(\lambda_L+\lambda_R)k_BT}}. \qquad (4.6)$$

H_{M_L,M_R} is the bridge-mediated M_L-M_R tunneling matrix element and λ_L, λ_R are the M_L, M_R reorganization energies, respectively. $\Delta G = \varepsilon_{M_R}(V) - \varepsilon_{M_L}(V)$ is the energy gap for bias voltage V, where $\varepsilon_{M_L}(V)$, $\varepsilon_{M_R}(V)$ are the redox energies of M_L and M_R.

The forward and backward rates for ET between M_L (M_R) and the L (R) electrode are described using nonadiabatic Marcus theory for heterogeneous ET where $\vec{k}_L(V)$ and $\overleftarrow{k}_L(V)$ are given by eq. (4.2) with M replaced by M_L and $\vec{k}_R(V)$ and $\overleftarrow{k}_R(V)$ are given by eq. (4.3) with M replaced by M_R. The underlying assumption for using eqs (4.2) and (4.3) is that the M_L-L and M_R-R electronic couplings and widths (H_{M_L,M_R} and $\Gamma_{L(R)}$) are relatively weak. Thus, the M_L and M_R redox levels are localized on the redox units as would be the case for the solution-phase system.

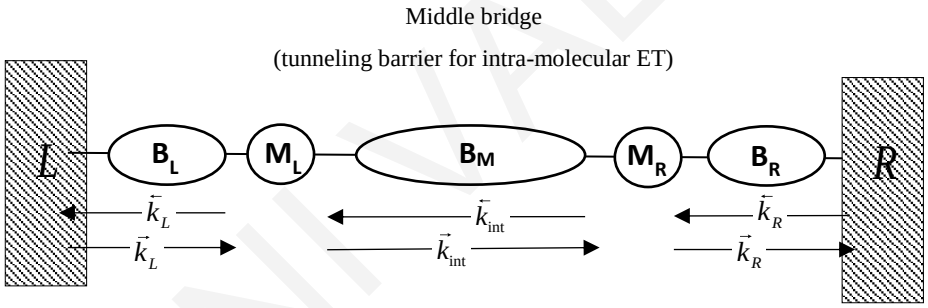

Figure 4.5 Schematic representation of the linear redox junction model. Donor (M_L) and acceptor (M_R) redox groups are connected to left (L) and right (R) electrodes, respectively via left (B_L) and right (B_R) bridges and also connected to each other by a middle bridge (B_M). All bridge units are tunneling barriers for the transferring electrons. The model assumes that the ET mechanism between M_L and M_R is incoherent hopping with forward and backward intra-molecular ET rates given by eq. (4.6). ET between M_L (M_R) and the L (R) electrode is also incoherent hopping with forward and backward heterogeneous ET rates given by eqs (4.2) and (4.3).

To calculate the steady state current in this model, we use the method in refs [33-35]. We obtain the stationary occupations $P_i^{(ss)}$ for each site i (i = M_L, M_R, L/R) by solving the following kinetic equations with $\dot{P}_i^{(ss)} = 0$:

$$
\begin{aligned}
&-\left(\vec{k}_L+\vec{k}_{\text{int}}\right)P_{M_L}^{(ss)}+\vec{k}_{\text{int}}P_{M_R}^{(ss)}+\vec{k}_L P_{L,R}^{(ss)}=0\\
&\vec{k}_{\text{int}}P_{M_L}^{(ss)}-\left(\vec{k}_{\text{int}}+\vec{k}_R\right)P_{M_R}^{(ss)}+\vec{k}_R P_{L,R}^{(ss)}=0\\
&P_{M_L}^{(ss)}+P_{M_R}^{(ss)}+P_{L,R}^{(ss)}=1
\end{aligned}
\tag{4.7}
$$

The steady state current (evaluated for the left interface) is:

$$
I(V)=-e\left(\vec{k}_L P_{L,R}^{(ss)}-\vec{k}_L P_{M_L}^{(ss)}\right), \tag{4.8}
$$

leading to the following exact expression for the steady state current (see Supplement section):

$$
I(V)=-e\left[\frac{\vec{k}_L\vec{k}_{\text{int}}\vec{k}_R-\vec{k}_L\vec{k}_{\text{int}}\vec{k}_R}{\vec{k}_{\text{int}}\vec{k}_L+\vec{k}_{\text{int}}\vec{k}_L+\vec{k}_{\text{int}}\vec{k}_L+\vec{k}_{\text{int}}\vec{k}_R+\vec{k}_L\vec{k}_R+\vec{k}_{\text{int}}\vec{k}_R+\vec{k}_{\text{int}}\vec{k}_R+\vec{k}_L\vec{k}_R+\vec{k}_L\vec{k}_R}\right] \tag{4.9}
$$

To describe the bias-voltage dependence of the redox-level energies ($\varepsilon_i(V)$, i = M_L, M_R), we assume that a fraction $\alpha_L\,(\alpha_R)$ of the bias voltage drops at the left (right) electrode-molecule interface, and a fraction α_M drops along the molecular bridge between the M_L and M_R redox groups $(\alpha_L+\alpha_M+\alpha_R=1)$. In terms of these parameters, the bias-voltage dependence of the M_L and M_R redox-level energies are described by

$$
\varepsilon_{M_L}(V)=\varepsilon_{M_L,0}+(\alpha_L-1/2)eV\,, \tag{4.10}
$$

and

$$
\varepsilon_{M_R}(V)=\varepsilon_{M_R,0}-(\alpha_R-1/2)eV\,, \tag{4.11}
$$

where $\varepsilon_{i,0}$ (i = M_L, M_R) are the zero-bias redox energies of M_L and M_R. Therefore, the M_L-M_R energy gap that determines the intra-molecular ET rates (eq. (4.6)) is given by

$$
\Delta G(V)=\varepsilon_{M_R}(V)-\varepsilon_{M_L}(V)=\left(\varepsilon_{M_R,0}-\varepsilon_{M_L,0}\right)-(\alpha_L+\alpha_R-1)eV\,. \tag{4.12}
$$

This equation expresses the energy gap as a function of the Fermi window of the junction, as shown in Fig. 4.6 for a positive bias voltage and for $\varepsilon_{M_L,0}=\varepsilon_{M_R,0}$.

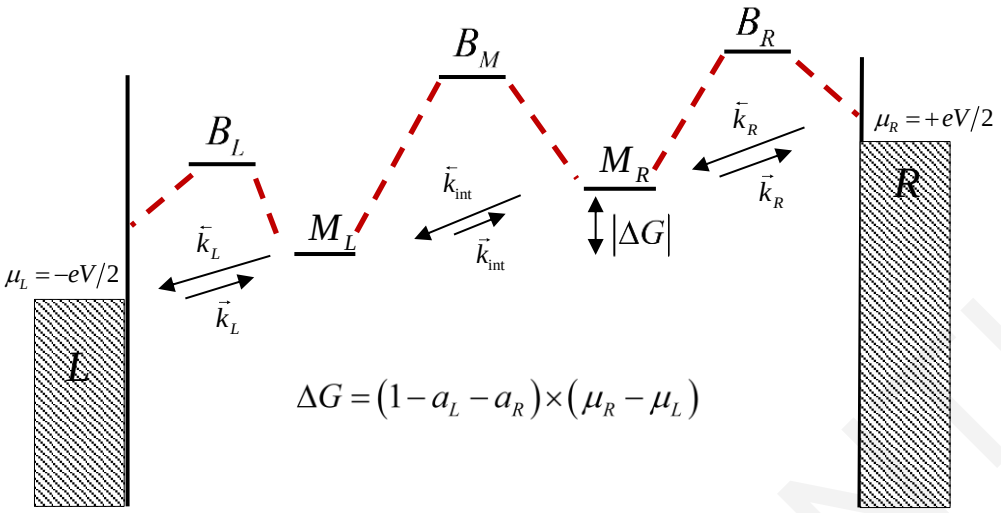

Figure 4.6 Schematic representation of the levels in the $B_L M_L B_M M_R B_R$ junction of Figure 4.5. Electronic couplings between the levels are represented by red dotted lines. The diagram shows a positive bias situation with the M_L (M_R) DA energy gap written as a function of the total bias across the junction. In our model this fraction is controlled by the parameters α_L and α_R. The figure shows that the bridge levels act as deep tunneling barriers for the transferring electron such that only M_L and M_R change their oxidation state during transfer. Positive bias leads to a positive L-to-R current (R-to-L electron flow).

The model assumes that the junction only accesses states with one extra electron (or hole) on the bridge (as implied by the constraint in the third line of eq. (4.7)). Further it assumes that the extra charge is either localized on M_L and/or M_R units but not on the bridge units B_i whose levels act as high energy virtual intermediates. Thus, the junction M_L-to-M_R ET step is analogous to a M_L-to-M_R charge shift process in solution phase. In summary, apart from the bias voltage and temperature, the main parameters of the model are: λ_i and $\varepsilon_{i,0}$ (reorganization energies and redox energies of redox groups i = M_L, M_R), α_i (electrode-to-M_L (M_R) voltage-drop fraction), $c_{L(R)}$ (prefactors for the ET rates from the levels to the leads, related to the level broadenings) and c (prefactor for the intra-molecular ET rates, $c = \frac{2\pi}{\hbar} \frac{1}{\sqrt{4\pi(\lambda_L + \lambda_R)}} H^2_{M_L, M_R}$).

In the following we give examples of different regimes that could be observable in the proposed junction (Figs 4.5 and 4.6) under the abovementioned conditions. We consider the simplest junction setup, a symmetric system of identical M_L and M_R groups (

$\varepsilon_{M_L,0} = \varepsilon_{M_R,0} = \varepsilon_0$ in eqs (4.10) and (4.11)) connected by a symmetric bridge and having identical L and R leads and M_L-L and M_R-R couplings. The model's ET parameters are given values that are typical of molecular and electrochemical nonadiabatic ET.

4.2 Results and Discussion

In all of the examples of the figures that follow, the energy, coupling and reorganization energy values are such that the intra-molecular and heterogeneous ET rates are nonadiabatic (see the discussion in section 4.4.3 of the Supplement). Further, all of the ET rates can be described by thermal-equilibrium theories because they are slower than typical vibrational relaxation times.

In order to explore the behavior of the current in the proposed quasi-linear symmetric junction, it is necessary to model the voltage profile across the junction, i.e., to justify values for α_L and α_R in eq. (4.12). We first consider the model of a linear voltage drop across the junction. Denoting the L-M_L, M_L-M_R and M_R-R distances as D_{L,M_L}, D_{M_L,M_R} and $D_{M_R,R}$ respectively, a linear voltage profile leads to $\alpha_R \approx D_{M_R,R}/D_{tot}$ and $\alpha_L \approx D_{L,M_L}/D_{tot}$, where $D_{tot} = D_{L,M_L} + D_{M_L,M_R} + D_{M_R,R}$ is the total length of the junction. For example, for a symmetric junction with $D_{L,M_L} \approx D_{M_R,R} \approx D_{M_L,M_R}$, $\alpha_L = \alpha_R \approx 1/3$. For a linear voltage profile with $\alpha_L = \alpha_R \approx 1/3$, the energy gap between M_L and M_R redox levels (free energy for the intra-molecular ET reaction) is $|\Delta G(V)| = |eV|/3$ (eq. (4.12)), lower than $\Delta\mu$ across the junction (see Fig. 4.6).

For a meaningful comparison to solution-phase M_L-M_R ET rates, the in-junction redox levels of M_L and M_R should not be hybridized with the electrodes even if the redox-level energies are close to the Fermi levels, i.e., $\Gamma_{L(R)} \ll \lambda_{L(R)}/4$. To this end, the B_L and B_R bridges connecting the redox groups to the electrodes should be high tunneling barriers for ET between the electrodes and the redox levels. This property can be achieved by using fully saturated organic bridges and metal M_L and M_R groups. [11] The $M_{L(R)}$-L(R) electronic couplings will be very weak for the B_L and B_R bridge lengths of the order of 10 Å and can be estimated from experiments. [29]

We first present the simplest junction case where the redox energies of M_L and M_R groups are quasi-resonant to the Fermi level of the L and R electrodes at zero bias (

$\varepsilon_{M_L,0} = \varepsilon_{M_R,0} = \varepsilon_0 \approx 0$ in eq. (4.12)), and then relax this condition (i.e., set $\varepsilon_0 \neq 0$). Figure 4.7 shows the I-V behavior of such a junction at T = 308 K ($\alpha_L = \alpha_R = 1/3$, $\varepsilon_0 = 0$, $\lambda_L = \lambda_R = 0.1eV$, $c_L = c_R = 0.22 \times 10^1\, eV^{-1/2}\, ns^{-1}$ and $c = 0.15\, eV^{1/2}\, ns^{-1}$). The reorganization energy values are low (inner sphere), typical of a "dry" junction environment. The $c_{L(R)}$ values are consistent with those derived from voltammetric experiments of heterogeneous ET between metal redox centers connected to electrodes by saturated bridges of 7 - 10 Å length. [29] Since $c_{L(R)} = \frac{2\Gamma_{L(R)}}{\hbar} \frac{1}{\sqrt{4\pi\lambda_{L(R)}}}$, for reorganization energies of $0.1eV$, the $c_{L(R)}$ values correspond to $\Gamma_{L(R)} = 0.8 \times 10^{-6} eV \ll \lambda_{L(R)}$ (consistent with a localized redox-level regime and with the nonadiabatic limit). Choosing $c = 0.15\, eV^{1/2}\, ns^{-1}$ for $c = \frac{2\pi}{\hbar} \frac{1}{\sqrt{4\pi\left(\lambda_L + \lambda_R\right)}} H^2_{M_L,M_R}$ of the intra-molecular rate (eq. (4.6)), corresponds to a weak bridge-mediated coupling of $H_{M_L,M_R} = 1.6 \times 10^{-4} eV$, a plausible value for metals connected by a saturated bridge of a few Angstroms length. [11] In this parameter regime the intra-molecular M_L-to-M_R ET rates are the slowest, and all ET rates (intra-molecular and heterogeneous) are much slower than $(psec)^{-1}$, a typical vibrational relaxation rate. Thus thermal-equilibrium nonadiabatic theory is justified for all ET rates, intra-molecular and heterogeneous. The conditions of $\Gamma_{L(R)} \ll \lambda_{L(R)}$ and of rates slower than $(psec)^{-1}$ are important for enabling correlations with solution-phase ET.

The I-V behavior in Fig. 4.7 shows current maxima at the bias-voltage values $\pm V_{max}$. At higher (lower) bias voltages than $+V_{max}$ ($-V_{max}$) the current drops, showing a type of Negative Differential Resistance (NDR) behavior. NDR can arise from a variety of mechanisms and has been observed in several cases. [36-39] We will show that in the context of the proposed quasi-linear junction, this behavior is due to the fact that the intra-molecular M_R-to-M_L ET rates $\left(\vec{k}_{int}, \vec{k}_{int}\right)$ limit the overall current and they are also driven by the bias voltage from the normal to the activationless and back to their inverted regimes. In an actual experiment the current will likely not drop completely to zero at the highest bias-voltage values because other high-voltage channels may start contributing to the current. However, for the proposed parameter regime and for a quasi-linear (stretched) junction geometry, such additional channels will be weaker tunneling currents and the peak region of the current around $\pm V_{max}$ will be observable (see Supplement section 4.4.4).

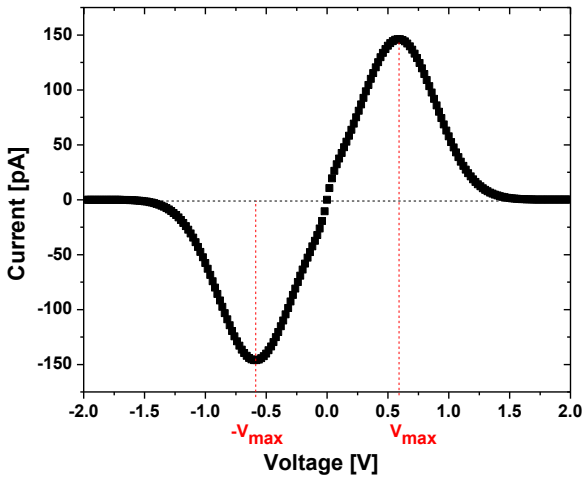

Figure 4.7 Current I (eqs (4.8) and (4.9)) versus the bias voltage V at T = 308 K for the partially pinned system of Fig. 4.6. Parameter values: $\alpha_L = \alpha_R = 0.33$, $\varepsilon_0 = 0$, $\lambda_L = \lambda_R = 0.1$ *eV*, $c_L = c_R = 0.22 \times 10^1$ $eV^{-1/2}$ ns^{-1} and $c = 0.15$ $eV^{1/2}$ ns^{-1}. The current shows a gaussian dependence on the voltage that reflects the energy gap dependence of the intra-molecular ET rates $\overleftarrow{k}_{\text{int}}$ or $\vec{k}_{\text{int}}$.

To clarify the dependence of the current on the intra-molecular ET rates, we focus on the positive bias region of Fig. 4.7, where $\mu_R > \mu_L$ and the forward intra-molecular M_L-to-M_R ET rate is slower than the backward M_R-to-M_L rate, $\vec{k}_{\text{int}} << \overleftarrow{k}_{\text{int}}$, since $\Delta G = \Delta\mu/3$. Fig. 4.8a shows the M_R-to-M_L ET rate $\overleftarrow{k}_{\text{int}}$ as a function of bias voltage (bottom x axis) and as a function of the M_LM_R energy gap (top x axis), which is given by $\Delta G(V) = \varepsilon_{M_R}(V) - \varepsilon_{M_L}(V) = eV/3$. The ET rate has the expected gaussian energy-gap behavior (normal, activationless and inverted) with a maximum at $\Delta G\left(V^{\max}\right) = \Delta G^* = \lambda_L + \lambda_R$. Figure 4.8b shows the corresponding current (eqs (4.8) and (4.9)) in the positive voltage region and also an approximate expression for the current, $I(V) \approx e\overleftarrow{k}_{\text{int}}$. The figure demonstrates that, in this ET-rate limited regime, the current is determined by the ET rate and the current's voltage dependence reflects the free energy gap dependence of the rate. The maximum current voltage is at $V^{\max} = 3\Delta G^*/e = 3(\lambda_L + \lambda_R)/e$ and the voltage width of the current's gaussian region is $\Delta V \equiv \sigma_I = 3\sqrt{2(\lambda_L + \lambda_R)k_BT}/e$. Both of these variables could be used to predict the reorganization energy of the intra-molecular ET reaction in the junction environment. The approximate expression for the

current, $I(V) \approx e\vec{k}_{\text{int}}$, can be derived from eq. (4.8) in the limit where $\vec{k}_{\text{int}} < \vec{k}_{L(R)}, \vec{k}_{L(R)}$ (Supplement section 4.4.2, eqs (4.20) and (4.21)). For negative voltages the current in this example is given by $I(V) \approx -e\vec{k}_{\text{int}}$. This type of experiment can be readily correlated to one involving the solution-phase ET reaction for an identical DBA system.

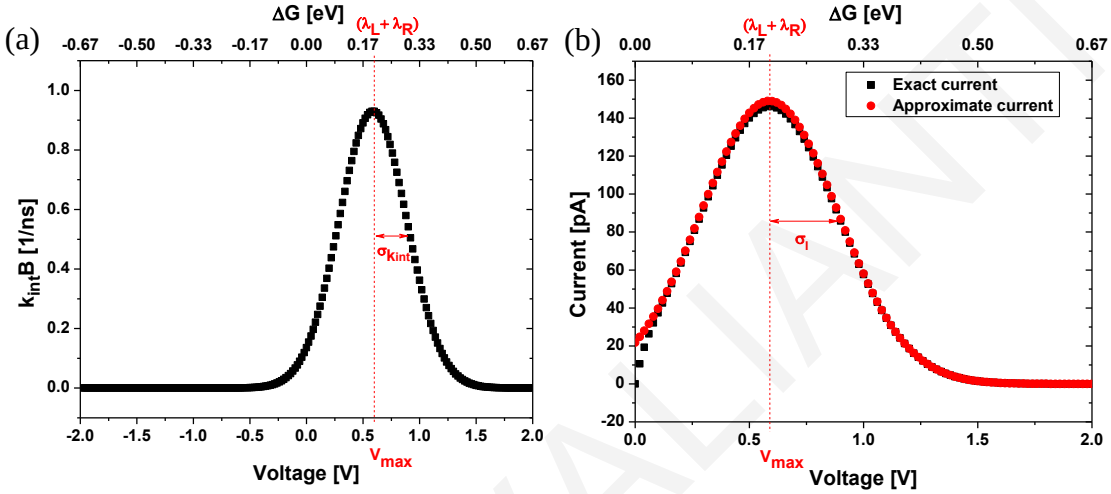

Figure 4.8 (a) Backward intra-molecular rate $\vec{k}_{\text{int}}$ versus the bias voltage *V* and Gibbs free energy *ΔG* at T = 308 K. (b) Current *I* versus the bias voltage *V* and Gibbs free energy *ΔG* at T = 308 K (covering the positive *V* region of Figure 7). Exact current expression (eq (4.9) black dots) and approximate current expression ($I(V) \approx e\vec{k}_{\text{int}}$ red dots). Parameter values for both graphs: $\alpha_L = \alpha_R = 0.33$, $\varepsilon_0 = 0$, $\lambda_L = \lambda_R = 0.1$ *eV*, $c_L = c_R = 0.22 \times 10^1$ $eV^{-1/2}$ ns^{-1} and $c = 0.15$ $eV^{1/2}$ ns^{-1}. $V^{\max} = 3\Delta G^*/e = 3(\lambda_L + \lambda_R)/e$ and $\sigma_I = \sigma_{k_{\text{int}}} = 3\sqrt{2(\lambda_L + \lambda_R)k_B T}/e$.

Figure 4.9 is similar to Fig. 4.8 showing the I-V behavior for positive bias voltage in the case of larger reorganization energy $(\lambda_L = \lambda_R = 0.2\,eV)$ and larger bridge-mediated DA coupling $H_{M_L,M_R} = 3.0 \times 10^{-4}\,eV$ (all other parameters are the same as in Figs 4.7 and 4.8). The current is still rate limited by the intra-molecular rate, but the maximum current bias voltage $V^{\max}$ and the width of the gaussian region σ_I are higher due to the larger reorganization energy $(\lambda_L + \lambda_R)$ of the intra-molecular ET rate.

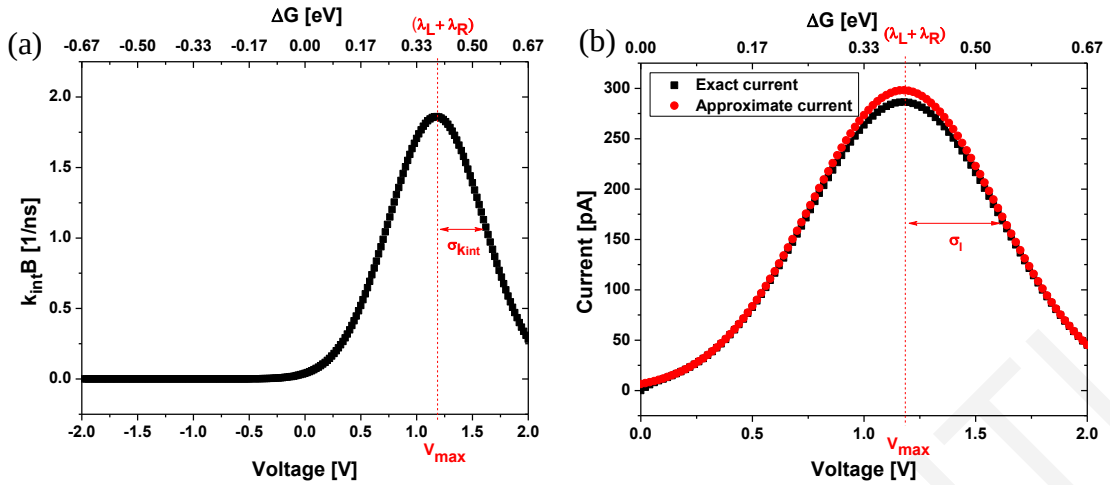

Figure 4.9 (a) Backward intra-molecular rate $\vec{k}_{\text{int}}$ versus the bias voltage *V* and Gibbs free energy ΔG at T = 308 K. (b) Current *I* versus the bias voltage *V* and Gibbs free energy ΔG at T = 308 K. Exact current expression (eq. (4.9) black dots) and approximate current expression ($I(V) \approx e\vec{k}_{\text{int}}$ red dots). Parameter values for both graphs: $\alpha_L = \alpha_R = 0.33$, $\varepsilon_0 = 0$, $\lambda_L = \lambda_R = 0.2\ eV$, $c_L = c_R = 0.15 \times 10^1\ eV^{-1/2}\ ns^{-1}$ and $c = 0.38\ eV^{1/2}\ ns^{-1}$. $V^{\max} = 3\Delta G^*/e = 3(\lambda_L + \lambda_R)/e$ and $\sigma_I = \sigma_{k_{\text{int}}} = 3\sqrt{2(\lambda_L + \lambda_R)k_B T}/e$.

Figure 4.10a shows the I-V behavior of the symmetric junction in the case where all parameters are identical to those of Figs 4.7 and 4.8 apart from the zero-bias redox energy of M_L (M_R) which is now taken to be off-resonant with respect to the Fermi level $\left(\varepsilon_{M_L,0} = \varepsilon_{M_R,0} = \varepsilon_0 = 0.1eV\right)$. Figure 4.10a shows the corresponding current (eqs (4.8) and (4.9)) and also an approximate expression for the current, $I(V) \approx \dfrac{e\vec{k}_R\vec{k}_{\text{int}}}{\vec{k}_{\text{int}} + \vec{k}_R + \vec{k}_R}$ for positive voltages and $I(V) \approx -\dfrac{e\vec{k}_L\vec{k}_{\text{int}}}{\vec{k}_{\text{int}} + \vec{k}_L + \vec{k}_L}$ for negative bias voltages (Supplement section 4.4.2).

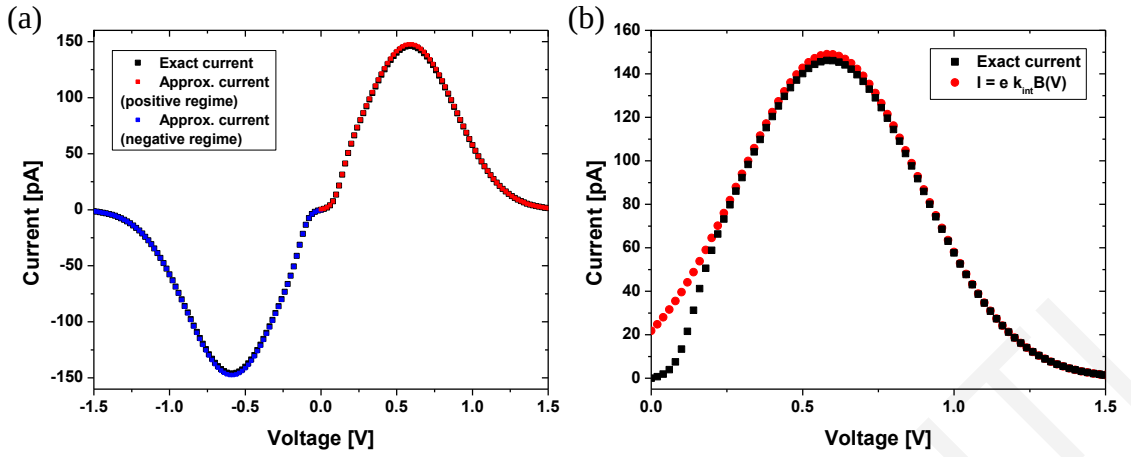

Figure 4.10 Current I versus the bias voltage V at T = 308 K for a junction with off-resonant M_L and M_R redox levels at zero bias. Parameter values for both graphs: $\alpha_L = \alpha_R = 0.33$, $\varepsilon_0 = 0.1$ eV, $\lambda_L = \lambda_R = 0.1$ eV, $c_L = c_R = 0.22 \times 10^1$ $eV^{-1/2}$ ns^{-1} and $c = 0.15$ $eV^{1/2}$ ns^{-1}. (a) Exact current expression (eq. (4.9) black dots) and approximate current expressions for the positive bias voltage regime ($I(V) \approx \frac{e\overleftarrow{k}_R \overleftarrow{k}_{\text{int}}}{\overleftarrow{k}_{\text{int}} + \overleftarrow{k}_R + \vec{k}_R}$ red dots) and for the negative bias regime ($I(V) \approx -\frac{e\vec{k}_L \vec{k}_{\text{int}}}{\vec{k}_{\text{int}} + \vec{k}_L + \overleftarrow{k}_L}$ blue dots). (b) Current I versus the bias voltage V at T = 308 K (covering the positive V region). Exact current expression (eq. (4.9) black dots) and rate-limited approximate current expression ($I(V) \approx e\overleftarrow{k}_{\text{int}}$ red dots).

Apart from a low-bias activated region for bias voltages between $-0.2\ V$ and $+0.2\ V$, (due to the off-resonant redox levels at zero bias), the I-V curve shows the inverted Marcus behavior expected of a current that is limited by the intra-molecular rate. Figure 4.10b shows that the current is limited by the intra-molecular rate $\left(I(V) \approx e\overleftarrow{k}_{\text{int}}\right)$ in region around the current maximum. Thus, the rise and fall in current with voltage reflects the inverted Marcus behavior of the current-limiting intra-molecular rate (see more examples in the Supplement section 4.4.2).

The behaviors shown in Figs 4.7 to 4.10 are accessible experimentally if the voltage profile inside the molecule is such that it induces an energy gap between the donor and acceptor ($M_{L(R)}$) groups. However, if the voltage profile is very flat and $\Delta G(V) \approx 0$, it will not be possible to observe the inverted and normal regime for the intra-molecular rates even if the

latter are the slowest rates. In this case $\vec{k}_{\text{int}} = \overleftarrow{k}_{\text{int}} = k_{\text{int}}$, where k_{int} is an intra-molecular rate (eq. (4.6)) with activation energy $(\lambda_L + \lambda_R)/4$. For positive bias, $k_{\text{int}} < \vec{k}_i, \overleftarrow{k}_i$ (i = M_L, M_R), $\overleftarrow{k}_L \approx \overleftarrow{k}_R$ and assuming that the intra-molecular rate is not much smaller than the rest of the heterogeneous rates, the current is given by the approximate expression $I(V) \approx \frac{e\overleftarrow{k}_R k_{\text{int}}}{3k_{\text{int}} + \overleftarrow{k}_R + \vec{k}_R}$. For negative bias it is given by $I(V) \approx -\frac{e\vec{k}_L k_{\text{int}}}{3k_{\text{int}} + \overleftarrow{k}_L + \vec{k}_L}$ (Supplement section 4.4.2, eq. (4.23)).

Figure 4.11b shows the I-V behavior of a $B_L M_L B_M M_R B_R$ junction at T = 308 K for the case where M_L and M_R remain resonant at the center of the Fermi window for all voltages (i.e., a flat voltage profile for the M_L-M_R section). The parameter values are identical to those of Figs 4.7 and 4.8, $\lambda_L = \lambda_R = 0.1eV$, $c_L = c_R = 0.22 \times 10^1\, eV^{-1/2}\, ns^{-1}$ and $c = 0.15\, eV^{1/2}\, ns^{-1}$, apart from the pinning parameters ($\alpha_L = \alpha_R = 0.50$ and $\varepsilon_0 = 0$). The current's voltage dependence is determined by the heterogeneous ET rates (since the M_L-M_R energy gap remains zero) and the abovementioned approximate formulas give good approximations to the current. In this situation the current's dependence on the intra-molecular rate is masked by the heterogeneous rates because the intra-molecular rate energy gap is not affected by the bias voltage.

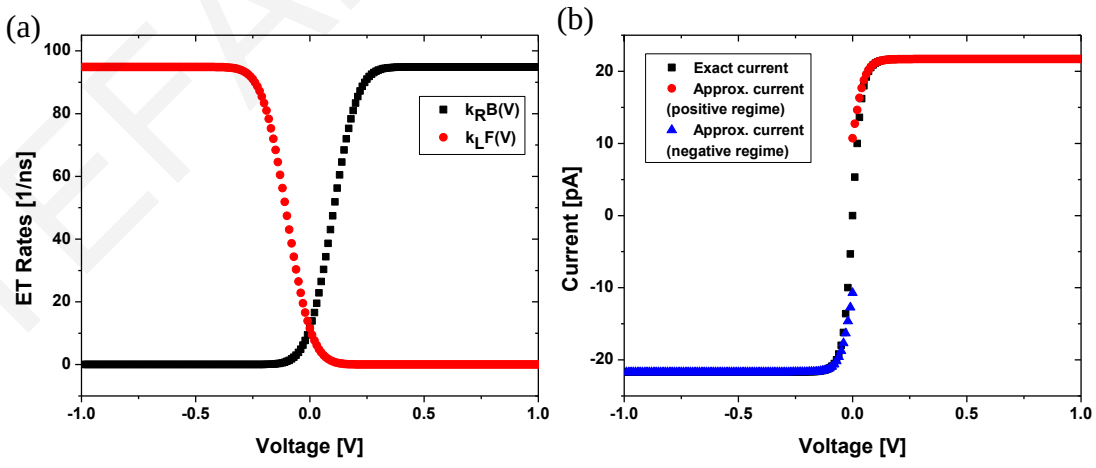

Figure 4.11 (a) Right backward injection rate $\overleftarrow{k}_R$ (black dots) and left forward injection rate $\vec{k}_L$ (red dots) versus the bias voltage V at T = 308 K. (b) Current I versus the bias voltage V at T = 308 K. Exact current expression (eq. (4.9) black dots) and approximate current

expressions for the positive bias voltage regime ($I(V) \approx \frac{e\overleftarrow{k}_R k_{\text{int}}}{3k_{\text{int}} + \overleftarrow{k}_R + \vec{k}_R}$ red dots) and for the negative bias regime ($I(V) \approx -\frac{e\vec{k}_L k_{\text{int}}}{3k_{\text{int}} + \overleftarrow{k}_L + \vec{k}_L}$ blue dots). Parameter values for both graphs: $\alpha_L = \alpha_R = 0.50$, $\varepsilon_0 = 0$, $\lambda_L = \lambda_R = 0.1$ eV, $c_L = c_R = 0.22 \times 10^1$ $eV^{-1/2}$ ns^{-1} and $c = 0.15$ $eV^{1/2}$ ns^{-1}.

Finally, in the limit where the intra-molecular rate is fast compared to the heterogeneous ET rates, the current is either limited by a heterogeneous rate or a combination of heterogeneous rates. In this situation the current voltage is sigmoidal-like and resembles the profile expected from the model in Fig. 4.2 (e.g., Fig. 4.4). The intra-molecular rate is not observable in this regime. An example is given in Fig. 4.12.

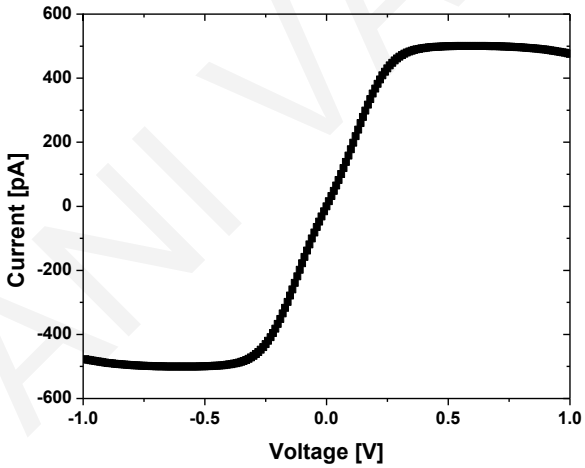

Figure 4.12 Current I versus the bias voltage V at T = 308 K for a junction with partially pinned M_L and M_R. Parameter values: $\alpha_L = \alpha_R = 0.33$, $\varepsilon_0 = 0$, $\lambda_L = \lambda_R = 0.1$ eV, $c_L = c_R = 0.15$ $eV^{-1/2}$ ns^{-1} and $c = 0.15 \times 10^2$ $eV^{1/2}$ ns^{-1}. The timescale of ET between the M_L and M_R sites is of the order of tens of psec. The ET timescale between the M_i and the leads is of the order of nsec.

In addition to the bias-voltage dependence of the current, its temperature dependence contains information about transport mechanism. When the current is limited by an intra-molecular ET rate, the temperature dependence of the current will be identical to that of the rate (eq. (4.6)). The nonadiabatic intra-molecular rate is thermally activated in both the

inverted and normal regimes (in contrast to the heterogeneous ET rates which are activationless in the inverted regime). Figure 4.13 shows the temperature dependence of the current for the case of Figs 4.7 and 4.8, where the current is limited by the backward intra-molecular rate for positive V, $I(V) \approx e\bar{k}_{\text{int}}$. Figure 4.13a shows the I-V curves for positive V at different temperatures. For $V < V_{\max} - \sigma_I$ the intra-molecular rate (and thus the current) is well inside in the normal Marcus regime and for $V > V_{\max} + \sigma_I$ it is inside the inverted Marcus regime.

For both of these voltage regions the current has a specific activated Arrhenius temperature dependence with a bias-voltage-dependent activation energy. Namely, since $I(V) \approx e\bar{k}_{\text{int}}$ and $\bar{k}_{\text{int}}$ is given by eq 6, $\ln\left[I(V)\right] \approx \frac{1}{2}\ln\left[const \times T^{-1}\right] - \left(E_{act}(V)/k_B\right) \times T^{-1}$ (denoted as current behavior "A" in Fig. 4.13b). In this equation $const = e\,2\pi\, H^2_{M_L,M_R} \Big/ \left(\hbar\sqrt{4\pi\left(\lambda_L + \lambda_R\right)k_B}\right)$ and $E_{act}(V) = \left(\Delta G(V) - \left(\lambda_L + \lambda_R\right)\right)^2 \Big/ 4\left(\lambda_L + \lambda_R\right)$ with $\Delta G(V)$ given by eq. (4.12). In contrast, for $V \approx V_{\max}$ the rate is in the Marcus activationless regime and the current decreases with temperature as $\ln\left[I(V)\right] \approx \frac{1}{2}\ln\left[const \times T^{-1}\right]$ (denoted as current behavior "B" in Fig. 4.13b). In particular, as the bias voltage is increased from $V = V_{\max} - \Delta$ (normal region of intra-molecular rate, $V = V_1$ in Fig. 4.13a) to $V = V_{\max}$ (activationless, $V = V_2$ in Fig. 4.13a) to $V = V_{\max} + \Delta$ (inverted region, $V = V_3$ in Fig. 4.13a) the temperature dependence changes from the activated Arrhenius form "A" to the non-activated $\ln\left[const \times T^{-1}\right]$ dependence and back to the activated Arrhenius. The behavior shown in Fig. 4.13b should be compared to the temperature dependence in Fig. 4.4b which is indicative of a heterogeneous ET rate. In the latter case as the voltage increases the current just switches from thermally activated to $\sim \ln\left[const \times T^{-1}\right]$, never reversing to activated at higher voltages.

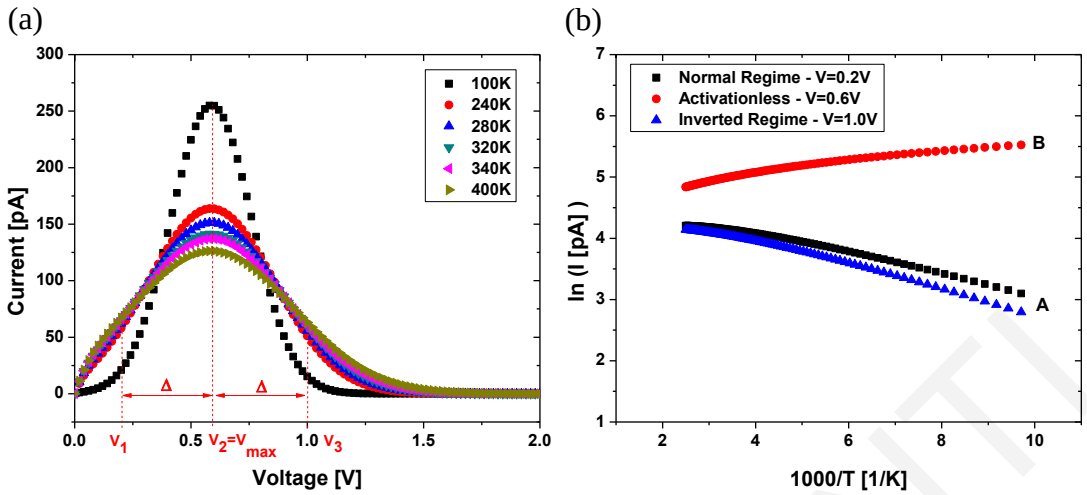

Figure 4.13 (a) Current (eq. (4.9)) I versus the bias voltage V at T = 100-400 K. (b) The natural logarithm of the current versus *1000/T* at V = 0.2 V (black dots) indicates the temperature dependence of the intra-molecular Marcus rate: 0.2 V (black dots) normal Marcus regime (current behavior "A" of main text), 0.6 V (red dots) activationless regime (current behavior "B" of main text), 1.0 V (blue dots) inverted regime (current behavior "A"). Parameter values for both graphs: $\alpha_L = \alpha_R = 0.33$, $\varepsilon_0 = 0$, $\lambda_L = \lambda_R = 0.1$ *eV*, $c_L = c_R = 0.22 \times 10^1\ eV^{-1/2}\ ns^{-1}$ and $c = 0.15\ eV^{1/2}\ ns^{-1}$. The current is limited by the intra-molecular M_L-to-M_R rate.

Figure 4.14 shows another example of this temperature dependence as a function of bias voltage for larger reorganization energies (the parameters are those of Fig. 4.9). The switch from the "A" to the "B" form and back to the "A" form as the voltage is scanned across V_{max} (shown in Figs 4.13b and 4.14b) is a clear signature of a current that is limited by an intra-molecular nonadiabatic ET rate. Mechanisms involving simple coherent off-resonant or resonant tunneling are expected to give activationless, temperature-independent current behaviors as the voltage is increased, as long as the resonant/off-resonant regime is maintained at all voltage values (i.e., $\hbar\Gamma_{L(R)} < eV$ in the case of resonant tunneling and $eV < \varepsilon(V) \mp \hbar\Gamma_{L(R)}$ in the case of off-resonant tunneling [20]).

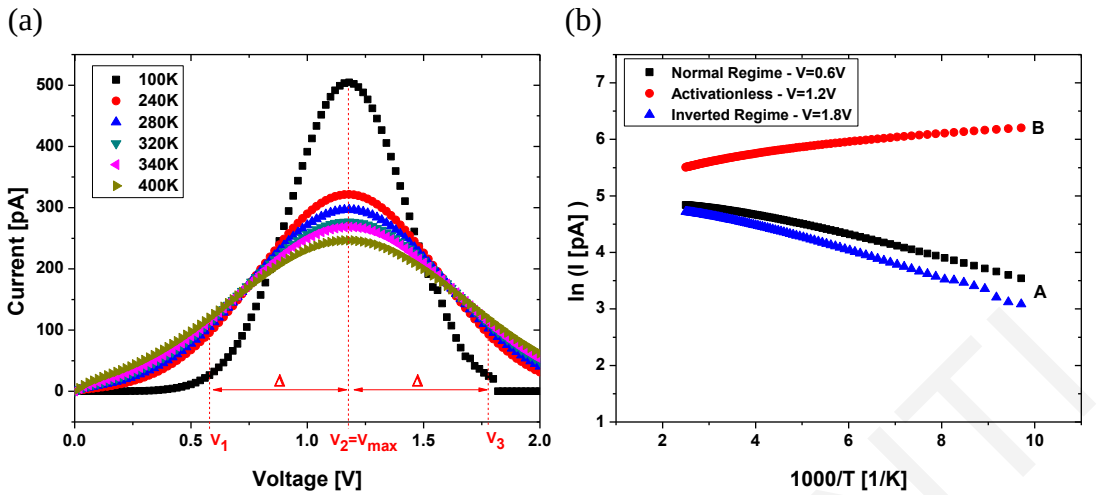

Figure 4.14 (a) Exact current *I* (eq. (4.9)) versus the bias voltage *V* at T = 100-400 K. (b) The natural logarithm of the current versus *1000/T* at V = 0.6 V (black dots) indicates the temperature dependence of the intra-molecular Marcus rate: 0.6 V (black dots) normal Marcus regime (current behavior "A"), 1.2 V (red dots) activationless regime (current behavior "B"), 1.8 V (blue dots) inverted regime (current behavior "A"). Parameter values for both graphs: $\alpha_L = \alpha_R = 0.33$, $\varepsilon_0 = 0$, $\lambda_L = \lambda_R = 0.2$ *eV*, $c_L = c_R = 0.15 \times 10^1$ $eV^{-1/2}$ ns^{-1} and $c = 0.38$ $eV^{1/2}$ ns^{-1}. The current is limited by the intra-molecular M_L-to-M_R rate.

As a final example we consider the case where M_L and M_R redox levels are nearly pinned to the L and R electrodes, respectively, i.e., $\varepsilon_{M_L}(V) \approx \mu_L$ and $\varepsilon_{M_R}(V) \approx \mu_R$ $(\alpha_L = \alpha_R << 1)$. Such pinning would imply that the voltage drop across the junction is a large fraction of the M_L-to-M_R voltage drop and the M_L-M_R energy gap for the intra-molecular ET reaction (eq. (4.12)) would be approximately equal to $\Delta\mu$ across the junction ($|\Delta G| \approx |\Delta\mu|$ in Fig. 4.6). In this situation, for a linear voltage profile in a quasi-linear junction where $\alpha_{L(R)} \approx D_{M_{L(R)},L(R)} / D_{tot}$, the redox groups would have to be close to an electrode to increase the pinning, i.e., $D_{M_{L(R)},L(R)} / D_{tot} \ll 1$. Thus, the electronic couplings M_L-L and M_R-R would be stronger compared to the values considered in the previous examples and the forward and backward heterogeneous ET rates would most likely be adiabatic. Given the aim that the in-junction redox-level localization resembles the solution-phase redox-level localization, we still require that $\Gamma_{L(R)} < \lambda_{L(R)}$. To maximize pinning of M_L and M_R while avoiding hybridization with the electrodes, the B_L and B_R bridges should be shorter than 7 Å (assuming saturated organic bridges [29]), but should not be so short that the redox centers directly contact the electrodes (in the stretched junction geometry). The central bridge B_M

should be larger than 7 Å so that most of the voltage drops in the M_L-M_R segment, i.e., $D_{M_R,R}/D_{tot} = D_{L,M_L}/D_{tot} << D_{M_L,M_R}/D_{tot}$.

Consider such a junction with approximately 25 Å length and with $B_{L(R)}$ bridges of approximately 6 Å lengths. This system would give $\alpha_{L(R)} \approx 0.2$, and level broadenings $\Gamma_{L(R)}$ of a few meV. [29] For a reorganization energy of 0.2 eV and classical ET-active modes of $M_{L(R)}$ with average frequency of the order of 0.01 $(psec)^{-1}$, the heterogeneous ET rates would be adiabatic (see the discussion of the adiabaticity parameter in Supplement section 4.4.3). To estimate minimum (zero-bias) values for the heterogeneous adiabatic ET rates in this example, we use an expression that approximates well the rate for $\Gamma_{L(R)} << \lambda_{L(R)}$ (large reorganization energies) and for low overpotentials with high activation energies $\left(\left|\mu_{L(R)} - \varepsilon_{M_{L(R)}}\right| \ll \lambda_{L(R)}/4\right)$ (eqs (4.26) – (4.29)). [40] For the case of quasi-resonant redox levels at zero bias, $(\varepsilon_0 = 0)$, we predict minimum (zero-bias) heterogeneous rates of the order of 1.0 $(psec)^{-1}$. Therefore, the current will be limited by the intra-molecular M_L-M_R rates, which will be even slower compared to the cases described previously, since the length of the central off-resonant bridge (B_M) is increased in order to minimize $\alpha_{L(R)}$.

In this example a non-zero bias voltage likely leads to heterogeneous rates faster than $(psec)^{-1}$. Thermal-equilibrium theories and models of adiabatic reactions are not applicable for describing sub-psec rates. Further, if the heterogeneous ET rates are of the order of or faster than the typical vibrational relaxation rate, $(psec)^{-1}$, the ET-active vibrations of the M_L (M_R) group never equilibrate thermally when the group accepts an electron from M_R (M_L) because the electron transfers to the connecting electrode faster than the vibrational relaxation time scale. Therefore, the in-junction intra-molecular rates may not be promoted by thermally equilibrated vibrations and cannot be described by simple Marcus theory as in the previous examples. In conclusion, although in this example $\Gamma_{L(R)} \ll \lambda/4$ such that each redox level remains localized in the redox group (as in solution-phase ET), we expect differences between the in-junction intra-molecular rate and the solution-phase one that are due to nonequilibrium vibrational effects of the in-junction redox groups. The current will be proportional to the in-junction intra-molecular rate, since it is the slowest rate, but the voltage dependence of the current will not be described by thermally equilibrated Marcus theory.

If the redox groups are even more strongly coupled to the electrodes, i.e., $\Gamma_{L(R)} \geq \lambda_{L(R)}$, the in-junction redox levels, although fully pinned, will be very hybridized with electrode levels.

Also, the L(R) injection time scales are likely much faster than psec for all bias voltages. In this case the hybridized in-junction redox levels are very different from the solution-phase ones and vibrational nonequilibrium effects are very prominent. The I-V behavior will not give information about the solution-phase intra-molecular rate even if the in-junction intra-molecular rate is current limiting.

The examples considered above are not exhaustive, but they demonstrate how different system parameters affect the phenomenology of the observed current. Achieving a variation with bias of the M_L -M_R energy gap that is greater than the total reorganization energy $\lambda_L + \lambda_R$ of the current-limiting intra-molecular rate is a necessary condition for observing the full energy-gap dependence of the rate and current. Good choices for M_L and M_R are metal-containing redox groups with redox energies slightly higher than the Fermi level of the metal leads at zero bias. In our model this situation is described by setting $\varepsilon_{M_i,0} > 0$ in eqs (4.10) and (4.11) such that there is an activation energy for heterogeneous ET from the lead to the redox center (Fig. 4.10). Figure 4.14 shows examples of the I-V behavior in this regime where, in addition to activated charge injection rates, the M_L-to-M_R ET rates are current limiting. The Marcus-inverted-parabola behavior of the intra-molecular ET rate is observable for a wide range of parameters, although it is partially masked by the sigmoidal behavior of the activated heterogeneous ET rates. It is possible that at higher voltages in the inverted Marcus regime the current-limiting rate shows a softer drop with voltage as compared to the normal region due to quantum-vibrational effects. In this situation a mixed quantum-classical expression should be used to describe the nonadiabatic intra-molecular rate. [12,19]

In the context of the proposed quasi-linear junction architecture with metal redox centers, good choices for bridges are saturated organic bridges that are known to act as high tunneling barriers when connected to metal centers and that also support off-resonant tunneling currents when connected directly to metal (e.g., Au) electrodes for bias voltages of 1.0 - 2.0 V and for lengths of the order of 10 Å. [41] Within the experimental voltage window such bridges remain tunneling barriers for electrode to $M_{L(R)}$ and M_L-M_R electron transfer steps, although they give voltage-dependent tunneling matrix elements. This voltage dependence does not destroy the observation of the inverted Marcus regime (see Supplement section 4.4.4 for a model of this dependence). Further, if the connecting bridges are rigid, they are likely to preserve weak mixing (charge transfer) between the redox levels and the lead levels in the presence of thermal structural fluctuations and under the influence of the external electric field. Tuning the bridge-mediated tunneling between the redox levels (thus the intra-

molecular rate) may be done by varying the length of the central bridge or by changing the bridge chemical structure so as to alter through-bond and/or through-space tunneling pathways, as in the case of solution-phase and biological ET studies. [11,15,42]

Only transport channels that involve current-limiting intra-molecular M_L-M_R ET will give an inverted Marcus behavior of the current as a function of voltage. Therefore, from an experimental point of view, it is important to use experimental methods that measure current traces for the maximally stretched geometries of the bridge-redox system between the leads, [43] and analysis methods such as clustering [44] that can identify the traces of the most linear geometries. Given the quasi-linear form of the bridge-redox molecular assembly and the high tunneling barriers provided by saturated bridges, stretched geometries cannot support other transport channels that bypass ET between the redox groups (Supplement section 4.4.4).

Incoherent transport has been shown to occur in small-molecule junctions containing a metal redox group connected to the leads by organic linkers. The redox group is involved in incoherent transport channels as a charge donor and acceptor. [24,26] Even in junctions comprised of metal-containing ET proteins, transport can be dominated by the metal's redox states that are near-resonant to the gold electrode Fermi levels and that contribute to incoherent transport channels as electron donors and acceptors (e.g., the Cu center of Azurin [9,25,45-47]). In solution-phase chemical and biological ET, metal - organic bridge - metal systems are ubiquitous and most often ET between the metals takes place via through-bridge tunneling. [11,14,15] Further, heterogeneous ET rates for metal - organic bridge - electrode systems are well characterized. [27,28-30] Therefore, the use of metal redox groups with redox energies close to the lead Fermi levels is a good choice for observing a donor-to-acceptor ET rate in the current of a molecular junction experiment and comparing it to the corresponding rate in a solution-phase ET experiment.

Observing the Marcus inverted region for chemical and biological nonadiabatic ET has been a difficult task as it requires varying sufficiently the free energy gap of an ET reaction by altering one of the redox groups, while keeping other parameters constant. [48-53] Alternatively, applying an external electric field in solution or in a polymer matrix to tune the free energy gap for a fixed D-A pair is often hampered due to disorder and ensemble effects. [53-56] These difficulties may be partially overcome at the single-molecule level by using the proposed molecular-junction setup.

4.3 Conclusions

We propose a type of donor-bridge-acceptor junction that could be used to observe directly an intra-molecular donor-to-acceptor electron transfer rate through the measured current. The junction's architecture and energetics may enable the comparison between intra-molecular donor-to-acceptor electron transfer rates in solution phase and the corresponding rates in the junction environment. Under specific conditions, the junction could be used to vary the donor-to-acceptor energy gap and to observe the Marcus-inverted-parabola dependence of the corresponding rate in the nonadiabatic regime. We discuss the optimal junction parameters and experimental conditions that would lead to a direct relation between the current and the intra-molecular rate. The junction should be quasi-linear (lead – linker – donor – bridge – acceptor – linker - lead). In the quasi-linear geometry, the only lead-to-lead transport channel should involve incoherent electron hopping between donor and acceptor moieties, with the bridge and the linkers acting as tunneling barriers. It is critical that the donor-to-acceptor electron transfer hopping rates be slow enough compared to the heterogeneous electron transfer hopping rates such that the overall current be limited by the donor-to-acceptor rates. Slowing down the latter is possible by varying the length of the central bridge (tunneling barrier for donor-to-acceptor transfer) or the bridge's chemical structure. The ability to vary the donor the donor-to-acceptor energy gap from the normal to the inverted regime by applying a bias depends critically on the voltage profile within the junction. This profile may be partially controlled by the (linear) positions of the redox groups along the junction with the aim that a good part of the bias-voltage drop across the junction would occur in the region between donor and acceptor. The donor and acceptor redox energies should be close to the Fermi levels of the leads at zero bias and should not be strongly coupled to the leads (the coupling tuned by the linker lengths), so that their electron donating and accepting levels retain their localized character, as in solution phase. Metal donors and acceptor moieties such as those encountered in biological electron transfer chains are good candidates for the proposed junction. Even if the above conditions are realized, the donor and acceptor electronic levels involved in solution-phase electron transfer may not be identical to the levels involved in molecular junction electron transfer. Nevertheless, the proposed architecture and optimal conditions lead to a junction intra-molecular rate whose parameters are as close as possible to the parameters of the solution-phase rate. Thus, any differences between the energy gap, bridge-length, and temperature dependencies of the donor-to-acceptor rates in the two environments (solution-phase versus junction) would

contain important information about environmental effects on electron-transfer mechanism and would provide insights about the junction's local environment.

4.4 Supplement

Derivations of all approximate expressions for the current that are described in the main text for junctions with one and two redox groups and comparisons of these expressions with the exact current. Descriptions of the nonadiabatic and adiabatic regimes for donor-acceptor and heterogeneous ET, and of the adiabatic heterogenous ET rate equation used in the main text. Description of the tight-binding model of B_L, B_M and B_R bridges used to explore the voltage dependence of the bridge electronic couplings between the redox levels and between the redox levels and the electrodes. Discussion of the effects of voltage dependent couplings on the rate-limited current behavior and on the observation of the Marcus inverted regime.

4.4.1 Junction with one redox level: Heterogeneous ET rate limits the current

We review the single-site hopping model (see Fig. 4.1) that is often used to describe the incoherent hopping mechanism. We are interested in cases where the M redox site is partially pinned to the R electrode and the M-R electrode coupling is greater than the M-L electrode coupling. Therefore $H_L << H_R$ and $\vec{k}_L, \overleftarrow{k}_L << \vec{k}_R, \overleftarrow{k}_R$ given that the other rate parameters are not too different.

For positive high bias and $\vec{k}_L \vec{k}_R \ll \overleftarrow{k}_L \overleftarrow{k}_R$, $\vec{k}_L + \vec{k}_R \ll \overleftarrow{k}_L + \overleftarrow{k}_R$, charge flows from R to L direction at much higher rates than it does from the L to R direction. Then,

$$I(V) = -e\frac{\vec{k}_L\vec{k}_R - \overleftarrow{k}_L\overleftarrow{k}_R}{\vec{k}_L + \overleftarrow{k}_L + \vec{k}_R + \overleftarrow{k}_R} = e\left(\frac{\overleftarrow{k}_L\overleftarrow{k}_R}{\overleftarrow{k}_L + \overleftarrow{k}_R}\right)\frac{1-\left(\vec{k}_L\vec{k}_R/\overleftarrow{k}_L\overleftarrow{k}_R\right)}{1+\left(\left(\vec{k}_L + \vec{k}_R\right)/\left(\overleftarrow{k}_L + \overleftarrow{k}_R\right)\right)} \approx e\frac{\overleftarrow{k}_L\overleftarrow{k}_R}{\overleftarrow{k}_L + \overleftarrow{k}_R} \qquad (4.13)$$

Further, since $\overleftarrow{k}_L << \overleftarrow{k}_R$,

$$I(V) \approx e\frac{\overleftarrow{k}_L\overleftarrow{k}_R}{\overleftarrow{k}_L + \overleftarrow{k}_R} \approx e\frac{\overleftarrow{k}_L}{1+\left(\overleftarrow{k}_L/\overleftarrow{k}_R\right)} \approx e\overleftarrow{k}_L, \qquad (4.14)$$

and the current is rate-limited by $\overleftarrow{k}_L$. In this limit the behavior of the current with temperature or voltage is just the behavior of $\overleftarrow{k}_L$ (see relevant Fig. 4.4a).

4.4.2 Junction with two redox groups quasi-resonant to the Fermi levels at zero bias: Approximate expressions for the rate-limited current

To determine the steady-state current for the case of two redox sites M_L, M_R (see Fig. 4.5), we need to compute the stationary occupations $\left(\dot{P}_i^{(ss)}=0\right)$ of the M_L, M_R sites by solving the corresponding kinetics equations:

$$\begin{aligned}
&-\left(\overleftarrow{k}_L+\vec{k}_{\text{int}}\right)P_{M_L}^{(ss)}+\overleftarrow{k}_{\text{int}}P_{M_R}^{(ss)}+\vec{k}_L P_{L,R}^{(ss)}=0\\
&\vec{k}_{\text{int}}P_{M_L}^{(ss)}-\left(\overleftarrow{k}_{\text{int}}+\vec{k}_R\right)P_{M_R}^{(ss)}+\overleftarrow{k}_R P_{L,R}^{(ss)}=0\\
&P_{M_L}^{(ss)}+P_{M_R}^{(ss)}+P_{L,R}^{(ss)}=1
\end{aligned} \tag{4.15}$$

The steady state current (evaluated in the left interface) is given by:

$$I\left(V\right)=-e\left(\vec{k}_L P_{L,R}^{(ss)}-\overleftarrow{k}_L P_{M_L}^{(ss)}\right) \tag{4.16}$$

By solving the above kinetics equations and calculating the stationary occupations, we end up with the following expression for the steady state current:

$$I\left(V\right)=-e\left[\frac{\vec{k}_L\vec{k}_{\text{int}}\vec{k}_R-\overleftarrow{k}_L\overleftarrow{k}_{\text{int}}\overleftarrow{k}_R}{\overleftarrow{k}_{\text{int}}\overleftarrow{k}_L+\overleftarrow{k}_{\text{int}}\vec{k}_L+\vec{k}_{\text{int}}\vec{k}_L+\overleftarrow{k}_{\text{int}}\overleftarrow{k}_R+\overleftarrow{k}_L\overleftarrow{k}_R+\vec{k}_{\text{int}}\overleftarrow{k}_R+\vec{k}_{\text{int}}\vec{k}_R+\overleftarrow{k}_L\vec{k}_R+\vec{k}_L\overleftarrow{k}_R}\right] \tag{4.17}$$

The above equation can be rewritten as

$$I\left(V\right)=-e\left[\frac{\overleftarrow{k}_L\overleftarrow{k}_{\text{int}}\overleftarrow{k}_R\left(\frac{\vec{k}_L\vec{k}_{\text{int}}\vec{k}_R}{\overleftarrow{k}_L\overleftarrow{k}_{\text{int}}\overleftarrow{k}_R}-1\right)}{\overleftarrow{k}_L\overleftarrow{k}_R\left(1+\frac{\vec{k}_L\vec{k}_R}{\overleftarrow{k}_L\overleftarrow{k}_R}\right)+\vec{k}_L\overleftarrow{k}_{\text{int}}\left(1+\frac{\vec{k}_{\text{int}}}{\overleftarrow{k}_{\text{int}}}\right)+\vec{k}_{\text{int}}\overleftarrow{k}_R\left(1+\frac{\vec{k}_R}{\overleftarrow{k}_R}\right)+\vec{k}_L\vec{k}_R+\vec{k}_{\text{int}}\left(\overleftarrow{k}_L+\overleftarrow{k}_R\right)}\right] \tag{4.18}$$

For $V>0$ suppose that $\vec{k}_L\ll\overleftarrow{k}_L$, $\vec{k}_R\ll\overleftarrow{k}_R$, $\vec{k}_{\text{int}}\ll\overleftarrow{k}_{\text{int}}$ such that $\vec{k}_L\vec{k}_R\ll\overleftarrow{k}_L\overleftarrow{k}_R$, $\vec{k}_L\vec{k}_{\text{int}}\vec{k}_R\ll\overleftarrow{k}_L\overleftarrow{k}_R\overleftarrow{k}_{\text{int}}$, $\vec{k}_L+\vec{k}_R\ll\overleftarrow{k}_L+\overleftarrow{k}_R$ and $\vec{k}_L+\vec{k}_{\text{int}}+\vec{k}_R\ll\overleftarrow{k}_L+\overleftarrow{k}_R+\overleftarrow{k}_{\text{int}}$. Charge flows from the R to L direction at much higher rates than it does from the L to R direction. Then,

$$I(V) \approx -e\left[\frac{-\overleftarrow{k}_L \overleftarrow{k}_{\text{int}} \overleftarrow{k}_R}{\overleftarrow{k}_L \overleftarrow{k}_R + \vec{k}_L \overleftarrow{k}_{\text{int}} + \vec{k}_{\text{int}} \overleftarrow{k}_R + \vec{k}_L \vec{k}_R + \overleftarrow{k}_{\text{int}}\left(\overleftarrow{k}_L + \vec{k}_R\right)}\right]$$

$$= -e\left[\frac{-\overleftarrow{k}_L \overleftarrow{k}_{\text{int}} \overleftarrow{k}_R}{\overleftarrow{k}_L \overleftarrow{k}_R\left(1+\frac{\vec{k}_{\text{int}}}{\overleftarrow{k}_L}\right) + \overleftarrow{k}_{\text{int}}\left(\overleftarrow{k}_L + \vec{k}_R\right)\left(1+\frac{\vec{k}_L}{\left(\overleftarrow{k}_L + \overleftarrow{k}_R\right)}\right) + \overleftarrow{k}_L \vec{k}_R}\right]. \quad (4.19)$$

Given that the intra-molecular rates are much smaller than the remaining rates (either forward or backward), $\vec{k}_{\text{int}}, \overleftarrow{k}_{\text{int}} \ll \vec{k}_L, \overleftarrow{k}_L, \vec{k}_R, \overleftarrow{k}_R$. Therefore,

$$I(V) \approx -e\left[\frac{-\overleftarrow{k}_L \overleftarrow{k}_{\text{int}} \overleftarrow{k}_R}{\overleftarrow{k}_L \overleftarrow{k}_R + \overleftarrow{k}_{\text{int}} \overleftarrow{k}_R + \overleftarrow{k}_{\text{int}} \vec{k}_L + \vec{k}_L \vec{k}_R}\right] = -e\left[\frac{-\overleftarrow{k}_L \overleftarrow{k}_{\text{int}} \overleftarrow{k}_R}{\overleftarrow{k}_L \overleftarrow{k}_R\left(1+\frac{\overleftarrow{k}_{\text{int}}}{\overleftarrow{k}_L}\right) + \overleftarrow{k}_L \vec{k}_R\left(1+\frac{\overleftarrow{k}_{\text{int}}}{\vec{k}_R}\right)}\right] \approx -e\left[\frac{-\overleftarrow{k}_L \overleftarrow{k}_{\text{int}} \overleftarrow{k}_R}{\overleftarrow{k}_L \overleftarrow{k}_R + \overleftarrow{k}_L \vec{k}_R}\right] \quad (4.20)$$

In this situation, the steady state current becomes

$$I(V) \approx e\frac{\overleftarrow{k}_L \overleftarrow{k}_R \overleftarrow{k}_{\text{int}}}{\overleftarrow{k}_L \overleftarrow{k}_R\left(1+\frac{\vec{k}_R}{\overleftarrow{k}_R}\right)} \approx e\overleftarrow{k}_{\text{int}} \quad (4.21)$$

Thus, the current is rate-limited by $\overleftarrow{k}_{\text{int}}$ and the behavior of the current with temperature or voltage is just the behavior of $\overleftarrow{k}_{\text{int}}$. In this parameter regime, where the intra-molecular M_L-to-M_R ET rates are the slowest rates, the I-V behavior reflects the energy-gap dependence of these ET rates (see relevant Figs 4.8b and 4.9b).

4.4.3 Junction with two redox levels quasi-resonant to the Fermi level at zero bias whose relative energies are unaffected by the voltage bias

We now consider the case where the two redox sites M_L, M_R (see Fig. 4.5) remain in the middle of the Fermi window. Thus, the M_LM_R energy gap is zero and does not change with bias voltage so that the forward and backward intra-molecular rates are equal at for all bias voltages, $\vec{k}_{\text{int}} = \overleftarrow{k}_{\text{int}} = k_{\text{int}}$. We will assume that k_{int} is the slowest rate but that it is not much smaller than the rest of the heterogeneous rates (this regime is relevant to the system in Fig.

4.11). For $V>0$ $\vec{k}_L \ll \overleftarrow{k}_L$, $\vec{k}_R \ll \overleftarrow{k}_R$, $\vec{k}_L\vec{k}_R \ll \overleftarrow{k}_L\overleftarrow{k}_R$, $\vec{k}_L+\vec{k}_R \ll \overleftarrow{k}_L+\overleftarrow{k}_R$, and net charge flows from the R to the L direction. Then, from eq. (4.17),

$$\begin{aligned} I(V) &= -e\frac{k_{\text{int}}}{k_{\text{int}}}\left(\frac{\vec{k}_L\vec{k}_R-\overleftarrow{k}_L\overleftarrow{k}_R}{\overleftarrow{k}_L+\vec{k}_L+\vec{k}_L+\overleftarrow{k}_R+\frac{\overleftarrow{k}_L\vec{k}_R}{k_{\text{int}}}+\overleftarrow{k}_R+\vec{k}_R+\frac{\overleftarrow{k}_L\vec{k}_R}{k_{\text{int}}}+\frac{\vec{k}_L\vec{k}_R}{k_{\text{int}}}}\right) \\ &= -e\left(\frac{\overleftarrow{k}_L\overleftarrow{k}_R\left(\frac{\vec{k}_L\vec{k}_R}{\overleftarrow{k}_L\overleftarrow{k}_R}-1\right)}{\overleftarrow{k}_L\left(1+\frac{\vec{k}_L}{\overleftarrow{k}_L}\right)+\overleftarrow{k}_R\left(1+\frac{\vec{k}_R}{\overleftarrow{k}_R}\right)+\frac{\overleftarrow{k}_L\vec{k}_R}{k_{\text{int}}}\left(1+\frac{\vec{k}_L\vec{k}_R}{\overleftarrow{k}_L\overleftarrow{k}_R}\right)+\vec{k}_L+\overleftarrow{k}_R+\frac{\overleftarrow{k}_L\vec{k}_R}{k_{\text{int}}}}\right) \approx e\left(\frac{\overleftarrow{k}_L\overleftarrow{k}_R}{\overleftarrow{k}_L+\overleftarrow{k}_R+\frac{\overleftarrow{k}_L\vec{k}_R}{k_{\text{int}}}+\vec{k}_L+\overleftarrow{k}_R+\frac{\overleftarrow{k}_L\vec{k}_R}{k_{\text{int}}}}\right) \end{aligned} \tag{4.22}$$

Considering also that, $\overleftarrow{k}_L \approx \overleftarrow{k}_R$,

$$I(V) \approx e\left(\frac{\overleftarrow{k}_L\overleftarrow{k}_R}{\overleftarrow{k}_L\left(1+\frac{\vec{k}_L}{\overleftarrow{k}_L}\right)+\frac{\overleftarrow{k}_L\vec{k}_R}{k_{\text{int}}}+2\overleftarrow{k}_R+\frac{\overleftarrow{k}_L\vec{k}_R}{k_{\text{int}}}}\right) \approx e\left(\frac{\overleftarrow{k}_L\overleftarrow{k}_R}{\overleftarrow{k}_L\left(1+\frac{\overleftarrow{k}_R}{k_{\text{int}}}+\frac{2\overleftarrow{k}_R}{\overleftarrow{k}_L}+\frac{\vec{k}_R}{k_{\text{int}}}\right)}\right) = e\left(\frac{\overleftarrow{k}_R}{\left(3+\frac{\overleftarrow{k}_R}{k_{\text{int}}}+\frac{\vec{k}_R}{k_{\text{int}}}\right)}\right) = ek_{\text{int}}\left(\frac{\overleftarrow{k}_R}{3k_{\text{int}}+\overleftarrow{k}_R+\vec{k}_R}\right). \tag{4.23}$$

4.4.4 Junction with two redox levels off-resonant to the Fermi level at zero bias: Approximate expressions for the rate-limited current

We consider the parameter regime with $\varepsilon_{M_L,0}=\varepsilon_{M_R,0}=\varepsilon_0>0$ in eqs (4.10) and (4.11) such that there is an activation energy for heterogeneous ET from the lead to the redox center (see Fig. 4.15). Figure 4.16 shows examples of the I-V behavior in this regime. The Marcus-inverted-parabola behavior is observable for a wide range of parameters. In Fig. 4.16 the case where $\varepsilon_0 = 0.25$ eV could correspond to M_L, M_R = Ferrocene Fc(+)/Fc redox group (with reduction potential $E_0 = 400$ mV versus SHE) [28] and to Au electrodes (Fermi level of -5.1 eV). [57] The case $\varepsilon_0 = 0.35$ eV could correspond to Azurin' s Cu(2+)/Cu(+) center redox groups (with reduction potential $E_0 = 310$ mV versus SHE) [58] and to Au electrodes.

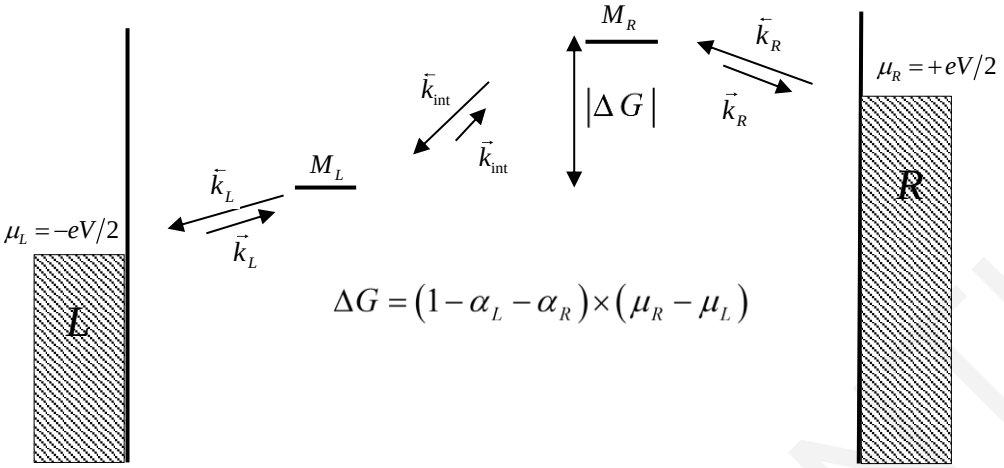

Figure 4.15 Schematic representation of the levels in the $B_LM_LB_MM_RB_R$ junction. The diagram shows a positive bias situation with the M_L (M_R) energy gap written as a function of the total bias across the junction. The bridge levels act as deep tunneling barriers for the transferring electron such that only M_L and M_R change their oxidation state during transfer. The M_L and M_R redox energies are slightly higher than the Fermi levels of the leads at zero bias such that the charge injection rates from the leads are activated and possibly current limiting for a voltage bias range.

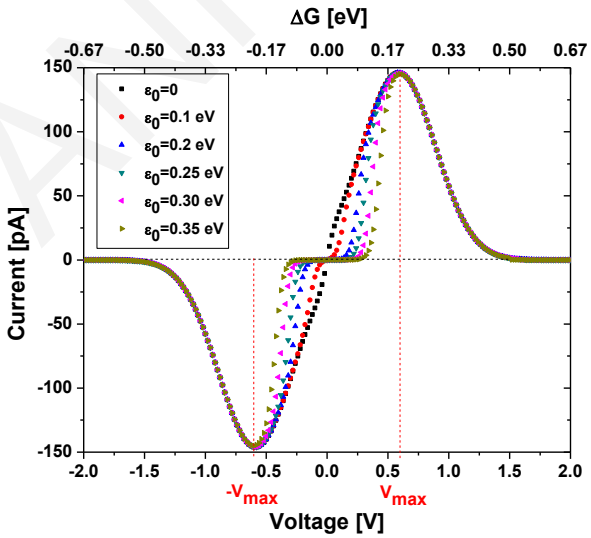

Figure 4.16 Current *I* versus the bias voltage *V* and the Gibbs free energy ΔG at T = 308 K for a junction with off-resonant redox levels at zero bias (Fig. 4.15). The energy gap is given by $\Delta G(V) = eV/3$. Parameter values: $\alpha_L = \alpha_R = 0.33$, $\lambda_L = \lambda_R = 0.1$ *eV*, $c_L = c_R = 0.22 \times 10^1$ $eV^{-1/2}$ ns^{-1} (the timescale of ET between the M_i and the leads is in the order of tens of psec), $c = 0.15$ $eV^{1/2}$ ns^{-1} (the timescale of ET between the M_L and M_R sites is in the order of nsec)

and $\varepsilon_0 = 0$ (black dots), $\varepsilon_0 = 0.1\ eV$ (red dots), $\varepsilon_0 = 0.2\ eV$ (blue dots), $\varepsilon_0 = 0.25\ eV$ (cyan dots, could correspond to Ferrocene M_L and M_R redox groups with Au leads), $\varepsilon_0 = 0.3\ eV$ (magenta dots), and $\varepsilon_0 = 0.35\ eV$ (yellow dots, could correspond to Azurin Cu center redox groups with Au leads). The low bias current decreases as the ε_0 value increases (charge injection becomes more activated), but the current has the expected intra-molecular-rate energy gap behavior (inverted and normal).

The behaviors shown in Fig. 4.16 corresponds to an energy gap between the M_L and M_R groups equal to one third of the chemical potential drop across the junction. For positive bias voltage, the left backward heterogeneous ET rate is faster than the forward rate $\left(\vec{k}_L \ll \overleftarrow{k}_L\right)$ and the same is true for the intra-molecular ET rates $\left(\vec{k}_{\text{int}} \ll \overleftarrow{k}_{\text{int}}\right)$, such that $\vec{k}_L \vec{k}_{\text{int}} \vec{k}_R \ll \overleftarrow{k}_L \overleftarrow{k}_{\text{int}} \overleftarrow{k}_R$. In the regime of Fig. 4.16 both $\overleftarrow{k}_R$ and $\overleftarrow{k}_{\text{int}}$ can be of comparable magnitude and both can be current limiting for the net R to L charge flow. Therefore, we always consider the product $\overleftarrow{k}_{\text{int}} \overleftarrow{k}_R$ as having a small value. Then, from eq. (4.17),

$$I(V) = -e\left[\frac{\overleftarrow{k}_L \overleftarrow{k}_{\text{int}} \overleftarrow{k}_R \left(\frac{\vec{k}_L \vec{k}_{\text{int}} \vec{k}_R}{\overleftarrow{k}_L \overleftarrow{k}_{\text{int}} \overleftarrow{k}_R} - 1\right)}{\overleftarrow{k}_L \overleftarrow{k}_R \left(1 + \frac{\vec{k}_L \vec{k}_R}{\overleftarrow{k}_L \overleftarrow{k}_R}\right) + \overleftarrow{k}_{\text{int}} \overleftarrow{k}_L \left(1 + \frac{\vec{k}_L}{\overleftarrow{k}_L}\right) + \overleftarrow{k}_{\text{int}} \overleftarrow{k}_R \left(1 + \frac{\vec{k}_R}{\overleftarrow{k}_R}\right) + \vec{k}_L \vec{k}_R + \overleftarrow{k}_{\text{int}} \overleftarrow{k}_R + \vec{k}_{\text{int}} \vec{k}_L}\right]$$
$$\approx e\left[\frac{\overleftarrow{k}_L \overleftarrow{k}_{\text{int}} \overleftarrow{k}_R}{\overleftarrow{k}_L \overleftarrow{k}_R + \vec{k}_L \vec{k}_R + \overleftarrow{k}_{\text{int}} \overleftarrow{k}_L \left(1 + \frac{\vec{k}_{\text{int}} \vec{k}_L}{\overleftarrow{k}_{\text{int}} \overleftarrow{k}_L}\right) + \overleftarrow{k}_{\text{int}} \overleftarrow{k}_R \left(1 + \frac{\vec{k}_{\text{int}}}{\overleftarrow{k}_{\text{int}}}\right)}\right] \tag{4.24}$$

Given that $\vec{k}_{\text{int}} \ll \overleftarrow{k}_{\text{int}}$ and $\vec{k}_{\text{int}} \vec{k}_L \ll \overleftarrow{k}_{\text{int}} \overleftarrow{k}_L$ the above expression simplifies to

$$I(V) \approx e\left[\frac{\overleftarrow{k}_L \overleftarrow{k}_{\text{int}} \overleftarrow{k}_R}{\overleftarrow{k}_L \left(\overleftarrow{k}_{\text{int}} + \overleftarrow{k}_R + \frac{\overleftarrow{k}_{\text{int}} \overleftarrow{k}_R}{\overleftarrow{k}_L} + \vec{k}_R\right)}\right]. \tag{4.25}$$

In the regime of Fig. 4.16, $\overleftarrow{k}_{\text{int}}\overleftarrow{k}_R \ll \overleftarrow{k}_L$, and the approximate current expression for the positive bias voltage is $I(V) \approx \frac{e\overleftarrow{k}_R\overleftarrow{k}_{\text{int}}}{\overleftarrow{k}_{\text{int}}+\overleftarrow{k}_R+\overrightarrow{k}_R}$. Similar arguments for negative bias lead to the approximate equation $I(V) \approx -\frac{e\overrightarrow{k}_L\overrightarrow{k}_{\text{int}}}{\overrightarrow{k}_{\text{int}}+\overrightarrow{k}_L+\overleftarrow{k}_L}$.

Figure 4.17 shows the exact current (eqs (4.8) and (4.9)) and the approximate expressions for the current, $I(V) \approx \frac{e\overleftarrow{k}_R\overleftarrow{k}_{\text{int}}}{\overleftarrow{k}_{\text{int}}+\overleftarrow{k}_R+\overrightarrow{k}_R}$ and $I(V) \approx e\overleftarrow{k}_{\text{int}}$, for positive bias voltages in the case of the system of Fig. 4.16 with the highest redox-level energies ($\varepsilon_0 = 0.35$ *eV*, $\alpha_L = \alpha_R = 0.33$, $\lambda_L = \lambda_R = 0.1$ *eV*, $c_L = c_R = 0.22 \times 10^1$ $eV^{-1/2}$ ns^{-1} and $c = 0.15$ $eV^{1/2}$ ns^{-1}). The figure demonstrates that the expression $I(V) \approx \frac{e\overleftarrow{k}_R\overleftarrow{k}_{\text{int}}}{\overleftarrow{k}_{\text{int}}+\overleftarrow{k}_R+\overleftarrow{k}_R}$ is a very good approximation to the exact current for the case of off-resonant redox levels at zero bias $(\varepsilon_0 > 0)$. Further, its shows that $I(V) \approx e\overleftarrow{k}_{\text{int}}$ starts to become a good approximation to the exact current just before the inverted regime peak at $V_{\max}$ (because the current becomes limited by $\overleftarrow{k}_{\text{int}}$). For $\varepsilon_0 < 0.35$ *eV* (Fig. 4.16) the expression $I(V) \approx e\overleftarrow{k}_{\text{int}}$ starts to become a good approximation to the exact current for lower voltages.

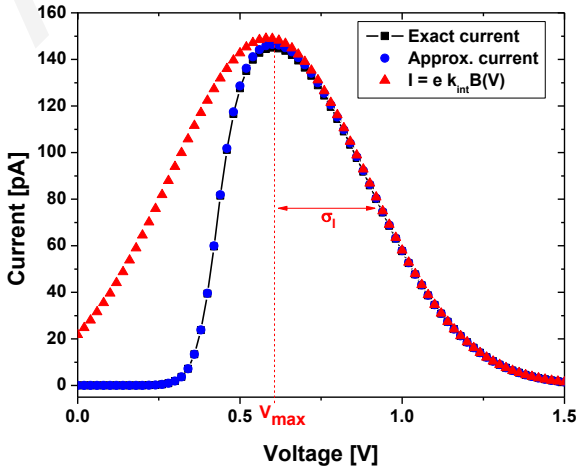

Figure 4.17 Current I versus bias voltage V at T = 308 K (positive V region). Parameter values: $\alpha_L = \alpha_R = 0.33$, $\varepsilon_0 = 0.35$ *eV*, $\lambda_L = \lambda_R = 0.1$ *eV*, $c_L = c_R = 0.22 \times 10^1$ $eV^{-1/2}$ ns^{-1} and c =

0.15 $eV^{1/2}$ ns^{-1}. Exact current expression (eq. (4.9) black line) and approximate current expressions ($I(V) \approx \frac{e\vec{k}_R \vec{k}_{\text{int}}}{\vec{k}_{\text{int}} + \vec{k}_R + \vec{k}_R}$ blue dots, $I(V) \approx e\vec{k}_{\text{int}}$ red dots).

4.4.5 Two-state and heterogeneous electron transfer – Nonadiabatic to Adiabatic Limit

To describe the transition from the nonadiabatic to the adiabatic regimes for two-state (D-A) solution-phase ET with classical ET-active vibrations, it is common to use the Landau-Zener parameter $\gamma_{LZ} = \pi H_{D,A}^2 \Big/ \left(\hbar\bar{\omega}\sqrt{\pi\lambda k_B T}\right)$, [59] $\bar{\omega} = 2\pi\bar{\nu}$ is the average frequency of the ET active vibrations (with $\hbar\bar{\omega} < k_B T$ since they are classical vibrations), $H_{D,A}$ is the D-A coupling and $\lambda = \lambda_D + \lambda_A$ is the reorganization energy. For $\gamma_{LZ} < 1$ $(\gamma_{LZ} \geq 1)$ the D-A ET rate is nonadiabatic (adiabatic). In all examples of the main text the parameters of the M_L-M_R ET rates are such that $\gamma_{LZ} \ll 1$.

For heterogeneous ET between an electrode L(R) and a redox moiety M = $M_{L(R)}$, the adiabaticity parameter is defined as $\gamma = \gamma_{LZ}\rho k_B T$, where the electrode is approximated as multiple D(A) states of a total number equal to $\rho k_B T$ (ρ the density of state). [40,59] Thus

$$\gamma = \frac{\Gamma}{\hbar\bar{\omega}}\sqrt{\frac{k_B T}{\pi\lambda}}, \tag{4.26}$$

where, $\Gamma = \Gamma_{L(R)}$, $\lambda = \lambda_{L(R)}$ and $\bar{\omega} = 2\pi\bar{\nu}$ is the average nuclear vibration frequency of all classical vibrations that promote ET. For $\gamma < 1$ $(\gamma \geq 1)$ the heterogeneous ET rate is nonadiabatic (adiabatic). In all the examples of the figures in the main text $\gamma << 1$.

An approximate expression for the heterogeneous ET rate that interpolates between nonadiabatic and adiabatic regimes, [40] is

$$k \simeq \bar{\nu} \times \left[\frac{2\left(1 - \exp\left(-\gamma/2\right)\right)}{2 - \exp\left(-\gamma/2\right)}\right] \times C \tag{4.27}$$

where $\bar{\nu} = \bar{\omega}/2\pi$ and

$$C = \left(k_B T\right)^{-1} \int dE\, f\left(E-\mu\right) e^{-\frac{\left(\lambda-\left(\mu(V)+E\right)+\varepsilon_M(V)\right)^2}{4\lambda k_B T}} \tag{4.28}$$

for electrode-to-M ET, and

$$C = \left(k_B T\right)^{-1} \int dE\left[1-f\left(E-\mu\right)\right] e^{-\frac{\left(\lambda+\left(\mu(V)+E\right)-\varepsilon_M(V)\right)^2}{4\lambda k_B T}} \tag{4.29}$$

for M-to-electrode ET. The above expression, eq. (4.27), is valid for large reorganization energies and small overpotentials, i.e., for $\left|\mu(V)-\varepsilon_M(V)\right| \ll \lambda/4$ and $\Gamma \ll \lambda/4$.

In the limit where $\gamma < 1$ such that $\exp\left(-\gamma/2\right) \approx 1-\left(\gamma/2\right)$, the above formula leads to the nonadiabatic heterogeneous ET rate expressions (eqs (4.2) – (4.4) in the main text). Consider the zero bias $\left(\mu = 0\ eV\right)$ rates of eq. (4.27) where $\Gamma \approx 1.0\times 10^{-3} eV$, $\lambda = 0.2\ eV$, $\varepsilon_M \approx 0\ eV$ and $\bar{v} \approx 0.04\ \left(\text{psec}\right)^{-1}$. In this case $\gamma \approx 7$ (strong adiabatic regime) and from eq. (4.27), $k \simeq 1.0\left(\text{psec}\right)^{-1}$.

4.4.6 Voltage-dependent tunneling matrix elements – A tight-binding model

For the proposed quasi-linear junction architecture with metal redox centers, good choices for the connecting bridges are saturated organic bridges. These are known to be high tunneling barriers for solution-phase ET between metal donors and acceptors [11,14,15] and for heterogeneous ET between metal redox sites and electrodes. [29,30] Such bridges also maintain off-resonant tunneling currents when connecting directly metal (e.g., Au) electrodes for bias voltages of 1.0 - 2.0 V and for lengths of the order of few tens of Angstroms. [41] Within the experimental voltage window, saturated organic bridges should remain tunneling barriers for electrode-to-$M_{L(R)}$ and M_L-M_R ET steps, even though they may give voltage-dependent tunneling matrix elements, as shown below.

To calculate the dependence of the tunneling matrix elements on bias voltage, and to explore how this dependence affects the observation of the Marcus inverted regime, we consider a linear nearest-neighbor tight-binding model consisting of B_R, B_M and B_L bridges with n_{B_R}, n_{B_M} and n_{B_L} tight-binding levels (sites), respectively (Fig. 4.18). The i_{M_L} and i_{M_R} sites of the model represent the redox levels, which are assumed to be off-resonant to the bridge levels and also quasi-resonant to the electrodes at zero bias. At non-zero bias the bridge site-

energies and the redox-site energies will be shifted, and we model how these shifts affect the through-bridge tunneling barriers.

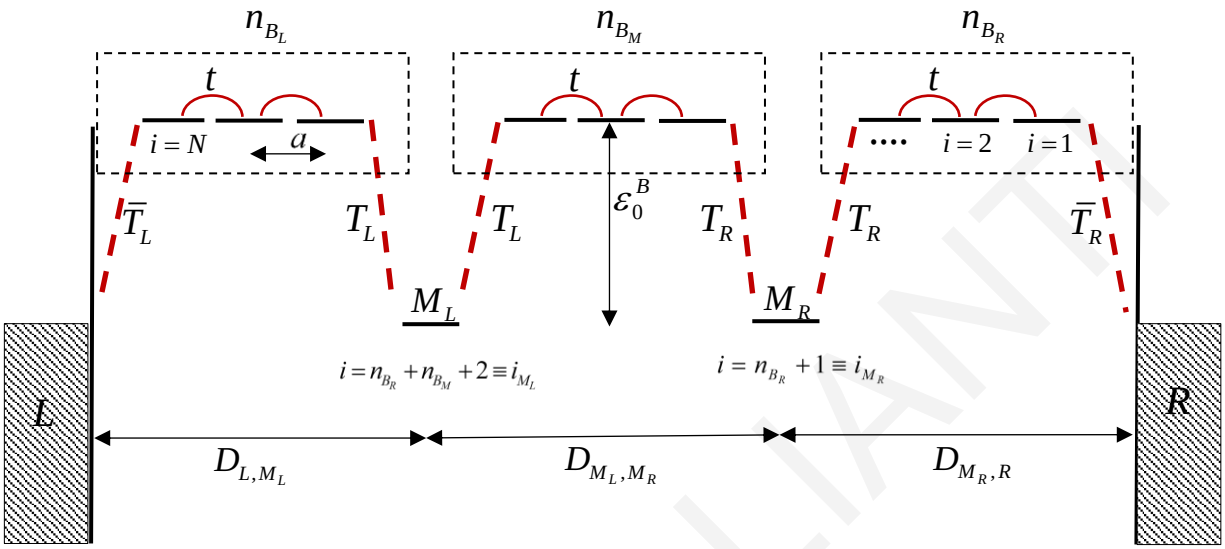

Figure 4.18 Schematic representation of a tight-binding nearest-neighbor model of a $B_L M_L B_M M_R B_R$ junction. The B_L, B_M and B_R linear bridges consist of n_{B_L}, n_{B_M} and n_{B_R} sites, respectively. At zero bias the bridge site-energies are equal, of value ε_0^B (measured with respect to the Fermi level of the electrodes). The redox level $M_{L(R)}$ energies are off-resonant to the bridge energies and resonant to the electrodes. The nearest-neighbor electronic couplings between bridge sites are denoted t (curved red lines). The nearest-neighbor electronic couplings between $M_{L(R)}$ and the bridge sites are denoted $T_{L(R)}$ and those between the last (first) bridge site and the L (R) electrode, are denoted $\bar{T}_{L(R)}$ (red dotted lines). D_{L,M_L}, D_{M_L,M_R} and $D_{M_R,R}$ are the distances of the L-M_L, M_L-M_R and M_R-R segments of the junction. The diagram shows a symmetric junction with $D_{L,M_L} = D_{M_R,R} = D_{M_L,M_R}$. $D_{tot} = D_{L,M_L} + D_{M_L,M_R} + D_{M_R,R}$ is the total length of the junction. The distance between nearest neighbor sites is $a = D_{tot}/(N+1)$.

We assume linear voltage drop profile under bias where the voltage drop is measured with respect to the R electrode Fermi level μ_R $(\mu_R = \Delta\mu/2 = eV/2)$. If the site belongs to a bridge the energy of the i^{th} site is given by $\varepsilon_i^B(V) = \frac{eV}{2} - i\left(\frac{a}{D_{tot}}\right)eV + \varepsilon_{i,0}^B$, where $\varepsilon_{i,0}^B = \varepsilon_0^B$ and

$a = \frac{D_{tot}}{N+1}$ is the distance between nearest-neighbor sites. For a redox site, $i = n_{B_R} + 1 \equiv i_{M_R}$ and $i = n_{B_R} + n_{B_M} + 2 \equiv i_{M_L}$ (Fig. 4.18). Therefore, the redox-site energies under bias are $\varepsilon_{i_{M_R}}(V) = \frac{eV}{2} - i_{M_R}\left(\frac{a}{D_{tot}}\right)eV + \varepsilon_{M_R,0}$ and $\varepsilon_{i_{M_L}}(V) = \frac{eV}{2} - i_{M_L}\left(\frac{a}{D_{tot}}\right)eV + \varepsilon_{M_L,0}$ (in Fig. 4.18 $\varepsilon_{M_L,0} = \varepsilon_{M_R,0} = 0$). These expressions reduce to eqs (4.10) and (4.11) of the main text when $i_{M_R} = 1$ and $i_{M_L} = 2$ (with $\alpha_L = \alpha_R = a/D_{tot}$).

Given the above model, we derive the bias voltage dependence of the bridge-mediated M_L-M_R tunneling matrix element and of the $M_{L(R)}$-L(R) tunneling matrix elements. The M_L-M_R tunneling matrix element is [60]

$$H_{M_L,M_R}(V) = T_L\, T_R\, G^{(B_M)}_{i_{M_L}-1,\, i_{M_R}+1}(E_{tun}) \tag{4.30}$$

where $\hat{G}^{(B_M)}(E)$ is the Green's function of the B_M bridge segment, defined as $\hat{G}^{(B_M)}(E) = \left(E\,\hat{I} - \hat{H}^{(B_M)}(V)\right)^{-1}$. $\hat{H}^{(B_M)}(V)$ is the voltage-dependent Hamiltonian of the B_M bridge segment,

$$\hat{H}^{(B_M)}(V) = \sum_{i=i_{M_R}+1}^{i_{M_L}-1} \varepsilon_i^B(V)\,|i\rangle\langle i| + \sum_{i=i_{M_R}+1}^{i_{M_L}-1} t\left(|i\rangle\langle i+1| + h.c\right). \tag{4.31}$$

$E_{tun} = \left(\varepsilon_{M_R}(V) - \varepsilon_{M_L}(V)\right)/2$ is the tunneling energy and $T_{L(R)}$ are the electronic couplings between $M_{L(R)}$ and the nearest-neighbor B_M bridge site. We model the bias-voltage dependence of the level broadenings in a similar way, i.e., $\Gamma_{L(R)}(V) = \pi\rho H^2_{M_{L(R)},L(R)}(V)$, where

$H_{L,M_L}(V) = \bar{T}_L\, T_L\, G^{(B_L)}_{N,\, i_{M_L}+1}(E_{tun})$ and $H_{R,M_R}(V) = \bar{T}_R\, T_R\, G^{(B_R)}_{1,\, i_{M_R}-1}(E_{tun})$. $\hat{G}^{(B_{L(R)})}(E)$ is the Green's function of the $B_{L(R)}$ bridge segment, $E_{tun} = \left(\mu_{L(R)} - \varepsilon_{M_L(M_R)}(V)\right)/2$ and the couplings $T_{L(R)}$ and $\bar{T}_{L(R)}$ are shown in Fig. 4.18.

Consider saturated linear bridges (e.g., linear alkanes) that are known to mediate hole tunneling pathways through C-C sigma bonds. [61-63] Each bridge site of the tight binding model is interpreted as a sigma bond orbital in a tetrahedral geometry. The distance between the centers of nearest-neighbor sigma bonds in an extended alkane chain is $a \approx 1.26\,\text{Å}$. The

magnitude of the electronic matrix element between the nearest-neighbor bond orbitals is $t \approx 4 eV$.[61-63] For linear alkane chains connected to metal electrodes, the dependence of the conductance as a function of bridge length D is given by $G(D) = A\exp(-\beta D)$, with a decay parameter value $\beta \approx 1.0 \text{ Å}^{-1}$.[41] A similar exponential length decay parameter value is derived for redox currents in voltammetric studies involving redox metals connected to gold electrodes by alkanethiol bridges.[29,30] We use this experimental β value in our model to fix the ratio $\left|t/\varepsilon_0^B\right|$, since $\left|G_{1,n+1}^{(n+1)}(E_{tun})\right|^2 \Big/ \left|G_{1,n}^{(n)}(E_{tun})\right|^2 \approx \exp(-\beta a)$ (where (n+1) and (n) denote bridges of n+1 and n sites, respectively). Thus, given the computed value of $t \approx 4\ eV$,[61-63] we can determine the effective site energy ε_0^B of the sigma bond (with respect to the Fermi level of the electrodes at zero bias) that produces $\beta \approx 1.0 \text{ Å}^{-1}$ for $a \approx 1.26 \text{ Å}$ (assuming gold electrodes).

As an example, consider linear bridges with $n_{B_R} = n_{B_M} = n_{B_L} = 5$ sigma bonds, each of a total length of $6-7$ Å (e.g., a total length of the junction, $D_{tot} \approx 20-25 \text{ Å}$ taking into account few Angstrom sizes of the metal redox sites). With the $t = 4\ eV$ and $\varepsilon_0^B = 10\ eV$ we get $\beta \approx 1.0$ Å^{-1}. For these t and ε_0^B values, and for $H_{M_L,M_R}(V=0) = 1.6\times10^{-4} eV$ (of Figs 4.7 and 4.8), eq. (4.30) gives $T_L T_R = 2.5\times10^{-2} eV^2$ (i.e., $T_L = T_R = 0.15 eV$ for a symmetric system). Further, for the zero-bias level broadenings $\Gamma_{L(R)}(V=0) = 1.0\times10^{-6} eV$ (of Figs 4.7 and 4.8) we get $\bar{T}_{L(R)} = 1.0\times10^{-3} eV$.

Given the above parameters we compute the voltage dependence of the coupling and the level shifts, i.e., $H_{M_L,M_R}(V)$ and $\Gamma_{L(R)}(V)$, and use them in eqs (4.2)-(4.11) where, at each voltage, we substitute $H^2_{M_L,M_R}(V)$ and $\Gamma_{L(R)}(V)$. Figures 4.19a and 4.19b show $H^2_{M_L,M_R}(V)$ and $\Gamma_{L(R)}(V)$ for positive bias voltages and for the junction parameters of Figs 4.7 and 4.8 ($\Delta G = \Delta\mu/3$). Figure 4.19c compares the I-V dependence computed using eqs (4.2)-(4.11) with $H^2_{M_L,M_R}(V)$ and $\Gamma_{L(R)}(V)$ of Figs 4.19a and 4.19b to the I-V dependence computed using eqs (4.2)-(4.11) with $H^2_{M_L,M_R}(V)$ and $\Gamma_{L(R)}(V=0)$. The current obtained with voltage-dependent couplings remains rate-limited by intra-molecular rates, having a Gaussian voltage dependence. The current's maximum shifts to a higher bias $V_{\max,2}$ and has

a higher maximum value compared to the case of the current with voltage-independent (zero-bias) couplings (maximum at $V_{max,1}$).

These changes are due to the lowering of the tunneling barriers with bias voltage (Figs 4.19a and 4.19b). The minimum bridge eigenvalue of this tight-binding model is 3.07 eV above the Fermi level of the electrodes at zero bias, while at bias voltages of 1.0 V and 2.0 V the minimum eigenvalue has dropped 2.24 eV and 1.4 eV above μ_R, respectively (μ_R is the highest Fermi level for positive bias). Thus, the tunneling mechanism is maintained for the entire bias voltage range. The preservation of tunneling is expected for saturated organic bridges and also for some unsaturated bridges that sustain tunneling currents for lengths of tens of Angstroms and for bias voltages of 1.0 – 2.0 V. [64-65]

(a)

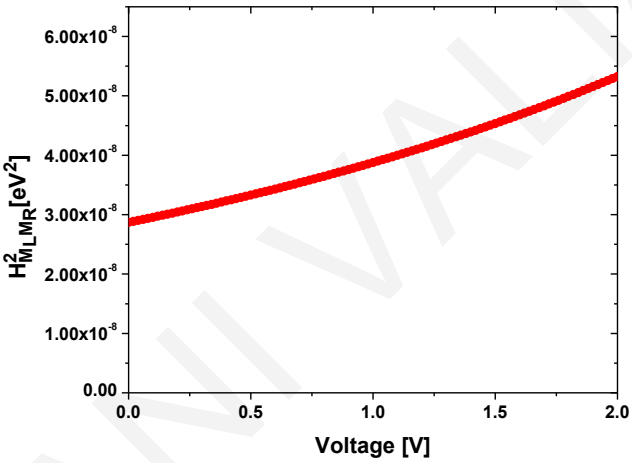

(b)

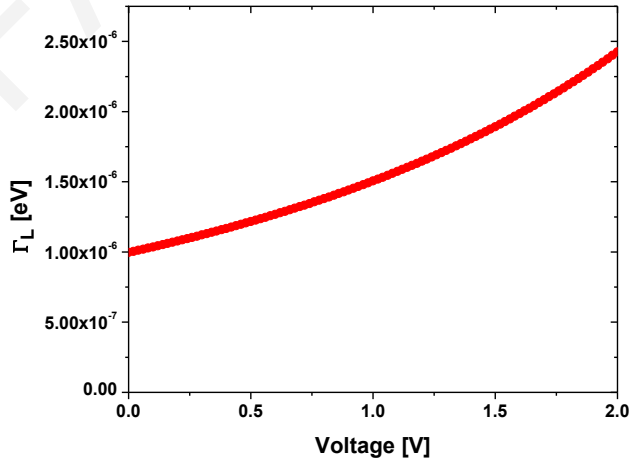

(c)

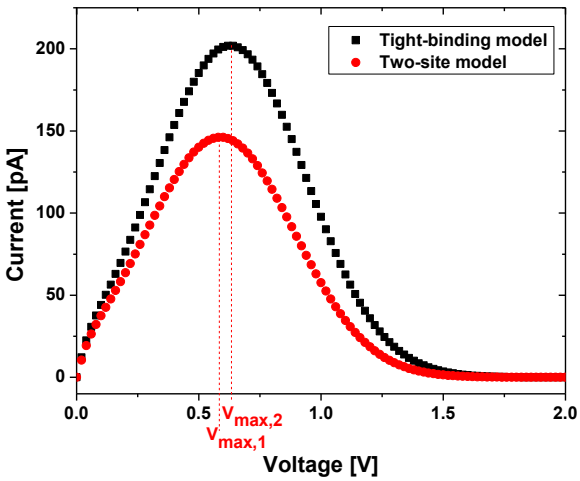

Figure 4.19 (a) Bias-dependent $H^2_{M_L,M_R}(V)$ (eq. (4.30)) versus the bias voltage V at T = 308 K for the positive bias region, (b) Bias-dependent broadening $\Gamma_{L(R)}(V)$ versus bias voltage V. (c) Current (eqs (4.2)-(4.11)) versus bias voltage V using $H_{M_L,M_R}(V=0)$ and $\Gamma_{L(R)}(V=0)$ (red dots, as in Fig. 4.7), and using the $H_{M_L,M_R}(V)$ and $\Gamma_{L(R)}(V)$ (black dots). Parameter values for all graphs: $n_{B_R} = n_{B_M} = n_{B_L} = 5$, $\varepsilon_0{}^B$ = *10.0 eV*, $\lambda_L = \lambda_R$ = *0.1 eV*, *t = 4.0 eV*, $T_L = T_R$ = *1.5 x* 10^{-1} *eV* and $\overline{T}_L = \overline{T}_R = 1.0 \times 10^{-3} eV$.

The specific research work presented in this chapter has been published during the doctoral program (see ref. [66]).

4.5 References

[1] Nitzan, A. A Relationship between Electron-Transfer Rates and Molecular Conduction. *J. Phys. Chem. A.* **2001**, *105 (12)*, 2677-2679.

[2] Nitzan, A. The Relationship Between Electron Transfer Rate and Molecular Conduction. 2. The Sequential Hopping Case. *Isr. J. Chem.* **2002**, *42*, 163-166.

[3] Berlin, Y. A.; Ratner, M. A. Intra-Molecular Electron Transfer and Electric Conductance via Sequential Hopping: Unified Theoretical Description. *Radiat. Phys. Chem.* **2005**, *74*, 124-131.

[4] Traub, M. C.; Brunschwig, B. S.; Lewis, N. S. Relationships between Nonadiabatic Bridged Intramolecular, Electrochemical, and Electrical Electron-Transfer Processes. *J. Phys. Chem. B.* **2007**, *111*, 6676-6683.

[5] Venkatramani, R.; Wierzbinski, E.; Waldeck, D. H.; Beratan, D. N. Breaking the Simple Proportionality Between Molecular Conductances and Charge Transfer Rates. *Faraday Discuss*. **2014**, *174*, 57-78.

[6] Zhou, X.-S.; Liu, L.; Fortgang, P.; Lefevre, A.-S.; Serra-Muns, A.; Raouafi, N.; Amatore, C.; Mao, B.-W.; Maisonhaute, E.; Schöllhorn, B. Do Molecular Conductances Correlate with Electrochemical Rate Constants? Experimental Insights. *J. Am. Chem. Soc.* **2011**, *133*, 7509-7516.

[7] Bueno, P. R. Common Principles of Molecular Electronics and Nanoscale Electrochemistry. *Anal. Chem*. **2018**, *90*, 7095-7106.

[8] Kalantar, N; Segal D. Mean First-Passage Time and Steady-State Transfer Rate in Classical Chains. *J. Phys. Chem. C.* **2019**, *123 (2)*, 1021-1031.

[9] Amdursky, N.; Marchak, D.; Sepunaru, L.; Pecht, I.; Sheves, M.; Cahen, D. Electronic Transport via Proteins. *Adv. Mater*. **2014**, *26*, 7142−7161.

[10] Ruiz, M. P.; Aragonés, A. C.; Camarero, N.; Vilhena, J. G.; Ortega, M.; Zotti, L. A.; Pérez, R.; Cuevas, J. C.; Gorostiza, P.; Díez- Pérez, I. Bioengineering a Single-Protein Junction. *J. Am. Chem. Soc*. **2017**, *139*, 15337−15346.

[11] Balzani, V.; Piotrowiak, P.; Rodgers, M. A. J.; Mattay, J.; Astruc, D.; Gray, H. B.; Wrinkler, J.; Fukuzumi, S.; Mallouk, T. E.; Haas, Y.; et al. *Electron Transfer in Chemistry*; Wiley VCH: Weinheim, Germany, 2001; Vols. *1−4*.

[12] Jortner, J.; Bixon, M.; Prigogine, I.; Rice, S. A. *Electron Transfer - From Isolated Molecules to Biomolecules*; John Wiley & Sons: New York, 1999.

[13] *Long-Range Charge Transfer in DNA I and II*; Schuster, G. B., Ed.; Topics in Current Chemistry *236−237*; Springer: Berlin, 2004.

[14] Beratan, D. N.; Skourtis, S. S. Electron Transfer through Proteins. *Encyclopedia of Biophysics*. **2013**, 625−630.

[15] Winkler, J. R.; Gray, H. B. Electron Flow through Metalloproteins. *Chem. Rev.* **2014**, *114*, 3369−3380.

[16] Skourtis, S. S. Probing Protein Electron Transfer Mechanisms from the Molecular to the Cellular Length Scales. *Biopolymers* **2013**, *100*, 82−92.

[17] *Energy/Mechanistic Biology*; Beratan, D. N., Skourtis, S. S., Erb, T. J., Gerlt, J. A., Eds.; Current Opinion in Chemical Biology *47*; Elsevier, 2018; pp 1−142.

[18] Blumberger, J. Recent Advances in the Theory and Molecular Simulation of Biological Electron Transfer Reactions. *Chem. Rev*. **2015**, *115*, 11191−11238.

[19] Nitzan, A. *Chemical Dynamics in Condensed Phases*; Oxford University Press, 2006.

[20] Cuevas, J. C.; Scheer, E. *Molecular Electronics: An Introduction to Theory and Experiment,* 2nd ed.; World Scientific: Singapore, 2017.

[21] Zhang, J.; Kuznetsov, A. M.; Medvedev, I. G.; Chi, Q.; Albrecht, T.; Jensen, P. S.; Ulstrup, J. Single-Molecule Electron Transfer in Electrochemical Environments. *Chem. Rev.* **2008**, *108*, 2737−2791.

[22] Migliore, A.; Schiff, P.; Nitzan, A. On the Relationship Between Molecular State and Single Electron Pictures in Simple Electrochemical Junctions. *Phys. Chem. Chem. Phys.* **2012**, *14 (40)*, 13746−13753.

[23] Migliore, A.; Nitzan, A. Irreversibility and Hysteresis in Redox Molecular Conduction Junctions. *J. Am. Chem. Soc.* **2013**, *135*, 9420−9432.

[24] Yuan, L.; Wang, L.; Garrigues, A. R.; Jiang, L.; Annadata, H. V.; Anguera Antonana, M.; Barco, E.; Nijhuis, C. A. Transition from Direct to Inverted Charge Transport Marcus Regions in Molecular Junctions via Molecular Orbital Gating. *Nat. Nanotechnol.* **2018**, *13*, 322−329.

[25] Valianti, S.; Cuevas, J. C; Skourtis S. S. Charge-Transport Mechanisms in Azurin-Based Monolayer Junctions. *J. Phys. Chem. C*. **2019**, *123 (10)*, 5907-5922.

[26] Li, Y; Wang, H., Wang, Z., Qiao, Y.; Ulstrup, J.; Chen, H. Y.; Zhou, G.; Tao N. Transition from Stochastic Events to Deterministic Ensemble Average in Electron Transfer Reactions Revealed by Single-Molecule Conductance Measurement. *Proc. Natl. Acad. Sci. USA* **2019**, *116 (9)*, 3407-3412.

[27] Schmickler, W.; Santos, E. *Interfacial Electrochemistry*, 2nd ed.; Springer: Berlin, 2010.

[28] Bard, A. J.; Faulkner, L. R. *Electrochemical Methods. Fundamentals and Applications*, 2nd ed.; John Wiley & Sons, Inc.: New York, 2000.

[29] Smalley, J. F.; Feldberg, S. W.; Chidsey, C. E. D.; Linford, M. R.; Newton, M. D.; Liu, Y-P. The Kinetics of Electron Transfer through Feroccene-Terminated Alkanethiol Monolayers on Gold. *J. Phys. Chem.* **1995**, *99*, 13141-13149.

[30] Eckermann, A. L.; Feld, D. J.; Shaw, J. A.; Meade, T. J. Electrochemistry of Redox-Active Self-Assembled Monolayers. *Coord. Chem. Rev*. **2010**, *254*, 1796-1802.

[31] Marcus, R. A.; Sutin, N. Electron Transfers in Chemistry and Biology. *Biochim. Biophys. Acta, Rev. Bioenerg*. **1985**, *811*, 265−322.

[32] Closs G. L.; Miller, J. R. Intramolecular Long-Distance Electron Transfer in Organic Molecules, *Science* **1988** 240, 440-447.

[33] Lehmann, L.; Ingold, G.-L.; Hanggi, P. Incoherent Charge Transport through Molecular Wires: Interplay of Coulomb Interaction and Wire Population. *Chem. Phys*. **2002**, *281*, 199−209.

[34] Polizzi, N. F.; Skourtis, S. S.; Beratan, D. N. Physical Constraints on Charge Transport through Bacterial Nanowires. *Faraday Discuss*. **2012**, *155*, 43–62.

[35] Livshits, G.; Stern, A.; Rotem, D.; Borovok, N.; Eidelshtein, G.; Migliore, A.; Penzo, E.; Wind, S.; Di Felice, R.; Skourtis, S. S.; et al. Long-Range Charge Transport in Single G-quadruplex DNA Molecules. *Nat. Nanotechnol*. **2014**, *9*, 1040−1046.

[36] Galperin, M.; Ratner, M. A., Nitzan, A. Hysterisis, Switching, and Negative Differential Resistance in Molecular Junctions: A Polaron Model. *Nano Lett*. **2005**, *5 (1)*, 125-130.

[37] Perrin, M. L.; Frisenda, R.; Koole, M.; Seldenthuis, J. S.; Gil, J. A. C.; Valkenier, H.; Hummelen, J. C.; Renaud, N.; Grozema, F. C.; Thijssen, J. M.; et al. Large Negative Differential Conductance in Single-Molecule Break Junctions. *Nat. Nanotechnol*. **2014**, *9*, 830-834.

[38] Chen, J.; Wang, W.; Reed, M. A.; Rawlett, A. M.; Price, D. W.; Tour, J. M. Room-Temperature Negative Differential Resistance in Nanoscale Molecular Junctions. *Appl. Phys. Lett.* **2000**, *77*, 1224-1226.

[39] Guisinger, N. P.; Greene, M. E.; Basu, R.; Baluch, A. S.; Hersam, M. C. Room Temperature Negative Differential Resistance through Individual Organic Moleculer on Silicon Surfaces. *Nano Lett*. **2004**, *4(1)*, 55-59.

[40] Feldberg, S. W.; Sutin, N. Distance Dependence of Heterogeneous Electron Transfer through the Nonadiabatic and Adiabatic Regimes. *Chem. Phys*. **2006**, *324*, 216-225.

[41] Akkerman, H. B.; de Boer, B. Electrical Conduction through Single Molecules and Self-Assembled Monolayers. *J. Phys.: Condens. Matter*. **2008**, *20*, 013001.

[42] Beratan, D. N.; Betts, J. N.; Onuchic, J. N.; Protein Electron Transfer Rates Set by the Bridging Secondary and Tertiary Structure. *Science*. **1991**, *252 (5010)*, 1285-1288.

[43] Gehring, P.; Thijssen, J. M.; van der Zant, H. S. J. Single-Molecule Quantum-Transport Phenomena in Break Junctions. *Nat. Rev. Phys*. **2019**, *1*, 381-396.

[44] Cabosart, D.; Abbassi, M. E.; Stefani, D.; Frisenda, R.; Calame, M.; van der Zant, H. S. J.; Perrin, M. L. A Reference-Free Clustering Method for the Analysis of Molecular Break-Junction Measurements. *Appl. Phys. Lett.* **2019**, *114*, 143102.

[45] Chi, Q.; Farver, O.; Ulstrup, J. Long-Range Protein Electron Transfer Observed at the Single-Molecule Level: In Situ Mapping of Redox-Gated Tunneling Resonance. *Proc. Natl. Acad. Sci. U. S. A.* **2005**, *102*, 16203−16208.

[46] Alessandrini, A.; Salerno, M.; Frabboni, S.; Facci, P. Single- Metalloprotein Wet Biotransistor. *Appl. Phys. Lett*. **2005**, *86*, 133902.

[47] Alessandrini, A.; Corni, S.; Facci, P. Unravelling Single Metalloprotein Electron Transfer by Scanning Probe Techniques. *Phys. Chem. Chem. Phys*. **2006**, *8*, 4383−4397.

[48] Miller, J. R.; Calcaterra, L. T.; Closs, G. L. Intramolecular Long-Distance Electron Transfer in Radical Anions. The Effects of Free Energy and Solvent on the Reaction Rates. *J. Am. Chem. Soc.* **1984**, *106*, 3047-3049.

[49] Gunner, M. R.; Dutton, P. L. Temperature and $-\Delta G^0$ Dependence of the Electron Transfer from BPh- to QA in Reaction Center Protein from Rhodobacter sphaeroides with Different Quinones as QA. *J. Am. Chem. Soc.* **1989**, *111*, 3400-3412.

[50] Fox, L. S.; Kozik, M.; Winkler, J. R.; Gray, H. B. Gaussian Free-Energy Dependence of Electron Transfer Rates in Iridium Complexes. *Science* **1990**, *247*, 1069-1071.

[51] Scott, J. R.; Willie, A.; McLean, M.; Stayton, P. S.; Sligar, S. G.; Durham, B.; Millett, F. Intramolecular Electron Transfer in Cytochrome b_5 Labeled with Ruthenium (II) Polypyridine Complexes: Rate Measurements in the Marcus Inverted Region. *J. Am. Chem. Soc.* **1993**, *115*, 6820-6824.

[52] Winkler, J. R.; Malmstroem, B. G.; Gray, H. B. Rapid Electron Injection into Multisite Metalloproteins: Intramolecular Electron Transfer in Cytochrome Oxidase. *Biophys. Chem.* **1995**, *54*, 199-209.

[53] Farver, O.; Hosseinzadeh, P.; Marshall, N. M.; Wherland, S.; Lu, Y.; Pecht, I. Long-Range Electron Transfer in Engineered Azurins Exhibits Marcus Inverted Region Behavior. *J. Phys. Chem. Lett*. **2015**, *6*, 100-105.

[54] Hilczer, M.; Tachiya, M. Electric Field Effects on Fluorescence Quenching due to Electron Transfer. II. Linked Donor-Acceptor Systems. *J. Chem. Phys.* **2002**, *117 (4)*, 1759-1767.

[55] Hilczer, M.; Bandyopadhyay, T.; Tachiya, M. Electric Field on Electron Transfer between Donor and Acceptor in Polymer Matrix. *J. Photochem. Photobiol.* **2004**, *166*, 33-44.

[56] Boxer, S. C. Stark Realities. *J. Phys. Chem. B*. **2009**, *113*, 2972-2983.

[57] Sachtler, W. M. H.; Dorgelo, G. J. H.; Holsher, A. A. The work function of gold. *Surf. Sci*. **1966**, *5*, 221-229.

[58] Fereiro, J.; Yu, X.; Pecht, I.; Sheves, M.; Cuevas, J. C.; Cahen, D. Tunneling Explains Efficient Electron Transport via Protein Junctions. *Proc. Natl. Acad. Sci. U. S. A.* **2018**, *115*, E4577-E4583.

[59] *Adiabatic versus Non-Adiabatic Electron Transfer*; Sumi, H., Balzani, V., Piotrowiak, P., Rodgers, M. A. J., Mattay, J., Astruc, D., Gray, H. B., Winkler, J., Fukuzumi, S., Mallouk, T. E., Haas, Y., et al. Eds.; Electron Transfer in Chemistry; Wiley VCH: Weinheim, Germany, 2001; pp 65-108.

[60] Skourtis, S. S.; Beratan, D. N. Theories of Structure-Function Relationships for Bridge-Mediated Electron Transfer Reactions. *Adv. Chem. Phys*. **1999,** *106*, 377–452.

[61] Jordan, K. D.; Paddon-Row, M. N. Analysis of the Interactions Responsible for Long-Range through-Bond-Mediated Electronic Coupling between Remote Chromophores Attached to Rigid Polynorbornyl Bridges. *Chem. Rev*. **1992**, *92 (3)*, 395-410.

[62] Liang, C. X.; Newton, M. D. Ab Initio Studies of Electron Transfer: Pathway Analysis of Effective Transfer Integrals. *J. Phys. Chem.* **1992,** *96*, 2855–2866.

[63] Curtiss, L. A.; Naleway, C. A.; Miller, J. R. Superexchange Pathway Calculation of Long-Distance Electronic Coupling in $H_2C(CH_2)_{m-2}CH_2$ Chains. *Chem. Phys.* **1993,** *176,* 387–405.

[64] Choi, S. H.; Kim, B.; Frisbie, C. D. Electrical Resistance of Long Conjugated Molecular Wires. *Science* **2008,** *320,* 1482-1486.

[65] Zhao, X.; Huang, C.; Gulcur, M.; Batsanov, A.S.; Baghernejad, M.; Hong, W.; Bryce, M. R.; Wandlowski, T. Oligo(aryleneethynylene)s with Terminal Pyridyl Groups: Synthesis and Length Dependence of the Tunneling-to-Hopping Transition of Single-Molecule Conductances. *Chem. Mater*. **2013,** *25,* 4340−4347.

[66] Valianti, S.; Skourtis, S. S. Observing Donor-to-Acceptor Electron-Transfer Rates and the Marcus Inverted Parabola in Molecular Junctions. *J. Phys. Chem. B* **2019**, *123 (45),* 9641–9653.

CHAPTER 5

The Role of Bridge-state Intermediates in Singlet Fission for Donor-bridge-acceptor Systems: A Semi-analytical Approach to Bridge-tuning of the Donor-acceptor Fission Coupling

We describe a semi-analytical / computational framework to explore structure-function relationships for singlet fission in Donor (D) – Bridge (B) – Acceptor (A) molecular architectures. The aim of introducing a bridging linker between the D and A molecules is to tune, by modifying the bridge structure, the electronic pathways that lead to fission and to D-A-separated correlated triplets. We identify different bridge-mediation regimes for the effective singlet-fission coupling in the coherent tunneling limit and show how to derive the dominant fission pathways in each regime. We describe the dependence of these regimes on D-B-A many-electron state energetics and on D-B (A-B) one-electron and two-electron matrix elements. This semi-analytical approach can be used to guide computational and experimental searches for D-B-A systems with tuned singlet fission rates. We use this approach to interpret the bridge-resonance effect of singlet fission that has been observed in recent experiments.

Singlet Fission (SF) is a spin-allowed process in which a photo-excited singlet state S_1 in a molecular system is converted into two correlated triplet excited states $2\times T_1$. [1-4] SF offers a promising way to overcome the Shockley-Queisser limit on the efficiency of single-junction photovoltaics, [1-3,5] and it is possible if a material satisfies the exoergicity criterion $\text{Energy}(S_1) \geq 2\,\text{Energy}(T_1)$. An extensive body of work has examined SF in different materials due to its potential for photovoltaics applications. [6-13] There are many experimental, computational [14-17] and theoretical studies [3,4,14,18,19] of SF mechanisms and of the roles of SF intermediate states in dimeric systems (donor(D)-acceptor(A)). More recently, systems in which a bridge (B) unit connects the D and A moieties [11-13] have received attention with the purpose of understanding how a bridge linker mediates SF. [5,20-26] Recent experiments [24-26] have observed a correlation between SF-rate enhancement and the lowering of the B HOMO-LUMO gap (the "bridge-resonance effect" of SF [26]). Another important

direction in the field is the computational design of SF molecular assemblies with tunable SF rates. [27-31]

In this paper, we introduce an analytical framework, supported by ab-initio computations, to explore structure-function relationships for bridge-mediated SF in D-B-A molecular architectures. The aim of this type of analysis is to understand how the bridge affects the SF coupling based on parametrized analytical models, and ultimately to guide the synthesis of D-B-A systems for tuned SF. We apply our method to bridge-mediated SF in the coherent tunneling regime. We also use our analytical results to interpret the recent experiments on bridge-resonance effects of SF.

5.1 Theoretical methods

Consider a D-B-A molecular assembly to be used as a tunable singlet-fission / triplet-separation device. Suppose that initial photoexcitation leads to a singlet excited state localized on the D moiety that subsequently undergoes SF to create a Correlated Triplet-Pair (CTP) state where one triplet is localized in the D moiety and the other is localized in the A moiety. In the coherent tunneling regime, where all SF intermediates are off(quasi)-resonant to the initial and final states, the SF rate is given by $k_{SF} = |V_{SF}|^2 \rho_{FC}$, where V_{SF} is the bridge-mediated effective SF coupling between initial (D singlet) and final (D-A CTP) states, and ρ_{FC} is the Franck-Condon factor. Therefore, the efficiency of D-A CTP creation can be tuned by controlling V_{SF} through structural modifications of the bridge. To this end it is necessary to obtain structure-function relationships for the bridge-mediated SF pathways that contribute to V_{SF}.

The electronic Hamiltonian operator of the system is given by $\hat{H}^{el} = \hat{h}^{1e} + \hat{V}^{2e}$, where $\hat{h}^{1e} = \sum_{I=1}^{N} \frac{\hat{p}_I^2}{2m_{el}} - \sum_{I}^{N} \sum_{n}^{N_{nuc}} \frac{1}{4\pi\varepsilon_0} \frac{Z_n e^2}{|\vec{r}_I - \vec{R}_n|}$ is the Hamiltonian for N independent electrons in the field of N_{nuc} atomic nuclei, and $\hat{V}^{2e} = \frac{1}{2} \sum_{I \neq J}^{N} \sum_{J=1}^{N} \frac{1}{4\pi\varepsilon_0} \frac{e^2}{|\vec{r}_I - \vec{r}_J|}$ is the total electron-electron Coulombic operator. In our modelling, we use a D, B, A fragment-orbital basis set to describe many-electron states for the D-B-A system. [32-34] This is a natural representation since any approach to the design of SF molecular assemblies is necessarily fragment-based. We construct the many-electron basis to represent $\hat{H}^{el}$ using the Configuration Interaction

method with single and double excitations (CISD). [35,36] The active space consists of six electrons (out of N) in six fragment orbitals. For the applications considered below, the active orbitals are taken to be the frontier orbitals of each fragment (HOMO and LUMO denoted as $H_D, L_D, H_B, L_B, H_A, L_A$). The use of frontier orbitals is common in SF studies. [1-3,19,23,28,30] Our method does not depend on the particular choice of fragment-orbital basis and is not limited to two active orbitals per fragment (see Supplement section 5.4.5).

In the first step of the SF process both the initial and final states are singlets, so we consider only singlet states as SF intermediates. For this active space and using the branching diagram method we derive analytically 40 singlet spin-spatial eigenstates $\left|\Psi_n\right\rangle^{SA}$ (SA denotes Spin-Adapted) that include single and double inter- and intra-fragment excitationsd (see the discussion in section 5.4.1 of the Supplement). [37-39] We use this set and the Slater-Condon rules [35,36] to obtain analytical expressions for all Hamiltonian matrix elements between these states, $H^{el}_{n,m} = {}^{SA}\left\langle \Psi_n \left| \hat{H}^{el} \right| \Psi_m \right\rangle^{SA}$ (see Supplement section 5.4.2).

The singly-excited basis states can be categorized as locally-excited (LE) and charge-transfer (CT). LE states have an excited electron and a hole on the same fragment (intra-fragment excitation). An example is the bridge exciton (BE) with an electron-hole (e-h) pair in the B fragment (see Fig. 5.1). For CT states the excited electron is on a different fragment than the hole (inter-fragment e-h excitation). An example is the D-A excitonic state (DAE) with an inter-fragment e-h excitation among the D, A fragments. The doubly-excited (DE) states include many more excitation combinations. We denote locally doubly-excited states (LDE) those that contain two intra-fragment excitons (each exciton is localized within D, B or A). In addition to locally doubly-excited (LDE) there are CT doubly-excited states (CTDE) that combine a CT and a LE exciton, e.g., $\left|D^{+-}B^{-}A^{+}\right\rangle^{SA}$ (see Fig. 5.1). The LDE and CTDE include both correlated triplet-pair and correlated singlet-pair states (CTP and CSP, respectively). [3,15,40,41]

In general, the basis-state energies are functions of ionization potentials, electron affinities, core terms, Coulomb and exchange two-electron (2e) integrals, i.e.,

$$ {}^{SA}\left\langle \Psi_n \left| \hat{H}^{el} \right| \Psi_n \right\rangle^{SA} = E_n\left(\left\{IP^i\right\},\ \left\{EA^i\right\},\ \left\{\left\langle L_i \left| \hat{V}^{e-n_j} \right| L_i \right\rangle\right\},\ \left\{\left\langle H_i \left| \hat{V}^{e-n_j} \right| H_i \right\rangle\right\},\ \left\{J_{P_iQ_j}\right\},\ \left\{K_{P_iQ_j}\right\}\right)\cdot \quad (5.1)$$

(see Supplement section 5.4.2 for analytical expressions). The off-diagonal matrix elements are functions of one-electron (1e) Fock matrix elements, overlap matrix elements and 2e integrals,

$$ {}^{SA}\langle \Psi_n | \hat{H}^{el} | \Psi_m \rangle^{SA} = H_{n,m}\left(\left\{ \langle P_i | \hat{F} | Q_j \rangle \right\},\ \left\{ \left(P_i\, Q_j \middle| R_i\, Z_j \right) \right\},\ \left\{ S_{P_i Q_j} \right\},\ \left\{ J_{P_i Q_j} \right\},\ \left\{ K_{P_i Q_j} \right\} \right) \quad (5.2) $$

where $P, Q, R, Z = H, L$ and $i, j = D, B, A$ (see Supplement section 5.4.2).

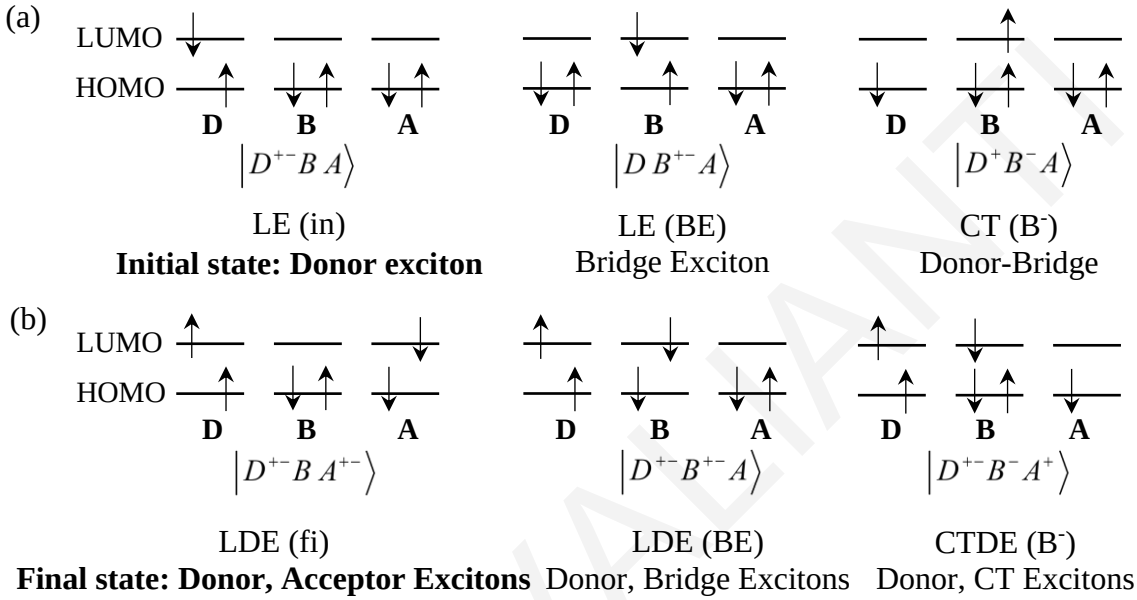

Figure 5.1 Schematic illustration of the notation used to describe the many-electron basis states relevant to the SF pathways. (a) Examples of singly-excited (LE and CT) and (b) doubly-excited (LDE and CTDE) states using the minimum set of orbitals per fragment (HOMO and LUMO). The kets denote Slater determinants with the spin distributions shown in the diagrams. The actual basis states used in the calculations (Table 5.1 and Supplement section 5.4.1), are spin-adapted (singlet) states that are linear combinations of Slater determinants.

Table 5.1 describes the nomenclature and notation used to group the basis states. The table contains the most important groups for the discussion that follows. The first column shows the group names and the second the mathematical notation for the states. The third column gives approximate expressions for the excitation energies within each group (with respect to the DBA ground state). The approximate expressions are derived from the exact equations in the Supplement section 5.4.2 using ab-initio computations on reference systems to determine small terms that can be ignored (see below). These approximate energies are written in terms of the fragment variables x (X), y (Y) and z which are separately defined for the D-B fragment or A-B fragment,

$$X \equiv x - J_{H_{D(A)}L_{D(A)}} + 2K_{H_{D(A)}L_{D(A)}}\ ,\ \ Y \equiv y - J_{H_BL_B} + 2K_{H_BL_B}\ ,\ z = IP^{D(A)} - IP^B \tag{5.3}$$

where

$$x = IP^{D(A)} - EA^{D(A)},\ y = IP^B - EA^B. \tag{5.4}$$

IP denotes ionization potential and EA denotes electron affinity. The variables X and Y are the HOMO – to – LUMO exciton energies of the isolated D(A) and B fragments and are functions of x (y) and intra-molecular (intra-fragment) Coulomb (J) and exchange (K) integrals. We choose to write the basis-state excitation energies in terms of these variables because values for these variables are easily obtainable from experiments or computations on the fragments. The state energies in Table 5.1 are also functions of inter-fragment Coulomb and exchange integrals (denoted as inter).

Group Name	**Hole and Electron distribution notation**	**Approximate excitation energy**
LE (in)	$\left\|D^{+-}BA\right\rangle^{SA}$	X
LDE_{CTP} (fi)	$\left\|D^{+-}BA^{+-}\right\rangle_{CTP}^{SA}$	$2X - 2K_{H_DL_D} - 2K_{H_AL_A}$
LDE_{CTP} (BE)	$\left\|D^{+-}B^{+-}A\right\rangle_{CTP}^{SA}, \left\|DB^{+-}A^{+-}\right\rangle_{CTP}^{SA}$	$X + Y - 2K_{H_{D(A)}L_{D(A)}} - 2K_{H_BL_B}$
LE (BE)	$\left\|DB^{+-}A\right\rangle^{SA}$	Y
CT (B^+)	$\left\|D^-B^+A\right\rangle^{SA}, \left\|DB^+A^-\right\rangle^{SA}$	$X - z + J_{H_{D(A)}L_{D(A)}} - 2K_{H_{D(A)}L_{D(A)}} + J^{inter}_{H_BL_{D(A)}} - 2J^{inter}_{H_BH_D} - 2J^{inter}_{H_BH_A}$
CT (B^-)	$\left\|D^+B^-A\right\rangle^{SA}, \left\|DB^-A^+\right\rangle^{SA}$	$Y + z + J_{H_BL_B} - 2K_{H_BL_B} + J^{inter}_{H_{D(A)}L_B} + 2J^{inter}_{H_{A(D)}L_B} - 2J^{inter}_{H_{D(A)}H_B}$
CT (DAE)	$\left\|D^-BA^+\right\rangle^{SA}, \left\|D^+BA^-\right\rangle^{SA}$	$X + J_{H_{D(A)}L_{D(A)}} - 2K_{H_{D(A)}L_{D(A)}} + 2J^{inter}_{H_BL_{D(A)}} - 2J^{inter}_{H_{A(D)}H_B}$

Table 5.1 Approximate excitation energies of the lowest-lying basis states of the D-B-A system. 1st column: Names of the different groups of the most important singlet basis states

for the D-B-A system. CTP (CSP) denotes Correlated-Triplet-Pair (Correlated-Singlet-Pair). 2nd column: Mathematical notation for the spin-adapted states in each group. 3rd column: Approximate excitation energies of the lowest-lying states of the D-B-A system (derived from the exact expressions in Table 5.4) as a function of the X, Y, z parameters (see text and Fig. 5.2) and 2e integrals. The first two groups refer to the initial and final CTP states, denoted as (in) and (fi) respectively. In most remaining cases the grouping is according to the B state, such as B^+, B^- and bridge excitonic (BE) state.

The excitation energies will depend on the type of solvent the D-B-A system is in. In particular, the energies of states with CT excitations are most sensitive to the solvent dielectric constant. Since we have not included an effective dielectric constant in the analytical expressions, the following analysis is more relevant to non-polar solvents. In Fig. 5.2 we describe three different energetic regimes defined by the x, y and z values for the D-B fragment. We label these regimes as type-I, type-II and type-III. [42]

5.2 Results and Discussion

In the following we consider the situation where initial photo-excitation of D-B-A creates a D-localized singlet exciton that can be approximated by $|in\rangle \approx |D^{+-}BA\rangle^{SA}$ (first row in Table 5.1). The coherent SF process should lead to a final state that is approximated by the D-A CTP state $|fi\rangle \approx |D^{+-}BA^{+-}\rangle^{SA}_{CTP}$ (second row of Table 5.1). All other intermediate states (third-to-final rows of Tables 5.1 and 5.4) are off-resonant to $|in\rangle$ and to $|fi\rangle$ such that SF takes place by tunneling when the initial and final states come to resonance at an energy E_{res} (the SF rate being $k_{SF} = |V_{SF}|^2 \rho_{FC}$). The aim of our analysis is to understand how the V_{SF} is tuned by the identities of the D, B and A fragments and by their relative geometries.

To make contact with realistic systems, we use some reference D-B-A groups (Fig. 5.3) where the D and A moieties are taken to be pentacenes in a face-to-face geometry and B is either pentacene (in pi-stacking or non-pi stacking conformation), tetracene (in non-pi-stacking conformation) or the non-conjugated 1,3-diethynyladamantyl spacer (NC1 in ref. [12]). Pentacene has been studied extensively both experimentally and computationally as an individual (monomer) and as part of a larger system (dimer, trimer etc.) for the study of various SF mechanisms. [10-13,21,26] Although the systems considered below are symmetric

(D=A), the method is general and applicable to non-symmetric systems (see Supplement section 5.4.5).

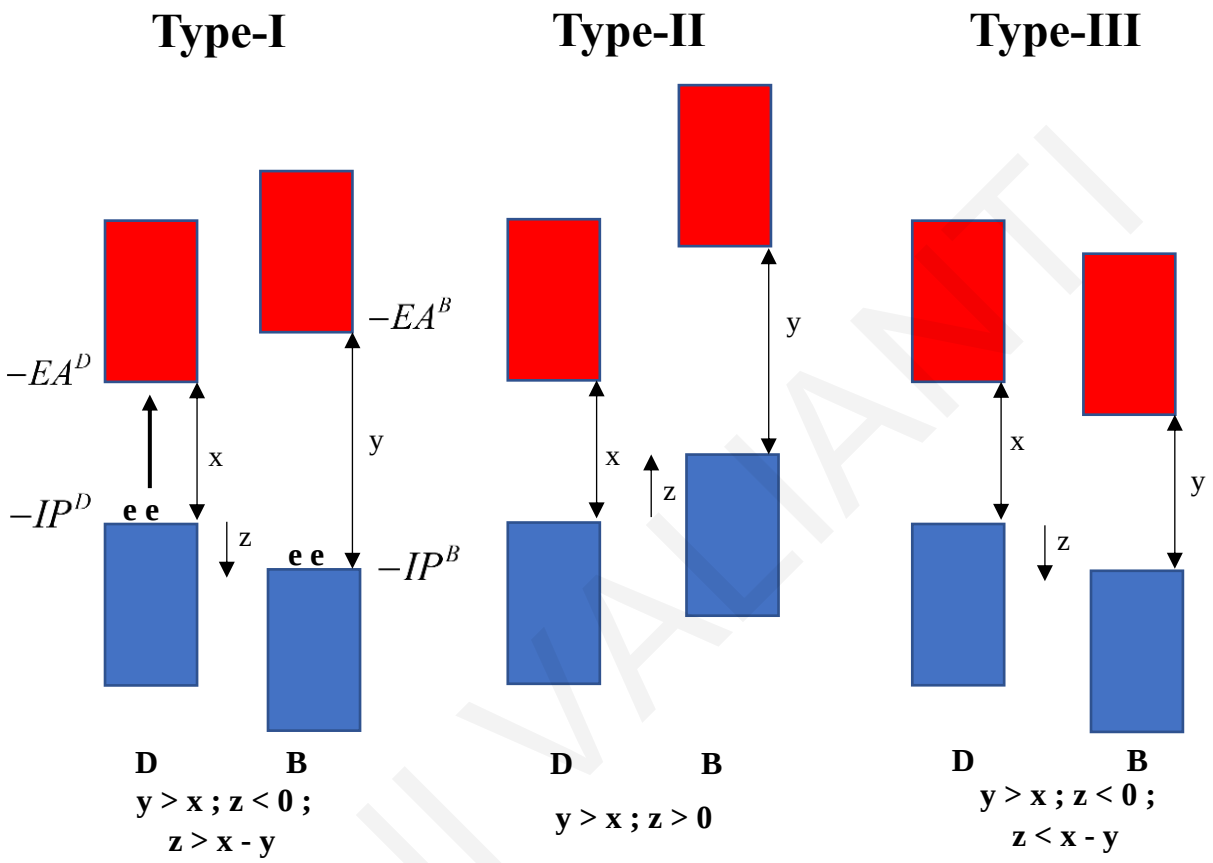

Figure 5.2 Schematic representation of type-I, type-II and type-III D-B regimes in the independent-electron approximation. Virtual orbitals are shown in red and occupied orbitals in blue. Since we only consider bridge-mediated tunneling case, $y > x$.

For these reference systems, we use the GAMESS-US [43-45] program in the fragment-orbital representation (6-31G(d) basis set) to compute the reference values for the 1e and 2e variables in the analytical expressions of the diagonal and off-diagonal elements of the CISD Hamiltonian (eqs (5.1) and (5.2), and discussion in 5.4.2 section). These variables include IPs, EAs, core terms, Fock and overlap matrix elements, Coulomb and exchange integrals. The computed 1e and 2e variables set reference values for x, y and z (thus for X, Y) in eqs (5.3) and (5.4). Following this step, for each reference system, we vary y and z while keeping all other 1e and 2e parameters and x fixed to the reference values.

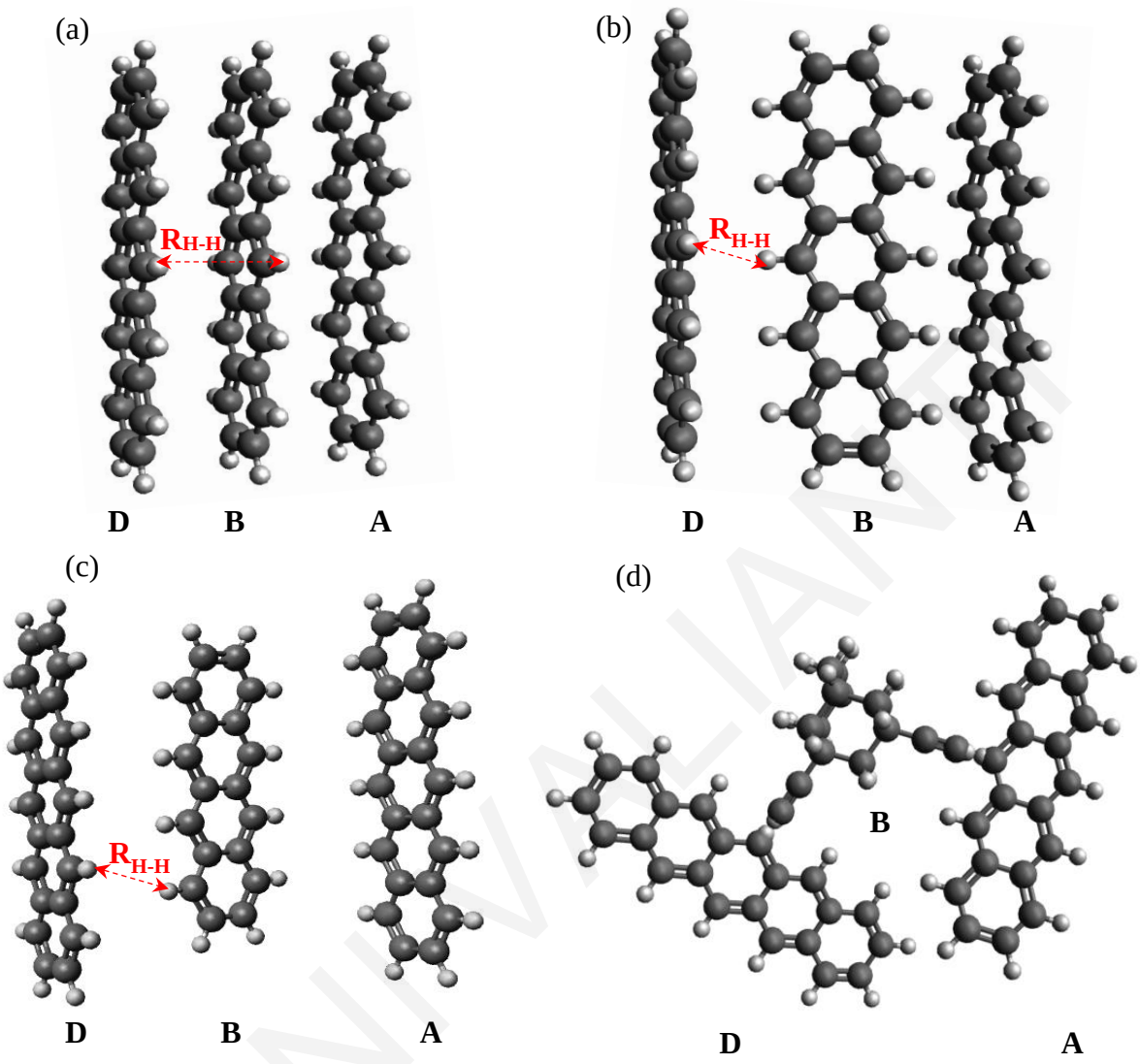

Figure 5.3 Reference D-B-A systems. (a) Pi-stacking pentacene trimer, (b) non-pi-stacking pentacene trimer, (c) pentacene-tetracene-pentacene trimer, (d) NC1 system of ref. [12]. For (a)-(c) $R_{H\text{-}H} \approx 3.5$ Å.

This process mimics a transformation of the B structure, with respect to the reference one, via a variation of the IP^B and EA^B (while keeping D and A parameters fixed). An alternative point of view is that we are varying the B fragment exciton energy with respect to the D-fragment exciton energy (Y with respect to X). We explore how such transformations alter V_{SF} and the SF pathways for the fully-coupled D-B-A system in the tunneling regime. V_{SF} is computed by exact diagonalization of the full Hamiltonian (40 states, with the exact matrix elements), setting both initial and final state-energies equal to the resonance (tunneling) energy $E_{res} = \left(E_{in} + E_{fi}\right)/2$ (Fig. 5.5 and Supplement section 5.4.3). Pathway contributions to V_{SF} are obtained by Green's function methods and by deleting intermediate states in the

Hamiltonian and computing the effect on V_{SF} (Supplement section 5.4.3). [46-49] Thus, the V_{SF} plots in Fig. 5.4 are exact, involving diagonalization, whereas the dominant pathway structures in Fig. 5.5 are approximate interpretations of the exact results.

Figure 5.4 shows contour plots of $ln\left|V_{SF}\left(Y/X\,,\,z/X\right)\right|$ for the reference systems of Fig. 5.3, where X is fixed to the D(A) pentacene value. Figures 5.4a, 5.4b, 5.4c, 5.4d relate to the reference systems 5.3a, 5.3b, 5.3c, 5.3d, respectively. The circles in the plots correspond to the coupling values for the computed Y and z of the reference systems. The labels (i), (ii), (iii) and (iv) refer to the pathway structures contributing to the SF couplings (see following discussion).

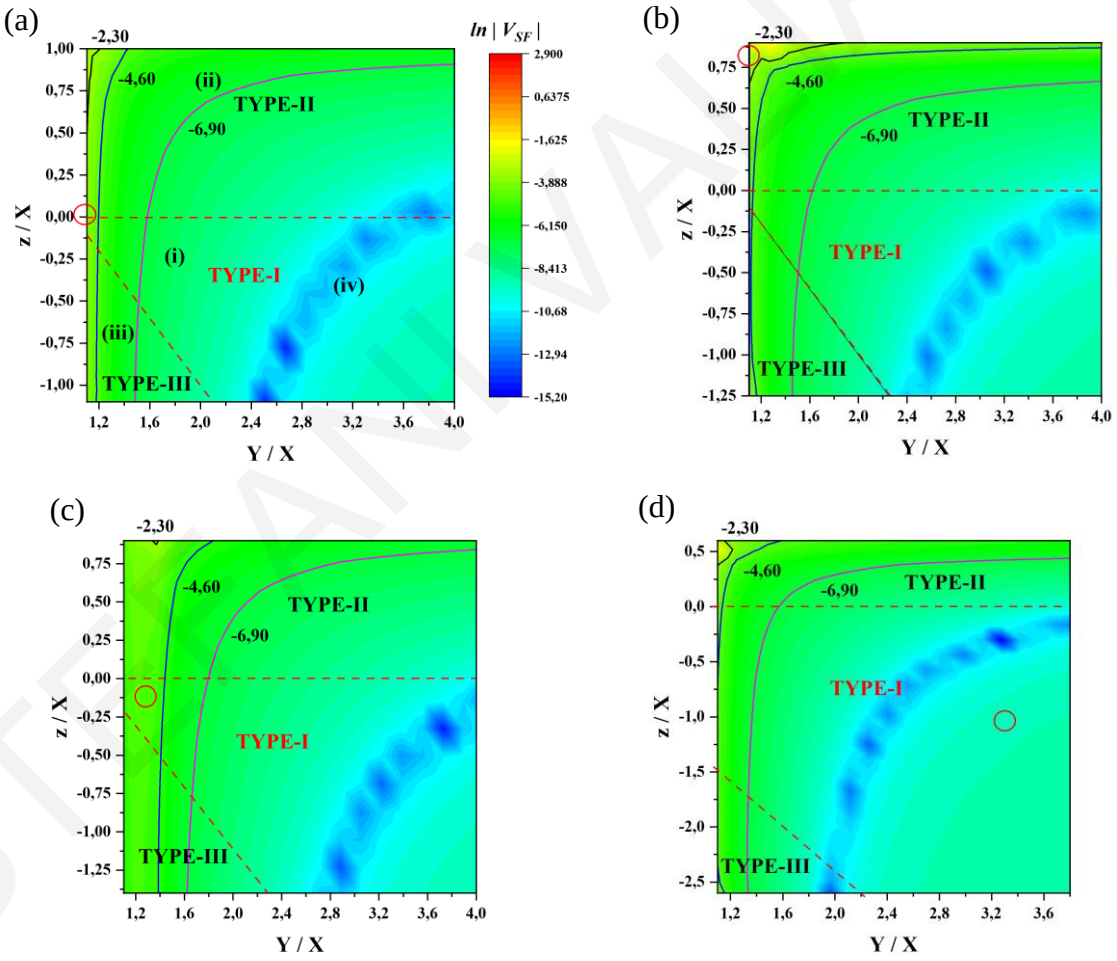

Figure 5.4 $ln\left|V_{SF}\right|$ plot as a function of Y/X and z/X parameters for (a) pi-stacking conformation shown in Fig. 5.3a, (b) the non-pi-stacking conformation shown in Fig. 5.3b, (c) the pentacene-tetracene-pentacene molecular system of Fig. 5.3c and (d) the NC1 molecular system of Fig. 5.3d. The dashed lines outline the three regimes defined in Fig. 5.2.

The black contour corresponds to a coupling $|V_{SF}| = 10^{-1} eV$, the blue to $|V_{SF}| = 10^{-2} eV$ and the magenta lines to $|V_{SF}| = 10^{-3} eV$. The colormap scaling is the same for all plots. The circles represent the Y/X, z/X and V_{SF} values of the reference systems in Fig. 5.3. The labels (i) to (iv) refer to the pathway structures discussed in the text.

The above contour plots for the SF coupling variation relating to the different system types (and to the different reference systems) have similar generic features. $|V_{SF}|$ increases as $Y \to X$ ($Y > X$), i.e., as quasi-resonance between the initial (final) state and the BE states is approached from off-resonance (quasi-resonance corresponds to the leftmost side of contour plots). The maximum $|V_{SF}|$ value for all types (I-III) is $|V_{SF}| \sim 10^{-1} eV$ ($ln|V_{SF}| \sim -2.3$). For the type-I case the maximum coupling is only due to the BE-character states because these are the closest in energy to the initial and final states. The dominant type-I pathway structure is (i): $LE(in) \overset{V_{2e}}{\leftrightarrow} LE(BE) \overset{V_{2e}}{\leftrightarrow} LDE_{CTP}(BE) \overset{V_{2e}}{\leftrightarrow} LDE_{CTP}(fi)$ and it is mediated by purely 2e interactions, i.e., $V_{2e} = \langle \Psi_n | \hat{V}^{2e} | \Psi_m \rangle$. In contrast, the maximum coupling region for type-II or type-III involves CT (B^+) or (B^-) excitons, respectively, in addition to the above-mentioned BE states. These D(A)-B CT states have lower energies as compared to the type-I case, and approach the energies of the BE-character states. Thus, the dominant pathway structure for type-II is (ii): $LE(in) \overset{V_{1e}}{\leftrightarrow} CT(B^+) \overset{V_{1e}}{\leftrightarrow} LE(BE) \overset{V_{2e}}{\leftrightarrow} LDE_{CTP}(BE) \overset{V_{2e}}{\leftrightarrow} LDE_{CTP}(fi)$ and for type-III is (iii): $LE(in) \overset{V_{1e}}{\leftrightarrow} CT(B^-) \overset{V_{1e}}{\leftrightarrow} LE(BE) \overset{V_{2e}}{\leftrightarrow} LDE_{CTP}(BE) \overset{V_{2e}}{\leftrightarrow} LDE_{CTP}(fi)$. Both pathways involve 2e and 1e interactions ($V_{1e} = \langle \Psi_n | \hat{h}^{1e} | \Psi_m \rangle$). These pathway structures relate to symmetric D-B-A systems (D=A) and to non-polar solvents. Polar solvents would lower CT-state energies.

The three pathway structures are largely preserved as Y increases with respect to X, i.e. moving from the quasi-resonant to the off-resonant regime (from the left to the right side of the contour plots). The Y/X increase implies an increase in the energies of the BE-character states, thus a weakening of the $|V_{SF}|$ magnitude for all the system types. In the deep-tunneling regime ($Y/X \gg 1.0$, rightmost side of contour plots), the relative contribution from the high-energy BE-character states is reduced and D-A CT excitons (DAE) become important. For example, for the NC1 reference structure, $|V_{SF}| \sim 10^{-4} eV$ (red circle in type-I region of Fig.

5.4d). This value is consistent with the results from Basel *et al.* [12] who studied this molecular system using CASSCF calculations on a 4e4o active space with D(A)-centered orbitals (XMCQDPT/DZV level of theory). Our computations, which also include bridge-centered states, show that the dominant pathway structure is (iv): $LE(in) \overset{V_{1e}}{\leftrightarrow} CT(B^+) \overset{V_{1e}}{\leftrightarrow} CT(DAE) \overset{V_{2e}}{\leftrightarrow} LDE_{CTP}(BE) \overset{V_{2e}}{\leftrightarrow} LDE_{CTP}(fi)$. D-A CT excitons have the lowest energies and are major contributors to $|V_{SF}|$. The lowest-coupling blue region in the deep-tunneling regime arises from destructive pathway interferences.

Below, we show schematic representations of the most important states (energies) and the corresponding inter-state coupling topology for the different types of systems discussed above. We find that the CT doubly-excited states (CTDE in Fig. 5.1) and all the CSP states (included in the full-Hamiltonian computations) do not contribute significantly to V_{SF} due to their high energies.

(a)

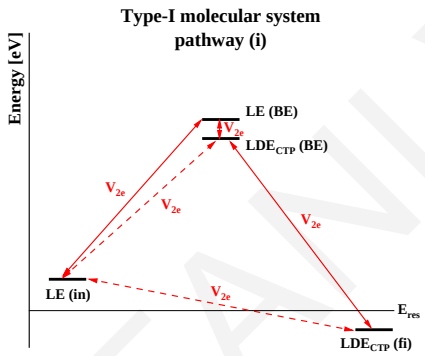

(b)

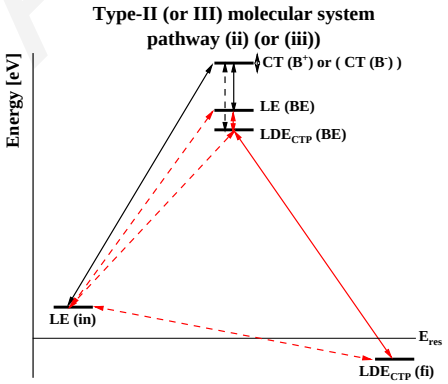

(c)

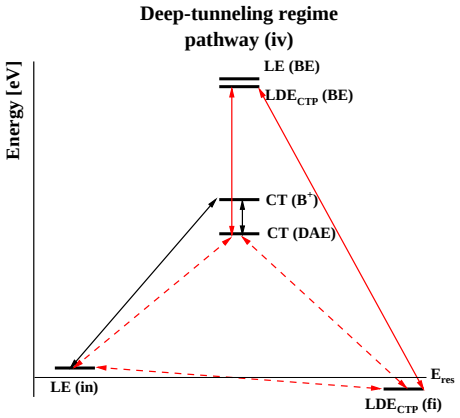

Figure 5.5 Schematic representation of the energies and the couplings structure of the intermediate states of Table 5.1, for (a) the type-I, (b) the type-II (or -III) energetic regime and (c) the deep-tunneling case with $Y/X \gg 1.0$. V_{2e} (red arrows) denotes coupling dominated by 2e matrix elements, $V_{2e} = \langle \Psi_n | \hat{V}^{2e} | \Psi_m \rangle$, and V_{1e} (black arrows) denotes coupling dominated by 1e matrix elements, $V_{1e} = \langle \Psi_n | \hat{h}^{1e} | \Psi_m \rangle$. The weaker matrix elements are represented by dotted lines and $E_{res} = \left(E_{in} + E_{fi} \right) / 2$. These dominant pathway structures relate to symmetric D-B-A systems for which (D=A) and to non-polar solvents.

5.3 Conclusions

In summary, for each system type considered here and for symmetric D-B-A systems, we identified the dominant bridge-mediated SF pathways and the corresponding SF intermediates (Fig. 5.5). We find that all system types can give similar magnitudes for the SF coupling even though the underlying pathway structures differ. An important conclusion is that for all system types the bridge can enhance V_{SF} through the CTP states $\left| D^{+-} B^{+-} A \right\rangle_{CTP}$ $\left(\left| D B^{+-} A^{+-} \right\rangle_{CTP} \right)$ and the single-exciton state $\left| D B^{+-} A \right\rangle$. For type-II and type-III systems, D(A)-B CT states $\left| D^{-} B^{+} A \right\rangle$ $\left(\left| D B^{+} A^{-} \right\rangle \right)$ or $\left| D^{+} B^{-} A \right\rangle$ $\left(\left| D B^{-} A^{+} \right\rangle \right)$ also contribute significantly to V_{SF}. Explicit expressions for all these intermediate states are given in the Supplement section 5.4.1. We also find that the differences between the $ln|V_{SF}|$ contour plots in Fig. 5.4 are mainly due to differences in intermediate-state energies rather than the inter-state couplings V_{1e} and V_{2e} shown in Fig. 5.5 (see Supplement section 5.4.4). However, molecular motions and disorder could modulate the inter-state couplings such that the pathways contributing to the ensemble-averaged $\sqrt{\langle V_{SF}^2 \rangle}$ may show some differences as compared to the static V_{SF}.

Nevertheless, the bridge-tuning of V_{SF} is most sensitive to energy differences between the above-mentioned intermediate states and the initial $|in\rangle = \left| D^{+-} BA \right\rangle$ (given that the final state $\left| D^{+-} BA^{+-} \right\rangle_{CTP}$ has lower energy than the initial). We have shown analytically that these energy differences, $\Delta E_{\Psi} = E_{|\Psi\rangle} - E_{|in\rangle}$, can be approximated in terms of D(A) and B fragment exciton energies X and Y, a few intra-fragment and inter-fragment Coulomb and exchange

integrals and differences in fragment *IPs*, $z = IP^B - IP^D$ (Table 5.1). These variables are easily computed using fragment calculations. Some of them, such as *IPs* and fragment singlet-exciton energies (X and Y), can be approximated from experiments on the fragments.

Figures 5.5a and 5.5b show that the bi-excitonic CTP states $\left|D^{+-}B^{+-}A\right\rangle_{CTP}$ $\left(\left|D\,B^{+-}A^{+-}\right\rangle_{CTP}\right)$, whose equations are given in Table 5.4, are "bottleneck" states for V_{SF} for all system types, in the sense that they are the only intermediates that are strongly coupled to the fission product $\left|D^{+-}BA^{+-}\right\rangle_{CTP}$. Therefore, an approximate approach to bridge-tuning of V_{SF} is to modulate the energies of the "bottleneck" intermediates and their couplings to the final SF state. From Table 5.1 we conclude that rough estimates of these energies (for the systems under study in the off-resonant regime), are given by the sums of the energies of the D(A) and B fragment triplet excitons (exact energies are shown in Table 5.4),

$$\begin{aligned} E_{(D^{+-}B^{+-}A)_{CTP}} &\approx \left(X - 2K_{H_DL_D}\right) + \left(Y - 2K_{H_BL_B}\right) \approx E^{tripl}_{D^{+-}} + E^{tripl}_{B^{+-}} \\ E_{(D\,B^{+-}A^{+-})_{CTP}} &\approx \left(X - 2K_{H_AL_A}\right) + \left(Y - 2K_{H_BL_B}\right) \approx E^{tripl}_{A^{+-}} + E^{tripl}_{B^{+-}} \end{aligned} \tag{5.5}$$

The couplings to the final SF state are simple exchange integrals that are easy to compute,

$$\begin{aligned} {}^{SA}_{CTP}\left\langle D^{+-}B^{+-}A\middle|\hat{H}^{el}\middle|D^{+-}B\,A^{+-}\right\rangle^{SA}_{CTP} &= \sqrt{3/2}\left(L_AL_B\middle|H_AH_B\right) \\ {}^{SA}_{CTP}\left\langle D\,B^{+-}A^{+-}\middle|\hat{H}^{el}\middle|D^{+-}B\,A^{+-}\right\rangle^{SA}_{CTP} &= \sqrt{3/2}\left(L_DL_B\middle|H_DH_B\right) \end{aligned} \tag{5.6}$$

(we find maximum values of 0.1 eV). The "bottleneck" intermediates are accessed from the initial $\left|D^{+-}B\,A\right\rangle^{SA}$ state through different pathways, depending on the system type. For type-I, they are mainly accessed through the LE (BE) state $\left|D\,B^{+-}A\right\rangle^{SA}$ via 2e interactions that involve pairs of exchange integrals. For type-II and -III the "bottleneck" states are mainly accessed from the initial state via BE and D-B CT states (II: $\left|D^{-}\,B^{+}A\right\rangle^{SA}$, III: $\left|D^{+}\,B^{-}A\right\rangle^{SA}$) with pathways that involve both 1e and 2e interactions (Supplement section 5.4.2).

The concept of "bottleneck" states sheds light on the bridge-resonance effect in SF. The systems studied in refs [25,26] are type-I (Fig. 5.5a). The D(A) and B HOMO LUMO gaps in our notation are x and y. Lowering the B HOMO-LUMO gap corresponds to $y \to x$ ($Y/X \to 1$), leading to an enhancement of the SF coupling (moving towards the leftmost side

of the contour plots in Fig. 5.4). As $y \to x$ the "bottleneck"-state energy is reduced due to lowering of the bridge triplet-exciton energy (eq. (5.5) and Table 5.1).

In conclusion the semi-analytical approach is a useful tool to derive, interpret and predict structure-function relationships and electronic pathways for bridge-mediated SF rates. It can also be used to guide searches of candidate D-B-A systems given target SF coupling magnitudes. These candidate systems may then be studied at a higher level of quantum chemical theory and tested by experiment.

5.4 Supplement

Derivation of the many-electron spin-adapted basis set using the branching diagram method in the context of CISD method and D, B, A HOMO/LUMO orbitals. Derivation of the many-electron DBA Hamiltonian matrix elements using the above basis set. Description of SF effective coupling computation using exact diagonalization of the Hamiltonian and SF coupling pathways. Analysis of the relative importance of intermediate-state energies as compared to inter-state couplings in determining the SF effective coupling. Discussion of the generality of the method (non-frontier-orbital basis, non-symmetric D-B-A systems, fragment excitations that involve more than one pair of electron and hole orbitals).

5.4.1 Many-electron Spin-adapted States

In the first step of the SF process both the initial and final states are singlets, so we consider only singlet states as intermediates for this step (within the CISD formalism, these include single and double excitations). The many-electron states we use describe the D, B or A localization of the excited electron (e) and the hole (h), and are eigenstates of the total spin. They can be represented by linear combinations of singly- and doubly-excited $N-$ electron determinants.

The spin eigenfunctions are constructed via the branching diagram method (using the Yamanouchi-Kotani functions). [37-39] For N $s = 1/2$ spins we construct eigenfunctions of $\hat{S}_N^2$, $\hat{S}_{z,N}$ (with quantum numbers S_N and M_S, respectively). For a given quantum number S_N there are different groups of such eigenfunctions, each group containing $2S_N + 1$ $\hat{S}_{z,N}$ eigenfunctions. Given a value of S_N, the number of such groups for N spins is

$f\left(N,S_N\right)=\begin{pmatrix} N \\ \frac{1}{2}N-S_N \end{pmatrix}-\begin{pmatrix} N \\ \frac{1}{2}N-S_N-1 \end{pmatrix}$. We denote the eigenfunctions of $\hat{S}_N^2$ and $\hat{S}_{z,N}$ belonging to the k^{th} group by $X\left(k\right)\equiv X\left(N,S_N,M_S;k\right)$. The construction of the eigenfunctions in each group is done iteratively. Given the $X\left(N-1,S_{N-1},M_{S_{N-1}};k\right)$ eigenfunctions we obtain new eigenfunctions corresponding to either $S_N=S_{N-1}+1/2$ or $S_N=S_{N-1}-1/2$ by adding or subtracting the spin of the N^{th} electron, respectively. [37,38]

The spin-spatial state with a prespecified occupation of spatial orbitals, is constructed by first multiplying a $X\left(k\right)$ by a product of the prespecified spatial orbitals, $\Psi(A,B,...,\Omega)=\psi_A\left(1\right)\psi_B\left(2\right)...\psi_\Omega\left(N\right)$. The $\psi's$ are one-electron (1e) orbitals and $A,B,...,\Omega$ are the orbital labels (e.g., H_D for the HOMO of the Donor fragment, L_A for the LUMO of Acceptor fragment, etc.). Thus, the spin-spatial antisymmetric wavefunctions can be written in a multi-determinant form as $\left|\Psi\left(A,B,...,\Omega\right);X\left(k\right)\right\rangle^{SA}=\hat{A}_N\Psi\left(A,B,...,\Omega\right)X\left(k\right)$ where $\hat{A}_N$ is the antisymmetrization operator. [15,35] $\left|...\right\rangle^{SA}$ denotes a "Spin-Adapted" state that most often involves a linear combination of Slater determinants of 1e spin orbitals (denoted simply by $\left|...\right\rangle$).

Since we consider only singlet states, we will not use a total-spin label in our notation. For our active space we can create $f\left(N=4,S_N=0\right)=2$ groups of spin eigenfunctions of $\hat{S}_N^2$ that describe the possible states of the system. Below in Table 5.2, are shown some examples of the most important singly-excited states (LE and CT) used in SF pathways. Some of these states are illustrated in Fig. 5.1 of the main text. $\left|\Psi_a^r\right\rangle$ denotes a singly-excited determinant in which an electron, which occupied spin-orbital χ_a in the Hartree-Fock (HF) ground state of the D-B-A $N-$ electron system $\left|\Psi_{0,N}\right\rangle$, has been promoted to a virtual spin-orbital χ_r. In such determinants, χ_a (or a) is used to denote spin-orbital with spin up and $\bar{\chi}_a$ (or $\bar{a}$) spin-orbital with spin down. [35,50] The superscript "+" ("-") denotes hole (electron).

h-e distribution notation	Expression
$\left\vert D^{+-}BA\right\rangle^{SA}$	$\frac{1}{\sqrt{2}}\left(\left\vert \Psi_{H_D}^{L_D}\right\rangle+\left\vert \Psi_{\bar{H}_D}^{\bar{L}_D}\right\rangle\right)$
$\left\vert DB^{+-}A\right\rangle^{SA}$	$\frac{1}{\sqrt{2}}\left(\left\vert \Psi_{H_B}^{L_B}\right\rangle+\left\vert \Psi_{\bar{H}_B}^{\bar{L}_B}\right\rangle\right)$
$\left\vert D^{+}B^{-}A\right\rangle^{SA}$	$\frac{1}{\sqrt{2}}\left(\left\vert \Psi_{H_D}^{L_B}\right\rangle+\left\vert \Psi_{\bar{H}_D}^{\bar{L}_B}\right\rangle\right)$
$\left\vert D^{-}B^{+}A\right\rangle^{SA}$	$\frac{1}{\sqrt{2}}\left(\left\vert \Psi_{H_B}^{L_D}\right\rangle+\left\vert \Psi_{\bar{H}_B}^{\bar{L}_D}\right\rangle\right)$
$\left\vert D^{+}BA^{-}\right\rangle^{SA}$	$\frac{1}{\sqrt{2}}\left(\left\vert \Psi_{H_D}^{L_A}\right\rangle+\left\vert \Psi_{\bar{H}_D}^{\bar{L}_A}\right\rangle\right)$

Table 5.2 The most important singly-excited spin-adapted (SA) singlet states used as a basis to represent the D-B-A many-electron Hamiltonian. 1st column: Mathematical notation for the spin-adapted many-electron basis states. 2nd column: Spin-spatial multi-electronic states as linear combinations of singly-excited Slater determinants.

The doubly-excited (DE) states include many more excitation combinations. In these cases, using the branching diagram method, we can construct correlated triplet-pair DE states (denoted by CTP) and correlated singlet-pair DE states (denoted by CSP). Below in Table 5.3, we give some examples of the most important CTP and CSP doubly-excited states (LDE and CTDE). [3,15,40,41] $\left\vert \Psi_{a,b}^{r,p}\right\rangle$ denotes doubly-excited determinants.

h-e distribution notation	Expression
$\left\vert D^{+-}BA^{+-}\right\rangle_{CTP}^{SA}$	$\sqrt{\frac{1}{3}}\left(\left\vert \Psi_{\bar{H}_D H_A}^{\bar{L}_A L_D}\right\rangle+\left\vert \Psi_{H_D \bar{H}_A}^{L_A \bar{L}_D}\right\rangle-\frac{1}{2}\left(\begin{array}{l}\left\vert \Psi_{\bar{H}_D \bar{H}_A}^{\bar{L}_D \bar{L}_A}\right\rangle-\left\vert \Psi_{H_D \bar{H}_A}^{L_D \bar{L}_A}\right\rangle \\ -\left\vert \Psi_{\bar{H}_D H_A}^{\bar{L}_D L_A}\right\rangle+\left\vert \Psi_{H_D H_A}^{L_D L_A}\right\rangle\end{array}\right)\right)$
$\left\vert D^{+-}BA^{+-}\right\rangle_{CSP}$	$\frac{1}{2}\left(\left\vert \Psi_{\bar{H}_D \bar{H}_A}^{\bar{L}_D \bar{L}_A}\right\rangle+\left\vert \Psi_{H_D \bar{H}_A}^{L_D \bar{L}_A}\right\rangle+\left\vert \Psi_{\bar{H}_D H_A}^{\bar{L}_D L_A}\right\rangle+\left\vert \Psi_{H_D H_A}^{L_D L_A}\right\rangle\right)$
$\left\vert D^{+-}B^{+-}A\right\rangle_{CTP}^{SA}$	$\sqrt{\frac{1}{3}}\left(\left\vert \Psi_{\bar{H}_D H_B}^{\bar{L}_B L_D}\right\rangle+\left\vert \Psi_{H_D \bar{H}_B}^{L_B \bar{L}_D}\right\rangle-\frac{1}{2}\left(\begin{array}{l}\left\vert \Psi_{\bar{H}_D \bar{H}_B}^{\bar{L}_D \bar{L}_B}\right\rangle-\left\vert \Psi_{H_D \bar{H}_B}^{L_D \bar{L}_B}\right\rangle \\ -\left\vert \Psi_{\bar{H}_D H_B}^{\bar{L}_D L_A}\right\rangle+\left\vert \Psi_{H_D H_B}^{L_D L_B}\right\rangle\end{array}\right)\right)$

$\left\vert D^{+-}B^{+-}A\right\rangle_{CSP}$	$\frac{1}{2}\left(\left\vert \Psi^{\bar{L}_D\,\bar{L}_B}_{\bar{H}_D\,\bar{H}_B}\right\rangle+\left\vert \Psi^{L_D\,\bar{L}_B}_{H_D\,\bar{H}_B}\right\rangle+\left\vert \Psi^{\bar{L}_D\,L_B}_{\bar{H}_D\,H_B}\right\rangle+\left\vert \Psi^{L_D\,L_B}_{H_D\,H_B}\right\rangle\right)$
$\left\vert DB^{+-}A^{+-}\right\rangle^{SA}_{CTP}$	$\sqrt{\frac{1}{3}}\left(\left\vert \Psi^{\bar{L}_B\,L_A}_{\bar{H}_A\,H_B}\right\rangle+\left\vert \Psi^{L_B\,\bar{L}_A}_{H_A\,\bar{H}_B}\right\rangle-\frac{1}{2}\left(\begin{matrix}\left\vert \Psi^{\bar{L}_A\,\bar{L}_B}_{\bar{H}_A\,\bar{H}_B}\right\rangle-\left\vert \Psi^{L_A\,\bar{L}_B}_{H_A\,\bar{H}_B}\right\rangle\\ -\left\vert \Psi^{\bar{L}_A\,L_A}_{\bar{H}_A\,H_B}\right\rangle+\left\vert \Psi^{L_A\,L_B}_{H_A\,H_B}\right\rangle\end{matrix}\right)\right)$
$\left\vert DB^{+-}A^{+-}\right\rangle^{SA}_{CSP}$	$\frac{1}{2}\left(\left\vert \Psi^{\bar{L}_A\,\bar{L}_B}_{\bar{H}_A\,\bar{H}_B}\right\rangle+\left\vert \Psi^{L_A\,\bar{L}_B}_{H_A\,\bar{H}_B}\right\rangle+\left\vert \Psi^{\bar{L}_A\,L_B}_{\bar{H}_A\,H_B}\right\rangle+\left\vert \Psi^{L_A\,L_B}_{H_A\,H_B}\right\rangle\right)$
$\left\vert D^{-}B^{+}A^{+-}\right\rangle^{SA}_{CTP}$	$\sqrt{\frac{1}{3}}\left(\left\vert \Psi^{\bar{L}_D\,L_A}_{\bar{H}_B\,H_D}\right\rangle+\left\vert \Psi^{L_D\,\bar{L}_A}_{H_B\,\bar{H}_D}\right\rangle-\frac{1}{2}\left(\begin{matrix}\left\vert \Psi^{\bar{L}_A\,\bar{L}_D}_{\bar{H}_B\,\bar{H}_D}\right\rangle-\left\vert \Psi^{L_A\,\bar{L}_D}_{H_B\,\bar{H}_D}\right\rangle\\ -\left\vert \Psi^{\bar{L}_A\,L_D}_{\bar{H}_B\,H_D}\right\rangle+\left\vert \Psi^{L_A\,L_D}_{H_B\,H_D}\right\rangle\end{matrix}\right)\right)$
$\left\vert D^{-}B^{+}A^{+-}\right\rangle^{SA}_{CSP}$	$\frac{1}{2}\left(\left\vert \Psi^{\bar{L}_A\,\bar{L}_D}_{\bar{H}_B\,\bar{H}_D}\right\rangle+\left\vert \Psi^{L_A\,\bar{L}_D}_{H_B\,\bar{H}_D}\right\rangle+\left\vert \Psi^{\bar{L}_A\,L_D}_{\bar{H}_B\,H_D}\right\rangle+\left\vert \Psi^{L_A\,L_D}_{H_B\,H_D}\right\rangle\right)$
$\left\vert D^{-}B^{+-}A^{+}\right\rangle_{CTP}$	$\sqrt{\frac{1}{3}}\left(\left\vert \Psi^{\bar{L}_D\,L_B}_{\bar{H}_A\,H_{D(A)}}\right\rangle+\left\vert \Psi^{L_D\,\bar{L}_B}_{H_A\,\bar{H}_{D(A)}}\right\rangle-\frac{1}{2}\left(\begin{matrix}\left\vert \Psi^{\bar{L}_B\,\bar{L}_D}_{\bar{H}_A\,\bar{H}_D}\right\rangle-\left\vert \Psi^{L_B\,\bar{L}_D}_{H_A\,\bar{H}_D}\right\rangle\\ -\left\vert \Psi^{\bar{L}_B\,L_D}_{\bar{H}_A\,H_D}\right\rangle+\left\vert \Psi^{L_B\,L_D}_{H_A\,H_D}\right\rangle\end{matrix}\right)\right)$
$\left\vert D^{-}B^{+-}A^{+}\right\rangle_{CSP}$	$\frac{1}{2}\left(\left\vert \Psi^{\bar{L}_B\,\bar{L}_D}_{\bar{H}_A\,\bar{H}_D}\right\rangle+\left\vert \Psi^{L_B\,\bar{L}_D}_{H_A\,\bar{H}_D}\right\rangle+\left\vert \Psi^{\bar{L}_B\,L_D}_{\bar{H}_A\,H_D}\right\rangle+\left\vert \Psi^{L_B\,L_D}_{H_A\,H_D}\right\rangle\right)$

Table 5.3 Examples of doubly-excited spin-adapted (SA) states used as a basis to represent the D-B-A Hamiltonian. 1st column: Mathematical notation for the spin-adapted many-electron basis states. 2nd column: Spin-spatial multi-electronic states as linear combinations of doubly-excited Slater determinants (CTP: correlated Triplet-Pair; CSP: correlated Singlet-Pair).

5.4.2 Hamiltonian Matrix Elements

Diagonal Matrix Elements

In the table below, we give exact expressions for the diagonal elements ${}^{SA}\left\langle \Psi_n\left\vert \hat{H}^{el}\right\vert \Psi_n\right\rangle^{SA}$ of the Hamiltonian $\hat{H}^{el}=\hat{h}^{1e}+\hat{V}^{2e}$. Each element is given as a function of ionization potentials (IP), electron affinities (EA), core terms, Coulomb and exchange integrals, calculated using the Slater-Cordon rules in the above-mentioned basis of states. [35,51]

In our computations we use these exact expressions to compute the Hamiltonian for the reference systems and for the coupling plots. In particular, we compute the 1e and 2e contributions in each equation of Table 5.4 using the GAMESS-US [43-45] program in the

fragment-orbital representation. The section 5.2 presents approximate expressions for the lowest-lying states (Table 5.1). The validity of each approximate expression is verified from the ab-initio computations of the different contributions in the exact expressions shown in Table 5.4.

In the equations of Table 5.4, $\hat{V}_{e-n_k}$ denote Coulombic attractive interactions between the electrons and the k^{th} fragment nuclei (part of the core term in the Hamiltonian). $J_{P_i Q_j}$ and $K_{P_i Q_j}$ are Coulomb and exchange 2e integrals involving the ψ_{P_i} and ψ_{Q_j} fragment molecular orbitals (MOs), where $P,Q = H,L$ and $i,j = D,B,A$, [35]

$$J_{P_i Q_j} \equiv \left(P_i\, P_i \middle| Q_j\, Q_j\right) = \int d^3\vec{r}_1\; d^3\vec{r}_2\; \psi^*_{P_i}\left(\vec{r}_1\right) \psi_{P_i}\left(\vec{r}_1\right) r^{-1}{}_{12}\; \psi^*_{Q_j}\left(\vec{r}_2\right) \psi_{Q_j}\left(\vec{r}_2\right), \qquad (5.7)$$

$$K_{P_i Q_j} \equiv \left(P_i\, Q_j \middle| Q_j P_i\right) = \int d^3\vec{r}_1\; d^3\vec{r}_2\; \psi^*_{P_i}\left(\vec{r}_1\right) \psi_{Q_j}\left(\vec{r}_1\right) r^{-1}{}_{12}\; \psi^*_{Q_j}\left(\vec{r}_2\right) \psi_{P_i}\left(\vec{r}_2\right). \qquad (5.8)$$

State	**char.**	$^{SA}\left\langle \Psi_n \middle\| \hat{H}^{el} \middle\| \Psi_n \right\rangle^{SA}$
Singly - Excited States		
$\left\| D^{+-} B\, A \right\rangle^{SA}$	LE (in)	$IP^D - EA^D - J_{H_D L_D} + 2K_{H_D L_D}$ $+\left\langle L_D \middle\| \hat{V}_{e-n_A} \middle\| L_D \right\rangle + \left\langle L_D \middle\| \hat{V}_{e-n_B} \middle\| L_D \right\rangle - \left\langle H_D \middle\| \hat{V}_{e-n_A} \middle\| H_D \right\rangle - \left\langle H_D \middle\| \hat{V}_{e-n_B} \middle\| H_D \right\rangle$ $+2J_{H_A L_D} + 2J_{H_B L_D} - 2J_{H_D H_A} - 2J_{H_D H_B}$ $-K_{H_A L_D} - K_{H_B L_D} + K_{H_D H_A} + K_{H_D H_B}$
$\left\| D^{+} B^{-} A \right\rangle^{SA}$	CT (B^-)	$IP^D - EA^B$ $+\left\langle L_B \middle\| \hat{V}_{e-n_D} \middle\| L_B \right\rangle + \left\langle L_B \middle\| \hat{V}_{e-n_A} \middle\| L_B \right\rangle - \left\langle H_D \middle\| \hat{V}_{e-n_A} \middle\| H_D \right\rangle - \left\langle H_D \middle\| \hat{V}_{e-n_B} \middle\| H_D \right\rangle$ $+J_{H_D L_B} + 2J_{H_A L_B} - 2J_{H_D H_B} - 2J_{H_D H_A}$ $+K_{H_D L_B} - K_{H_A L_B} + K_{H_D H_B} + K_{H_D H_A}$
$\left\| D^{-} B^{+} A \right\rangle^{SA}$	CT (B^+)	$IP^B - EA^D$ $+\left\langle L_D \middle\| \hat{V}_{e-n_B} \middle\| L_D \right\rangle + \left\langle L_D \middle\| \hat{V}_{e-n_A} \middle\| L_D \right\rangle - \left\langle H_B \middle\| \hat{V}_{e-n_A} \middle\| H_B \right\rangle - \left\langle H_B \middle\| \hat{V}_{e-n_D} \middle\| H_B \right\rangle$ $+J_{H_B L_D} + 2J_{H_A L_D} - 2J_{H_D H_B} - 2J_{H_B H_A}$ $+K_{H_B L_D} - K_{H_A L_D} + K_{H_D H_B} + K_{H_B H_A}$

$\left\|D^{-}BA^{+}\right\rangle^{SA}$	CT (DAE)	$IP^{A}-EA^{D}$ $+\left\langle L_D\left\|\hat{V}_{e-n_A}\right\|L_D\right\rangle+\left\langle L_D\left\|\hat{V}_{e-n_B}\right\|L_D\right\rangle-\left\langle H_A\left\|\hat{V}_{e-n_B}\right\|H_A\right\rangle-\left\langle H_A\left\|\hat{V}_{e-n_D}\right\|H_A\right\rangle$ $+J_{H_AL_D}+2J_{H_BL_D}-2J_{H_DH_A}-2J_{H_BH_A}$ $+K_{H_AL_D}-K_{H_BL_D}+K_{H_DH_A}+K_{H_BH_A}$
$\left\|D^{+}BA^{-}\right\rangle^{SA}$	CT (DAE)	$IP^{D}-EA^{A}$ $+\left\langle L_A\left\|\hat{V}_{e-n_D}\right\|L_A\right\rangle+\left\langle L_A\left\|\hat{V}_{e-n_B}\right\|L_A\right\rangle-\left\langle H_D\left\|\hat{V}_{e-n_B}\right\|H_D\right\rangle-\left\langle H_D\left\|\hat{V}_{e-n_A}\right\|H_D\right\rangle$ $+J_{H_DL_A}+2J_{H_BL_A}-2J_{H_DH_A}-2J_{H_DH_B}$ $+K_{H_DL_A}-K_{H_BL_A}+K_{H_DH_A}+K_{H_DH_B}$
$\left\|DB^{+-}A\right\rangle^{SA}$	LE (BE)	$IP^{B}-EA^{B}-J_{H_BL_B}+2K_{H_BL_B}$ $+\left\langle L_B\left\|\hat{V}_{e-n_A}\right\|L_B\right\rangle+\left\langle L_B\left\|\hat{V}_{e-n_D}\right\|L_B\right\rangle-\left\langle H_B\left\|\hat{V}_{e-n_A}\right\|H_B\right\rangle-\left\langle H_B\left\|\hat{V}_{e-n_D}\right\|H_B\right\rangle$ $+2J_{H_AL_B}+2J_{H_DL_B}-2J_{H_BH_A}-2J_{H_DH_B}$ $-K_{H_AL_B}-K_{H_DL_B}+K_{H_BH_A}+K_{H_DH_B}$
$\left\|DB^{+}A^{-}\right\rangle^{SA}$	CT (B^{+})	$IP^{B}-EA^{A}$ $+\left\langle L_A\left\|\hat{V}_{e-n_B}\right\|L_A\right\rangle+\left\langle L_A\left\|\hat{V}_{e-n_D}\right\|L_A\right\rangle-\left\langle H_B\left\|\hat{V}_{e-n_D}\right\|H_B\right\rangle-\left\langle H_B\left\|\hat{V}_{e-n_A}\right\|H_B\right\rangle$ $+J_{H_BL_A}+2J_{H_DL_A}-2J_{H_BH_A}-2J_{H_DH_B}$ $+K_{H_BL_A}-K_{H_DL_A}+K_{H_BH_A}+K_{H_DH_B}$
$\left\|DB^{-}A^{+}\right\rangle^{SA}$	CT (B^{-})	$IP^{A}-EA^{B}$ $+\left\langle L_B\left\|\hat{V}_{e-n_A}\right\|L_B\right\rangle+\left\langle L_B\left\|\hat{V}_{e-n_D}\right\|L_B\right\rangle-\left\langle H_A\left\|\hat{V}_{e-n_D}\right\|H_A\right\rangle-\left\langle H_A\left\|\hat{V}_{e-n_B}\right\|H_A\right\rangle$ $+J_{H_AL_B}+2J_{H_DL_B}-2J_{H_BH_A}-2J_{H_DH_A}$ $+K_{H_AL_B}-K_{H_DL_B}+K_{H_BH_A}+K_{H_DH_A}$
Doubly – Excited States (DE)		
$\left\|D^{+-}BA^{+-}\right\rangle_{CTP}^{SA}$	LDE_{CTP} (fi)	$IP^{D}+IP^{A}-EA^{D}-EA^{A}-J_{H_DL_D}-J_{H_AL_A}$ $+\left\langle L_D\left\|\hat{V}_{e-n_A}\right\|L_D\right\rangle+\left\langle L_D\left\|\hat{V}_{e-n_B}\right\|L_D\right\rangle+\left\langle L_A\left\|\hat{V}_{e-n_D}\right\|L_A\right\rangle+\left\langle L_A\left\|\hat{V}_{e-n_B}\right\|L_A\right\rangle$ $-\left\langle H_A\left\|\hat{V}_{e-n_D}\right\|H_A\right\rangle-\left\langle H_A\left\|\hat{V}_{e-n_B}\right\|H_A\right\rangle-\left\langle H_D\left\|\hat{V}_{e-n_A}\right\|H_D\right\rangle-\left\langle H_D\left\|\hat{V}_{e-n_B}\right\|H_D\right\rangle$ $-3J_{H_DH_A}-2J_{H_DH_B}-2J_{H_BH_A}+J_{L_DL_A}+J_{H_DL_A}+2J_{H_BL_A}+J_{H_AL_D}+2J_{H_BL_D}$ $+\frac{5}{2}K_{H_DH_A}+K_{H_DH_B}+K_{H_BH_A}+\frac{1}{2}K_{L_DL_A}+\frac{1}{2}K_{H_DL_A}-K_{H_BL_A}+\frac{1}{2}K_{H_AL_D}-K_{H_BL_D}$

$\left\|D^{+}B^{-}A^{+-}\right\rangle_{CTP}^{SA}$	$CTDE_{CTP}$ (B^{-})	$IP^{D}+IP^{A}-EA^{B}-EA^{A}-J_{H_AL_A}$ $+\left\langle L_B\left\|\hat{V}_{e-n_D}\right\|L_B\right\rangle+\left\langle L_B\left\|\hat{V}_{e-n_A}\right\|L_B\right\rangle+\left\langle L_A\left\|\hat{V}_{e-n_D}\right\|L_A\right\rangle+\left\langle L_A\left\|\hat{V}_{e-n_B}\right\|L_A\right\rangle$ $-\left\langle H_A\left\|\hat{V}_{e-n_D}\right\|H_A\right\rangle-\left\langle H_A\left\|\hat{V}_{e-n_B}\right\|H_A\right\rangle-\left\langle H_D\left\|\hat{V}_{e-n_A}\right\|H_D\right\rangle-\left\langle H_D\left\|\hat{V}_{e-n_B}\right\|H_D\right\rangle$ $-3J_{H_DH_A}-2J_{H_DH_B}-2J_{H_BH_A}+J_{L_BL_A}+J_{H_DL_B}+J_{H_AL_B}+J_{H_DL_A}+2J_{H_BL_A}$ $+\frac{5}{2}K_{H_DH_A}+K_{H_DH_B}+K_{H_BH_A}+\frac{1}{2}K_{L_BL_A}-K_{H_DL_B}+\frac{1}{2}K_{H_AL_B}+\frac{1}{2}K_{H_DL_A}-K_{H_BL_A}$
$\left\|D^{+-}B^{-}A^{+}\right\rangle_{CTP}^{SA}$	$CTDE_{CTP}$ (B^{-})	$IP^{D}+IP^{A}-EA^{B}-EA^{D}-J_{H_DL_D}$ $+\left\langle L_B\left\|\hat{V}_{e-n_D}\right\|L_B\right\rangle+\left\langle L_B\left\|\hat{V}_{e-n_A}\right\|L_B\right\rangle+\left\langle L_D\left\|\hat{V}_{e-n_A}\right\|L_D\right\rangle+\left\langle L_D\left\|\hat{V}_{e-n_B}\right\|L_D\right\rangle$ $-\left\langle H_D\left\|\hat{V}_{e-n_A}\right\|H_D\right\rangle-\left\langle H_D\left\|\hat{V}_{e-n_B}\right\|H_D\right\rangle-\left\langle H_A\left\|\hat{V}_{e-n_D}\right\|H_A\right\rangle-\left\langle H_A\left\|\hat{V}_{e-n_B}\right\|H_A\right\rangle$ $-3J_{H_DH_A}-2J_{H_BH_A}-2J_{H_DH_B}+J_{L_DL_B}+J_{H_AL_B}+J_{H_DL_B}+J_{H_AL_D}+2J_{H_BL_D}$ $+\frac{5}{2}K_{H_DH_A}+K_{H_BH_A}+K_{H_DH_B}+\frac{1}{2}K_{L_DL_B}-K_{H_AL_B}+\frac{1}{2}K_{H_DL_B}+\frac{1}{2}K_{H_AL_D}-K_{H_BL_D}$
$\left\|D^{+-}B^{+}A^{-}\right\rangle_{CTP}^{SA}$	$CTDE_{CTP}$ (B^{+})	$IP^{D}+IP^{B}-EA^{D}-EA^{A}-J_{H_DL_D}$ $+\left\langle L_D\left\|\hat{V}_{e-n_A}\right\|L_D\right\rangle+\left\langle L_D\left\|\hat{V}_{e-n_B}\right\|L_D\right\rangle+\left\langle L_A\left\|\hat{V}_{e-n_D}\right\|L_A\right\rangle+\left\langle L_A\left\|\hat{V}_{e-n_B}\right\|L_A\right\rangle$ $-\left\langle H_D\left\|\hat{V}_{e-n_A}\right\|H_D\right\rangle-\left\langle H_D\left\|\hat{V}_{e-n_B}\right\|H_D\right\rangle-\left\langle H_B\left\|\hat{V}_{e-n_D}\right\|H_B\right\rangle-\left\langle H_B\left\|\hat{V}_{e-n_A}\right\|H_B\right\rangle$ $-3J_{H_DH_B}-2J_{H_DH_A}-2J_{H_BH_A}+J_{L_DL_A}+J_{H_BL_D}+2J_{H_AL_D}+J_{H_DL_A}+J_{H_BL_A}$ $+\frac{5}{2}K_{H_DH_B}+K_{H_DH_A}+K_{H_BH_A}+\frac{1}{2}K_{L_DL_A}+\frac{1}{2}K_{H_BL_D}-K_{H_AL_D}+\frac{1}{2}K_{H_DL_A}-K_{H_BL_A}$
$\left\|D^{-}B^{+}A^{+-}\right\rangle_{CTP}^{SA}$	$CTDE_{CTP}$ (B^{+})	$IP^{A}+IP^{B}-EA^{A}-EA^{D}-J_{H_AL_A}$ $+\left\langle L_A\left\|\hat{V}_{e-n_D}\right\|L_A\right\rangle+\left\langle L_A\left\|\hat{V}_{e-n_B}\right\|L_A\right\rangle+\left\langle L_D\left\|\hat{V}_{e-n_A}\right\|L_D\right\rangle+\left\langle L_D\left\|\hat{V}_{e-n_B}\right\|L_D\right\rangle$ $-\left\langle H_A\left\|\hat{V}_{e-n_D}\right\|H_A\right\rangle-\left\langle H_A\left\|\hat{V}_{e-n_B}\right\|H_A\right\rangle-\left\langle H_B\left\|\hat{V}_{e-n_D}\right\|H_B\right\rangle-\left\langle H_B\left\|\hat{V}_{e-n_A}\right\|H_B\right\rangle$ $-3J_{H_BH_A}-2J_{H_DH_A}-2J_{H_DH_B}+J_{L_DL_A}+J_{H_BL_A}+2J_{H_DL_A}+J_{H_AL_D}+J_{H_BL_D}$ $+\frac{5}{2}K_{H_BH_A}+K_{H_DH_A}+K_{H_DH_B}+\frac{1}{2}K_{L_DL_A}+\frac{1}{2}K_{H_BL_A}-K_{H_DL_A}+\frac{1}{2}K_{H_AL_D}-K_{H_BL_D}$
$\left\|D\,B^{+-}A^{+-}\right\rangle_{CTP}^{SA}$	LDE_{CTP} (BE)	$IP^{B}+IP^{A}-EA^{B}-EA^{A}-J_{H_BL_B}-J_{H_AL_A}$ $+\left\langle L_B\left\|\hat{V}_{e-n_A}\right\|L_B\right\rangle+\left\langle L_B\left\|\hat{V}_{e-n_D}\right\|L_B\right\rangle+\left\langle L_A\left\|\hat{V}_{e-n_D}\right\|L_A\right\rangle+\left\langle L_A\left\|\hat{V}_{e-n_B}\right\|L_A\right\rangle$ $-\left\langle H_A\left\|\hat{V}_{e-n_D}\right\|H_A\right\rangle-\left\langle H_A\left\|\hat{V}_{e-n_B}\right\|H_A\right\rangle-\left\langle H_B\left\|\hat{V}_{e-n_A}\right\|H_B\right\rangle-\left\langle H_B\left\|\hat{V}_{e-n_D}\right\|H_B\right\rangle$ $-3J_{H_BH_A}-2J_{H_DH_B}-2J_{H_DH_A}+J_{L_BL_A}+J_{H_BL_A}+2J_{H_DL_A}+J_{H_AL_B}+2J_{H_DL_B}$ $+\frac{5}{2}K_{H_BH_A}+K_{H_DH_B}+K_{H_DH_A}+\frac{1}{2}K_{L_BL_A}+\frac{1}{2}K_{H_BL_A}-K_{H_DL_A}+\frac{1}{2}K_{H_AL_B}-K_{H_DL_B}$

$\left\vert D^{-}B^{+-}A^{+}\right\rangle_{CTP}^{SA}$	$\mathrm{CTDE}_{\mathrm{CTP}}$ (BE)	$IP^{A}+IP^{B}-EA^{D}-EA^{B}-J_{H_BL_B}$ $+\left\langle L_B\left\vert \hat{V}_{e-n_D}\right\vert L_B\right\rangle+\left\langle L_B\left\vert \hat{V}_{e-n_A}\right\vert L_B\right\rangle+\left\langle L_D\left\vert \hat{V}_{e-n_A}\right\vert L_D\right\rangle+\left\langle L_D\left\vert \hat{V}_{e-n_B}\right\vert L_D\right\rangle$ $-\left\langle H_B\left\vert \hat{V}_{e-n_D}\right\vert H_B\right\rangle-\left\langle H_B\left\vert \hat{V}_{e-n_A}\right\vert H_B\right\rangle-\left\langle H_A\left\vert \hat{V}_{e-n_D}\right\vert H_A\right\rangle-\left\langle H_A\left\vert \hat{V}_{e-n_B}\right\vert H_A\right\rangle$ $-3J_{H_BH_A}-2J_{H_DH_B}-2J_{H_DH_A}+J_{L_DL_B}+J_{H_AL_B}+2J_{H_DL_B}+J_{H_BL_D}+J_{H_AL_D}$ $+\frac{5}{2}K_{H_BH_A}+K_{H_DH_B}+K_{H_DH_A}+\frac{1}{2}K_{L_DL_B}+\frac{1}{2}K_{H_AL_B}-K_{H_DL_B}+\frac{1}{2}K_{H_BL_D}-K_{H_AL_D}$
$\left\vert D^{+}B^{+-}A^{-}\right\rangle_{CTP}^{SA}$	$\mathrm{CTDE}_{\mathrm{CTP}}$ (BE)	$IP^{D}+IP^{B}-EA^{A}-EA^{B}-J_{H_BL_B}$ $+\left\langle L_B\left\vert \hat{V}_{e-n_D}\right\vert L_B\right\rangle+\left\langle L_B\left\vert \hat{V}_{e-n_A}\right\vert L_B\right\rangle+\left\langle L_A\left\vert \hat{V}_{e-n_D}\right\vert L_A\right\rangle+\left\langle L_A\left\vert \hat{V}_{e-n_B}\right\vert L_A\right\rangle$ $-\left\langle H_B\left\vert \hat{V}_{e-n_D}\right\vert H_B\right\rangle-\left\langle H_B\left\vert \hat{V}_{e-n_A}\right\vert H_B\right\rangle-\left\langle H_D\left\vert \hat{V}_{e-n_A}\right\vert H_D\right\rangle-\left\langle H_D\left\vert \hat{V}_{e-n_B}\right\vert H_D\right\rangle$ $-3J_{H_DH_B}-2J_{H_BH_A}-2J_{H_DH_A}+J_{L_BL_A}+J_{H_DL_B}+2J_{H_AL_B}+J_{H_BL_A}+J_{H_DL_A}$ $+\frac{5}{2}K_{H_DH_B}+K_{H_BH_A}+K_{H_DH_A}+\frac{1}{2}K_{L_BL_A}+\frac{1}{2}K_{H_DL_B}-K_{H_AL_B}+\frac{1}{2}K_{H_BL_A}-K_{H_DL_A}$

Table 5.4 Examples of analytical expressions for the basis-state energies (diagonal elements of the many-electron Hamiltonian). 1st column: Mathematical notation of the spin-adapted (SA) many-electron basis states. 2nd column: Names of the different groups of these states for the D-B-A system. 3rd column: Exact expressions for the excitation energies of these states for the D-B-A system as a function of ionization potentials, electron affinities, core terms and two-electron integrals.

Off-diagonal Matrix Elements

In the table below, we present some of the most important off-diagonal elements, among the above-mentioned spin-adapted states. As with the diagonal elements, the expressions are evaluated using ab-initio computations. In the equations below F_{P_i,Q_j} denote Fock matrix elements between the P_i and Q_j MOs. Also, for simplicity of presentation we do not include terms proportional to $S_{P_iQ_j}\left(P_i\neq Q_j\right)$. The off-diagonal elements of the overlap matrix between orbitals in different fragments are very close to zero ($S_{P_iQ_j}\approx 0$, $P_i\neq Q_j$).

Coupling Notation	**States Involved**	**Coupling expression**
V_{2e}	LE (in) –	$\sqrt{3/2}\left(\left(H_DL_A\vert H_DH_A\right)-\left(L_DL_A\vert H_AL_D\right)\right)$

	LDE_{CTP} (fi)	
V_{2e}	LE (in) – LE (BE)	$2\left(H_D L_D \middle\| H_B L_B\right) - \left(L_D L_B \middle\| H_D H_B\right)$
V_{2e}	LE (BE) – LDE_{CTP} (BE)	$\sqrt{3/2}\left(\left(H_B L_{D(A)} \middle\| H_{D(A)} H_B\right) - \left(L_{D(A)} L_B \middle\| H_{D(A)} L_B\right)\right)$
V_{2e}	LE (in) – LDE_{CTP} (BE)	$\sqrt{3/2}\left(\left(H_D L_B \middle\| H_D H_B\right) - \left(L_D L_B \middle\| H_B L_D\right)\right)$
-----	LE (BE) – LDE_{CTP} (fi)	-----
V_{2e}	LDE_{CTP} (BE) – LDE_{CTP} (fi)	$\sqrt{3/2}\left(L_{D(A)} L_B \middle\| H_{D(A)} H_B\right)$
V_{1e}	CT (B^+) – LE (in)	$-F_{H_D H_B} + 2\left(H_D L_D \middle\| H_B L_D\right) - \left(H_D H_B \middle\| L_D L_D\right)$
V_{1e}	CT (B^+) – LE (BE)	$F_{L_{D(A)} L_B} + 2\left(H_B L_B \middle\| H_B L_{D(A)}\right) - \left(L_{D(A)} L_B \middle\| H_B H_B\right)$
V_{1e}	CT (B^+) – LDE_{CTP} (BE)	$\frac{1}{\sqrt{2}}\begin{pmatrix} F_{H_{D(A)} L_B} + 2\left(H_{D(A)} H_B \middle\| H_B L_B\right) \\ -2\left(H_{D(A)} L_{D(A)} \middle\| L_{D(A)} L_B\right) + \left(H_{D(A)} L_B \middle\| L_{D(A)} L_{D(A)}\right) \end{pmatrix}$

-----	CT (B^+) – LDE_{CTP} (fi)	-----
V_{1e}	CT (B^-) – LE (in)	$F_{L_D L_B} + 2\left(H_D L_D \middle\| H_D L_B\right) - \left(L_D L_B \middle\| H_D H_D\right)$
V_{1e}	CT (B^-) – LE (BE)	$-F_{H_{D(A)} H_B} + 2\left(H_{D(A)} L_B \middle\| H_B L_B\right) - \left(H_{D(A)} H_B \middle\| L_B L_B\right)$
V_{1e}	CT (B^-) – LDE_{CTP} (BE)	$\frac{1}{\sqrt{2}}\begin{pmatrix} F_{H_B L_{D(A)}} + 2\left(H_B H_{D(A)} \middle\| H_{D(A)} L_{D(A)}\right) \\ -2\left(H_B L_B \middle\| L_{D(A)} L_B\right) + \left(H_B L_{D(A)} \middle\| L_B L_B\right) \end{pmatrix}$
-----	CT (B^-) – LDE_{CTP} (fi)	-----

Table 5.5 Analytical expressions for Hamiltonian matrix elements between spin-adapted states. 1st column: Coupling Notation, V_{1e} denotes coupling dominated by the 1e matrix element (Fock matrix element), while V_{2e} is a coupling dominated entirely by 2e matrix elements. 2nd column: notation of the states involved in the corresponding coupling. 3rd column: Exact expressions for the off-diagonal matrix elements as a function of Fock matrix elements and 2e integrals ignoring overlap off-diagonal matrix elements.

5.4.3 Effective Coupling Analysis

As mentioned in the main text, we explore the situation where the initial photo-excitation creates a D-localized singlet exciton that can be approximated by $|in\rangle \approx \left|D^{+-}BA\right\rangle^{SA}$ (first row in Table 5.1). The coherent SF process leads to a final state that is approximated by the D-A separated correlated triplet-pair $|fi\rangle \approx \left|D^{+-}BA^{+-}\right\rangle_{CTP}^{SA}$ (second row of Table 5.1). The

assumption of a D-localized $|in\rangle$ implies that all other intermediate states (third-to-final rows of Table 5.1) are off-resonant to $|in\rangle$ (and also to $|fi\rangle$, since it has lower energy than $|in\rangle$). We denote this regime of SF as the coherent tunneling regime. Singlet fission will take place when the initial and final states come to resonance at an energy E_{res}. Using standard projection methods, [46-48] we approximate the effective coupling for the SF process by

$$V_{SF} = \langle fi|\hat{H}^{el}\hat{G}^{(int)}(E_{res})\hat{H}^{el}|in\rangle = \sum_k \frac{\langle fi|\hat{H}^{el}|\tilde{\Psi}_k\rangle\langle\tilde{\Psi}_k|\hat{H}^{el}|in\rangle}{E_{res}+i\delta-\tilde{E}_k}. \quad (5.9)$$

In the equation above $E_{res} = (E_{in}+E_{fi})/2$ and

$$\hat{G}^{(int)}(E_{res}) = \left(E_{res}\,\hat{I}^{(int)} + i\delta - \hat{H}^{(int)}\right)^{-1} \quad (5.10)$$

is the Green's function operator for the exact Hamiltonian of the subspace of all intermediate states. That is, $\hat{H}^{(int)} = \hat{Q}^{(int)}\hat{H}^{el}\hat{Q}^{(int)}$, where $\hat{Q}^{(int)} = \hat{I} - (|in\rangle\langle in| + |fi\rangle\langle fi|)$. $\tilde{E}_k$ and $|\tilde{\Psi}_k\rangle$ are the eigenenergies and eigenstates of this Hamiltonian $\left(\hat{H}^{(int)}|\tilde{\Psi}_k\rangle = \tilde{E}_k|\tilde{\Psi}_k\rangle\right)$. The eigenstate expression for V_{SF} enables decomposing the SF coupling into channel contributions from each eigenstate. Using perturbation theory, V_{SF} can be further decomposed into sums of terms each of which can be interpreted as a SF pathway that contributes to the total SF coupling. Each pathway starts in $|in\rangle$, visits some of the intermediate states and ends in $|fi\rangle$. The validity of eq. (5.9) in approximating the effective SF coupling is checked via exact diagonalization performed by setting $E_{in} \to E_{res}$ and $E_{fi} \to E_{res}$. In the off-resonant tunneling regime exact diagonalization for resonant $|in\rangle$ and $|fi\rangle$ gives two eigenstates $|\Psi_{\pm}\rangle \approx \frac{1}{\sqrt{2}}(|in\rangle \pm |fi\rangle)$ with energy splitting between them $|E_+ - E_-| \approx 2|V_{SF}|$. As quasi-resonance is approached the two lowest eigenstates have main (equal) contributions from the initial and final states but there is more mixing with the other intermediate states (as compared to the off-resonance case).

We analyse the SF pathways for each set of V_{SF} plots by turning-off off-diagonal matrix elements in the Hamiltonian connecting a specific state with the rest, and observing how the effective coupling is affected. Specifically, we compute the ratio $\eta_{|\Psi_k\rangle}$ of V_{SF} when we turn-off the contribution of a specific intermediate state in the Hamiltonian matrix to the exact

V_{SF} value. The higher the ratio $\eta_{|\Psi_k\rangle}$, the greater the contribution of the particular intermediate state to the exact effective coupling. In addition to the above analysis we also derive pathways by doing a perturbative expansion of eqs (5.9) and (5.10) in powers of the off-diagonal matrix elements of the Hamiltonian and keeping the highest terms (strongest pathways).

5.4.4 Difference among Contour Plots

To explore the relative importance between intermediate-state energies as compared to inter-state couplings in determining the $|V_{SF}|$ values we focus on the cases of the pi-stacking and non-pi-stacking conformations as shown in the Figs 5.3a, 5.3b. We produce two different plots $\left|ln|V_{SF}|/|V'_{SF}|\right|$ and $\left|ln|V_{SF}|/|V''_{SF}|\right|$ as a function Y/X and z/X, where V_{SF} is the effective coupling for the non-pi-stacking conformation (as in the original Fig. 5.4b). V'_{SF} is the corresponding value if we replace only the off-diagonal elements of the non-pi-stacking system with the ones of the pi-stacking system and V''_{SF} is the value when we replace only the diagonal elements.

As can be seen from Fig. 5.6 the largest change in effective coupling comes from the diagonal Hamiltonian elements, as they can cause a change in effective coupling up to four orders of magnitude (OM). In the case of off-diagonal elements (inter-state couplings) the maximum change is limited to one OM. We find that the magnitudes of the V_{1e} and V_{2e} do not vary significantly among the reference structures of Fig. 5.3 (maximum percentage changes and average percentage for V_{1e} of the order of 40% and 16%, respectively, and for V_{2e} 33% and 15%, respectively). The maximum coupling magnitude is of the order of $0.1eV$.

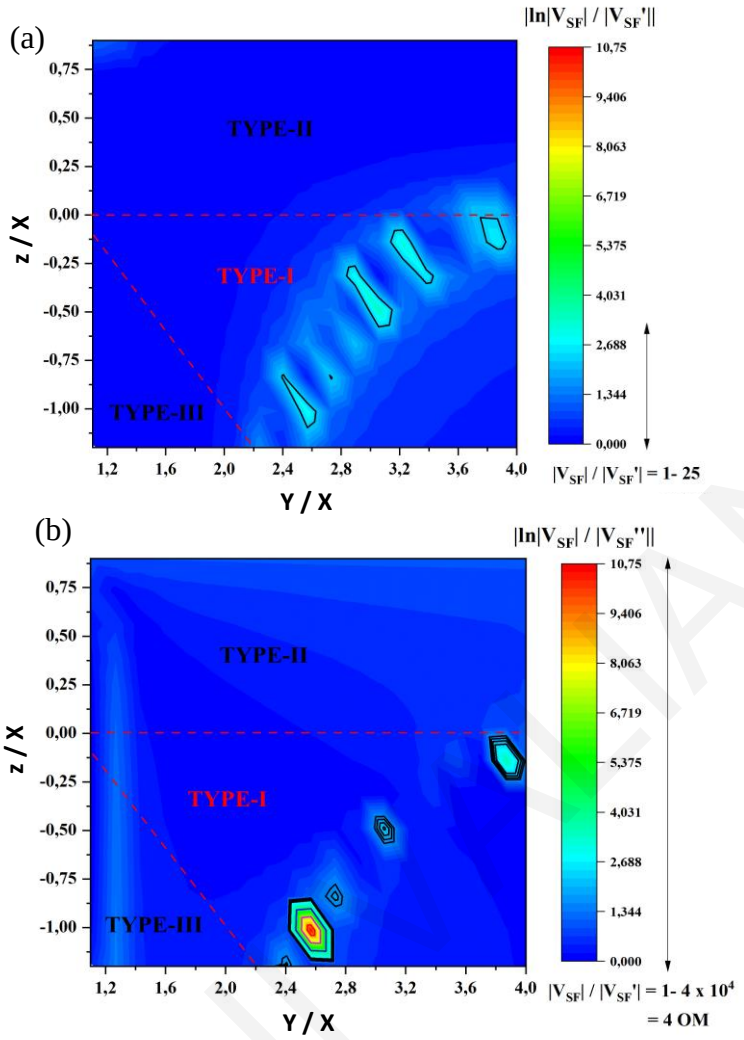

Figure 5.6 Difference contour plots. (a) $\left|ln|V_{SF}|/|V'_{SF}|\right|$ and (b) $\left|ln|V_{SF}|/|V''_{SF}|\right|$ as a function of Y/X and z/X. The dashed lines outline the three regimes defined in Fig. 5.2. The black contour corresponds to a coupling ratio equal to 10 which roughly corresponds to a difference of an order of magnitude (OM), the blue to 2 OM, magenta to 3 OM and red to 4 OM. The colormap scaling is the same for both plots.

5.4.5 Generality of the analytical model

In the Supplement sections 5.4.1 and 5.4.2, the analytical formulas for energies and couplings are presented in a fragment HOMO-LUMO basis because we want to correlate our analysis with *IPs* and *EAs* that are known for many molecules that may be used as potential fragments (and that are used as indicators of bridge-resonance in the experiments mentioned in text). However, the formulas presented in the Tables 5.2-5.5, from a

mathematical point of view, are general (i.e., not restricted to HOMO and LUMO fragment orbitals). We illustrate this with some examples for singly and doubly-excited states.

From Tables 5.2 and 5.3 consider the spin-adapted singly-excited states, $\left|D^{+-}BA\right\rangle^{SA}$ (intra-fragment excitation) and $\left|D^{+}B^{-}A\right\rangle^{SA}$ (inter-fragment excitation) and the spin-adapted doubly-excited state that is one of the bridge-mixed CTP states, which we find to be a "bottleneck" state, $\left|D^{+-}B^{+-}A\right\rangle_{CTP}^{SA}$. These formulas are valid even if the fragment hole and electron orbitals are not HOMO and LUMO. Namely, one just needs to replace in the equations H_F, L_F with O_F, V_F where O_F, V_F is an occupied and a virtual orbital, respectively, of fragment F ($F = D, B, A$),

$$\left|D^{+-}BA\right\rangle^{SA} = \frac{1}{\sqrt{2}}\left(\left|\Psi_{O_D}^{V_D}\right\rangle + \left|\Psi_{\bar{O}_D}^{\bar{V}_D}\right\rangle\right), \left|D^{+}B^{-}A\right\rangle^{SA} = \frac{1}{\sqrt{2}}\left(\left|\Psi_{O_D}^{V_B}\right\rangle + \left|\Psi_{\bar{O}_D}^{\bar{V}_B}\right\rangle\right) \ldots \qquad (5.11)$$

What these orbitals are is system-specific and should be deduced from experiment coupled with ab-initio computations on the system under study.

The corresponding energies and coupling expressions between diabatic states are also general. Again, for the fragment HOMO-LUMO basis some examples are given in Tables 5.4 and 5.5. In Table 5.4, we have written the energies in terms of fragment *IPs* and *EAs*. However, if we substitute the equations for each fragment *IP* and *EA* in these expressions, e.g., $IP^D = -\left\langle H_D\left|\hat{h}^{1e}\right|H_D\right\rangle - J_{H_DH_D}$, $EA^D = -\left\langle L_D\left|\hat{h}^{1e}\right|L_D\right\rangle - 2J_{H_DL_D} + K_{H_DL_D}$ etc., we get the energies of Table 5.4 as functions only of 1e and 2e matrix elements that are derivable from ab-initio computations. Having written these energies in terms of 1e and 2e matrix elements we only need to replace H_F, L_F with O_F, V_F to get the generalized expressions. For example, for the first state in eq. (5.11),

$$\begin{aligned} E_{\left|D^{+-}BA\right\rangle^{SA}} = {} & \left\langle V_D\left|\hat{h}^{1e}\right|V_D\right\rangle - \left\langle O_D\left|\hat{h}^{1e}\right|O_D\right\rangle - J_{O_DO_D} + J_{O_DV_D} + K_{O_DV_D} \\ & + \left\langle V_D\left|\hat{V}_{e-n_A}\right|V_D\right\rangle + \left\langle V_D\left|\hat{V}_{e-n_B}\right|V_D\right\rangle - \left\langle O_D\left|\hat{V}_{e-n_A}\right|O_D\right\rangle - \left\langle O_D\left|\hat{V}_{e-n_B}\right|O_D\right\rangle \\ & + 2J_{V_DO_A} + 2J_{V_DO_B} - 2J_{O_DO_A} - 2J_{O_DO_B} \\ & - K_{V_DO_A} - K_{V_DO_B} + K_{O_DO_A} + K_{O_DO_B} \end{aligned} \qquad (5.12)$$

For a CTP state involving fragment orbitals O_D, V_D and O_B, V_B,

$$
\begin{aligned}
E_{\left|D^{+-}B^{+-}A\right\rangle_{CTP}^{SA}} &= \langle V_D|\hat{h}^{1e}|V_D\rangle + \langle V_B|\hat{h}^{1e}|V_B\rangle - \langle O_D|\hat{h}^{1e}|O_D\rangle - \langle O_B|\hat{h}^{1e}|O_B\rangle \\
&- J_{O_BO_B} - J_{O_DO_D} + J_{O_BV_B} + J_{O_DV_D} - K_{O_DO_D} - K_{O_BV_B} \\
&+ \left\langle V_B\left|\hat{V}_{e-n_A}\right|V_B\right\rangle + \left\langle V_B\left|\hat{V}_{e-n_D}\right|V_B\right\rangle + \left\langle V_D\left|\hat{V}_{e-n_A}\right|V_D\right\rangle + \left\langle V_D\left|\hat{V}_{e-n_B}\right|V_D\right\rangle \\
&- \left\langle O_D\left|\hat{V}_{e-n_A}\right|O_D\right\rangle - \left\langle O_D\left|\hat{V}_{e-n_B}\right|O_D\right\rangle - \left\langle O_B\left|\hat{V}_{e-n_A}\right|O_B\right\rangle - \left\langle O_B\left|\hat{V}_{e-n_D}\right|O_B\right\rangle \\
&- 3J_{O_BO_D} - 2J_{O_AO_B} - 2J_{O_DO_A} + J_{V_BV_D} + J_{O_BV_D} + 2J_{O_AV_D} + J_{V_BO_D} + 2J_{V_BO_A} \\
&+ \frac{5}{2}K_{O_BO_D} + K_{O_AO_B} + K_{O_DO_A} + \frac{1}{2}K_{V_BV_D} + \frac{1}{2}K_{O_BV_D} - K_{O_AV_D} + \frac{1}{2}K_{V_BO_D} - K_{V_BO_A}
\end{aligned}
\tag{5.13}
$$

The same holds for the analytical expressions of the off-diagonal matrix elements between the many-electron states (Table 5.5), e.g.,

$$
{}^{SA}_{CTP}\left\langle D\,B^{+-}A^{+-}\left|\hat{H}^{el}\right|D^{+-}B\,A^{+-}\right\rangle^{SA}_{CTP} = \sqrt{3/2}\left(L_DL_B|H_DH_B\right) \rightarrow \sqrt{3/2}\left(V_DV_B|O_DO_B\right) \tag{5.14}
$$

These general formulas allow us to consider cases where the fragment excited states are not intra-fragment $O_F \rightarrow V_F$ or inter-fragment $O_F \rightarrow V_{F'}$ excitations, but rather linear combinations of excitations involving more than a pair of occupied and virtual orbitals. For example, rather than having the $\left|D^{+-}B\,A\right\rangle^{SA}$ expression of eq. (5.11), we could have chosen the excitation to be more complex, such as the linear combination of $\left|D^{+-}B\,A\right\rangle^{SA} = C\frac{1}{\sqrt{2}}\left(\left|\Psi^{V_D}_{O_D}\right\rangle + \left|\Psi^{\bar{V}_D}_{\bar{O}_D}\right\rangle\right) + C'\frac{1}{\sqrt{2}}\left(\left|\Psi^{V'_D}_{O'_D}\right\rangle + \left|\Psi^{\bar{V}'_D}_{\bar{O}'_D}\right\rangle\right)$ with $O'_D = H_D - 1$ and $V'_D = L_D + 1$.

The choice of fragment excited-states will depend on the systems considered and on the experimental and computational information we can get for the nature of their excitations (i.e., if they are single excitations or linear combinations of single excitations). Since we have analytical expressions of the Hamiltonian matrix elements in terms of any O_F, V_F orbitals, we can deduce analytically and computationally the relevant minimum model and approximate pathways that describe the specific system. Finally, the exact formulas for the basis states, their energies and their Hamiltonian interactions are not based on any assumption about the strengths of the interactions. Since the effective coupling is computed exactly by diagonalization of the full Hamiltonian at the initial-to-final state resonance (tunneling) energy (see section 5.4.3), the method can treat both asymmetric D-B-A systems and strongly-interacting fragments.

5.5 References

[1] Smith, M. B.; Michl, J. Singlet Fission. *Chem. Rev.* **2010**, *110*, 6891-6936.

[2] Smith, M. B.; Michl, J. Recent Advances in Singlet Fission. *Annu. Rev. Phys. Chem.* **2013**, *64*, 361-386.

[3] Casanova, D. Theoretical Modeling of Singlet Fission. *Chem. Rev.* **2018**, *118*, 7164-7207.

[4] Japahuge, A.; Zeng, T. Theoretical Studies of Singlet Fission: Searching for Materials and Exploring Mechanisms. *ChemPlusChem* **2018**, *83*, 146-182.

[5] Hanna, M. C.; Nozik, A. J. Solar conversion efficiency of photovoltaic and photoelectrolysis cells with carrier multiplication absorbers. *J. Appl. Phys.* **2006**, *100*, 074510.

[6] Burdett, J. J.; Bardeen, C.J. The Dynamics of Singlet Fission in Crystalline Tetracene and Covalent Analogs. *Acc. Chem. Res.* **2013**, *46 (6)*, 1312–1320.

[7] Pensack, R.D. *et al*. Exciton Delocalization Drives Rapid Singlet Fission in Nanoparticles of Acene Derivatives. *J. Am. Chem. Soc.* **2015**, *137 (21)*, 6790–6803.

[8] Burdett, J. J.; Bardeen, C. J. Quantum Beats in Crystalline Tetracene Delayed Fluorescence Due to Triplet Pair Coherences Produced by Direct Singlet Fission. *J. Am. Chem. Soc.* **2012**, *134*, 8597-8607.

[9] Zeng, T.; Hoffmann, R.; Ananth, N. The Low-Lying Electronic States and Their Roles in Singlet Fission. *J. Am. Chem. Soc.* **2014**, *136*, 5755−5764.

[10] Zimmerman, P. M.; Zhang, Z.; Musgrave, C. B. Singlet Fission in pentacene through multi-exciton quantum states. *Nat. Chem.* **2010**, *2*, 648-652.

[11] Basel, B. S. *et al*. Evidence for Charge-Transfer Mediation in the Primary Events of Singlet Fission in a Weakly Coupled Pentacene Dimer. *Chem.* **2018**, *4 (5)*, 1092-1111.

[12] Basel, B. S. *et al*. Unified model for singlet fission within a non-conjugated covalent pentacene dimer. *Nat Commun.* **2017**, *8*, 15171.

[13] Papadopoulos, I. *et al*. Varying the Interpentacene Electronic Coupling to Tune Singlet Fission. *J. Am. Chem. Soc.* **2019**, *141*, 6191-6203.

[14] Abraham, V.; Mayhall, N. J. Revealing the contest between triplet-triplet exchange and triplet-triplet energy transfer coupling in correlated triplet pair states in singlet fission. *J. Phys. Chem. Lett.* **2021**, *12*, 10505-10514.

[15] Scholes, G. D. Correlated Pair States Formed by Singlet Fission and Exciton-Exciton Annihilation. *J. Phys. Chem. A* **2015**, *119*, 12699−12705.

[16] Pensack, R. D. *et al.* Observation of Two Triplet-Pair Intermediates in Singlet Exciton Fission. *J. Phys. Chem. Lett*. **2016**, *7*, 2370-2375.

[17] Taffet, E. J.; Beljonne, D.; Scholes, G. D. Overlap-Driven Splitting of Triplet Pairs in Singlet Fission. *J. Am. Chem. Soc.* **2020**, *142*, 20040−20047.

[18] Li, X.; Parrish, R. M.; Liu, F.; Schumacher, S. I. L. K; Martínez, T. J. An Ab Initio Exciton Model Including Charge-Transfer Excited States. *J. Chem. Theory Comput.* **2017**, *13*, 3493-3504.

[19] Mirjani, F.; Renaud, N.; Gorczak, N.; Grozema, F. C. Theoretical Investigation of Singlet Fission in Molecular Dimers: The Role of Charge Transfer States and Quantum Interference. *J. Phys. Chem. C* **2014**, *118*, 14192-14199.

[20] Korovina, N.V. *et al*. Singlet Fission in a Covalently Linked Cofacial Alkynyltetracene Dimer. *J. Am. Chem. Soc.* **2016**, *138*, 617−627.

[21] Zirzlmeier, J. *et al*. Solution-based intramolecular singlet fission in cross-conjugated pentacene dimers. *Nanoscale.* **2016**, *8*, 10113-10123.

[22] Ito, S.; Nagami, T.; Nakano, M. Design Principles of Electronic Couplings for Intramolecular Singlet Fission in Covalently-Linked Systems. *J. Phys. Chem. A* **2016**, *120*, 6236−6241.

[23] Ito, S.; Nagami, T.; Nakano, M. Molecular design for efficient singlet fission. *J. Photochem. Photobiol.* **2018**, *34*, 85-120.

[24] Kumarasamy, E. *et al*. Tuning Singlet Fission in π-Bridge-π Chromophores. *J. Am. Chem. Soc.* **2017**, *139*, 12488−12494.

[25] Korovina, N. V. *et al*. Linker-Dependent Singlet Fission in Tetracene Dimers. *J. Am. Chem. Soc.* **2018**, *140*, 10179−10190.

[26] Parenti, K. R.; He, G.; Sanders, S. N.; Pun, A. B.; Kumarasamy, E.; Sfeir, M. Y.; Campos, L. M. Bridge Resonance Effects in Singlet Fission. *J. Phys. Chem. A* **2020**, *124*, 9392−9399.

[27] Rais, D. *et al*. Singlet Fission in Thin Solid Films of Bis(thienyl) diketopyrrolopyrroles. *ChemPlusChem* **2020**, *85*, 2689-2703.

[28] Buchanan, E. A.; Havlas, Z.; Michl, J. Optimal Arrangements of Tetracene Molecule Pairs for Fast Singlet Fission. *Bull. Chem. Soc. Jpn.* **2019**, *92*, 1960-1971.

[29] Zaykov, A. *et al*. Singlet Fission Rate: Optimized Packing of a Molecular Pair. Ethylene as a Model. *J. Am. Chem. Soc.* **2019**, *141*, 17729-17743.

[30] Buchanan, E. A.; Havlas, Z.; Michl, J. Singlet Fission: Optimization of Chromophore Dimer Geometry. *Adv. Quantum Chem*. **2017**, *75*, 175-227.

[31] Havlas, Z.; Michl, J. Guidance for Mutual Disposition of Chromophores for Singlet Fission. *Isr. J. Chem.* **2016**, *56*, 96-106.

[32] Sandoval-Salinas, M. E.; Casanova, D. The Doubly Excited State in Singlet Fission. *ChemPhotoChem.* **2021**, *5*, 282-293.

[33] Casanova, D.; Krylov, A. I. Quantifying local exciton, charge resonance, and multiexciton character in correlated wave functions of multichromophoric systems. *J. Chem. Phys.* **2016**, *144*, 014102.

[34] Luzanov, A. V.; Casanova, D.; Feng, X.; Krylov, A. I. Quantifying charge resonance and multiexciton character in coupled chromophores by charge and spin cumulant analysis. *J. Chem. Phys.* **2015**, *142*, 224104.

[35] Szabo, A.; Ostlund, N. S. *Modern Quantum Chemistry: Introduction to Advanced Electronic Structure Theory*; Dover, Mineola, New York, 1996.

[36] Sherrill, C. D. Derivation of the Configuration Interaction Singles (CIS) Method for Various Single Determinant References and Extensions to Include Selected Double Substitutions (XCIS). *Sch. Chem. Biochem*. 1996, 1-14.

[37] Pauncz, R. *The Construction of Spin Eigenfunctions: An Exercise Book*; 1st Ed.; Springer, Boston, MA, 2000.

[38] Pauncz, R. *The Symmetric Group in Quantum Chemistry*; CRC Press, Florida, 1995.

[39] Grabenstetter, J. E.; Tseng, T. J.; Grein, F. Generation of genealogical spin eigenfunctions. *Int. J. Quantum Chem*. **1976**, *10 (1)*, 143-149.

[40] Miyata, K.; Conrad-Burton, F. S.; Geyer, F. L.; Zhu, X.-Y. Triplet Pair States in Singlet Fission. *Chem. Rev.* **2019**, *19*, 4261-4292.

[41] Breen, I.; Tempelaar, R.; Bizimana, L. A.; Kloss, B.; Reichman, D. R.; Turner, D. B. Triplet Separation Drives Singlet Fission after Femtosecond Correlated Triplet Pair Production in Rubrene. *J. Am. Chem. Soc.* **2017**, *139*, 11745-11751.

[42] Wang, S.; Tian, H.; Ren, C.; Yu, J.; Sun, M. Electronic and optical properties of heterostructures based on transition metal dichalcogenides and graphene-like zinc oxide. *Sci Rep.* **2018**, *8*, 12009.

[43] Dupuis, M.; Spangler, D.; Wendolowski, J. J. *National Resource for Computations in Chemistry Software Catalog*; University of California, Berkeley, CA, Program QG01, 1980.

[44] Schmidt, M. W. *et al*. General Atomic and Molecular Electronic Structure System. *J. Comput. Chem.* **1983**, *14 (11)*, 1347-1363.

[45] Advances in electronic structure theory: GAMESS a decade later; Gordon, M. S., Schmidt, M. W., Dykstra, C. E., Frenking, G., Kim, K. S., Scuseria, G. E., Eds.; Theory and Applications of Computational Chemistry: the first forty years; Elsevier, Amsterdam, 2005; pp 1167-1189.

[46] Lowdin, P-O. Studies in Perturbation Theory. IV. Solution of Eigenvalue Problem by Projection Operator Formalism. *J. Math. Phys.* **1962**, *3 (5)*, 969-982.

[47] Skourtis, S. S.; Beratan, D. N.; Onuchic, J. N. The two-state reduction for electron and hole transfer in bridge-mediated electron-transfer reactions. *Chem. Phys.* **1993**, *176*, 501-520.

[48] Skourtis, S. S.; Beratan, D. N. Theories of Structure-Function Relationships for Bridge-Mediated Electron Transfer Reactions. *Adv. Chem. Phys.* **1999**, *106*, 377-452.

[49] Castellanos, M. A.; Huo, P. Enhancing Singlet Fission Dynamics by Suppressing Destructive Interference between Charge-Transfer Pathways. *J. Phys. Chem. Lett.* **2017**, *8*, 2480-2488.

[50] Atkins, P.; Friedman, R. *Molecular Quantum Mechanics*; 5th ed.; Oxford Univ. Press, New York, 2011.

[51] Slater, J. C. A Simplification of the Hartree-Fock Method. *Phys. Rev.* **1951**, *81*, 385-390.

CHAPTER 6

Construction of Spin-Spatial Many-electron Basis

One of the most fundamental principles for a many-electron system, is the construction of $N-$ electron wavefunctions that satisfy the antisymmetry principle. This chapter describes the creation of spin-spatial multi-electronic states (spin-spatial antisymmetric wavefunctions) that are used as a basis for representing the many-electron Hamiltonian in the CISD approximation. This construction is the key to the semi-analytical / computational framework that we used in Chapter 5, in the study of the singlet fission process in donor (D) - bridge (B) - Acceptor (A) molecular systems. Initially through the branching diagram method we construct spin eigenfunctions for a given number of electrons (N) and spin quantum number (S_N). Then, we combine these spin eigenfunctions with the appropriate spatial part we create $N-$ electron states. [1-3] The principle goal is the study of the structure of the wavefunction and the derivation of the rules for the calculation of the matrix elements of the Hamiltonian. Namely, we apply this methodology for creating the basis set (singly- and doubly-excited states) that describes all the possible states within the CISD formalism.

6.1 Genealogical Construction of Spin Eigenfunctions

Let us assume that we know the spin eigenfunctions of the $N-1$ electronic system and we want to construct spin eigenfunctions for the $N-$ electronic system. We can start by considering $N=1$ and knowing that the electron can have a spin eigenfunction χ_α (or α) corresponding to spin-orbital with spin up and $\bar{\chi}_\alpha$ (or $\bar{\alpha}$) corresponding to spin-orbital with spin down. This case corresponds to the addition theorem on angular momenta where one subsystem consists of $N-1$ electrons with spin quantum number S_{N-1}, while the other subsystem consists of one electron with spin quantum number $1/2$. Then, the S_N quantum number of the system can have only two values: $S_{N-1}-1/2$ and $S_{N-1}+1/2$.

Using the branching diagram method (and the Yamanouchi-Kotani functions), [1-3] from a given quantum number S_{N-1}, we can obtain new eigenfunctions corresponding to either $S_N = S_{N-1}+1/2$ or $S_N = S_{N-1}-1/2$ (by adding or subtracting the spin of the N^{th} electron).

For a given quantum number S_N there are different groups of such eigenfunctions, each group containing $2S_N+1$ $\hat{S}_{z,N}$ eigenfunctions. The spin degeneracy of state N, S_N is obtained as follows,

$$f\left(N, S_N\right) = f\left(N-1, S_{N-1}+1/2\right) - f\left(N-1, S_{N-1}-1/2\right). \tag{6.1}$$

Using the indicative method, we prove that $f\left(N, S_N\right)$ is given by the following formula,

$$f\left(N, S_N\right) = \begin{pmatrix} N \\ \frac{1}{2}N - S_N \end{pmatrix} - \begin{pmatrix} N \\ \frac{1}{2}N - S_N - 1 \end{pmatrix}. \tag{6.2}$$

The spin degeneracy can be represented in a pictorial way by the branching diagram (Fig. 6.1). [1-3] Each state is represented by a circle with the coordinates N and S_N, and in each circle is written the corresponding $f\left(N, S_N\right)$ value. As can be observed, the number of independent spin states increases sharply as N increases.

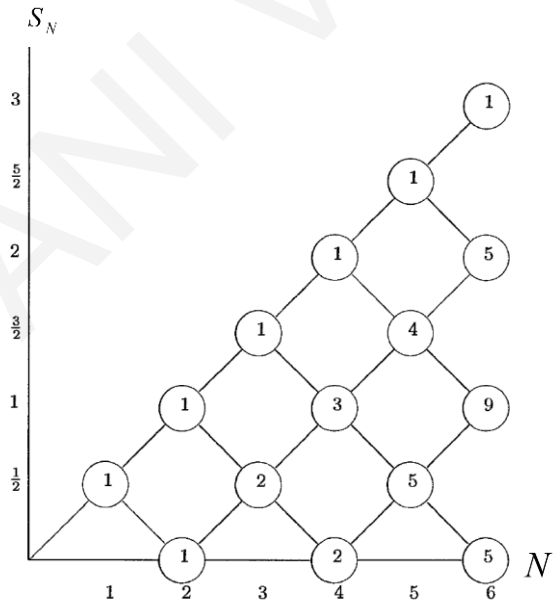

Figure 6.1 Schematic representation of the branching diagram, S_N as a function of the number of electrons, *N*. Circles represent the different states and the number in each circle corresponds to the *f (N, S_N)* values.

We denote the eigenfunctions of $\hat{S}_N^2$ and $\hat{S}_{z,N}$ belonging to the k^{th} group by $X(k) \equiv X(N, S_N, M_S; k)$. The formulas for adding and subtracting the N^{th} electron are given by the following equations, [1-3]

$$X(N, S_{N-1}+1/2, M_S+1/2) = 1/\sqrt{2S_{N-1}+1} \begin{bmatrix} \sqrt{S_{N-1}+M_S+1}\, X(N-1, S_{N-1}, M_S)\alpha(N) \\ +\sqrt{S_{N-1}-M_S}\, X(N-1, S_{N-1}, M_S+1)\bar{\alpha}(N) \end{bmatrix} \tag{6.3}$$

$$X(N, S_{N-1}-1/2, M_S+1/2) = 1/\sqrt{2S_{N-1}+1} \begin{bmatrix} -\sqrt{S_{N-1}-M_S}\, X(N-1, S_{N-1}, M_S)\alpha(N) \\ +\sqrt{S_{N-1}+M_S+1}\, X(N-1, S_{N-1}, M_S+1)\bar{\alpha}(N) \end{bmatrix} \tag{6.4}$$

Spin orbitals with spin up are symbolized with a and orbitals with spin down with $\bar{a}$.

6.2 Antisymmetry Principle

A many-electron wavefunction is antisymmetric with respect to interchange of the coordinates (both spin and spatial) of any two electrons (the wavefunction changes sign). This principle should be taken into account in the construction of full spin-spatial functions. In the remaining chapter we will deal with the creation of total wavefunctions that include both spatial and spin part that satisfy the antisymmetry principle. For this purpose, we must define the antisymmetrization operator as follows, [4,5]

$$\hat{A}_N = \frac{1}{\sqrt{N!}} \sum_p (-1)^p \hat{P} \tag{6.5}$$

where $\hat{P}$ is the permutation operator and p keeps track of the number of permutations from 0 to N. The antisymmetrization operator has the property of commuting with the Hamiltonian. This follows from the fact that the Hamiltonian is invariant with respect to the permutation of the coordinates of the electrons, so the Hamiltonian commutes with every permutation and therefore it commutes with the antisymmetrization operator.

6.3 Combination of Spatial and Spin Functions

Let us choose a spatial function consisting of prespecified orbitals determined by the state we want to create, $\Psi(A,B,...,\Omega) = \psi_A(1)\,\psi_B(2)...\psi_\Omega(N)$. The $\psi's$ are one-electron orbitals and $A,B,...,\Omega$ are the orbitals labels (e.g., HOMO, LUMO, etc.).

The total wavefunction is obtained by multiplying the eigenfunction $X(k) \equiv X(N, S_N, M_S; k)$ by the spatial function $\Psi(A,B,...,\Omega)$ and by antisymmetrizing the product. The wavefunction obtained in this way satisfies the antisymmetry principle. Thus, the spin-spatial antisymmetric wavefunction can be written in a multi-determinant form as,

$$|\Psi_k\rangle \equiv |\Psi(A,B,...,\Omega); X(k)\rangle^{SA} = \hat{A}_N \Psi(A,B,...,\Omega) X(k). \quad (6.6)$$

$|...\rangle^{SA}$ denotes a "Spin Adapted" state that most often involves a linear combination of Slater determinants of one-electron spin orbitals (denoted simply by $|...\rangle$).

6.4 The Many-electron Spin-adapted Basis Set

In the first step of the Singlet Fission (SF) process that studied extensively in Chapter 5 both the initial and final states are singlets, so we consider only singlet states as intermediates for this step (within the CISD formalism, these include single and double excitations). The many-electron basis states we use describe the D, B or A localization of the excited electron (e) and the hole (h), and are eigenstates of the total spin. They can be represented by linear combinations of singly- and doubly-excited $N-$ electron determinants. The spin eigenfunctions are constructed via the branching diagram method (using the Yamanouchi-Kotani functions) as described previously. [1-3] For N $s = 1/2$ spins we construct eigenfunctions of $\hat{S}_N^2$, $\hat{S}_{z,N}$ (with quantum numbers S_N and M_S, respectively). For a given quantum number S_N there are different groups of such eigenfunctions, each group containing $2S_N + 1$ $\hat{S}_{z,N}$ eigenfunctions. Given a value of S_N, the number of such groups for N spins is $f(N,S_N) = \binom{N}{\frac{1}{2}N - S_N} - \binom{N}{\frac{1}{2}N - S_N - 1}$. We denote the eigenfunctions of $\hat{S}_N^2$ and $\hat{S}_{z,N}$ belonging to the k^{th} group by $X(k) \equiv X(N, S_N, M_S; k)$. The construction of the eigenfunctions in each group is done iteratively. Given the $X(N-1, S_{N-1}, M_{S_{N-1}}; k)$ eigenfunctions we obtain new eigenfunctions corresponding to either $S_N = S_{N-1} + 1/2$ or $S_N = S_{N-1} - 1/2$ by adding or subtracting the spin of the N^{th} electron, respectively.

The Table 6.1 below shows the $f(6,0)=5$ (apply an active space with $N=6$ electrons looking for singlet spin eigenfunctions, $S_N=0$) spin eigenfunctions as generated using the above procedure as a function of the appropriate 20 primitive spin functions, θ_i.

i	$X(1)$	$X(2)$	$X(3)$	$X(4)$	$X(5)$	θ_i
1	3					$\alpha\alpha\alpha\bar{\alpha}\bar{\alpha}\bar{\alpha}$
2	-1	4				$\alpha\alpha\bar{\alpha}\alpha\bar{\alpha}\bar{\alpha}$
3	-1	-2	2			$\alpha\bar{\alpha}\alpha\alpha\bar{\alpha}\bar{\alpha}$
4	-1	-2	-2			$\bar{\alpha}\alpha\alpha\alpha\bar{\alpha}\bar{\alpha}$
5	-1	-2		2		$\alpha\alpha\bar{\alpha}\bar{\alpha}\alpha\bar{\alpha}$
6	-1	1	-1	-1	1	$\alpha\bar{\alpha}\alpha\bar{\alpha}\alpha\bar{\alpha}$
7	-1	1	1	-1	-1	$\bar{\alpha}\alpha\alpha\bar{\alpha}\alpha\bar{\alpha}$
8	1	-1	-1	-1	-1	$\alpha\bar{\alpha}\bar{\alpha}\alpha\alpha\bar{\alpha}$
9	1	-1	1	-1	1	$\bar{\alpha}\alpha\bar{\alpha}\alpha\alpha\bar{\alpha}$
10	1	2		2		$\bar{\alpha}\bar{\alpha}\alpha\alpha\alpha\bar{\alpha}$
11	-1	-2		-2		$\alpha\alpha\bar{\alpha}\bar{\alpha}\bar{\alpha}\alpha$
12	-1	1	-1	1	-1	$\alpha\bar{\alpha}\alpha\bar{\alpha}\bar{\alpha}\alpha$
13	-1	1	1	1	1	$\bar{\alpha}\alpha\alpha\bar{\alpha}\bar{\alpha}\alpha$
14	1	-1	-1	1	1	$\alpha\bar{\alpha}\bar{\alpha}\alpha\bar{\alpha}\alpha$
15	1	-1	1	1	-1	$\bar{\alpha}\alpha\bar{\alpha}\alpha\bar{\alpha}\alpha$
16	1	2		-2		$\bar{\alpha}\bar{\alpha}\alpha\alpha\bar{\alpha}\alpha$
17	1	2	2			$\alpha\bar{\alpha}\bar{\alpha}\bar{\alpha}\alpha\alpha$
18	1	2	-2			$\bar{\alpha}\alpha\bar{\alpha}\bar{\alpha}\alpha\alpha$
19	1	-4				$\bar{\alpha}\bar{\alpha}\alpha\bar{\alpha}\alpha\alpha$
20	-3					$\bar{\alpha}\bar{\alpha}\bar{\alpha}\alpha\alpha\alpha$
$\boldsymbol{c^{-2}}$	**36**	**72**	**24**	**24**	**8**	

Table 6.1 Spin eigenfunctions $X(k)$ ($k=1-5$) as linear combinations of primitive spin functions, θ_i (i keeps track of the number of primitive functions from 0 to 20) multiplying with the appropriate coefficients, c.

The spin-spatial multi-electronic state with a prespecified occupation of spatial orbitals, is constructed by first multiplying $X(k)$ by a product of the prespecified orbitals,

$\Psi(A,B,...,\Omega)=\psi_A(1)\,\psi_B(2)...\psi_\Omega(N)$. The $\psi's$ are 1e orbitals and $A,B,...,\Omega$ are the orbital labels (e.g., H_D for the HOMO of the Donor fragment, L_A for the LUMO of Acceptor fragment, etc.). Thus, the spin-spatial antisymmetric wavefunctions can be written in a multi-determinant form as $\left|\Psi(A,B,...,\Omega);X(k)\right\rangle^{SA}=\hat{A}_N\,\Psi(A,B,...,\Omega)\,X(k)$ where $\hat{A}_N$ is the antisymmetrization operator as described above.

Since we consider only singlet states, we will not use a total-spin label in our notation. Combining the spin eigenfunctions with an active space of 6 HOMO and LUMO orbitals ($H_D, L_D,\ H_B, L_B,\ H_A, L_A$) to create single and double excitations, we derive 40 singlet spin-spatial eigenstates $\left|\Psi_n\right\rangle^{SA}\ (n=1-40)$. For an active space of 4 electrons in 6 orbitals, the degeneracy is reduced to $f(N=4,S_N=0)=2$ groups of spin eigenfunctions of $\hat{S}_N^2$ (the other 3 groups of spin eigenfunctions vanish when we add the spatial part, since of the 6 total electrons, only the 4 are active). We use the basis set of $\left|\Psi_n\right\rangle^{SA}$ and the Slater-Condon rules to obtain analytical expressions for $H_{n,m}^{el}={}^{SA}\left\langle\Psi_n\right|\hat{H}^{el}\left|\Psi_m\right\rangle^{SA}$ where $\hat{H}^{el}=\hat{h}^{1e}+\hat{V}^{2e}$. [4,6]

The singly-excited states can be categorized as locally-excited (LE) and charge-transfer (CT). LE states have an excited electron and a hole on the same fragment (intra-fragment excitation). Such a state is the bridge excitonic (BE) state with an electron-hole (e-h) pair in the B fragment. For CT states the excited electron is on a different fragment than the hole (inter-fragment e-h excitation). Such a state is the Donor-Acceptor excitonic (DAE) state.

The doubly-excited (DE) states include many more excitation combinations. We denote locally doubly-excited states (LDE) those that contain two intra-fragment excitons (each exciton is localized within D, B or A). In addition to locally doubly-excited (LDE) there are doubly-excited CT states (CTDE) that combine a CT and LE exciton, e.g., $\left|D^{+-}B^{+}A^{-}\right\rangle^{SA}$. In these cases, using the branching diagram method, we can construct correlated triplet-pair DE states (denoted by CTP) and correlated singlet-pair DE states (denoted by CSP).

Table 6.2 shows the many-electron basis states as generated using the above procedure as linear combinations of $N-$ electron Slater determinants. In the notation used below, $\left|\Psi_a^r\right\rangle$ denotes a singly-excited determinant in which an electron, which occupied spin-orbital χ_a in the Hartree-Fock (HF) ground state of the D-B-A $N-$ electron system $\left|\Psi_{0,N}\right\rangle$, has been

promoted to a virtual spin-orbital χ_r. In addition, $\left|\Psi_{a\,a'}^{r\,r'}\right\rangle$ denotes a doubly-excited determinant in which two electrons, which occupied spin-orbitals $\chi_a, \chi_{a'}$ in the Hartree-Fock (HF) ground state of the D-B-A $N-$ electron system $\left|\Psi_{0,N}\right\rangle$, have been promoted to virtual spin-orbitals $\chi_r, \chi_{r'}$, respectively. In such determinants, χ_a (or a) is used to denote spin-orbital with spin up and $\bar{\chi}_a$ (or $\bar{a}$) spin-orbital with spin down. [4] The superscript "+" ("-") denotes hole (electron).

char.	h-e distribution notation	Expression
Singly-Excited states		
LE (in)	$\left\|D^{+-}BA\right\rangle^{SA}$	$\frac{1}{\sqrt{2}}\left(\left\|\Psi_{H_D}^{L_D}\right\rangle+\left\|\Psi_{\bar{H}_D}^{\bar{L}_D}\right\rangle\right)$
LE (BE)	$\left\|DB^{+-}A\right\rangle^{SA}$	$\frac{1}{\sqrt{2}}\left(\left\|\Psi_{H_B}^{L_B}\right\rangle+\left\|\Psi_{\bar{H}_B}^{\bar{L}_B}\right\rangle\right)$
CT (B^-)	$\left\|D^{+}B^{-}A\right\rangle^{SA}$ $\left\|DB^{-}A^{+}\right\rangle^{SA}$	$\frac{1}{\sqrt{2}}\left(\left\|\Psi_{H_{D(A)}}^{L_B}\right\rangle+\left\|\Psi_{\bar{H}_{D(A)}}^{\bar{L}_B}\right\rangle\right)$
CT (B^+)	$\left\|D^{-}B^{+}A\right\rangle^{SA}$ $\left\|DB^{+}A^{-}\right\rangle^{SA}$	$\frac{1}{\sqrt{2}}\left(\left\|\Psi_{H_B}^{L_{D(A)}}\right\rangle+\left\|\Psi_{\bar{H}_B}^{\bar{L}_{D(A)}}\right\rangle\right)$
CT (DAE)	$\left\|D^{+}BA^{-}\right\rangle^{SA}$ $\left\|D^{-}BA^{+}\right\rangle^{SA}$	$\frac{1}{\sqrt{2}}\left(\left\|\Psi_{H_{D(A)}}^{L_{A(D)}}\right\rangle+\left\|\Psi_{\bar{H}_{D(A)}}^{\bar{L}_{A(D)}}\right\rangle\right)$
Doubly-Excited states		
LDE_{CTP} (fi)	$\left\|D^{+-}BA^{+-}\right\rangle_{CTP}^{SA}$	$\sqrt{\frac{1}{3}}\left(\left\|\Psi_{\bar{H}_D\,H_A}^{\bar{L}_A\,L_D}\right\rangle+\left\|\Psi_{H_D\,\bar{H}_A}^{L_A\,\bar{L}_D}\right\rangle-\frac{1}{2}\left(\begin{array}{l}\left\|\Psi_{\bar{H}_D\,\bar{H}_A}^{\bar{L}_D\,\bar{L}_A}\right\rangle-\left\|\Psi_{H_D\,\bar{H}_A}^{L_D\,\bar{L}_A}\right\rangle\\ -\left\|\Psi_{\bar{H}_D\,H_A}^{\bar{L}_D\,L_A}\right\rangle+\left\|\Psi_{H_D\,H_A}^{L_D\,L_A}\right\rangle\end{array}\right)\right)$
LDE_{CSP}	$\left\|D^{+-}BA^{+-}\right\rangle_{CSP}$	$\frac{1}{2}\left(\left\|\Psi_{\bar{H}_D\,\bar{H}_A}^{\bar{L}_D\,\bar{L}_A}\right\rangle+\left\|\Psi_{H_D\,\bar{H}_A}^{L_D\,\bar{L}_A}\right\rangle+\left\|\Psi_{\bar{H}_D\,H_A}^{\bar{L}_D\,L_A}\right\rangle+\left\|\Psi_{H_D\,H_A}^{L_D\,L_A}\right\rangle\right)$
LDE_{CTP} (BE)	$\left\|D^{+-}B^{+-}A\right\rangle_{CTP}^{SA}$ $\left\|DB^{+-}A^{+-}\right\rangle_{CTP}^{SA}$	$\sqrt{\frac{1}{3}}\left(\left\|\Psi_{\bar{H}_{D(A)}\,H_B}^{\bar{L}_B\,L_{D(A)}}\right\rangle+\left\|\Psi_{H_{D(A)}\,\bar{H}_B}^{L_B\,\bar{L}_{D(A)}}\right\rangle-\frac{1}{2}\left(\begin{array}{l}\left\|\Psi_{\bar{H}_{D(A)}\,\bar{H}_B}^{\bar{L}_{D(A)}\,\bar{L}_B}\right\rangle-\left\|\Psi_{H_{D(A)}\,\bar{H}_B}^{L_{D(A)}\,\bar{L}_B}\right\rangle\\ -\left\|\Psi_{\bar{H}_{D(A)}\,H_B}^{\bar{L}_{D(A)}\,L_A}\right\rangle+\left\|\Psi_{H_{D(A)}\,H_B}^{L_{D(A)}\,L_B}\right\rangle\end{array}\right)\right)$

LDE_{CSP} (BE)	$\left\vert D^{+-}B^{+-}A\right\rangle_{CSP}^{SA}$ $\left\vert DB^{+-}A^{+-}\right\rangle_{CSP}^{SA}$	$\frac{1}{2}\left(\left\vert \Psi^{\bar{L}_{D(A)}\ \bar{L}_B}_{\bar{H}_{D(A)}\ \bar{H}_B}\right\rangle+\left\vert \Psi^{L_{D(A)}\ \bar{L}_B}_{H_{D(A)}\ \bar{H}_B}\right\rangle+\left\vert \Psi^{\bar{L}_{D(A)}\ L_B}_{\bar{H}_{D(A)}\ H_B}\right\rangle+\left\vert \Psi^{L_{D(A)}\ L_B}_{H_{D(A)}\ H_B}\right\rangle\right)$
$CTDE_{CTP}$ (BE)	$\left\vert D^{-}B^{+-}A^{+}\right\rangle_{CTP}$ $\left\vert D^{+}B^{+-}A^{-}\right\rangle_{CTP}$	$\sqrt{\frac{1}{3}}\left(\left\vert \Psi^{\bar{L}_{D(A)}\ L_B}_{\bar{H}_{A(D)}\ H_{D(A)}}\right\rangle+\left\vert \Psi^{L_{D(A)}\ \bar{L}_B}_{H_{A(D)}\ \bar{H}_{D(A)}}\right\rangle-\frac{1}{2}\left(\begin{array}{l}\left\vert \Psi^{\bar{L}_B\ \bar{L}_{D(A)}}_{\bar{H}_{A(D)}\ \bar{H}_{D(A)}}\right\rangle-\left\vert \Psi^{L_B\ \bar{L}_{D(A)}}_{H_A\ \bar{H}_{D(A)}}\right\rangle\\ -\left\vert \Psi^{\bar{L}_B\ L_{D(A)}}_{\bar{H}_{A(D)}\ H_{D(A)}}\right\rangle+\left\vert \Psi^{L_B\ L_{D(A)}}_{H_A\ H_{D(A)}}\right\rangle\end{array}\right)\right)$
$CTDE_{CSP}$ (BE)	$\left\vert D^{-}B^{+-}A^{+}\right\rangle_{CSP}$ $\left\vert D^{+}B^{+-}A^{-}\right\rangle_{CSP}$	$\frac{1}{2}\left(\left\vert \Psi^{\bar{L}_B\ \bar{L}_{D(A)}}_{\bar{H}_{A(D)}\ \bar{H}_{D(A)}}\right\rangle+\left\vert \Psi^{L_B\ \bar{L}_{D(A)}}_{H_A\ \bar{H}_{D(A)}}\right\rangle+\left\vert \Psi^{\bar{L}_B\ L_{D(A)}}_{\bar{H}_{A(D)}\ H_{D(A)}}\right\rangle+\left\vert \Psi^{L_B\ L_{D(A)}}_{H_A\ H_{D(A)}}\right\rangle\right)$
$CTDE_{CTP}$ (B^+)	$\left\vert D^{-}B^{+}A^{+-}\right\rangle_{CTP}$ $\left\vert D^{+-}B^{+}A^{-}\right\rangle_{CTP}$	$\sqrt{\frac{1}{3}}\left(\left\vert \Psi^{\bar{L}_{D(A)}\ L_{A(D)}}_{\bar{H}_B\ H_{D(A)}}\right\rangle+\left\vert \Psi^{L_{D(A)}\ \bar{L}_{A(D)}}_{H_B\ \bar{H}_{D(A)}}\right\rangle-\frac{1}{2}\left(\begin{array}{l}\left\vert \Psi^{\bar{L}_{A(D)}\ \bar{L}_{D(A)}}_{\bar{H}_B\ \bar{H}_{D(A)}}\right\rangle-\left\vert \Psi^{L_{A(D)}\ \bar{L}_{D(A)}}_{H_B\ \bar{H}_{D(A)}}\right\rangle\\ -\left\vert \Psi^{\bar{L}_{A(D)}\ L_{D(A)}}_{\bar{H}_B\ H_{D(A)}}\right\rangle+\left\vert \Psi^{L_{A(D)}\ L_{D(A)}}_{H_B\ H_{D(A)}}\right\rangle\end{array}\right)\right)$
$CTDE_{CSP}$ (B^+)	$\left\vert D^{-}B^{+}A^{+-}\right\rangle_{CSP}$ $\left\vert D^{+-}B^{+}A^{-}\right\rangle_{CSP}$	$\frac{1}{2}\left(\left\vert \Psi^{\bar{L}_{A(D)}\ \bar{L}_{D(A)}}_{\bar{H}_B\ \bar{H}_{D(A)}}\right\rangle+\left\vert \Psi^{L_{A(D)}\ \bar{L}_{D(A)}}_{H_B\ \bar{H}_{D(A)}}\right\rangle+\left\vert \Psi^{\bar{L}_{A(D)}\ L_{D(A)}}_{\bar{H}_B\ H_{D(A)}}\right\rangle+\left\vert \Psi^{L_{A(D)}\ L_{D(A)}}_{H_B\ H_{D(A)}}\right\rangle\right)$
$CTDE_{CTP}$ (B^-)	$\left\vert D^{+}B^{-}A^{+-}\right\rangle_{CTP}$ $\left\vert D^{+-}B^{-}A^{+}\right\rangle_{CTP}$	$\sqrt{\frac{1}{3}}\left(\left\vert \Psi^{\bar{L}_B\ L_{A(D)}}_{\bar{H}_{D(A)}\ H_B}\right\rangle+\left\vert \Psi^{L_B\ \bar{L}_{A(D)}}_{H_{D(A)}\ \bar{H}_B}\right\rangle-\frac{1}{2}\left(\begin{array}{l}\left\vert \Psi^{\bar{L}_{A(D)}\ \bar{L}_B}_{\bar{H}_{D(A)}\ \bar{H}_B}\right\rangle-\left\vert \Psi^{L_{A(D)}\ \bar{L}_B}_{H_{D(A)}\ \bar{H}_B}\right\rangle\\ -\left\vert \Psi^{\bar{L}_{A(D)}\ L_B}_{\bar{H}_{D(A)}\ H_B}\right\rangle+\left\vert \Psi^{L_{A(D)}\ L_B}_{H_{D(A)}\ H_B}\right\rangle\end{array}\right)\right)$
$CTDE_{CSP}$ (B^-)	$\left\vert D^{+}B^{-}A^{+-}\right\rangle_{CSP}$ $\left\vert D^{+-}B^{-}A^{+}\right\rangle_{CSP}$	$\frac{1}{2}\left(\left\vert \Psi^{\bar{L}_{A(D)}\ \bar{L}_B}_{\bar{H}_{D(A)}\ \bar{H}_B}\right\rangle+\left\vert \Psi^{L_{A(D)}\ \bar{L}_B}_{H_{D(A)}\ \bar{H}_B}\right\rangle+\left\vert \Psi^{\bar{L}_{A(D)}\ L_B}_{\bar{H}_{D(A)}\ H_B}\right\rangle+\left\vert \Psi^{L_{A(D)}\ L_B}_{H_{D(A)}\ H_B}\right\rangle\right)$
DE (B^+)	$\left\vert D^{+}B^{+}A^{--}\right\rangle$ $\left\vert D^{--}B^{+}A^{+}\right\rangle$	$\frac{1}{\sqrt{2}}\left(\left\vert \Psi^{L_{A(D)}\ \bar{L}_{A(D)}}_{H_{D(A)}\ \bar{H}_B}\right\rangle+\left\vert \Psi^{\bar{L}_{A(D)}\ L_{A(D)}}_{\bar{H}_{D(A)}\ H_B}\right\rangle\right)$
DE (B^-)	$\left\vert D^{+}B^{--}A^{+}\right\rangle$	$\frac{1}{\sqrt{2}}\left(\left\vert \Psi^{L_B\ \bar{L}_B}_{H_D\ \bar{H}_A}\right\rangle+\left\vert \Psi^{\bar{L}_B\ L_B}_{\bar{H}_D\ H_A}\right\rangle\right)$

Table 6.2 Spin-spatial multi-electronic states written as linear combinations of singly- and doubly-excited Slater determinants. 1st column: Names of the different groups of lowest-lying singlet basis states for the D-B-A system. 2nd column: Mathematical notation for the spin-adapted basis states in each group. 3rd column: Spin-spatial multi-electronic states as linear combinations of singly- and doubly-excited Slater determinants. In most cases the grouping is according to the B state, such as B^+, B^- and bridge excitonic (BE) state, while the initial and final CTP states are denoted as (in) and (fi).

In our analysis $\left|D^{+-}BA\right\rangle^{SA}$ is taken to be the initial photo-excited state that produces the CTP final state and the CSP locally doubly-excited state (described below, eqs (6.7) and (6.8))

$$\left|D^{+-}BA^{+-}\right\rangle_{CTP}^{SA}=\sqrt{\frac{1}{3}}\left(\left|\Psi_{\bar{H}_D\,H_A}^{\bar{L}_A\,L_D}\right\rangle+\left|\Psi_{H_D\,\bar{H}_A}^{L_A\,\bar{L}_D}\right\rangle-\frac{1}{2}\left(\begin{array}{l}\left|\Psi_{\bar{H}_D\,\bar{H}_A}^{\bar{L}_D\,\bar{L}_A}\right\rangle-\left|\Psi_{H_D\,\bar{H}_A}^{L_D\,\bar{L}_A}\right\rangle\\-\left|\Psi_{\bar{H}_D\,H_A}^{\bar{L}_D\,L_A}\right\rangle+\left|\Psi_{H_D\,H_A}^{L_D\,L_A}\right\rangle\end{array}\right)\right) \tag{6.7}$$

and

$$\left|D^{+-}BA^{+-}\right\rangle_{CSP}^{SA}=\frac{1}{2}\left(\left|\Psi_{\bar{H}_D\,\bar{H}_A}^{\bar{L}_D\,\bar{L}_A}\right\rangle+\left|\Psi_{H_D\,\bar{H}_A}^{L_D\,\bar{L}_A}\right\rangle+\left|\Psi_{\bar{H}_D\,H_A}^{\bar{L}_D\,L_A}\right\rangle+\left|\Psi_{H_D\,H_A}^{L_D\,L_A}\right\rangle\right). \tag{6.8}$$

$\left|D^{+-}BA^{+-}\right\rangle_{CTP}^{SA}$ is the generalization to D-B-A system of the correlated D-A triplet-pair state that is a linear combination of products of D- and A-localized triplet excitons. [7-10] In particular, for an $N-$ electron system,

$$\begin{aligned}\left|D^{+-}BA^{+-}\right\rangle_{CTP}^{SA}=&\sqrt{\frac{4(N-4)!}{N!}}\sum_{I}^{N}\sum_{J>I}^{N}\sum_{K}^{N}\sum_{L>K}^{N}(-1)^{I+J+1}\\&\left\{\sqrt{\frac{1}{3}}\left(\left|Tr_D^1\right\rangle_{I,J}\left|Tr_A^{-1}\right\rangle_{K,L}+\left|Tr_D^{-1}\right\rangle_{I,J}\left|Tr_A^1\right\rangle_{K,L}-\left|Tr_D^0\right\rangle_{I,J}\left|Tr_A^0\right\rangle_{K,L}\right)\right\}\left|\Psi_{0,N-4}\right\rangle\end{aligned} \tag{6.9}$$

where I,J,K,L are four electrons (out of N), $\left|Tr_{D(A)}^{m_S}\right\rangle_{I,J}$ is a two-electron triplet state formed by I^{th} and J^{th} electrons. For example, $\left|Tr_D^0\right\rangle_{I,J}=\frac{1}{\sqrt{2}}\left(\left|\Psi_{H_D}^{L_D}\right\rangle_{I,J}-\left|\Psi_{\bar{H}_D}^{\bar{L}_D}\right\rangle_{I,J}\right)$, where $\left|\Psi_{H_D}^{L_D}\right\rangle_{I,J}=\frac{1}{\sqrt{2}}\left(\psi_{L_D}\alpha(I)\psi_{H_D}\bar{\alpha}(J)-\psi_{H_D}\bar{\alpha}(I)\psi_{L_D}\alpha(J)\right)$ is a two-electron (I,J) Slater determinant (and similarly for $\left|\Psi_{\bar{H}_D}^{\bar{L}_D}\right\rangle_{I,J}$). $\left|Tr_{D(A)}^{m_S}\right\rangle_{K,L}$ is a two-electron triplet state formed by K^{th} and L^{th} electrons. $\left|\Psi_{0,N-4}\right\rangle$ is the Slater determinant for the remaining $N-4$ electrons of the remaining occupied orbitals that do not belong to the active space. $\left|D^{+-}BA^{+-}\right\rangle_{CSP}^{SA}$ is also known as the Correlated Singlet-Pair (CSP) and it is given by,

$$\left|D^{+-}BA^{+-}\right\rangle_{CSP}^{SA}=\sqrt{\frac{4(N-4)!}{N!}}\sum_{I}^{N}\sum_{J>I}^{N}\sum_{K}^{N}\sum_{L>K}^{N}(-1)^{I+J+1}\left|Si_D^0\right\rangle_{I,J}\left|Si_A^0\right\rangle_{K,L}\left|\Psi_{0,N-4}\right\rangle \tag{6.10}$$

where, e.g., $\left|Si_D^0\right\rangle_{I,J}=\frac{1}{\sqrt{2}}\left(\left|\Psi_{H_D}^{L_D}\right\rangle_{I,J}+\left|\Psi_{\bar{H}_D}^{\bar{L}_D}\right\rangle_{I,J}\right)$.

6.5 References

[1] Pauncz, R. *The Construction of Spin Eigenfunctions: An Exercise Book*; 1st Ed.; Springer, Boston, MA, 2000.

[2] Pauncz, R. *The Symmetric Group in Quantum Chemistry*; CRC Press, Florida, 1995.

[3] Grabenstetter, J. E.; Tseng, T. J.; Grein, F. Generation of genealogical spin eigenfunctions. *Int. J. Quantum Chem.* **1976**, *10 (1)*, 143-149.

[4] Szabo, A.; Ostlund, N. S. *Modern Quantum Chemistry: Introduction to Advanced Electronic Structure Theory*; Dover, Mineola, New York, 1996.

[5] Scholes, G. D. Correlated Pair States Formed by Singlet Fission and Exciton-Exciton Annihilation. *J. Phys. Chem. A* **2015**, *119*, 12699−12705.

[6] Atkins, P.; Friedman, R. *Molecular Quantum Mechanics*; 5th ed.; Oxford Univ. Press, New York, 2011.

[7] Casanova, D. Theoretical Modeling of Singlet Fission. *Chem. Rev.* **2018**, *118*, 7164-7207.

[8] Scholes, G. D. Correlated Pair States Formed by Singlet Fission and Exciton-Exciton Annihilation. *J. Phys. Chem. A* **2015**, *119*, 12699−12705.

[9] Miyata, K.; Conrad-Burton, F. S.; Geyer, F. L.; Zhu, X.-Y. Triplet Pair States in Singlet Fission. *Chem. Rev.* **2019**, *19*, 4261-4292.

[10] Breen, I.; Tempelaar, R.; Bizimana, L. A.; Kloss, B.; Reichman, D. R.; Turner, D. B. Triplet Separation Drives Singlet Fission after Femtosecond Correlated Triplet Pair Production in Rubrene. *J. Am. Chem. Soc.* **2017**, *139*, 11745-11751.

CHAPTER 7

Construction of the CISD Hamiltonian Matrix

In this chapter we describe how we construct the Configuration Interaction Singles and Doubles (CISD) Hamiltonian matrix using the spin-adapted (SA) basis set of Chapter 5. This matrix is used to study analytically and computationally the singlet fission (SF) process, described in detail in Chapter 5.

7.1 Calculation of the Hamiltonian Matrix

The following electronic Hamiltonian was introduced in Chapter 1 (see eq. (1.5)),

$$\hat{H}^{el}\left(\vec{r},\vec{R}\right)=\sum_{I=1}^{N}\frac{p_I^2}{2m_{el}}-\sum_{I}^{N}\sum_{n}^{N_{nuc}}\frac{1}{4\pi\varepsilon_0}\frac{Z_n e^2}{\left|\vec{r}_I-\vec{R}_n\right|}+\frac{1}{2}\sum_{I\neq J}^{N}\sum_{J=1}^{N}\frac{1}{4\pi\varepsilon_0}\frac{e^2}{\left|\vec{r}_I-\vec{r}_J\right|}. \tag{7.1}$$

The first term is the operator corresponding to the sum of the kinetic energy of the N electrons, the second term corresponds to the sum of the attractions between the N electrons and the N_{nuc} nuclei and the final term describes the inter-electronic repulsions. The first two terms constitute the one-electron operator,

$$\hat{h}^{1e}\equiv\sum_{I=1}^{N}\frac{p_I^2}{2m_{el}}-\sum_{I}^{N}\sum_{n}^{N_{nuc}}\frac{1}{4\pi\varepsilon_0}\frac{Z_n e^2}{\left|\vec{r}_I-\vec{R}_n\right|} \tag{7.2}$$

since it is the independent-electron Hamiltonian for N electrons in the field of N_{nuc} atomic nuclei. While, the last term is the two-electron repulsive Coulombic operator

$$\hat{V}^{2e}\equiv\frac{1}{2}\sum_{I\neq J}^{N}\sum_{J=1}^{N}\frac{1}{4\pi\varepsilon_0}\frac{e^2}{\left|\vec{r}_I-\vec{r}_J\right|}. \tag{7.3}$$

The spin-spatial antisymmetric wavefunctions are written in a multi-determinant form, so we can use the Slater-Condon rules to calculate the Hamiltonian matrix elements, [1-3]

$$H_{n,m}^{el}=\left\langle\Psi_n\left|\hat{H}^{el}\right|\Psi_m\right\rangle. \tag{7.4}$$

Using the Slater-Condon rules, we calculate analytically the energies (diagonal Hamiltonian matrix elements) and the corresponding couplings (off-diagonal Hamiltonian matrix

elements) as a function of ionization potentials (IP), electron affinities (EA), core terms, overlap matrix elements, Coulomb and exchange 2e integrals and 1e Fock matrix elements.

7.2 Excitation Energies and Couplings

Using the Slater-Condon rules [1-3] we obtain analytical expressions for the donor (D) – bridge (B) – acceptor (A) electronic Hamiltonian matrix in representation of the many-electron basis described in Chapter 5, based on the six-orbital active space with single and double excitations. The electronic Hamiltonian describing this type of system can be written as linear combination of the fragment electronic Hamiltonians and the inter-fragment interactions,

$$\hat{H}^{el}_{DBA} = \hat{H}^{el}_{D} + \hat{H}^{el}_{B} + \hat{H}^{el}_{A} + \hat{H}_{int} \tag{7.5}$$

where the first three terms are the electronic Hamiltonians of the three fragments D, B, A, while the last term includes all the inter-fragment interactions between the electrons and the nuclei of the fragments. These terms can be given as,

$$\hat{H}^{el}_{D} = \sum_{I=1}^{N_D} \frac{p_I^2}{2m_{el}} - \sum_{I}^{N_D} \sum_{n_D}^{N_{n_D}} \frac{1}{4\pi\varepsilon_0} \frac{Z_{n_D} e^2}{\left|\vec{r}_I - \vec{R}_{n_D}\right|} + \frac{1}{2} \sum_{I \neq J}^{N_D} \sum_{J=1}^{N_D} \frac{1}{4\pi\varepsilon_0} \frac{e^2}{\left|\vec{r}_I - \vec{r}_J\right|} \tag{7.6}$$

$$\hat{H}^{el}_{B} = \sum_{I=1}^{N_B} \frac{p_I^2}{2m_{el}} - \sum_{I}^{N_B} \sum_{n_B}^{N_{n_B}} \frac{1}{4\pi\varepsilon_0} \frac{Z_{n_B} e^2}{\left|\vec{r}_I - \vec{R}_{n_B}\right|} + \frac{1}{2} \sum_{I \neq J}^{N_B} \sum_{J=1}^{N_B} \frac{1}{4\pi\varepsilon_0} \frac{e^2}{\left|\vec{r}_I - \vec{r}_J\right|} \tag{7.7}$$

$$\hat{H}^{el}_{A} = \sum_{I=1}^{N_A} \frac{p_I^2}{2m_{el}} - \sum_{I}^{N_A} \sum_{n_A}^{N_{n_A}} \frac{1}{4\pi\varepsilon_0} \frac{Z_{n_A} e^2}{\left|\vec{r}_I - \vec{R}_{n_A}\right|} + \frac{1}{2} \sum_{I \neq J}^{N_A} \sum_{J=1}^{N_A} \frac{1}{4\pi\varepsilon_0} \frac{e^2}{\left|\vec{r}_I - \vec{r}_J\right|} \tag{7.8}$$

$$\begin{aligned} \hat{H}_{int} = &-\sum_{I}^{N_D} \left(\sum_{n_B}^{N_{n_B}} \frac{1}{4\pi\varepsilon_0} \frac{Z_{n_B} e^2}{\left|\vec{r}_I - \vec{R}_{n_B}\right|} + \sum_{n_A}^{N_{n_A}} \frac{1}{4\pi\varepsilon_0} \frac{Z_{n_A} e^2}{\left|\vec{r}_I - \vec{R}_{n_A}\right|} \right) - \sum_{I}^{N_B} \left(\sum_{n_D}^{N_{n_D}} \frac{1}{4\pi\varepsilon_0} \frac{Z_{n_D} e^2}{\left|\vec{r}_I - \vec{R}_{n_D}\right|} + \sum_{n_A}^{N_{n_A}} \frac{1}{4\pi\varepsilon_0} \frac{Z_{n_A} e^2}{\left|\vec{r}_I - \vec{R}_{n_A}\right|} \right) \\ &- \sum_{I}^{N_A} \left(\sum_{n_D}^{N_{n_D}} \frac{1}{4\pi\varepsilon_0} \frac{Z_{n_D} e^2}{\left|\vec{r}_I - \vec{R}_{n_D}\right|} + \sum_{n_B}^{N_{n_B}} \frac{1}{4\pi\varepsilon_0} \frac{Z_{n_B} e^2}{\left|\vec{r}_I - \vec{R}_{n_B}\right|} \right). \end{aligned} \tag{7.9}$$

In the above equations, I, J keep track of the number of electrons from 0 to N_i (total number of electrons in fragment i) and n_i keeps track of the number of nuclei from 0 to N_{n_i} (the number of nuclei in fragment i) ($i = D, B, A$). With $\vec{r}_I$ we denote the position of the I^{th} electron in space and with $\vec{R}_{n_i}$ the position of the n_i^{th} nucleus.

In general, the basis-state energies are functions of ionization potentials, electron affinities, core terms, Coulomb and exchange integrals, i.e.,

$$ {}^{SA}\langle \Psi_n | \hat{H}^{el} | \Psi_n \rangle^{SA} = E_n \left(\left\{ IP^i \right\},\ \left\{ EA^i \right\},\ \left\{ \left\langle L_i \left| \hat{V}_{e-n_j} \right| L_i \right\rangle \right\},\ \left\{ \left\langle H_i \left| \hat{V}_{e-n_j} \right| H_i \right\rangle \right\},\ \left\{ J_{P_i Q_j} \right\},\ \left\{ K_{P_i Q_j} \right\} \right) \cdot \quad (7.10) $$

The off-diagonal matrix elements are functions of one-electron Fock matrix elements, overlap matrix elements and two-electron integrals,

$$ {}^{SA}\langle \Psi_n | \hat{H}^{el} | \Psi_m \rangle^{SA} = H_{n,m} \left(\left\{ \langle P_i | \hat{F} | Q_j \rangle \right\},\ \left\{ \left(P_i Q_j \left| R_i Z_j \right. \right) \right\},\ \left\{ S_{P_i Q_j} \right\},\ \left\{ J_{P_i Q_j} \right\},\ \left\{ K_{P_i Q_j} \right\} \right) \quad (7.11) $$

In the equations above $\hat{V}_{e-n_k}$ denote Coulombic attractive interactions between the electrons and the k^{th} fragment nuclei (part of the core term in the Hamiltonian). $J_{P_i Q_j}$ and $K_{P_i Q_j}$ are Coulomb and exchange 2e integrals involving the ψ_{P_i} and ψ_{Q_j} fragment molecular orbitals (MOs),

$$ J_{P_i Q_j} \equiv \left(P_i P_i \left| Q_j Q_j \right. \right) = \int d^3\vec{r}_1\ d^3\vec{r}_2\ \psi^*_{P_i}(\vec{r}_1)\, \psi_{P_i}(\vec{r}_1)\, r^{-1}{}_{12}\, \psi^*_{Q_j}(\vec{r}_2)\, \psi_{Q_j}(\vec{r}_2), \quad (7.12) $$

$$ K_{P_i Q_j} \equiv \left(P_i Q_j \left| Q_j P_i \right. \right) = \int d^3\vec{r}_1\ d^3\vec{r}_2\ \psi^*_{P_i}(\vec{r}_1)\, \psi_{Q_j}(\vec{r}_1)\, r^{-1}{}_{12}\, \psi^*_{Q_j}(\vec{r}_2)\, \psi_{P_i}(\vec{r}_2). \quad (7.13) $$

where $P, Q, R, Z = H, L$ and $i, j = D, B, A$. [1-3]

Below we present analytical expressions for the diagonal and off-diagonal elements of the Hamiltonian calculated using the Slater Condon rules. The basis set includes singly-excited states (LE and CT) and doubly-excited (DE, correlated triplet- and correlated-singlet LDE and CTDE).

char.	notation	Exact Energy Expression
	Singly - Excited States	
LE (in)	$\left\| D^{+-} B\, A \right\rangle$	$IP^D - EA^D - J_{H_D L_D} + 2K_{H_D L_D}$ $+\left\langle L_D \left| \hat{V}_{e-n_A} \right| L_D \right\rangle + \left\langle L_D \left| \hat{V}_{e-n_B} \right| L_D \right\rangle - \left\langle H_D \left| \hat{V}_{e-n_A} \right| H_D \right\rangle - \left\langle H_D \left| \hat{V}_{e-n_B} \right| H_D \right\rangle$ $+2J_{L_D H_A} + 2J_{L_D H_B} - 2J_{H_D H_A} - 2J_{H_D H_B}$ $-K_{L_D H_A} - K_{L_D H_B} + K_{H_D H_A} + K_{H_D H_B}$
LE (BE)	$\left\| D\, B^{+-} A \right\rangle$	$IP^B - EA^B - J_{H_B L_B} + 2K_{H_B L_B}$ $+\left\langle L_B \left| \hat{V}_{e-n_A} \right| L_B \right\rangle + \left\langle L_B \left| \hat{V}_{e-n_D} \right| L_B \right\rangle - \left\langle H_B \left| \hat{V}_{e-n_A} \right| H_B \right\rangle - \left\langle H_B \left| \hat{V}_{e-n_D} \right| H_B \right\rangle$ $+2J_{L_B H_A} + 2J_{L_B H_D} - 2J_{H_B H_A} - 2J_{H_B H_D}$ $-K_{L_B H_A} - K_{L_B H_D} + K_{H_B H_A} + K_{H_B H_D}$

CT (B^-)	$\left\|D^+B^-A\right\rangle,$ $\left\|DB^-A^+\right\rangle$	$IP^{D(A)} - EA^{B}$ $+\left\langle L_B\left\|\hat{V}_{e-n_{D(A)}}\right\|L_B\right\rangle+\left\langle L_B\left\|\hat{V}_{e-n_{A(D)}}\right\|L_B\right\rangle-\left\langle H_{D(A)}\left\|\hat{V}_{e-n_{A(D)}}\right\|H_{D(A)}\right\rangle-\left\langle H_{D(A)}\left\|\hat{V}_{e-n_B}\right\|H_{D(A)}\right\rangle$ $+J_{H_{D(A)}L_B}+2J_{H_{A(D)}L_B}-2J_{H_{D(A)}H_B}-2J_{H_DH_A}$ $+K_{H_{D(A)}L_B}-K_{H_{A(D)}L_B}+K_{H_{D(A)}H_B}+K_{H_DH_A}$
CT (B^+)	$\left\|D^-B^+A\right\rangle,$ $\left\|DB^+A^-\right\rangle$	$IP^{B} - EA^{D(A)}$ $+\left\langle L_{D(A)}\left\|\hat{V}_{e-n_B}\right\|L_{D(A)}\right\rangle+\left\langle L_{D(A)}\left\|\hat{V}_{e-n_{A(D)}}\right\|L_{D(A)}\right\rangle-\left\langle H_B\left\|\hat{V}_{e-n_A}\right\|H_B\right\rangle-\left\langle H_B\left\|\hat{V}_{e-n_D}\right\|H_B\right\rangle$ $+J_{H_BL_{D(A)}}+2J_{H_{A(D)}L_{D(A)}}-2J_{H_BH_D}-2J_{H_BH_A}$ $+K_{H_BL_{D(A)}}-K_{H_{A(D)}L_{D(A)}}+K_{H_BH_D}+K_{H_BH_A}$
CT (DAE)	$\left\|D^-BA^+\right\rangle,$ $\left\|D^+BA^-\right\rangle$	$IP^{A(D)} - EA^{D(A)}$ $+\left\langle L_{D(A)}\left\|\hat{V}_{e-n_{A(D)}}\right\|L_{D(A)}\right\rangle+\left\langle L_{D(A)}\left\|\hat{V}_{e-n_B}\right\|L_{D(A)}\right\rangle-\left\langle H_{A(D)}\left\|\hat{V}_{e-n_B}\right\|H_{A(D)}\right\rangle-\left\langle H_{A(D)}\left\|\hat{V}_{e-n_{D(A)}}\right\|H_{A(D)}\right\rangle$ $+J_{H_{A(D)}L_{D(A)}}+2J_{H_BL_{D(A)}}-2J_{H_AH_D}-2J_{H_{A(D)}H_B}$ $+K_{H_{A(D)}L_{D(A)}}-K_{H_BL_{D(A)}}+K_{H_AH_D}+K_{H_{A(D)}H_B}$
	Doubly – Excited States	
LDE (fi)	$\left\|D^{+-}BA^{+-}\right\rangle_{CTP}$	$IP^{D} + IP^{A} - EA^{D} - EA^{A} - J_{H_DL_D} - J_{H_AL_A}$ $+\left\langle L_D\left\|\hat{V}_{e-n_A}\right\|L_D\right\rangle+\left\langle L_D\left\|\hat{V}_{e-n_B}\right\|L_D\right\rangle+\left\langle L_A\left\|\hat{V}_{e-n_D}\right\|L_A\right\rangle+\left\langle L_A\left\|\hat{V}_{e-n_B}\right\|L_A\right\rangle$ $-\left\langle H_A\left\|\hat{V}_{e-n_D}\right\|H_A\right\rangle-\left\langle H_A\left\|\hat{V}_{e-n_B}\right\|H_A\right\rangle-\left\langle H_D\left\|\hat{V}_{e-n_A}\right\|H_D\right\rangle-\left\langle H_D\left\|\hat{V}_{e-n_B}\right\|H_D\right\rangle$ $-3J_{H_DH_A}-2J_{H_DH_B}-2J_{H_BH_A}+J_{L_DL_A}+J_{H_DL_A}+2J_{H_BL_A}+J_{L_DH_A}+2J_{L_DH_B}$ $+\frac{5}{2}K_{H_DH_A}+K_{H_DH_B}+K_{H_BH_A}+\frac{1}{2}K_{L_DL_A}+\frac{1}{2}K_{H_DL_A}-K_{H_BL_A}+\frac{1}{2}K_{L_DH_A}-K_{L_DH_B}$
	$\left\|D^{+-}BA^{+-}\right\rangle_{CSP}$	$IP^{D} + IP^{A} - EA^{D} - EA^{A} - J_{H_DL_D} - J_{H_AL_A} + 2K_{H_DL_D} + 2K_{H_AL_A}$ $+\left\langle L_D\left\|\hat{V}_{e-n_A}\right\|L_D\right\rangle+\left\langle L_D\left\|\hat{V}_{e-n_B}\right\|L_D\right\rangle+\left\langle L_A\left\|\hat{V}_{e-n_D}\right\|L_A\right\rangle+\left\langle L_A\left\|\hat{V}_{e-n_B}\right\|L_A\right\rangle$ $-\left\langle H_A\left\|\hat{V}_{e-n_D}\right\|H_A\right\rangle-\left\langle H_A\left\|\hat{V}_{e-n_B}\right\|H_A\right\rangle-\left\langle H_D\left\|\hat{V}_{e-n_A}\right\|H_D\right\rangle-\left\langle H_D\left\|\hat{V}_{e-n_B}\right\|H_D\right\rangle$ $-3J_{H_DH_A}-2J_{H_DH_B}-2J_{H_BH_A}+J_{L_DL_A}+J_{H_DL_A}+2J_{H_BL_A}+J_{L_DH_A}+2J_{L_DH_B}$ $+\frac{3}{2}K_{H_DH_A}+K_{H_DH_B}+K_{H_BH_A}-\frac{1}{2}K_{L_DL_A}-\frac{1}{2}K_{H_DL_A}-K_{H_BL_A}-\frac{1}{2}K_{L_DH_A}-K_{L_DH_B}$
LDE (BE)	$\left\|DB^{+-}A^{+-}\right\rangle_{CTP}$ $\left\|D^{+-}B^{+-}A\right\rangle_{CTP}$	$IP^{B} + IP^{A(D)} - EA^{B} - EA^{A(D)} - J_{H_BL_B} - J_{H_{A(D)}L_{A(D)}}$ $+\left\langle L_B\left\|\hat{V}_{e-n_A}\right\|L_B\right\rangle+\left\langle L_B\left\|\hat{V}_{e-n_D}\right\|L_B\right\rangle+\left\langle L_{A(D)}\left\|\hat{V}_{e-n_{D(A)}}\right\|L_{A(D)}\right\rangle+\left\langle L_{A(D)}\left\|\hat{V}_{e-n_B}\right\|L_{A(D)}\right\rangle$ $-\left\langle H_{A(D)}\left\|\hat{V}_{e-n_{D(A)}}\right\|H_{A(D)}\right\rangle-\left\langle H_{A(D)}\left\|\hat{V}_{e-n_B}\right\|H_{A(D)}\right\rangle-\left\langle H_B\left\|\hat{V}_{e-n_A}\right\|H_B\right\rangle-\left\langle H_B\left\|\hat{V}_{e-n_D}\right\|H_B\right\rangle$ $-3J_{H_BH_{A(D)}}-2J_{H_{D(A)}H_B}-2J_{H_DH_A}+J_{L_BL_{A(D)}}+J_{H_BL_{A(D)}}+2J_{H_{D(A)}L_{A(D)}}+J_{L_BH_{A(D)}}+2J_{L_BH_{D(A)}}$ $+\frac{5}{2}K_{H_BH_{A(D)}}+K_{H_{D(A)}H_B}+K_{H_DH_A}+\frac{1}{2}K_{L_BL_{A(D)}}+\frac{1}{2}K_{H_BL_{A(D)}}-K_{H_{D(A)}L_{A(D)}}+\frac{1}{2}K_{L_BH_{A(D)}}-K_{L_BH_{D(A)}}$
	$\left\|DB^{+-}A^{+-}\right\rangle_{CSP}$ $\left\|D^{+-}B^{+-}A\right\rangle_{CSP}$	$IP^{B} + IP^{A(D)} - EA^{B} - EA^{A(D)} - J_{H_BL_B} - J_{H_{A(D)}L_{A(D)}} + 2K_{H_BL_B} + 2K_{H_{A(D)}L_{A(D)}}$ $+\left\langle L_B\left\|\hat{V}_{e-n_A}\right\|L_B\right\rangle+\left\langle L_B\left\|\hat{V}_{e-n_D}\right\|L_B\right\rangle+\left\langle L_{A(D)}\left\|\hat{V}_{e-n_B}\right\|L_{A(D)}\right\rangle+\left\langle L_{A(D)}\left\|\hat{V}_{e-n_{D(A)}}\right\|L_{A(D)}\right\rangle$ $-\left\langle H_{A(D)}\left\|\hat{V}_{e-n_{D(A)}}\right\|H_{A(D)}\right\rangle-\left\langle H_{A(D)}\left\|\hat{V}_{e-n_B}\right\|H_{A(D)}\right\rangle-\left\langle H_B\left\|\hat{V}_{e-n_A}\right\|H_B\right\rangle-\left\langle H_B\left\|\hat{V}_{e-n_D}\right\|H_B\right\rangle$ $-3J_{H_BH_{A(D)}}-2J_{H_{D(A)}H_B}-2J_{H_DH_A}+J_{L_BL_{A(D)}}+J_{H_BL_{A(D)}}+2J_{H_{D(A)}L_{A(D)}}+J_{L_BH_{A(D)}}+2J_{L_BH_{D(A)}}$ $+\frac{3}{2}K_{H_BH_{A(D)}}+K_{H_{D(A)}H_B}+K_{H_DH_A}-\frac{1}{2}K_{L_BL_{A(D)}}-\frac{1}{2}K_{H_BL_{A(D)}}-K_{H_{D(A)}L_{A(D)}}-\frac{1}{2}K_{L_BH_{A(D)}}-K_{L_BH_{D(A)}}$

CTDE (BE)	$\left\|D^{-}B^{+-}A^{+}\right\rangle_{CTP}$ $\left\|D^{+}B^{+-}A^{-}\right\rangle_{CTP}$	$IP^{B}+IP^{A(D)}-EA^{B}-EA^{D(A)}-J_{H_BL_B}$ $+\left\langle L_B\left\|\hat{V}_{e-n_A}\right\|L_B\right\rangle+\left\langle L_B\left\|\hat{V}_{e-n_D}\right\|L_B\right\rangle+\left\langle L_{D(A)}\left\|\hat{V}_{e-n_B}\right\|L_{D(A)}\right\rangle+\left\langle L_{D(A)}\left\|\hat{V}_{e-n_{A(D)}}\right\|L_{D(A)}\right\rangle$ $-\left\langle H_{A(D)}\left\|\hat{V}_{e-n_{D(A)}}\right\|H_{A(D)}\right\rangle-\left\langle H_{A(D)}\left\|\hat{V}_{e-n_B}\right\|H_{A(D)}\right\rangle-\left\langle H_B\left\|\hat{V}_{e-n_A}\right\|H_B\right\rangle-\left\langle H_B\left\|\hat{V}_{e-n_D}\right\|H_B\right\rangle$ $-3J_{H_BH_{A(D)}}-2J_{H_{D(A)}H_B}-2J_{H_DH_A}+J_{L_{D(A)}L_B}+J_{H_{A(D)}L_B}+2J_{H_{D(A)}L_B}+J_{H_BL_{D(A)}}+J_{H_{A(D)}L_{D(A)}}$ $+\frac{5}{2}K_{H_BH_{A(D)}}+K_{H_{D(A)}H_B}+K_{H_DH_A}+\frac{1}{2}K_{L_{D(A)}L_B}+\frac{1}{2}K_{H_{A(D)}L_B}-K_{H_{D(A)}L_B}+\frac{1}{2}K_{H_BL_{D(A)}}-K_{H_{A(D)}L_{D(A)}}$
	$\left\|D^{-}B^{+-}A^{+}\right\rangle_{CSP}$ $\left\|D^{+}B^{+-}A^{-}\right\rangle_{CSP}$	$IP^{B}+IP^{A(D)}-EA^{B}-EA^{D(A)}-J_{H_BL_B}+K_{H_BL_B}+K_{H_{D(A)}L_{D(A)}}$ $+\left\langle L_B\left\|\hat{V}_{e-n_A}\right\|L_B\right\rangle+\left\langle L_B\left\|\hat{V}_{e-n_D}\right\|L_B\right\rangle+\left\langle L_{D(A)}\left\|\hat{V}_{e-n_B}\right\|L_{D(A)}\right\rangle+\left\langle L_{D(A)}\left\|\hat{V}_{e-n_{A(D)}}\right\|L_{D(A)}\right\rangle$ $-\left\langle H_{A(D)}\left\|\hat{V}_{e-n_{D(A)}}\right\|H_{A(D)}\right\rangle-\left\langle H_{A(D)}\left\|\hat{V}_{e-n_B}\right\|H_{A(D)}\right\rangle-\left\langle H_B\left\|\hat{V}_{e-n_A}\right\|H_B\right\rangle-\left\langle H_B\left\|\hat{V}_{e-n_D}\right\|H_B\right\rangle$ $-3J_{H_BH_{A(D)}}-2J_{H_{D(A)}H_B}-2J_{H_DH_A}+J_{L_{D(A)}L_B}+J_{H_{A(D)}L_B}+2J_{H_{D(A)}L_B}+J_{H_BL_{D(A)}}+J_{H_{A(D)}L_{D(A)}}$ $+\frac{3}{2}K_{H_BH_{A(D)}}+K_{H_{D(A)}H_B}+K_{H_DH_A}-\frac{1}{2}K_{L_{D(A)}L_B}-\frac{1}{2}K_{H_{A(D)}L_B}+\frac{1}{2}K_{H_{D(A)}L_B}-K_{H_BL_{D(A)}}+\frac{1}{2}K_{H_{A(D)}L_{D(A)}}$
CTDE (B^{+})	$\left\|D^{+-}B^{+}A^{-}\right\rangle_{CTP}$ $\left\|D^{-}B^{+}A^{+-}\right\rangle_{CTP}$	$IP^{D(A)}+IP^{B}-EA^{D}-EA^{A}-J_{H_{D(A)}L_{D(A)}}$ $+\left\langle L_D\left\|\hat{V}_{e-n_A}\right\|L_D\right\rangle+\left\langle L_D\left\|\hat{V}_{e-n_B}\right\|L_D\right\rangle+\left\langle L_A\left\|\hat{V}_{e-n_D}\right\|L_A\right\rangle+\left\langle L_A\left\|\hat{V}_{e-n_B}\right\|L_A\right\rangle$ $-\left\langle H_{D(A)}\left\|\hat{V}_{e-n_{A(D)}}\right\|H_{D(A)}\right\rangle-\left\langle H_{D(A)}\left\|\hat{V}_{e-n_B}\right\|H_{D(A)}\right\rangle-\left\langle H_B\left\|\hat{V}_{e-n_D}\right\|H_B\right\rangle-\left\langle H_B\left\|\hat{V}_{e-n_A}\right\|H_B\right\rangle$ $-3J_{H_{D(A)}H_B}-2J_{H_DH_A}-2J_{H_BH_{A(D)}}+J_{L_DL_A}+J_{L_DH_B}+2J_{L_{D(A)}H_{A(D)}}+J_{H_{D(A)}L_{A(D)}}+J_{H_BL_A}$ $+\frac{5}{2}K_{H_{D(A)}H_B}+K_{H_DH_A}+K_{H_BH_{A(D)}}+\frac{1}{2}K_{L_DL_A}+\frac{1}{2}K_{L_{D(A)}H_B}-K_{L_{D(A)}H_{A(D)}}+\frac{1}{2}K_{H_{D(A)}L_{A(D)}}-K_{H_BL_{A(D)}}$
	$\left\|D^{+-}B^{+}A^{-}\right\rangle_{CSP}$ $\left\|D^{-}B^{+}A^{+-}\right\rangle_{CSP}$	$IP^{D(A)}+IP^{B}-EA^{D}-EA^{A}-J_{H_{D(A)}L_{D(A)}}+K_{H_DL_D}+K_{H_AL_A}$ $+\left\langle L_D\left\|\hat{V}_{e-n_A}\right\|L_D\right\rangle+\left\langle L_D\left\|\hat{V}_{e-n_B}\right\|L_D\right\rangle+\left\langle L_A\left\|\hat{V}_{e-n_D}\right\|L_A\right\rangle+\left\langle L_A\left\|\hat{V}_{e-n_B}\right\|L_A\right\rangle$ $-\left\langle H_{D(A)}\left\|\hat{V}_{e-n_{A(D)}}\right\|H_{D(A)}\right\rangle-\left\langle H_{D(A)}\left\|\hat{V}_{e-n_B}\right\|H_{D(A)}\right\rangle-\left\langle H_B\left\|\hat{V}_{e-n_D}\right\|H_B\right\rangle-\left\langle H_B\left\|\hat{V}_{e-n_A}\right\|H_B\right\rangle$ $-3J_{H_{D(A)}H_B}-2J_{H_DH_A}-2J_{H_BH_{A(D)}}+J_{L_DL_A}+J_{L_DH_B}+2J_{L_{D(A)}H_{A(D)}}+J_{H_{D(A)}L_{A(D)}}+J_{H_BL_A}$ $+\frac{3}{2}K_{H_{D(A)}H_B}+K_{H_DH_A}+K_{H_BH_{A(D)}}-\frac{1}{2}K_{L_DL_A}-\frac{1}{2}K_{L_{D(A)}H_B}+\frac{1}{2}K_{L_{D(A)}H_{A(D)}}-K_{H_{D(A)}L_{A(D)}}+\frac{1}{2}K_{H_BL_{A(D)}}$
CTDE (B^{-})	$\left\|D^{+}B^{-}A^{+-}\right\rangle_{CTP}$ $\left\|D^{+-}B^{-}A^{+}\right\rangle_{CTP}$	$IP^{D}+IP^{A}-EA^{B}-EA^{A(D)}-J_{H_{A(D)}L_{A(D)}}$ $+\left\langle L_B\left\|\hat{V}_{e-n_D}\right\|L_B\right\rangle+\left\langle L_B\left\|\hat{V}_{e-n_A}\right\|L_B\right\rangle+\left\langle L_{A(D)}\left\|\hat{V}_{e-n_{D(A)}}\right\|L_{A(D)}\right\rangle+\left\langle L_{A(D)}\left\|\hat{V}_{e-n_B}\right\|L_{A(D)}\right\rangle$ $-\left\langle H_A\left\|\hat{V}_{e-n_D}\right\|H_A\right\rangle-\left\langle H_A\left\|\hat{V}_{e-n_B}\right\|H_A\right\rangle-\left\langle H_D\left\|\hat{V}_{e-n_A}\right\|H_D\right\rangle-\left\langle H_D\left\|\hat{V}_{e-n_B}\right\|H_D\right\rangle$ $-3J_{H_DH_A}-2J_{H_DH_B}-2J_{H_BH_A}+J_{L_BL_{A(D)}}+J_{H_DL_B}+J_{H_AL_B}+J_{H_{D(A)}L_{A(D)}}+2J_{H_BL_{A(D)}}$ $+\frac{5}{2}K_{H_DH_A}+K_{H_DH_B}+K_{H_BH_A}+\frac{1}{2}K_{L_BL_{A(D)}}-K_{H_{D(A)}L_B}+\frac{1}{2}K_{H_{A(D)}L_B}+\frac{1}{2}K_{H_{D(A)}L_{A(D)}}-K_{H_BL_{A(D)}}$
	$\left\|D^{+}B^{-}A^{+-}\right\rangle_{CSP}$ $\left\|D^{+-}B^{-}A^{+}\right\rangle_{CSP}$	$IP^{D}+IP^{A}-EA^{B}-EA^{A(D)}-J_{H_{A(D)}L_{A(D)}}+K_{H_BL_B}+K_{H_{A(D)}L_{A(D)}}$ $+\left\langle L_B\left\|\hat{V}_{e-n_D}\right\|L_B\right\rangle+\left\langle L_B\left\|\hat{V}_{e-n_A}\right\|L_B\right\rangle+\left\langle L_{A(D)}\left\|\hat{V}_{e-n_{D(A)}}\right\|L_{A(D)}\right\rangle+\left\langle L_{A(D)}\left\|\hat{V}_{e-n_B}\right\|L_{A(D)}\right\rangle$ $-\left\langle H_A\left\|\hat{V}_{e-n_D}\right\|H_A\right\rangle-\left\langle H_A\left\|\hat{V}_{e-n_B}\right\|H_A\right\rangle-\left\langle H_D\left\|\hat{V}_{e-n_A}\right\|H_D\right\rangle-\left\langle H_D\left\|\hat{V}_{e-n_B}\right\|H_D\right\rangle$ $-3J_{H_DH_A}-2J_{H_DH_B}-2J_{H_BH_A}+J_{L_BL_{A(D)}}+J_{H_DL_B}+J_{H_AL_B}+J_{H_{D(A)}L_{A(D)}}+2J_{H_BL_{A(D)}}$ $+\frac{3}{2}K_{H_DH_A}+K_{H_DH_B}+K_{H_BH_A}-\frac{1}{2}K_{L_BL_{A(D)}}+K_{H_{D(A)}L_B}-\frac{1}{2}K_{H_{A(D)}L_B}-\frac{1}{2}K_{H_{D(A)}L_{A(D)}}-K_{H_BL_{A(D)}}$

DE (B^+)	$\left\|D^+B^+A^{--}\right\rangle$ $\left\|D^{--}B^+A^+\right\rangle$	$IP^{D(A)} + IP^B - 2EA^{A(D)} + J_{L_AL_A}$ $+2\left\langle L_A\left\|\hat{V}_{e-n_D}\right\|L_A\right\rangle + 2\left\langle L_A\left\|\hat{V}_{e-n_B}\right\|L_A\right\rangle$ $-\left\langle H_{D(A)}\left\|\hat{V}_{e-n_{A(D)}}\right\|H_{D(A)}\right\rangle - \left\langle H_{D(A)}\left\|\hat{V}_{e-n_B}\right\|H_{D(A)}\right\rangle - \left\langle H_B\left\|\hat{V}_{e-n_D}\right\|H_B\right\rangle - \left\langle H_B\left\|\hat{V}_{e-n_A}\right\|H_B\right\rangle$ $-3J_{H_{D(A)}H_B} - 2J_{H_DH_A} - 2J_{H_BH_{A(D)}} + 2J_{H_{D(A)}L_{A(D)}} + 2J_{H_BL_{A(D)}}$ $+2K_{H_{D(A)}H_B} + K_{H_DH_A} + K_{H_BH_{A(D)}} - K_{H_{D(A)}L_{A(D)}} - K_{H_BL_{A(D)}}$
DE (B^-)	$\left\|D^+B^{--}A^+\right\rangle$	$IP^D + IP^A - 2EA^B + J_{L_BL_B}$ $+2\left\langle L_B\left\|\hat{V}_{e-n_D}\right\|L_B\right\rangle + 2\left\langle L_B\left\|\hat{V}_{e-n_A}\right\|L_B\right\rangle$ $-\left\langle H_D\left\|\hat{V}_{e-n_A}\right\|H_D\right\rangle - \left\langle H_D\left\|\hat{V}_{e-n_B}\right\|H_D\right\rangle - \left\langle H_A\left\|\hat{V}_{e-n_D}\right\|H_A\right\rangle - \left\langle H_A\left\|\hat{V}_{e-n_B}\right\|H_A\right\rangle$ $-3J_{H_DH_A} - 2J_{H_DH_B} - 2J_{H_BH_A} + 2J_{H_DL_B} + 2J_{H_AL_B}$ $+2K_{H_DH_A} + K_{H_DH_B} + K_{H_BH_A} - K_{H_DL_B} - K_{H_AL_B}$

Table 7.1 Analytical exact expressions for basis-state energies. 1st column: Names of the different groups of the basis states for the D-B-A system. 2nd column: Mathematical notation of the spin-adapted (SA) many-electron basis states. 3rd column: Exact expressions for the excitation energies of these states of the D-B-A system as a function of ionization potentials, electron affinities, core terms and two-electron integrals.

The table below shows detailed expressions for the off-diagonal Hamiltonian elements as a function of 2e integrals and Fock Matrix elements. We separated them, into couplings between singly-excited states $\left(V_{LE-LE}, V_{LE-CT}, V_{CT-CT}\right)$, into couplings between singly- and doubly-excited and between doubly-excited states. It is worth noting that integrals containing molecular orbitals of all the three fragments are very weak compared to the rest (two to three orders of magnitude smaller) and thus can be ignored (e.g., $\left(P_i Q_j \left| Q_k P_k \right.\right) \approx 0$). In the following notation we use $i, j, k = D, B, A$ meaning different monomers and $i \to j$ for CT state where an electron is transferred from i to j monomer (e.g., $V_{LE-CTDE}^{D,D\to B;A}$ denote the coupling between a LE state on D monomer (initial) and a CTDE state that includes D-to-B CT exciton and a LE on A monomer state). Also, the off-diagonal elements of the overlap matrix are very close to zero and thus are vanishing ($S_{P_iQ_j} \approx 0$, $P_i \neq Q_j$) while the diagonal elements are unity ($S_{P_iP_i} = 1$). [1,4,5] For example, the exact expression of $V_{LE-CT}^{D,D\to A}$ coupling contains terms of the form $S_{L_DL_A}\left(\left\langle H_D\left|\hat{h}^{1e}\right|H_D\right\rangle + 2\left\langle H_A\left|\hat{h}^{1e}\right|H_A\right\rangle\right) + S_{H_DL_A}\left\langle H_D\left|\hat{h}^{1e}\right|L_D\right\rangle$, which can be ignored since the off-diagonal elements of the overlap matrix are too small and so the whole term is zeroed.

Matrix Element	not.	$\langle \lvert \hat{h}^{1e} \rvert \rangle$	$\langle \lvert \hat{V}^{2e} \rvert \rangle$
Couplings between Singly - Excited States			
$\langle D^{+-}BA\lvert \hat{H} \rvert D^{+}B^{-}A\rangle$	$V_{LE-CT}^{D,D\to B}$	$\langle L_D\lvert \hat{F}\rvert L_B\rangle + 2(L_DH_D\lvert H_DL_B) - (L_DL_B\lvert H_DH_D)$	
$\langle D^{+-}BA\lvert \hat{H} \rvert D^{+}BA^{-}\rangle$	$V_{LE-CT}^{D,D\to A}$	$\langle L_D\lvert \hat{F}\rvert L_A\rangle + 2(L_DH_D\lvert H_DL_A) - (L_DL_A\lvert H_DH_D)$	
$\langle D^{+-}BA\lvert \hat{H} \rvert D^{-}B^{+}A\rangle$	$V_{LE-CT}^{D,B\to D}$	$-\langle H_D\lvert \hat{F}\rvert H_B\rangle + 2(L_DH_D\lvert H_BL_D) - (H_DH_B\lvert L_DL_D)$	
$\langle D^{+-}BA\lvert \hat{H} \rvert D^{-}BA^{+}\rangle$	$V_{LE-CT}^{D,A\to D}$	$-\langle H_D\lvert \hat{F}\rvert H_A\rangle + 2(L_DH_D\lvert H_AL_D) - (H_DH_A\lvert L_DL_D)$	
$\langle D^{+-}BA\lvert \hat{H} \rvert DB^{+-}A\rangle$	$V_{LE-LE}^{D,B}$	----------	$2(L_DH_D\lvert H_BL_B) - (L_DL_B\lvert H_BH_D)$
$\langle D^{+-}BA\lvert \hat{H} \rvert DB^{+}A^{-}\rangle$	$V_{LE-CT}^{D,B\to A}$	----------	$2(L_DH_D\lvert H_BL_A) - (L_DL_A\lvert H_BH_D) \approx 0$
$\langle D^{+-}BA\lvert \hat{H} \rvert DB^{-}A^{+}\rangle$	$V_{LE-CT}^{D,A\to B}$	----------	$2(L_DH_D\lvert H_AL_B) - (L_DL_B\lvert H_AH_D) \approx 0$
$\langle D^{+}B^{-}A\lvert \hat{H} \rvert D^{+}BA^{-}\rangle$	$V_{CT-CT}^{D\to B,D\to A}$	$\langle L_B\lvert \hat{F}\rvert L_A\rangle + 2(L_BH_D\lvert H_DL_A) - (L_BL_A\lvert H_DH_D) \approx \langle L_B\lvert \hat{F}\rvert L_A\rangle$	
$\langle D^{+}B^{-}A\lvert \hat{H} \rvert D^{-}B^{+}A\rangle$	$V_{CT-CT}^{D\to B,B\to D}$	----------	$2(L_BH_D\lvert H_BL_D) - (L_BL_D\lvert H_BH_D)$
$\langle D^{+}B^{-}A\lvert \hat{H} \rvert D^{-}BA^{+}\rangle$	$V_{CT-CT}^{D\to B,A\to D}$	----------	$2(L_BH_D\lvert H_AL_D) - (L_BL_D\lvert H_AH_D) \approx 0$
$\langle D^{+}B^{-}A\lvert \hat{H} \rvert DB^{+-}A\rangle$	$V_{CT-LE}^{D\to B,B}$	$-\langle H_D\lvert \hat{F}\rvert H_B\rangle + 2(H_DL_B\lvert L_BH_B) - (H_DH_B\lvert L_BL_B)$	
$\langle D^{+}B^{-}A\lvert \hat{H} \rvert DB^{+}A^{-}\rangle$	$V_{CT-CT}^{D\to B,B\to A}$	----------	$2(H_DL_B\lvert L_AH_B) - (H_DH_B\lvert L_AL_B) \approx 0$
$\langle D^{+}B^{-}A\lvert \hat{H} \rvert DB^{-}A^{+}\rangle$	$V_{CT-CT}^{D\to B,A\to B}$	$-\langle H_D\lvert \hat{F}\rvert H_A\rangle + 2(H_DL_B\lvert L_BH_A) - (H_DH_A\lvert L_BL_B) \approx -\langle H_D\lvert \hat{F}\rvert H_A\rangle$	
$\langle D^{+}BA^{-}\lvert \hat{H} \rvert D^{-}B^{+}A\rangle$	$V_{CT-CT}^{D\to A,B\to D}$	----------	$2(L_AH_D\lvert H_BL_D) - (L_AL_D\lvert H_BH_D) \approx 0$
$\langle D^{+}BA^{-}\lvert \hat{H} \rvert D^{-}BA^{+}\rangle$	$V_{CT-CT}^{D\to A,A\to D}$	----------	$2(L_AH_D\lvert H_AL_D) - (L_AL_D\lvert H_AH_D)$
$\langle D^{+}BA^{-}\lvert \hat{H} \rvert DB^{+-}A\rangle$	$V_{CT-LE}^{D\to A,B}$	----------	$2(L_AH_D\lvert H_BL_B) - (L_AL_B\lvert H_BH_D) \approx 0$
$\langle D^{+}BA^{-}\lvert \hat{H} \rvert DB^{+}A^{-}\rangle$	$V_{CT-CT}^{D\to A,B\to A}$	$-\langle H_D\lvert \hat{F}\rvert H_B\rangle + 2(H_DL_A\lvert L_AH_B) - (H_DH_B\lvert L_AL_A) \approx -\langle H_D\lvert \hat{F}\rvert H_B\rangle$	
$\langle D^{+}BA^{-}\lvert \hat{H} \rvert DB^{-}A^{+}\rangle$	$V_{CT-CT}^{D\to A,A\to B}$	----------	$2(L_AH_D\lvert H_AL_B) - (L_AL_B\lvert H_AH_D) \approx 0$
$\langle D^{-}B^{+}A\lvert \hat{H} \rvert D^{-}BA^{+}\rangle$	$V_{CT-CT}^{B\to D,A\to D}$	$-\langle H_B\lvert \hat{F}\rvert H_A\rangle + 2(H_BL_D\lvert L_DH_A) - (H_BH_A\lvert L_DL_D) \approx -\langle H_B\lvert \hat{F}\rvert H_A\rangle$	
$\langle D^{-}B^{+}A\lvert \hat{H} \rvert DB^{+-}A\rangle$	$V_{CT-LE}^{B\to D,B}$	$\langle L_D\lvert \hat{F}\rvert L_B\rangle + 2(H_BL_D\lvert L_BH_B) - (H_BH_B\lvert L_DL_B)$	

$\langle D^- B^+ A \vert \hat{H} \vert D B^+ A^- \rangle$	$V_{CT-CT}^{B\to D, B\to A}$	$\langle L_D \vert \hat{F} \vert L_A \rangle + 2(H_B L_D \vert L_A H_B) - (H_B H_B \vert L_D L_A)$ $\approx \langle L_D \vert \hat{F} \vert L_A \rangle$	
$\langle D^- B^+ A \vert \hat{H} \vert D B^- A^+ \rangle$	$V_{CT-CT}^{B\to D, A\to B}$	----------	$2(H_B L_D \vert L_B H_A) - (H_A H_B \vert L_D L_B) \approx 0$
$\langle D^- B A^+ \vert \hat{H} \vert D B^{+-} A \rangle$	$V_{CT-LE}^{A\to D, B}$	----------	$2(L_D H_A \vert H_B L_B) - (L_D L_B \vert H_B H_A) \approx 0$
$\langle D^- B A^+ \vert \hat{H} \vert D B^+ A^- \rangle$	$V_{CT-CT}^{A\to D, B\to A}$	----------	$2(L_D H_A \vert H_B L_A) - (L_D L_A \vert H_B H_A) \approx 0$
$\langle D B^{+-} A \vert \hat{H} \vert D B^+ A^- \rangle$	$V_{LE-CT}^{B, B\to A}$	$\langle L_B \vert \hat{F} \vert L_A \rangle + 2(L_B H_B \vert H_B L_A) - (L_B L_A \vert H_B H_B)$	
$\langle D B^{+-} A \vert \hat{H} \vert D B^- A^+ \rangle$	$V_{LE-CT}^{B, A\to B}$	$-\langle H_B \vert \hat{F} \vert H_A \rangle + 2(H_B L_B \vert L_B H_A) - (H_B H_A \vert L_B L_B)$	
$\langle D B^+ A^- \vert \hat{H} \vert D B^- A^+ \rangle$	$V_{CT-CT}^{B\to A, A\to B}$	----------	$2(L_A H_B \vert H_A L_B) - (L_A L_B \vert H_A H_B)$
Couplings between Singly- and Doubly – Excited States			
$\langle D^{+-} B A \vert \hat{H} \vert D^{+-} B A^{+-} \rangle_{CSP}$	$V_{LE-LDE}^{D,D;A}$	$\frac{2}{\sqrt{2}} \langle L_A \vert \hat{h}^{1e} \vert H_A \rangle$	$\frac{1}{\sqrt{2}} \begin{bmatrix} 2(H_A L_A \vert H_D H_D) + 2(H_A L_A \vert L_D L_D) \\ +2(H_A L_A \vert H_A H_A) + 4(H_A L_A \vert H_B H_B) \\ -2(H_A H_B \vert H_B L_A) - (H_A H_D \vert H_D L_A) \\ -(H_A L_D \vert L_D L_A) \end{bmatrix}$
$\langle D^{+-} B A \vert \hat{H} \vert D^{+-} B A^{+-} \rangle_{CTP}$		----------	$\sqrt{\frac{3}{2}} (H_D L_A \vert H_A H_D) - \sqrt{\frac{3}{2}} (L_D L_A \vert H_A L_D)$
$\langle D^{+-} B A \vert \hat{H} \vert D^+ B^- A^{+-} \rangle_{CSP}$	$V_{LE-CTDE}^{D,D\to B;A}$	----------	$\frac{2}{\sqrt{2}} (L_D L_B \vert H_A L_A) - \frac{1}{\sqrt{2}} (L_D L_A \vert H_A L_B) \approx 0$
$\langle D^{+-} B A \vert \hat{H} \vert D^+ B^- A^{+-} \rangle_{CTP}$		----------	$-\sqrt{\frac{3}{2}} (L_D L_A \vert H_A L_B) \approx 0$
$\langle D^{+-} B A \vert \hat{H} \vert D^{+-} B^- A^+ \rangle_{CSP}$	$V_{LE-CTDE}^{D,A\to B;D}$	$\frac{2}{\sqrt{2}} \langle L_B \vert \hat{h}^{1e} \vert H_A \rangle$	$\frac{1}{\sqrt{2}} \begin{bmatrix} \cancel{2(H_A L_B \vert H_D H_D)} + \cancel{2(H_A L_B \vert L_D L_D)} \\ +2(H_A L_B \vert H_A H_A) + 4(H_A L_B \vert H_B H_B) \\ -2(H_A H_B \vert H_B L_B) - \cancel{(H_A H_D \vert H_D L_B)} \\ \cancel{-(H_A L_D \vert L_D L_B)} \end{bmatrix}$
$\langle D^{+-} B A \vert \hat{H} \vert D^{+-} B^- A^+ \rangle_{CTP}$		----------	$\sqrt{\frac{3}{2}} (H_D L_B \vert H_A H_D) - \sqrt{\frac{3}{2}} (L_D L_B \vert H_A L_D) \approx 0$

$\langle D^{+-}BA\vert\hat{H}\vert D^{+-}B^{+}A^{-}\rangle_{CSP}$	$V_{LE-CTDE}^{D,B\to A;D}$	$-\frac{2}{\sqrt{2}}\langle L_A\vert\hat{h}^{le}\vert H_B\rangle$	$-\frac{1}{\sqrt{2}}\begin{bmatrix}2\cancel{\left(H_BL_A\vert H_DH_D\right)}+2\cancel{\left(H_BL_A\vert L_DL_D\right)}\\+2\left(H_BL_A\vert H_BH_B\right)+4\left(H_BL_A\vert H_AH_A\right)\\-2\left(H_BH_A\vert H_AL_A\right)-\cancel{\left(H_BH_D\vert H_DL_A\right)}\\-\cancel{\left(H_BL_D\vert L_DL_A\right)}\end{bmatrix}$
$\langle D^{+-}BA\vert\hat{H}\vert D^{+-}B^{+}A^{-}\rangle_{CTP}$		----------	$-\sqrt{\frac{3}{2}}\left(H_DL_A\vert H_BH_D\right)+\sqrt{\frac{3}{2}}\left(L_DL_A\vert H_BL_D\right)\approx 0$
$\langle D^{+-}BA\vert\hat{H}\vert D^{-}B^{+}A^{+-}\rangle_{CSP}$	$V_{LE-CTDE}^{D,B\to D;A}$	----------	$\frac{2}{\sqrt{2}}\left(H_BH_D\vert H_AL_A\right)-\frac{1}{\sqrt{2}}\left(H_BL_A\vert H_AH_D\right)\approx 0$
$\langle D^{+-}BA\vert\hat{H}\vert D^{-}B^{+}A^{+-}\rangle_{CTP}$		----------	$-\sqrt{\frac{3}{2}}\left(H_BL_A\vert H_AH_D\right)\approx 0$
$\langle D^{+-}BA\vert\hat{H}\vert DB^{+-}A^{+-}\rangle_{CSP}$	$V_{LE-LDE}^{D,B;A}$	----------	----------
$\langle D^{+-}BA\vert\hat{H}\vert DB^{+-}A^{+-}\rangle_{CTP}$		----------	----------
$\langle D^{+}B^{-}A\vert\hat{H}\vert D^{+-}B^{+}A^{-}\rangle_{CSP}$	$V_{CT-CTDE}^{D\to B,B\to A;D}$	----------	$-\frac{2}{\sqrt{2}}\left(L_BL_D\vert H_BL_A\right)+\frac{1}{\sqrt{2}}\left(L_BL_A\vert H_BL_D\right)\approx 0$
$\langle D^{+}B^{-}A\vert\hat{H}\vert D^{+-}B^{+}A^{-}\rangle_{CTP}$		----------	$\sqrt{\frac{3}{2}}\left(L_BL_A\vert H_BL_D\right)\approx 0$
$\langle D^{+}B^{-}A\vert\hat{H}\vert D^{-}B^{+}A^{+-}\rangle_{CSP}$	$V_{CT-CTDE}^{D\to B,B\to D;A}$	----------	----------
$\langle D^{+}B^{-}A\vert\hat{H}\vert D^{-}B^{+}A^{+-}\rangle_{CTP}$		----------	----------
$\langle D^{+}B^{-}A\vert\hat{H}\vert D^{+-}BA^{+-}\rangle_{CSP}$	$V_{CT-LDE}^{D\to B,D;A}$	----------	$\frac{2}{\sqrt{2}}\left(L_BL_D\vert H_AL_A\right)-\frac{1}{\sqrt{2}}\left(L_BL_A\vert H_AL_D\right)\approx 0$
$\langle D^{+}B^{-}A\vert\hat{H}\vert D^{+-}BA^{+-}\rangle_{CTP}$		----------	$-\sqrt{\frac{3}{2}}\left(L_BL_A\vert H_AL_D\right)\approx 0$
$\langle D^{+}B^{-}A\vert\hat{H}\vert D^{+}B^{-}A^{+-}\rangle_{CSP}$	$V_{CT-CTDE}^{D\to B,D\to B;A}$	$\frac{2}{\sqrt{2}}\langle H_A\vert\hat{h}^{le}\vert L_A\rangle$	$\frac{1}{\sqrt{2}}\begin{bmatrix}2\left(H_AL_A\vert H_DH_D\right)+2\left(H_AL_A\vert L_BL_B\right)\\+2\left(H_AL_A\vert H_AH_A\right)+4\left(H_AL_A\vert H_BH_B\right)\\-2\left(H_AH_B\vert H_BL_A\right)-\left(H_AH_D\vert H_DL_A\right)\\-\left(H_AL_B\vert L_BL_A\right)\end{bmatrix}$
$\langle D^{+}B^{-}A\vert\hat{H}\vert D^{+}B^{-}A^{+-}\rangle_{CTP}$		----------	$\sqrt{\frac{3}{2}}\left(H_DL_A\vert H_AH_D\right)-\sqrt{\frac{3}{2}}\left(L_BL_A\vert H_AL_B\right)$

$\langle D^+B^-A\vert\hat{H}\vert D^{+-}B^-A^+\rangle_{CSP}$	$V_{CT-CTDE}^{D\to B,A\to B;D}$	$-\frac{1}{\sqrt{2}}\langle H_A\vert\hat{h}^{1e}\vert L_D\rangle$	$-\frac{1}{\sqrt{2}}\begin{bmatrix}2\cancel{\left(H_AL_D\vert H_BH_B\right)}-2\cancel{\left(H_AL_B\vert L_BL_D\right)}\\+\left(H_DL_D\vert H_AH_D\right)+\left(H_AL_D\vert H_DH_D\right)\\+\cancel{\left(H_AL_D\vert L_BL_B\right)}+\left(H_AL_D\vert H_AH_A\right)\\-\cancel{\left(H_AH_B\vert H_BL_D\right)}\end{bmatrix}$
$\langle D^+B^-A\vert\hat{H}\vert D^{+-}B^-A^+\rangle_{CTP}$		----------	$-\sqrt{\frac{3}{2}}\left(H_BL_D\vert H_AH_B\right)+\sqrt{\frac{3}{2}}\left(L_BL_D\vert H_AL_B\right)\approx 0$
$\langle D^+B^-A\vert\hat{H}\vert DB^{+-}A^{+-}\rangle_{CSP}$	$V_{CT-LDE}^{D\to B,B;A}$	----------	$\frac{2}{\sqrt{2}}\left(H_BH_D\vert H_AL_A\right)-\frac{1}{\sqrt{2}}\left(H_BL_A\vert H_AH_D\right)\approx 0$
$\langle D^+B^-A\vert\hat{H}\vert DB^{+-}A^{+-}\rangle_{CTP}$		----------	$-\sqrt{\frac{3}{2}}\left(H_BL_A\vert H_AH_D\right)\approx 0$
$\langle D^+BA^-\vert\hat{H}\vert D^{+-}BA^{+-}\rangle_{CSP}$	$V_{CT-LDE}^{D\to A,D;A}$	$-\frac{1}{\sqrt{2}}\langle H_A\vert\hat{h}^{1e}\vert L_D\rangle$	$-\frac{1}{\sqrt{2}}\begin{bmatrix}2\cancel{\left(H_AL_D\vert H_BH_B\right)}-2\left(H_AL_A\vert L_AL_D\right)\\+\left(H_DL_D\vert H_AH_D\right)+\left(H_AL_D\vert H_DH_D\right)\\+\left(H_AL_D\vert L_AL_A\right)+\left(H_AL_D\vert H_AH_A\right)\\-\cancel{\left(H_AH_B\vert H_BL_D\right)}\end{bmatrix}$
$\langle D^+BA^-\vert\hat{H}\vert D^{+-}BA^{+-}\rangle_{CTP}$		----------	$-\sqrt{\frac{3}{2}}\left(H_BL_D\vert H_AH_B\right)+\sqrt{\frac{3}{2}}\left(L_AL_D\vert H_AL_A\right)$ $\approx\sqrt{\frac{3}{2}}\left(L_AL_D\vert H_AL_A\right)$
$\langle D^+BA^-\vert\hat{H}\vert D^+B^-A^{+-}\rangle_{CSP}$	$V_{CT-CTDE}^{D\to A,D\to B;A}$	$-\frac{1}{\sqrt{2}}\langle H_A\vert\hat{h}^{1e}\vert L_B\rangle$	$-\frac{1}{\sqrt{2}}\begin{bmatrix}2\left(H_AL_B\vert H_BH_B\right)-2\left(H_AL_A\vert L_AL_B\right)\\+\cancel{\left(H_DL_B\vert H_AH_D\right)}+\cancel{\left(H_AL_B\vert H_DH_D\right)}\\+\left(H_AL_B\vert L_AL_A\right)+\left(H_AL_B\vert H_AH_A\right)\\-\left(H_AH_B\vert H_BL_B\right)\end{bmatrix}$
$\langle D^+BA^-\vert\hat{H}\vert D^+B^-A^{+-}\rangle_{CTP}$		----------	$-\sqrt{\frac{3}{2}}\left(H_BL_B\vert H_AH_B\right)+\sqrt{\frac{3}{2}}\left(L_AL_B\vert H_AL_A\right)$
$\langle D^+BA^-\vert\hat{H}\vert D^{+-}B^-A^+\rangle_{CSP}$	$V_{CT-CTDE}^{D\to A,A\to B;D}$	----------	$\frac{2}{\sqrt{2}}\left(L_AL_D\vert H_AL_B\right)-\frac{1}{\sqrt{2}}\left(L_AL_B\vert H_AL_D\right)\approx 0$
$\langle D^+BA^-\vert\hat{H}\vert D^{+-}B^-A^+\rangle_{CTP}$		----------	$-\sqrt{\frac{3}{2}}\left(L_AL_B\vert H_AL_D\right)\approx 0$

$\langle D^+BA^-\vert\hat{H}\vert D^{+-}B^+A^-\rangle_{CSP}$	$V_{CT-CTDE}^{D\to A,B\to A;D}$	$\frac{1}{\sqrt{2}}\langle H_B\vert\hat{h}^{1e}\vert L_D\rangle\frac{1}{\sqrt{2}}$	$\begin{bmatrix} \cancel{2\left(H_BL_D\vert H_AH_A\right)}-\cancel{2\left(H_BL_A\vert L_AL_D\right)} \\ +\left(H_DL_D\vert H_BH_D\right)+\left(H_BL_D\vert H_DH_D\right) \\ +\cancel{\left(H_BL_D\vert L_AL_A\right)}+\left(H_BL_D\vert H_BH_B\right) \\ -\cancel{\left(H_BH_A\vert H_AL_D\right)} \end{bmatrix}$
$\langle D^+BA^-\vert\hat{H}\vert D^{+-}B^+A^-\rangle_{CTP}$		----------	$\sqrt{\frac{3}{2}}\left(H_AL_D\vert H_BH_A\right)-\sqrt{\frac{3}{2}}\left(L_AL_D\vert H_BL_A\right)\approx 0$
$\langle D^+BA^-\vert\hat{H}\vert D^-B^+A^{+-}\rangle_{CSP}$	$V_{CT-CTDE}^{D\to A,B\to D;A}$	----------	$\frac{2}{\sqrt{2}}\left(H_BL_D\vert H_AH_D\right)-\frac{1}{\sqrt{2}}\left(H_BH_D\vert H_AL_D\right)\approx 0$
$\langle D^+BA^-\vert\hat{H}\vert D^-B^+A^{+-}\rangle_{CTP}$		----------	$-\sqrt{\frac{3}{2}}\left(H_BH_D\vert H_AL_D\right)\approx 0$
$\langle D^+BA^-\vert\hat{H}\vert DB^{+-}A^{+-}\rangle_{CSP}$	$V_{CT-LDE}^{D\to A,B;A}$	----------	$\frac{2}{\sqrt{2}}\left(H_BL_B\vert H_AH_D\right)-\frac{1}{\sqrt{2}}\left(H_BH_D\vert H_AL_B\right)\approx 0$
$\langle D^+BA^-\vert\hat{H}\vert DB^{+-}A^{+-}\rangle_{CTP}$		----------	$-\sqrt{\frac{3}{2}}\left(H_BH_D\vert H_AL_B\right)\approx 0$
$\langle D^-B^+A\vert\hat{H}\vert D^{+-}BA^{+-}\rangle_{CSP}$	$V_{CT-LDE}^{B\to D,D;A}$	----------	$-\frac{2}{\sqrt{2}}\left(H_DH_B\vert H_AL_A\right)+\frac{1}{\sqrt{2}}\left(H_DL_A\vert H_AH_B\right)\approx 0$
$\langle D^-B^+A\vert\hat{H}\vert D^{+-}BA^{+-}\rangle_{CTP}$		----------	$\sqrt{\frac{3}{2}}\left(H_DL_A\vert H_AH_B\right)\approx 0$
$\langle D^-B^+A\vert\hat{H}\vert D^+B^-A^{+-}\rangle_{CSP}$	$V_{CT-CTDE}^{B\to D,D\to B;A}$	----------	----------
$\langle D^-B^+A\vert\hat{H}\vert D^+B^-A^{+-}\rangle_{CTP}$		----------	----------
$\langle D^-B^+A\vert\hat{H}\vert D^{+-}B^-A^+\rangle_{CSP}$	$V_{CT-CTDE}^{B\to D,A\to B;D}$	----------	$-\frac{2}{\sqrt{2}}\left(H_DH_B\vert H_AL_B\right)+\frac{1}{\sqrt{2}}\left(H_DL_B\vert H_AH_B\right)\approx 0$
$\langle D^-B^+A\vert\hat{H}\vert D^{+-}B^-A^+\rangle_{CTP}$		----------	$\sqrt{\frac{3}{2}}\left(H_DL_B\vert H_AH_B\right)\approx 0$
$\langle D^-B^+A\vert\hat{H}\vert DB^{+-}A^{+-}\rangle_{CSP}$	$V_{CT-LDE}^{B\to D,B;A}$	----------	$-\frac{2}{\sqrt{2}}\left(L_DL_B\vert H_AL_A\right)+\frac{1}{\sqrt{2}}\left(L_DL_A\vert H_AL_B\right)\approx 0$
$\langle D^-B^+A\vert\hat{H}\vert DB^{+-}A^{+-}\rangle_{CTP}$		----------	$\sqrt{\frac{3}{2}}\left(L_DL_A\vert H_AL_B\right)\approx 0$

$\langle D^- B^+ A \vert \hat{H} \vert D^{+-} B^+ A^- \rangle_{CSP}$	$V_{CT-CTDE}^{B\to D, B\to A; D}$	$\frac{1}{\sqrt{2}}\langle H_D \vert \hat{h}^{1e} \vert L_A \rangle$	$\frac{1}{\sqrt{2}}\begin{bmatrix} 2(H_D L_A \vert H_A H_A) - 2(H_D L_D \vert L_D L_A) \\ +\cancel{(H_D H_B \vert H_B L_A)} + (H_D L_A \vert H_D H_D) \\ +\cancel{(H_D L_A \vert H_B H_B)} + (H_D L_A \vert L_D L_D) \\ -(H_D H_A \vert H_A L_A) \end{bmatrix}$
$\langle D^- B^+ A \vert \hat{H} \vert D^{+-} B^+ A^- \rangle_{CTP}$		----------	$\sqrt{\frac{3}{2}}(H_A L_A \vert H_D H_A) - \sqrt{\frac{3}{2}}(L_D L_A \vert H_D L_D)$
$\langle D^- B^+ A \vert \hat{H} \vert D^- B^+ A^{+-} \rangle_{CSP}$	$V_{CT-CTDE}^{B\to D, B\to D; A}$	$-\frac{2}{\sqrt{2}}\langle H_A \vert \hat{h}^{1e} \vert L_A \rangle$	$-\frac{1}{\sqrt{2}}\begin{bmatrix} 2(H_A L_A \vert H_B H_B) + 2(H_A L_A \vert L_D L_D) \\ +2(H_A L_A \vert H_A H_A) + 4(H_A L_A \vert H_D H_D) \\ -2(H_A H_D \vert H_D L_A) - (H_A H_B \vert H_B L_A) \\ -(H_A L_D \vert L_D L_A) \end{bmatrix}$
$\langle D^- B^+ A \vert \hat{H} \vert D^- B^+ A^{+-} \rangle_{CTP}$		----------	$-\sqrt{\frac{3}{2}}(H_A H_B \vert H_B L_A) + \sqrt{\frac{3}{2}}(H_A L_D \vert L_D L_A)$
$\langle D^- B A^+ \vert \hat{H} \vert D B^{+-} A^{+-} \rangle_{CSP}$	$V_{CT-LDE}^{A\to D, B; A}$	----------	$-\frac{2}{\sqrt{2}}(L_D L_A \vert H_B L_B) + \frac{1}{\sqrt{2}}(L_D L_B \vert H_B L_A) \approx 0$
$\langle D^- B A^+ \vert \hat{H} \vert D B^{+-} A^{+-} \rangle_{CTP}$		----------	$\sqrt{\frac{3}{2}}(L_D L_B \vert H_B L_A) \approx 0$
$\langle D^- B A^+ \vert \hat{H} \vert D^+ B^- A^{+-} \rangle_{CSP}$	$V_{CT-CTDE}^{A\to D, D\to B; A}$	----------	$\frac{2}{\sqrt{2}}(H_D L_B \vert L_D L_A) - \frac{1}{\sqrt{2}}(H_D L_A \vert L_D L_B) \approx 0$
$\langle D^- B A^+ \vert \hat{H} \vert D^+ B^- A^{+-} \rangle_{CTP}$		----------	$-\sqrt{\frac{3}{2}}(H_D L_A \vert L_D L_B) \approx 0$
$\langle D^- B A^+ \vert \hat{H} \vert D^{+-} B A^{+-} \rangle_{CSP}$	$V_{CT-LDE}^{A\to D, D; A}$	$-\frac{1}{\sqrt{2}}\langle H_D \vert \hat{h}^{1e} \vert L_A \rangle$	$-\frac{1}{\sqrt{2}}\begin{bmatrix} \cancel{2(H_D L_A \vert H_B H_B)} - 2(H_D L_D \vert L_D L_A) \\ +(H_A L_A \vert H_D H_A) + (H_D L_A \vert H_D H_D) \\ +(H_D L_A \vert L_D L_D) + (H_D L_A \vert H_A H_A) \\ -\cancel{(H_D H_B \vert H_B L_A)} \end{bmatrix}$
$\langle D^- B A^+ \vert \hat{H} \vert D^{+-} B A^{+-} \rangle_{CTP}$		----------	$-\sqrt{\frac{3}{2}}(H_B L_A \vert H_D H_B) + \sqrt{\frac{3}{2}}(L_D L_A \vert H_D L_D)$ $\approx \sqrt{\frac{3}{2}}(L_D L_A \vert H_D L_D)$

$\langle D^- B A^+ \vert \hat{H} \vert D^{+-} B^- A^+ \rangle_{CSP}$	$V_{CT-CTDE}^{A\to D, A\to B; D}$	$-\frac{1}{\sqrt{2}}\langle H_D \vert \hat{h}^{le} \vert L_B \rangle$	$-\frac{1}{\sqrt{2}}\begin{bmatrix} 2(H_D L_B \vert H_B H_B) - 2(H_D L_D \vert L_D L_B) \\ +\cancel{(H_A L_B \vert H_D H_A)} + \cancel{(H_D L_B \vert H_A H_A)} \\ +(H_D L_B \vert L_D L_D) + (H_D L_B \vert H_D H_D) \\ -(H_D H_B \vert H_B L_B) \end{bmatrix}$
$\langle D^- B A^+ \vert \hat{H} \vert D^{+-} B^- A^+ \rangle_{CTP}$		----------	$-\sqrt{\frac{3}{2}}(H_B L_B \vert H_D H_B) + \sqrt{\frac{3}{2}}(L_D L_B \vert H_D L_D)$
$\langle D^- B A^+ \vert \hat{H} \vert D^{+-} B^+ A^- \rangle_{CSP}$	$V_{CT-CTDE}^{A\to D, B\to A; D}$	---------- ---	$\frac{2}{\sqrt{2}}(H_B L_A \vert H_D H_A) - \frac{1}{\sqrt{2}}(H_B H_A \vert H_D L_A) \approx 0$
$\langle D^- B A^+ \vert \hat{H} \vert D^{+-} B^+ A^- \rangle_{CTP}$		----------	$-\sqrt{\frac{3}{2}}(H_B H_A \vert H_D L_A) \approx 0$
$\langle D^- B A^+ \vert \hat{H} \vert D^- B^+ A^{+-} \rangle_{CSP}$	$V_{CT-CTDE}^{A\to D, B\to D; A}$	$\frac{1}{\sqrt{2}}\langle H_B \vert \hat{h}^{le} \vert L_A \rangle$	$\frac{1}{\sqrt{2}}\begin{bmatrix} \cancel{2(H_B L_A \vert H_D H_D)} - \cancel{2(H_B L_D \vert L_D L_A)} \\ +(H_A L_A \vert H_B H_A) + (H_B L_A \vert H_A H_A) \\ +\cancel{(H_B L_A \vert L_D L_D)} + (H_B L_A \vert H_B H_B) \\ -\cancel{(H_B H_D \vert H_D L_A)} \end{bmatrix}$
$\langle D^- B A^+ \vert \hat{H} \vert D^- B^+ A^{+-} \rangle_{CTP}$		----------	$\sqrt{\frac{3}{2}}(H_D L_A \vert H_B H_D) - \sqrt{\frac{3}{2}}(L_D L_A \vert H_B L_D) \approx 0$
$\langle D B^{+-} A \vert \hat{H} \vert D^{+-} B^+ A^- \rangle_{CSP}$	$V_{LE-CTDE}^{B, B\to A; D}$	----------	$-\frac{2}{\sqrt{2}}(H_D L_D \vert L_B L_A) + \frac{1}{\sqrt{2}}(H_D L_A \vert L_B L_D) \approx 0$
$\langle D B^{+-} A \vert \hat{H} \vert D^{+-} B^+ A^- \rangle_{CTP}$		----------	$\sqrt{\frac{3}{2}}(H_D L_A \vert L_B L_D) \approx 0$
$\langle D B^{+-} A \vert \hat{H} \vert D^- B^+ A^{+-} \rangle_{CSP}$	$V_{LE-CTDE}^{B, B\to D; A}$	----------	$-\frac{2}{\sqrt{2}}(H_A L_A \vert L_B L_D) + \frac{1}{\sqrt{2}}(H_A L_D \vert L_B L_A) \approx 0$
$\langle D B^{+-} A \vert \hat{H} \vert D^- B^+ A^{+-} \rangle_{CTP}$		----------	$\sqrt{\frac{3}{2}}(H_A L_D \vert L_B L_A) \approx 0$
$\langle D B^{+-} A \vert \hat{H} \vert D^{+-} B A^{+-} \rangle_{CSP}$	$V_{LE-LDE}^{B, D; A}$	----------	----------
$\langle D B^{+-} A \vert \hat{H} \vert D^{+-} B A^{+-} \rangle_{CTP}$		----------	----------
$\langle D B^{+-} A \vert \hat{H} \vert D^+ B^- A^{+-} \rangle_{CSP}$	$V_{LE-CTDE}^{B, D\to B; A}$	----------	$-\frac{2}{\sqrt{2}}(H_A L_A \vert H_D H_B) + \frac{1}{\sqrt{2}}(H_D L_A \vert H_A H_B) \approx 0$
$\langle D B^{+-} A \vert \hat{H} \vert D^+ B^- A^{+-} \rangle_{CTP}$		----------	$\sqrt{\frac{3}{2}}(H_D L_A \vert H_A H_B) \approx 0$

$\left\langle DB^{+-}A\middle\vert\hat{H}\middle\vert D^{+-}B^{-}A^{+}\right\rangle_{CSP}$	$V_{LE-CTDE}^{B,A\to B;D}$	----------	$-\frac{2}{\sqrt{2}}\left(H_DL_D\middle\vert H_AH_B\right)+\frac{1}{\sqrt{2}}\left(H_AL_D\middle\vert H_DH_B\right)\approx 0$
$\left\langle DB^{+-}A\middle\vert\hat{H}\middle\vert D^{+-}B^{-}A^{+}\right\rangle_{CTP}$		----------	$\sqrt{\frac{3}{2}}\left(H_AL_D\middle\vert H_DH_B\right)\approx 0$
$\left\langle DB^{+-}A\middle\vert\hat{H}\middle\vert DB^{+-}A^{+-}\right\rangle_{CSP}$	$V_{LE-LDE}^{B,B;A}$	$-\frac{2}{\sqrt{2}}\langle H_A\vert\hat{h}^{le}\vert L_A\rangle$	$-\frac{1}{\sqrt{2}}\begin{bmatrix}2\left(H_AL_A\middle\vert H_AH_A\right)+2\left(H_AL_A\middle\vert L_BL_B\right)\\+2\left(H_AL_A\middle\vert H_BH_B\right)+4\left(H_AL_A\middle\vert H_DH_D\right)\\-2\left(H_AH_D\middle\vert H_DL_A\right)-\left(H_AH_B\middle\vert H_BL_A\right)\\-\left(H_AL_B\middle\vert L_BL_A\right)\end{bmatrix}$
$\left\langle DB^{+-}A\middle\vert\hat{H}\middle\vert DB^{+-}A^{+-}\right\rangle_{CTP}$		----------	$\sqrt{\frac{3}{2}}\left(H_BL_A\middle\vert H_AH_B\right)-\sqrt{\frac{3}{2}}\left(L_BL_A\middle\vert H_AL_B\right)$
$\left\langle DB^{+}A^{-}\middle\vert\hat{H}\middle\vert D^{+-}BA^{+-}\right\rangle_{CSP}$	$V_{CT-LDE}^{B\to A,D;A}$	----------	$-\frac{2}{\sqrt{2}}\left(H_DL_D\middle\vert H_AH_B\right)+\frac{1}{\sqrt{2}}\left(H_DH_B\middle\vert H_AL_D\right)\approx 0$
$\left\langle DB^{+}A^{-}\middle\vert\hat{H}\middle\vert D^{+-}BA^{+-}\right\rangle_{CTP}$		----------	$\sqrt{\frac{3}{2}}\left(H_DH_B\middle\vert H_AL_D\right)\approx 0$
$\left\langle DB^{+}A^{-}\middle\vert\hat{H}\middle\vert D^{+}B^{-}A^{+-}\right\rangle_{CSP}$	$V_{CT-CTDE}^{B\to A,D\to B;A}$	----------	$-\frac{2}{\sqrt{2}}\left(H_DL_B\middle\vert H_AH_B\right)+\frac{1}{\sqrt{2}}\left(H_DH_B\middle\vert H_AL_B\right)\approx 0$
$\left\langle DB^{+}A^{-}\middle\vert\hat{H}\middle\vert D^{+}B^{-}A^{+-}\right\rangle_{CTP}$		----------	$\sqrt{\frac{3}{2}}\left(H_DH_B\middle\vert H_AL_B\right)\approx 0$
$\left\langle DB^{+}A^{-}\middle\vert\hat{H}\middle\vert D^{+-}B^{-}A^{+}\right\rangle_{CSP}$	$V_{CT-CTDE}^{B\to A,A\to B;D}$	----------	----------
$\left\langle DB^{+}A^{-}\middle\vert\hat{H}\middle\vert D^{+-}B^{-}A^{+}\right\rangle_{CTP}$		----------	----------
$\left\langle DB^{+}A^{-}\middle\vert\hat{H}\middle\vert D^{+-}B^{+}A^{-}\right\rangle_{CSP}$	$V_{CT-CTDE}^{B\to A,B\to A;D}$	$-\frac{2}{\sqrt{2}}\langle H_D\vert\hat{h}^{le}\vert L_D\rangle$	$-\frac{1}{\sqrt{2}}\begin{bmatrix}2\left(H_DL_D\middle\vert H_DH_D\right)+2\left(H_DL_D\middle\vert L_AL_A\right)\\+2\left(H_DL_D\middle\vert H_BH_B\right)+4\left(H_DL_D\middle\vert H_AH_A\right)\\-2\left(H_DH_A\middle\vert H_AL_D\right)-\left(H_DH_B\middle\vert H_BL_D\right)\\-\left(H_DL_A\middle\vert L_AL_D\right)\end{bmatrix}$
$\left\langle DB^{+}A^{-}\middle\vert\hat{H}\middle\vert D^{+-}B^{+}A^{-}\right\rangle_{CTP}$		----------	$\sqrt{\frac{3}{2}}\left(H_BL_D\middle\vert H_DH_B\right)-\sqrt{\frac{3}{2}}\left(L_AL_D\middle\vert H_DL_A\right)$
$\left\langle DB^{+}A^{-}\middle\vert\hat{H}\middle\vert D^{-}B^{+}A^{+-}\right\rangle_{CSP}$	$V_{CT-CTDE}^{B\to A,B\to D;A}$	$\frac{1}{\sqrt{2}}\langle H_A\vert\hat{h}^{le}\vert L_D\rangle$	$\frac{1}{\sqrt{2}}\begin{bmatrix}2\left(H_AL_D\middle\vert H_DH_D\right)-2\left(H_AL_A\middle\vert L_AL_D\right)\\+\cancel{\left(H_AH_B\middle\vert H_BL_D\right)}+\cancel{\left(H_AL_D\middle\vert H_BH_B\right)}\\+\left(H_AL_D\middle\vert H_AH_A\right)+\left(H_AL_D\middle\vert L_AL_A\right)\\-\left(H_AH_D\middle\vert H_DL_D\right)\end{bmatrix}$

$\left\langle DB^{+}A^{-}\middle\vert\hat{H}\middle\vert D^{-}B^{+}A^{+-}\right\rangle_{CTP}$		----------	$\sqrt{\frac{3}{2}}\left(H_D L_D \middle\vert H_A H_D\right)-\sqrt{\frac{3}{2}}\left(L_A L_D \middle\vert H_A L_A\right)$
$\left\langle DB^{+}A^{-}\middle\vert\hat{H}\middle\vert DB^{+-}A^{+-}\right\rangle_{CSP}$	$V_{CT-LDE}^{B\to A,B;A}$	$\frac{1}{\sqrt{2}}\langle H_A\vert\hat{h}^{le}\vert L_B\rangle$	$\frac{1}{\sqrt{2}}\begin{bmatrix}2\cancel{\left(H_A L_B \middle\vert H_D H_D\right)}-2\left(H_A L_A \middle\vert L_A L_B\right)\\+\left(H_A H_B \middle\vert H_B L_B\right)+\left(H_A L_B \middle\vert H_B H_B\right)\\+\left(H_A L_B \middle\vert H_A H_A\right)+\left(H_A L_B \middle\vert L_A L_A\right)\\-\cancel{\left(H_A H_D \middle\vert H_D L_B\right)}\end{bmatrix}$
$\left\langle DB^{+}A^{-}\middle\vert\hat{H}\middle\vert DB^{+-}A^{+-}\right\rangle_{CTP}$		----------	$\sqrt{\frac{3}{2}}\left(H_D L_B \middle\vert H_A H_D\right)-\sqrt{\frac{3}{2}}\left(L_A L_B \middle\vert H_A L_A\right)$ $\approx-\sqrt{\frac{3}{2}}\left(L_A L_B \middle\vert H_A L_A\right)$
$\left\langle DB^{-}A^{+}\middle\vert\hat{H}\middle\vert D^{+-}BA^{+-}\right\rangle_{CSP}$	$V_{CT-LDE}^{A\to B,D;A}$	----------	$\frac{2}{\sqrt{2}}\left(H_D L_D \middle\vert L_B L_A\right)-\frac{1}{\sqrt{2}}\left(H_D L_A \middle\vert L_B L_D\right)\approx 0$
$\left\langle DB^{-}A^{+}\middle\vert\hat{H}\middle\vert D^{+-}BA^{+-}\right\rangle_{CTP}$		----------	$-\sqrt{\frac{3}{2}}\left(H_D L_A \middle\vert L_B L_D\right)\approx 0$
$\left\langle DB^{-}A^{+}\middle\vert\hat{H}\middle\vert D^{+}B^{-}A^{+-}\right\rangle_{CSP}$	$V_{CT-CTDE}^{A\to B,D\to B;A}$	$-\frac{1}{\sqrt{2}}\langle H_D\vert\hat{h}^{le}\vert L_A\rangle$	$-\frac{1}{\sqrt{2}}\begin{bmatrix}2\cancel{\left(H_D L_A \middle\vert H_B H_B\right)}-2\cancel{\left(H_D L_B \middle\vert L_B L_A\right)}\\+\left(H_A L_A \middle\vert H_D H_A\right)+\left(H_D L_A \middle\vert H_A H_A\right)\\+\left(H_D L_A \middle\vert H_D H_D\right)+\cancel{\left(H_D L_A \middle\vert L_B L_B\right)}\\-\cancel{\left(H_D H_B \middle\vert H_B L_A\right)}\end{bmatrix}$
$\left\langle DB^{-}A^{+}\middle\vert\hat{H}\middle\vert D^{+}B^{-}A^{+-}\right\rangle_{CTP}$		----------	$-\sqrt{\frac{3}{2}}\left(H_B L_A \middle\vert H_D H_B\right)+\sqrt{\frac{3}{2}}\left(L_B L_A \middle\vert H_D L_B\right)\approx 0$
$\left\langle DB^{-}A^{+}\middle\vert\hat{H}\middle\vert D^{+-}B^{-}A^{+}\right\rangle_{CSP}$	$V_{CT-CTDE}^{A\to B,A\to B;D}$	$\frac{2}{\sqrt{2}}\langle H_D\vert\hat{h}^{le}\vert L_D\rangle$	$\frac{1}{\sqrt{2}}\begin{bmatrix}2\left(H_D L_D \middle\vert H_A H_A\right)+2\left(H_D L_D \middle\vert L_B L_B\right)\\+2\left(H_D L_D \middle\vert H_D H_D\right)+4\left(H_D L_D \middle\vert H_B H_B\right)\\-2\left(H_D H_B \middle\vert H_B L_D\right)-\left(H_D L_B \middle\vert L_B L_D\right)\\-\left(H_D H_A \middle\vert H_A L_D\right)\end{bmatrix}$
$\left\langle DB^{-}A^{+}\middle\vert\hat{H}\middle\vert D^{+-}B^{-}A^{+}\right\rangle_{CTP}$		----------	$\sqrt{\frac{3}{2}}\left(H_A L_D \middle\vert H_D H_A\right)-\sqrt{\frac{3}{2}}\left(L_B L_D \middle\vert H_D L_B\right)$
$\left\langle DB^{-}A^{+}\middle\vert\hat{H}\middle\vert D^{+-}B^{+}A^{-}\right\rangle_{CSP}$	$V_{CT-CTDE}^{A\to B,B\to A;D}$	----------	----------
$\left\langle DB^{-}A^{+}\middle\vert\hat{H}\middle\vert D^{+-}B^{+}A^{-}\right\rangle_{CTP}$		----------	----------
$\left\langle DB^{-}A^{+}\middle\vert\hat{H}\middle\vert D^{-}B^{+}A^{+-}\right\rangle_{CSP}$	$V_{CT-CTDE}^{A\to B,B\to D;A}$	----------	$-\frac{2}{\sqrt{2}}\left(H_B L_D \middle\vert L_B L_A\right)+\frac{1}{\sqrt{2}}\left(H_B L_A \middle\vert L_B L_D\right)\approx 0$

$\left\langle DB^{-}A^{+}\middle\vert\hat{H}\middle\vert D^{-}B^{+}A^{+-}\right\rangle_{CTP}$		----------	$\sqrt{\frac{3}{2}}\left(H_B L_A \middle\vert L_B L_D\right)\approx 0$
$\left\langle DB^{-}A^{+}\middle\vert\hat{H}\middle\vert DB^{+-}A^{+-}\right\rangle_{CSP}$	$V_{CT-LDE}^{A\to B,B;A}$	----------	$-\frac{2}{\sqrt{2}}\left(H_B L_B \middle\vert L_B L_A\right)+\frac{1}{\sqrt{2}}\left(H_B L_A \middle\vert L_B L_B\right)$
$\left\langle DB^{-}A^{+}\middle\vert\hat{H}\middle\vert DB^{+-}A^{+-}\right\rangle_{CTP}$		----------	$\sqrt{\frac{3}{2}}\left(H_B L_A \middle\vert L_B L_B\right)$
Couplings between Doubly - Excited states			
${}_{CSP}\left\langle D^{+-}BA^{+-}\middle\vert\hat{H}\middle\vert D^{+-}BA^{+-}\right\rangle_{CTP}$	$V_{LDE_{CSP}-LDE_{CTP}}^{D;A,D;A}$	----------	$\frac{\sqrt{3}}{2}\left(K_{L_D H_A}+K_{H_D L_A}-K_{H_D H_A}-K_{L_D L_A}\right)\approx 0$
${}_{CSP}\left\langle D^{+-}BA^{+-}\middle\vert\hat{H}\middle\vert D^{+}B^{-}A^{+-}\right\rangle_{CSP}$	$V_{LDE_{CSP}-CTDE}^{D;A,D\to B;A}$	$\left\langle L_D\middle\vert\hat{h}^{1e}\middle\vert L_B\right\rangle$	$2\left(L_D L_B \middle\vert H_B H_B\right)+\left(L_D L_B \middle\vert H_D H_D\right)$ $+\cancel{\left(L_D L_B \middle\vert H_A H_A\right)}+\cancel{\left(L_D L_B \middle\vert L_A L_A\right)}$ $+\left(H_D L_B \middle\vert L_D H_D\right)-\left(L_D H_B \middle\vert H_B L_B\right)$ $-\frac{1}{2}\cancel{\left(L_D H_A \middle\vert H_A L_B\right)}-\frac{1}{2}\cancel{\left(L_D L_A \middle\vert L_A L_B\right)}$
${}_{CSP}\left\langle D^{+-}BA^{+-}\middle\vert\hat{H}\middle\vert D^{+}B^{-}A^{+-}\right\rangle_{CTP}$		----------	$-\frac{\sqrt{3}}{2}\left(L_D L_A \middle\vert L_A L_B\right)+\frac{\sqrt{3}}{2}\left(L_D H_A \middle\vert H_A L_B\right)\approx 0$
${}_{CSP}\left\langle D^{+-}BA^{+-}\middle\vert\hat{H}\middle\vert D^{+-}B^{-}A^{+}\right\rangle_{CSP}$	$V_{LDE_{CSP}-CTDE}^{D;A,A\to B;D}$	$\left\langle L_A\middle\vert\hat{h}^{1e}\middle\vert L_B\right\rangle$	$2\left(L_A L_B \middle\vert H_B H_B\right)+\left(L_A L_B \middle\vert H_A H_A\right)$ $+\cancel{\left(L_A L_B \middle\vert H_D H_D\right)}+\cancel{\left(L_A L_B \middle\vert L_D L_D\right)}$ $+\left(H_A L_B \middle\vert L_A H_A\right)-\left(L_A H_B \middle\vert H_B L_B\right)$ $-\frac{1}{2}\cancel{\left(L_A H_D \middle\vert H_D L_B\right)}-\frac{1}{2}\cancel{\left(L_A L_D \middle\vert L_D L_B\right)}$
${}_{CSP}\left\langle D^{+-}BA^{+-}\middle\vert\hat{H}\middle\vert D^{+-}B^{-}A^{+}\right\rangle_{CTP}$		----------	$-\frac{\sqrt{3}}{2}\left(L_A L_D \middle\vert L_D L_B\right)+\frac{\sqrt{3}}{2}\left(L_A H_D \middle\vert H_D L_B\right)\approx 0$
${}_{CSP}\left\langle D^{+-}BA^{+-}\middle\vert\hat{H}\middle\vert D^{+-}B^{+}A^{-}\right\rangle_{CSP}$	$V_{LDE_{CSP}-CTDE}^{D;A,B\to A;D}$	$\left\langle H_A\middle\vert\hat{h}^{1e}\middle\vert H_B\right\rangle$	$\cancel{\left(H_B H_A \middle\vert H_D H_D\right)}+\left(H_B H_A \middle\vert H_B H_B\right)$ $+\left(H_B H_A \middle\vert H_A H_A\right)+\cancel{\left(H_B H_A \middle\vert L_D L_D\right)}$ $+\left(H_B H_A \middle\vert L_A L_A\right)-2\left(H_B L_A \middle\vert L_A H_A\right)$ $-\frac{1}{2}\cancel{\left(H_B H_D \middle\vert H_D H_A\right)}-\frac{1}{2}\cancel{\left(H_B L_D \middle\vert L_D H_A\right)}$
${}_{CSP}\left\langle D^{+-}BA^{+-}\middle\vert\hat{H}\middle\vert D^{+-}B^{+}A^{-}\right\rangle_{CTP}$		----------	$-\frac{\sqrt{3}}{2}\left(H_B H_D \middle\vert H_D H_A\right)+\frac{\sqrt{3}}{2}\left(H_B L_D \middle\vert L_D H_A\right)\approx 0$

${}_{CSP}\left\langle D^{+-}BA^{+-}\middle\vert\hat{H}\middle\vert D^{-}B^{+}A^{+-}\right\rangle_{CSP}$	$V^{D;A,B\to D;A}_{LDE_{CSP}-CTDE}$	$\left\langle H_D\middle\vert\hat{h}^{1e}\middle\vert H_B\right\rangle$	$\cancel{\left(H_BH_D\middle\vert H_AH_A\right)}+\left(H_BH_D\middle\vert H_BH_B\right)$ $+\left(H_BH_D\middle\vert H_DH_D\right)+\cancel{\left(H_BH_D\middle\vert L_AL_A\right)}$ $+\left(H_BH_D\middle\vert L_DL_D\right)-2\left(H_BL_D\middle\vert L_DH_D\right)$ $-\frac{1}{2}\cancel{\left(H_BH_A\middle\vert H_AH_D\right)}-\frac{1}{2}\cancel{\left(H_BL_A\middle\vert L_AH_D\right)}$
${}_{CSP}\left\langle D^{+-}BA^{+-}\middle\vert\hat{H}\middle\vert D^{-}B^{+}A^{+-}\right\rangle_{CTP}$		----------	$-\frac{\sqrt{3}}{2}\left(H_BH_A\middle\vert H_AH_D\right)+\frac{\sqrt{3}}{2}\left(H_BL_A\middle\vert L_AH_D\right)\approx 0$
${}_{CSP}\left\langle D^{+-}BA^{+-}\middle\vert\hat{H}\middle\vert DB^{+-}A^{+-}\right\rangle_{CSP}$	$V^{D;A,B;A}_{LDE_{CSP}-LDE}$	$\left\langle H_D\middle\vert\hat{h}^{1e}\middle\vert H_B\right\rangle$	$\cancel{\left(H_BH_D\middle\vert H_AH_A\right)}+\left(H_BH_D\middle\vert H_BH_B\right)$ $+\left(H_BH_D\middle\vert H_DH_D\right)+\cancel{\left(H_BH_D\middle\vert L_AL_A\right)}$ $+\left(H_BH_D\middle\vert L_BL_B\right)-2\left(H_BL_B\middle\vert L_BH_D\right)$ $-\frac{1}{2}\cancel{\left(H_BH_A\middle\vert H_AH_D\right)}-\frac{1}{2}\cancel{\left(H_BL_A\middle\vert L_AH_D\right)}$
${}_{CSP}\left\langle D^{+-}BA^{+-}\middle\vert\hat{H}\middle\vert DB^{+-}A^{+-}\right\rangle_{CTP}$		----------	$-\frac{\sqrt{3}}{2}\left(H_BH_A\middle\vert H_AH_D\right)+\frac{\sqrt{3}}{2}\left(H_BL_A\middle\vert L_AH_D\right)\approx 0$
${}_{CSP}\left\langle D^{+}B^{-}A^{+-}\middle\vert\hat{H}\middle\vert D^{+-}BA^{+-}\right\rangle_{CTP}$	$V^{D\to B;A,D;A}_{CTDE_{CSP}-LDE_{CTP}}$	----------	$-\frac{\sqrt{3}}{2}\left(L_BL_A\middle\vert L_AL_D\right)+\frac{\sqrt{3}}{2}\left(L_BH_A\middle\vert H_AL_D\right)\approx 0$
${}_{CSP}\left\langle D^{+}B^{-}A^{+-}\middle\vert\hat{H}\middle\vert D^{+}B^{-}A^{+-}\right\rangle_{CTP}$	$V^{D\to B;A,D\to B;A}_{CTDE_{CSP}-CTDE_{CTP}}$	----------	$\frac{\sqrt{3}}{2}\left(K_{L_BH_A}+\cancel{K_{H_DL_A}}-\cancel{K_{H_DH_A}}-K_{L_BL_A}\right)$
${}_{CSP}\left\langle D^{+}B^{-}A^{+-}\middle\vert\hat{H}\middle\vert D^{+-}B^{-}A^{+}\right\rangle_{CSP}$	$V^{D\to B;A,A\to B;D}_{CTDE_{CSP}-CTDE}$	$\frac{1}{2}\left\langle L_D\middle\vert\hat{h}^{1e}\middle\vert L_A\right\rangle$	$\cancel{\left(L_BL_D\middle\vert L_AL_B\right)}-\cancel{\left(L_AL_D\middle\vert H_BH_B\right)}$ $-\frac{1}{2}\left(L_AL_D\middle\vert H_DH_D\right)-\frac{1}{2}\left(L_AL_D\middle\vert H_AH_A\right)$ $-\frac{1}{2}\cancel{\left(L_AL_D\middle\vert L_BL_B\right)}-\frac{1}{2}\left(H_DL_D\middle\vert L_AH_D\right)$ $+\frac{1}{2}\cancel{\left(L_AH_B\middle\vert H_BL_D\right)}$
${}_{CSP}\left\langle D^{+}B^{-}A^{+-}\middle\vert\hat{H}\middle\vert D^{+-}B^{-}A^{+}\right\rangle_{CTP}$		$-\frac{\sqrt{3}}{2}\left\langle L_D\middle\vert\hat{h}^{1e}\middle\vert L_A\right\rangle$	$-\sqrt{3}\cancel{\left(L_AL_D\middle\vert H_BH_B\right)}-\frac{\sqrt{3}}{2}\left(L_AL_D\middle\vert H_DH_D\right)$ $-\frac{\sqrt{3}}{2}\left(L_AL_D\middle\vert H_AH_A\right)-\frac{\sqrt{3}}{2}\cancel{\left(L_AL_D\middle\vert L_BL_B\right)}$ $+\frac{\sqrt{3}}{2}\left(L_AH_D\middle\vert H_DL_D\right)+\frac{\sqrt{3}}{2}\cancel{\left(L_AH_B\middle\vert H_BL_D\right)}$ $-\frac{\sqrt{3}}{2}\left(H_AL_D\middle\vert L_AH_A\right)$
${}_{CSP}\left\langle D^{+}B^{-}A^{+-}\middle\vert\hat{H}\middle\vert D^{+-}B^{+}A^{-}\right\rangle_{CSP}$	$V^{D\to B;A,B\to A;D}_{CTDE_{CSP}-CTDE}$	----------	$\left(L_BL_D\middle\vert H_BH_A\right)-\frac{1}{2}\left(L_BH_A\middle\vert H_BL_D\right)\approx 0$

$_{CSP}\langle D^{+}B^{-}A^{+-}\vert\hat{H}\vert D^{+-}B^{+}A^{-}\rangle_{CTP}$		----------	$\frac{\sqrt{3}}{6}\left(L_BL_D\vert H_BH_A\right)+\frac{\sqrt{3}}{3}\left(L_BH_A\vert H_BL_D\right)\approx 0$
$_{CSP}\langle D^{+}B^{-}A^{+-}\vert\hat{H}\vert D^{-}B^{+}A^{+-}\rangle_{CSP}$	$V^{D\to B;A,B\to D;A}_{CTDE_{CSP}-CTDE}$	----------	$\left(L_BL_D\vert H_BH_D\right)-2\left(L_BH_D\vert H_BL_D\right)$
$_{CSP}\langle D^{+}B^{-}A^{+-}\vert\hat{H}\vert D^{-}B^{+}A^{+-}\rangle_{CTP}$		----------	$\frac{\sqrt{3}}{6}\left(L_BL_D\vert H_BH_D\right)$
$_{CSP}\langle D^{+}B^{-}A^{+-}\vert\hat{H}\vert DB^{+-}A^{+-}\rangle_{CSP}$	$V^{D\to B;A,B;A}_{CTDE_{CSP}-LDE}$	$\langle H_D\vert\hat{h}^{1e}\vert H_B\rangle$	$\cancel{\left(H_BH_D\vert H_AH_A\right)}+\left(H_BH_D\vert H_BH_B\right)$ $+\left(H_BH_D\vert H_DH_D\right)+\cancel{\left(H_BH_D\vert L_AL_A\right)}$ $+\left(H_BH_D\vert L_BL_B\right)-2\left(H_BL_B\vert L_BH_D\right)$ $-\frac{1}{2}\cancel{\left(H_BH_A\vert H_AH_D\right)}-\frac{1}{2}\cancel{\left(H_BL_A\vert L_AH_D\right)}$
$_{CSP}\langle D^{+}B^{-}A^{+-}\vert\hat{H}\vert DB^{+-}A^{+-}\rangle_{CTP}$		----------	$-\frac{\sqrt{3}}{2}\left(H_BH_A\vert H_AH_D\right)+\frac{\sqrt{3}}{2}\left(H_BL_A\vert L_AH_D\right)\approx 0$
$_{CSP}\langle D^{+-}B^{-}A^{+}\vert\hat{H}\vert D^{+-}B^{-}A^{+}\rangle_{CTP}$	$V^{A\to B;D,A\to B;D}_{CTDE_{CSP}-CTDE_{CTP}}$	----------	$\frac{\sqrt{3}}{2}\left(\cancel{K_{L_DH_A}}+K_{H_DL_B}-\cancel{K_{H_DH_A}}-K_{L_DL_B}\right)$
$_{CSP}\langle D^{+-}B^{-}A^{+}\vert\hat{H}\vert D^{+-}B^{+}A^{-}\rangle_{CSP}$	$V^{A\to B;D,B\to A;D}_{CTDE_{CSP}-CTDE}$	----------	$\left(H_BH_A\vert L_BL_A\right)-2\left(H_BL_A\vert L_BH_A\right)$
$_{CSP}\langle D^{+-}B^{-}A^{+}\vert\hat{H}\vert D^{+-}B^{+}A^{-}\rangle_{CTP}$		----------	$\frac{\sqrt{3}}{6}\left(H_BH_A\vert L_BL_A\right)$
$_{CSP}\langle D^{+-}B^{-}A^{+}\vert\hat{H}\vert D^{-}B^{+}A^{+-}\rangle_{CSP}$	$V^{A\to B;D,B\to D;A}_{CTDE_{CSP}-CTDE}$	----------	$\left(H_BH_D\vert L_BL_A\right)-\frac{1}{2}\left(H_BL_A\vert L_BH_D\right)\approx 0$
$_{CSP}\langle D^{+-}B^{-}A^{+}\vert\hat{H}\vert D^{-}B^{+}A^{+-}\rangle_{CTP}$		----------	$\frac{\sqrt{3}}{6}\left(H_BH_D\vert L_BL_A\right)+\frac{\sqrt{3}}{3}\left(H_BL_A\vert L_BH_D\right)\approx 0$
$_{CSP}\langle D^{+-}B^{-}A^{+}\vert\hat{H}\vert DB^{+-}A^{+-}\rangle_{CSP}$	$V^{A\to B;D,B;A}_{CTDE_{CSP}-LDE}$	----------	$\left(L_DH_D\vert H_BL_A\right)-\frac{1}{2}\left(L_DL_A\vert H_BH_D\right)\approx 0$
$_{CSP}\langle D^{+-}B^{-}A^{+}\vert\hat{H}\vert DB^{+-}A^{+-}\rangle_{CTP}$		----------	$\frac{\sqrt{3}}{6}\left(L_DH_D\vert H_BL_A\right)+\frac{\sqrt{3}}{3}\left(L_DL_A\vert H_BH_D\right)\approx 0$
$_{CSP}\langle D^{+-}B^{+}A^{-}\vert\hat{H}\vert D^{+-}B^{+}A^{-}\rangle_{CTP}$	$V^{B\to A;D,B\to A;D}_{CTDE_{CSP}-CTDE_{CTP}}$	----------	$\frac{\sqrt{3}}{2}\left(K_{L_DH_B}+\cancel{K_{H_DL_A}}-K_{H_DH_B}-\cancel{K_{L_DL_A}}\right)$
$_{CSP}\langle D^{+-}B^{+}A^{-}\vert\hat{H}\vert D^{-}B^{+}A^{+-}\rangle_{CSP}$	$V^{B\to A;D,B\to D;A}_{CTDE_{CSP}-CTDE}$	$\frac{1}{2}\langle H_D\vert\hat{h}^{1e}\vert H_A\rangle$	$-\left(H_AL_D\vert L_DH_D\right)-\left(H_AL_A\vert L_AH_D\right)$ $+\frac{1}{2}\left(H_AH_D\vert H_DH_D\right)+\frac{1}{2}\left(H_AH_D\vert H_AH_A\right)$ $+\frac{1}{2}\cancel{\left(H_AH_D\vert H_BH_B\right)}+\frac{1}{2}\left(H_AH_D\vert L_DL_D\right)$ $+\frac{1}{2}\left(H_AH_D\vert L_AL_A\right)+\frac{1}{2}\cancel{\left(H_BH_D\vert H_AH_B\right)}$

${}_{CSP}\langle D^{+-}B^{+}A^{-}\vert\hat{H}\vert D^{-}B^{+}A^{+-}\rangle_{CTP}$		$\frac{\sqrt{3}}{2}\langle H_D\vert\hat{h}^{1e}\vert H_A\rangle$	$-\sqrt{3}\left(H_AL_D\vert L_DH_D\right)+\frac{\sqrt{3}}{2}\left(H_AH_D\vert H_DH_D\right)$ $+\frac{\sqrt{3}}{2}\left(H_AH_D\vert H_AH_A\right)+\frac{\sqrt{3}}{2}\cancel{\left(H_AH_D\vert H_BH_B\right)}$ $+\frac{\sqrt{3}}{2}\left(H_AH_D\vert L_DL_D\right)+\frac{\sqrt{3}}{2}\left(H_AH_D\vert L_AL_A\right)$ $-\frac{\sqrt{3}}{2}\cancel{\left(H_BH_D\vert H_AH_B\right)}$
${}_{CSP}\langle D^{+-}B^{+}A^{-}\vert\hat{H}\vert DB^{+-}A^{+-}\rangle_{CSP}$	$V^{B\to A;D,B;A}_{CTDE_{CSP}-LDE}$	----------	$-\left(L_DH_D\vert H_AL_B\right)+\frac{1}{2}\left(L_DL_B\vert H_AH_D\right)\approx 0$
${}_{CSP}\langle D^{+-}B^{+}A^{-}\vert\hat{H}\vert DB^{+-}A^{+-}\rangle_{CTP}$		----------	$-\frac{\sqrt{3}}{6}\left(L_DH_D\vert H_AL_B\right)-\frac{\sqrt{3}}{3}\left(L_DL_B\vert H_AH_D\right)\approx 0$
${}_{CSP}\langle D^{-}B^{+}A^{+-}\vert\hat{H}\vert D^{-}B^{+}A^{+-}\rangle_{CTP}$	$V^{B\to D;A,B\to D;A}_{CTDE_{CSP}-CTDEE_{CTP}}$	----------	$\frac{\sqrt{3}}{2}\left(K_{L_AH_B}+\cancel{K_{H_AL_D}}-K_{H_AH_B}-\cancel{K_{L_AL_D}}\right)$
${}_{CSP}\langle D^{-}B^{+}A^{+-}\vert\hat{H}\vert DB^{+-}A^{+-}\rangle_{CSP}$	$V^{B\to D;A,B;A}_{CTDE_{CSP}-LDE}$	$\langle L_D\vert\hat{h}^{1e}\vert L_B\rangle$	$2\left(L_DL_B\vert H_DH_D\right)+\cancel{\left(L_DL_B\vert H_AH_A\right)}$ $+\left(L_DL_B\vert H_BH_B\right)+\cancel{\left(L_DL_B\vert L_AL_A\right)}$ $+\left(H_BL_D\vert L_BH_B\right)-\left(L_DH_D\vert H_DL_B\right)$ $-\frac{1}{2}\cancel{\left(L_DH_A\vert H_AL_B\right)}-\frac{1}{2}\cancel{\left(L_DL_A\vert L_AL_B\right)}$
${}_{CSP}\langle D^{-}B^{+}A^{+-}\vert\hat{H}\vert DB^{+-}A^{+-}\rangle_{CTP}$		----------	$-\frac{\sqrt{3}}{2}\left(L_DL_A\vert L_AL_B\right)+\frac{\sqrt{3}}{2}\left(L_DH_A\vert H_AL_B\right)\approx 0$
${}_{CSP}\langle DB^{+-}A^{+-}\vert\hat{H}\vert DB^{+-}A^{+-}\rangle_{CTP}$	$V^{B;A,B;A}_{LDE_{CSP}-LDE_{CTP}}$	----------	$\frac{\sqrt{3}}{2}\left(K_{L_BH_A}+K_{H_BL_A}-K_{H_BH_A}-K_{L_BL_A}\right)$

Table 7.2 Analytical exact coupling expressions. 1st column: Mathematical notation of the Hamiltonian element. 2nd column: Symbolism of the calculated coupling, defining the diabatic states that it consists of. 3rd column: Exact expressions for the off-diagonal matrix elements as a function of Fock matrix elements, and two-electron integrals.

7.3 References

[1] Szabo, A.; Ostlund, N. S. *Modern Quantum Chemistry: Introduction to Advanced Electronic Structure Theory*; Dover, Mineola, New York, 1996.

[2] Slater, J. C. A Simplification of the Hartree-Fock Method. *Phys. Rev.* **1951**, *81*, 385-390.

[3] Sherrill, C. D. Derivation of the Configuration Interaction Singles (CIS) Method for Various Single Determinant References and Extensions to Include Selected Double Substitutions (XCIS). *Sch. Chem. Biochem*. 1996, 1-14.

[4] Havlas, Z.; Michl, J. Guidance for Mutual Disposition of Chromophores for Singlet Fission. *Isr. J. Chem.* **2016**, *56*, 96-106.

[5] Taffet, E. J.; Beljonne, D.; Scholes, G. D. Overlap-Driven Splitting of Triplet Pairs in Singlet Fission. *J. Am. Chem. Soc.* **2020**, *142*, 20040−20047.

CHAPTER 8

Computation of Hamiltonian Matrix Elements

As we have described in detail in the previous two chapters (Chapters 6 and 7), the diagonal and off-diagonal elements of the CISD Hamiltonian used for the model of Singlet Fission (SF) (see eqs (7.5)-(7.9) and Tables 7.1 and 7.2), are functions of several quantities, i.e.,

$$ {}^{SA}\langle \Psi_n | \hat{H}^{el} | \Psi_n \rangle^{SA} = E_n \left(\{IP^i\},\ \{EA^i\},\ \left\{ \left\langle L_i \left| \hat{V}_{e-n_j} \right| L_i \right\rangle \right\},\ \left\{ \left\langle H_i \left| \hat{V}_{e-n_j} \right| H_i \right\rangle \right\},\ \{J_{P_iQ_j}\},\ \{K_{P_iQ_j}\} \right), \quad (8.1) $$

$$ {}^{SA}\langle \Psi_n | \hat{H}^{el} | \Psi_m \rangle^{SA} = H_{n,m} \left(\left\{ \langle P_i | \hat{F} | Q_j \rangle \right\},\ \left\{ \left(P_i Q_j | R_i Z_j \right) \right\},\ \{S_{P_iQ_j}\},\ \{J_{P_iQ_j}\},\ \{K_{P_iQ_j}\} \right). \quad (8.2) $$

In general, the diagonal matrix elements (basis-state energies) are functions of ionization potentials (IP^i), electron affinities (EA^i), core terms ($\left\langle P_i \left| \hat{V}_{e-n_j} \right| P_i \right\rangle$), Coulomb ($J_{P_iQ_j}$) and exchange integrals ($K_{P_iQ_j}$). The off-diagonal matrix elements (inter-state couplings) are functions of one-electron Fock matrix elements ($\langle P_i | \hat{F} | Q_j \rangle$), overlap matrix elements ($S_{P_iQ_j}$) and two-electron integrals ($\left(P_i Q_j | R_i Z_j \right)$) where $P,Q,R,Z = H,L$ and $i,j = D,B,A$. All these quantities have been described in detail in the previous two chapters.

For the D-B-A systems discussed in Chapter 5, we need to compute the intra-fragment and inter-fragment quantities included in eqs (8.1) and (8.2) and Tables 7.1 and 7.2. We compute the relevant quantities using two quantum chemistry program packages, the General Atomic and Molecular Electronic Structure System (GAMESS-US) [1-3] and the Python Quantum Chemistry (PyQuante) [4,5]. The use of PyQuante is secondary in the sense that we recompute with this program all of the quantities in eqs (8.1) and (8.2), after computing them with GAMESS-US, in order to double check for errors.[6] The codes we wrote for use with PyQuante produce values identical to those generated by GAMESS-US. The results from these programs are combined in appropriate code in MATLAB which implements all equations in Tables 7.1 and 7.2 (Chapters 6 and 7) using input from the computations.

8.1 GAMESS-US Program

The General Atomic and Molecular Electronic Structure System (GAMESS-US) is a program for *ab initio* molecular quantum chemistry calculations. Briefly, GAMESS-US can compute SCF wavefunctions ranging from RHF, ROHF, UHF, GVB and MCSCF. The advantage of this program is that it can split a large system into fragments. The Fragment Molecular Orbital (FMO) method permits use of many of these sophisticated treatments to be used on very large systems, by dividing the computation into small fragments. [7-9] In our case, we use the program to perform SCF, RHF, CISD, [10] both on individual D, B, A fragments and on the entire D-B-A system.

Using the GAMESS-US program, we compute the desired intra-fragment quantities such as IP, EA, excitations energies, eigenvectors of the molecular orbitals, overlap matrix, Fock matrix, 1e and 2e integrals, as well as the corresponding inter-fragment ones (one- and two-electron integrals) (see Fig. 8.6).

First, to build the input file for such a calculation, we need to enter the $CONTRL keyword to specify the type of wavefunction ("SCFTYP"), the type of calculation ("RUNTYP"), the units of the coordinates ("UNITS"), the spherical harmonics ("ISPHER") and the gradient of the printed output ("NPRINT"). We also need to give to the program various control information about the computer's operation via the $SYSTEM keyword, such as the maximum replicated memory which the job can use on every core ("MWORDS") and the time limitation ("TIMLIM"). A necessary addition to the input file is the inclusion of the Gaussian basis set on which the calculation will be based, through the $BASIS keyword. Additionally, to perform the calculation in the fragment-orbital representation we must include the $FMO group keyword in the input file, specifying the number of FMO fragments ("NFRAG"), the charge ("ICHARG") and the name of each fragment ("FRGNAM"), identifying the active fragments ("IACTFG") and placing the atoms in the various fragments ("INDAT"). Optionally we can also enter the $INTGRL keyword to control atomic orbitals (AO) integral formats. The $FMOPRP keyword also helps define the various properties of FMOs. Finally, another necessary addition to the input file is to specify the x, y, z FMO coordinates (using the $FMOXYZ keyword), as well as the symmetry. Through a script, using these keywords, we apply the restricted HF (RHF) theories followed by CISD in the FMO basis to obtain the fragment-based quantities described above.

Below we present an example calculation in the FMO basis of a pentacene trimer molecular system (Fig. 8.1).

```
$CONTRL SCFTYP=RHF RUNTYP=GRADIENT UNITS=ANGS ISPHER=1 NPRINT=4
$END
$SYSTEM MWORDS=100 TIMLIM=1 $END
$BASIS GBASIS=N31 NGAUSS=6 NDFUNC=1 $END
$FMO NFRAG=3 ICHARG(1)=0,0,0
        FRGNAM(1)=Donor,Bridge,Acceptor
        INDAT(1)=0, 1,-36,0 37,-72,0 73,-108,0
        IACTFG(1)=1,2,3
$END
$INTGRL SCHWRZ=.FALSE. NINTMX=17290672 $END
$FMOPRP NPRINT=0 $END
$FMOXYZ
C C   -4.81562   -18.12637    48.36059
C C   -5.50427   -17.85160    47.16956
C C   -4.84244   -17.99081    45.92658
C C   -3.50174   -18.40273    45.89301
C C   -3.47496   -18.53838    48.32701
C C   -2.78683   -18.81320    49.51866
C C   -1.47220   -19.08972    47.04970
C C   -1.44672   -19.22516    49.48439
C C   -0.78447   -19.36446    48.24062
C C   -0.75411   -19.50138    50.67409
H H   -1.24394   -19.40053    51.63531
C C    0.55724   -19.77722    48.21128
C C    0.58133   -19.91148    50.63038
.
.
.
$END
$DATA
Basis set input, with no atomic coordinates
C1
H-1 1
C-1 6
$END
```

Figure 8.1 A script file of GAMESS-US for calculating the various properties of a pentacene trimer molecular system using FMO and SCF methods implementing RHF theories. The dots in the scheme imply the remaining coordinates of the molecule.

Using the FMO analysis, we can identify the fragment corresponding to each MO in a D-B-A system and extract from the output file intra-fragment and inter-fragment integrals between specific FMOs as linear combinations of the appropriate atomic orbitals (AOs) obtained from the basis set that we choose.

In Chapter 5 we used, in addition to the FMO method, CISD computations [10,11] to calculate intra-fragment properties (such as IP^i, EA^i, singlet or triplet excitation energies of specific fragment etc., where $i = D,B,A$).

The appropriate input file must be built to perform this calculation by entering the appropriate keywords, so that the output file contains all the necessary information. First in the $CONTRL group we should define as "RHF" the reference type of SCF wavefunction and then define as "CIS" the type of CI calculation. In the same group we can define the type of coordinates of the molecule, the units of the coordinates as well as the gradient of the printed output. In the $SYSTEM group we can give control information about the computer's operations while in the $BASIS group we are required to define the Gaussian basis set of the calculation. Once we have defined "CIS" as the type of CI calculation, we need to use the $CIS keyword to include some properties of the CIS method. In this group we must definitely define the number of chemical core orbitals ("NACORE"), the number of states to be found ("NSTATE"), the state for which properties and/or gradient will be calculated ("IROOT"), the type of CI Hamiltonian to use ("HAMTYP") and the multiplicity (1 or 3) of the singly excited SAPS ("MULT"). Finally, another necessary addition to the input file is to specify the coordinates of the molecule (using the $DATA keyword), as well as the symmetry. Below is presented an example of a script input file for the calculation of the CISD properties, excitation energies, 1e and 2e intra-fragment integrals of a pentacene molecule (Fig. 8.2).

```
$CONTRL SCFTYP=RHF CITYP=CIS RUNTYP=GRADIENT NZVAR=0 UNITS=ANGS
NPRINT=4 $END
$SYSTEM MWORDS=100 $END
$BASIS GBASIS=N31 NGAUSS=6 NDFUNC=1 $END
$CIS HAMTYP=SAPS MULT=3 NACORE=0 NSTATE=1 IROOT=0 DGAPRX=.FALSE.
$END
$DATA
Pentacene1 (Donor) CIS/6-31G(d) level of theory
C1
C 6.0      0.4983720000   -19.0037120000    42.7664130000
C 6.0     -0.1914010000   -18.7272860000    41.5764260000
C 6.0      0.4987210000   -18.7537600000    40.3413350000
C 6.0      1.8684090000   -19.0562680000    40.3145080000
C 6.0      1.8680390000   -19.3063110000    42.7395770000
C 6.0      2.5572890000   -19.5828570000    43.9301840000
.
.
.
$END
```

Figure 8.2 A script file of GAMESS-US for calculating the various CISD properties of a pentacene molecule using SCF methods implementing RHF theories. [10,11] The dots in the scheme imply the remaining coordinates of the molecule.

8.2 PyQuante Program

Using the Python Quantum Chemistry (PyQuante) program [4,5] one can include all the molecular integrals and the HF code in one file or split the code into several files. The suggested file structure is: “base.py” (to hold database information and construct the atomic orbital base), “oei.py” (to calculate the 1e integrals, “S”, “T”, “V”), “eri.py” (for the calculation of the 2e integrals, “G”) and “main.py” (to combine the first three files that will lead to the results in the HF code). Most of these code files need to import some modules from the PyQuante library to perform some specialized mathematical operations.

The initial input requires the molecule’s name, the coordinates of the atoms together with the atomic number of each atom (e.g., [(1, (0,0,0)), (1, (1.4,0,0)), ...]), the spin multiplicity, as well as the charge of the molecule. Starting from the above, we can run a simple HF calculation by inserting the appropriate modules (such as the SCF for self-consistent-field methods). The “SCF” module includes implementations of HF and Density Functional Theory (DFT) for restricted, unrestricted, closed-shell or open-shell Slater determinant references. To use this module, one specifies the molecule on which the calculation will be made, the base to be used (e.g., the minimum basis set “STO-3G”, “6-31G” etc.) as well as the self-consistent-field method (e.g., HF). Basis functions are constructed using the CGBF (contracted Gaussian basis function) object, which, in turn, uses the PGBF (primitive Gaussian basis function) object. Basis sets are simply lists of CGBF’s. In the “Ints” module there is a convenience function “getbasis” that constructs basis sets for different molecules. The calculation should then be repeated until it converges. At the end HF energy can be requested to be printed. Having determined the molecule with its x, y, z coordinates, as well as the basis function set, then we can calculate the 1e and 2e integrals at the base of the atomic orbitals. In this case the "onee_integrals" and "twoe_integrals" modules should be imported to calculate the 1e and 2e integrals, respectively. We can calculate the overlap matrix (“S”), the kinetic matrix (“T”), the nuclear attraction matrix (“V”), as well as the 2e integrals (“ERI_hgp”) on the basis of the atomic orbitals.

Below we present an example calculation of 1e integrals and the basis function set (Fig. 8.3) of a pentacene molecule (a molecule that has been extensively used and studied in Chapter 5). Then by saving the orbitals of the basis function set in a matrix we can calculate 2e integrals between them using the “ERI_hgp” module (Fig. 8.4).

```
import pyquante2
from pyquante2 import molecule # Construct the pentacene molecule
pentacene=molecule([(6,0.49837,-19.00371,42.76641), (6,-0.19140,-18.72729,41.57643),
(6,0.49872,-18.75376,40.34134), (6,1.86841,-19.05627,40.31451), (6,1.86804,-
19.30631,42.73958), (6,2.55729,-19.58286,43.93018), (6,3.92810,-19.63544,41.47689),
(6,3.92640,-19.88541,43.90264), (6,4.61696,-19.91190,42.66677), (6,4.62027,-
20.16291,45.09132), (1,4.10903,-20.14747,46.04654), (6,5.98766,-20.21536,42.64415),
(6,5.98473,-20.46352,45.05435), (1,6.53311,-20.24046,41.70825), (6,6.66609,-
20.48966,43.83494), (1,7.72275,-20.72311,43.81252), (1,6.51539,-20.67679,45.97328), (6,-
2.25033,-18.14878,40.41408), (6,-1.55978,-18.17527,39.17821), (6,-1.56139,-
18.42486,41.60399), (6,-0.19058,-18.47745,39.15070), (6,-4.29968,-17.57199,39.24582), (1,-
5.35643,-17.33895,39.26819), (6,-3.61832,-17.59813,38.02641), (6,-3.62114,-
17.84578,40.43665), (1,-4.14908,-17.38527,37.10743), (6,-2.25375,-17.89824,37.98949),
(1,2.02887,-19.56276,44.87743), (6,2.55816,-19.33278,41.50449), (1,-0.03072,-
18.98343,43.71331), (1,2.39750,-19.07658,39.36761), (1,4.45784,-19.65594,40.53040), (1,-
4.16660,-17.82072,41.37255), (1,-1.74252,-17.91371,37.03426), (1,-2.09113,-
18.40440,42.55049), (1,0.33782,-18.49758,38.20346)],units='Angstrom', multiplicity=1)

# Calculate the Hartree Fock energy of pentacene molecule
from pyquante2 import rhf, basisset
bfs=basisset(pentacene,'sto3g')
py2en=rhf(pentacene,bfs)
py2en.converge()

# Calculate all the one-electron integrals
from pyquante2.ints.integrals import onee_integrals
i1=onee_integrals(bfs,pentacene)
py2S=i1.S
py2T=i1.T
py2V=i1.V
py2h=py2T + py2V

# Print the Results
print 'Basis function set: \n ', bfs
print 'Hartree Fock energy: \n ', 'using pyquante2: EHF = ', py2en.energy
print '\n Overlap integral: \n ', 'using pyquante2: S = ', py2S
print '\n One-electron operators: \n ', 'using pyquante2: h = ', py2h
```

Figure 8.3 Code in python for calculating 1e integrals (“S”, “T” and “V” matrixes) in pentacene molecule in the minimum basis set, “STO-3G”, by import pyquante2, an open-source suite of programs for developing quantum chemistry methods and then introducing various modules needed for the calculation (such as, “molecule”, “rhf”, “basisset”, “onee_integrals” etc.).

```
import pyquante2
from pyquante2 import cgbf
from pyquante2.ctwo import ERI, ERI_hgp

t=[]
t.append(cgbf((0.9417827409280779, -35.911804666417176, 80.81679641522155),(0, 0,
0),[71.616837, 13.045096, 3.5305122],[0.15432897000916182, 0.53532814003178,
0.44463454002639596]))
t.append(cgbf((0.9417827409280779, -35.911804666417176, 80.81679641522155),(0, 0,
0),[2.9412494, 0.6834831, 0.2222899],[-0.09996723007596425, 0.39951283030358636,
0.7001154705320117]))
t.append(cgbf((0.9417827409280779, -35.911804666417176, 80.81679641522155),(1, 0,
0),[2.9412494, 0.6834831, 0.2222899],[0.15591627210510742, 0.607683728204657,
0.39195739529202256]))
t.append(cgbf((0.9417827409280779, -35.911804666417176, 80.81679641522155),(0, 1,
0),[2.9412494, 0.6834831, 0.2222899],[0.15591627210510742, 0.607683728204657,
0.39195739529202256]))
t.append(cgbf((0.9417827409280779, -35.911804666417176, 80.81679641522155),(0, 0,
1),[2.9412494, 0.6834831, 0.2222899],[0.15591627210510742, 0.607683728204657,
0.39195739529202256]))
t.append(cgbf((-0.3616935542140059, -35.38944660865418, 78.5680602833324),(0, 0,
0),[71.616837, 13.045096, 3.5305122],[0.15432897000916182, 0.53532814003178,
0.44463454002639596]))
t.append(cgbf((-0.3616935542140059, -35.38944660865418, 78.5680602833324),(0, 0,
0),[2.9412494, 0.6834831, 0.2222899],[-0.09996723007596425, 0.39951283030358636,
0.7001154705320117]))
.
.
.
out = open("pentacene_CGBS.txt", "r+")
for i in range(123):
    for j in range(123):
        for k in range(123):
            for l in range(123):
                a = f'(c{i}c{j}|c{k}c{l}) = {ERI_hgp(t[i],t[j],t[k],t[l])} \n'
                out.write(a)
```

Figure 8.4 Code in python for calculating various 2e integrals in a pentacene molecule in the minimum basis set, “STO-3G”, by import pyquante2 and then introducing “ERI” and “ERI_hgp” modules needed for the calculation. The dots in the scheme indicate the remaining functions of the basis set stored in the "t" matrix.

After using both programs and concluding that our results converge, for time-saving purposes we chose GAMESS-US to study the molecular systems used in the study of the SF process. So, in Chapter 5 we use GAMESS-US to calculate all the required quantities needed to build the electronic Hamiltonian (eqs (8.1) and (8.2)). First, we build our systems using the Avogadro molecular editor and then through ORCA [12] we optimize the structure (except for the NC1 molecular system where we got the original coordinates from the published

paper [13]). In the case of the NC1 molecular system, we create D, B and A fragments cutting the C=C bonds between the bridge and the pentacene D (A) and then capping with H. Then, we perform geometry optimization for each fragment without changing the inter-fragment geometries and distances. Next, using GAMESS-US we calculate all the required quantities (inter-fragment and intra-fragment terms) using scripts similar to those presented above (Figs 8.3 and 8.4). The results from these calculations together with the semi-analytical framework created earlier (see discussion in Chapters 6 and 7), are introduced in a script in MATLAB. There, numbers were essentially added to the quantities of eqs (8.1) and (8.2), thus building the $\hat{H}^{el}_{DBA}$. Finally, another script have to be used in MATLAB to calculate the SF effective coupling, V_{SF} via eqs (5.9) and (5.10) as well as the corresponding SF pathways (see discussion in section 5.4.3). Below, in Fig. 8.6 we present this whole process in the form of flowchart.

8.3 MATLAB code programming

MATLAB (MATrix LABoratory) is a programming language and numeric computing environment developed and owned by MathWorks. [14,15] Below I present an example of the scripts I wrote in MATLAB code that use the above-mentioned GAMESS-US and PyQuante computationsin order to compute the SF effective coupling (in the context of the semi-analytical framework described in detail in Chapter 5). In particular, I present a MATLAB script for the construction of the D-B-A Hamiltonian and the calculation of the effective coupling V_{SF} for the non-pi-stacking molecular system (see Fig. 5.3b). The script requests as input data: 1) the constant parameter X (constant D(A) HOMO-to-LUMO exciton energy), 2) maximum and minimum values for the variable parameters Y (B HOMO-to-LUMO exciton energy) and z (difference between ionization potentials of D(A) and B), 3) the step sizes δY and δz for the variation of Y and z. The script then constructs the Hamiltonian and uses perturbation-theory and Green's function methods to calculate the SF effective coupling V_{SF} as explained in detail in section 5.4.3 (see eqs (5.9)-(5.10)).

```
% This code computes the SF effective coupling of the Hamiltonian in the basis states set using
% perturbation and Green's function methods
clear all; clc;
global HAM P Q PQ QP d i j enQ vQ dQ enP vP dP E GQ G VSF
global x y z ymax ymin nsteps dsteps mx my mz

%%% Constants %%%
x = 2.86;        % D(A) HOMO-to-LUMO exciton energy
ymax = 12.46;        % maximum value of B HOMO-to-LUMO exciton energy
ymin = 3.16;        % minimum value
nsteps = 20;        % number of steps
dsteps = (ymax-ymin)/nsteps;
VSF = zeros (nsteps,1);
mx = zeros (nsteps,1);
my = zeros (nsteps,1);
mz = zeros (nsteps,1);

%%% Hamiltonian's Construction %%%
HAM = xlsread('Hamiltonian.xlsx');
d = size(HAM);
for i=1:17
   for j=1:17
      if gt(i,j)
         HAM(i,j) = HAM(j,i);
      else
         HAM(i,j) = HAM(i,j);
      end
   end
end

%%% SF effective coupling calculation %%%
for z=-7.9:0.5:3.5 % |IPD-IPB|
   data = ['VSF_funct_z=', num2str(z),'.csv'];
   y=ymin;
   for i=1:nsteps
      mx(i) = x; % x matrix
      my(i) = y;  % y matrix
      mz(i) = z; % z matrix
      HAM(1,1) = x;
      HAM(2,2) = (2*x)-3.35;
      HAM(3,3) = y;
      HAM(4,4) = z+y+3.4964;
      HAM(5,5) = x-z+2.50098;
      HAM(6,6) = x+3.133;
      HAM(7,7) = x+3.133;
      HAM(8,8) = x-z+2.50098;
      HAM(9,9) = z+y+3.4964;
      HAM(10,10) = y+z+x+2.3964;
      HAM(11,11) = (2*x)-z+0.2492;
      HAM(12,12) = y+z+x+2.3964;
      HAM(13,13) = (2*x)-z+0.2492;
      HAM(14,14) = x+y+1.1906;
      HAM(15,15) = x+y+1.1906;
      HAM(16,16) = x+y-3.0444;
      HAM(17,17) = x+y-3.0444;
      P = HAM(1:2,1:2); % P subspace construction
      Q = HAM(3:17,3:17); % Q subspace construction
      PQ = HAM(1:2,3:17); % PQ subspace construction
```

```
        QP = HAM(3:17,1:2); % QP subspace construction
        enQ = eig(Q); % find the eigenenergies of Q subspace
        [vQ,dQ] = eig(Q); % find the eigenstates of Q subspace: vQ
        enP = eig(P); % find the eigenenergies of Q subspace
        E = (HAM(1,1)+HAM(2,2))./2; % find the average value between the two eigenenergies
        [vP,dP] = eig(P); % find the eigenstates of Q subspace: vP
        GQ = inv(E*eye(15,15)-Q); % Green Function GQ
        G = PQ*GQ*QP;
        VSF(i) = G(2,1); % SF effective coupling
        y = ymin + i*dsteps;
    end
    dlmwrite(data,VSF,'precision','%1.16X');
end
```

Figure 8.5 MATLAB code for computing the D-B-A Hamiltonian and the SF effective coupling for the non-pi-stacking molecular system described in Chapter 5.

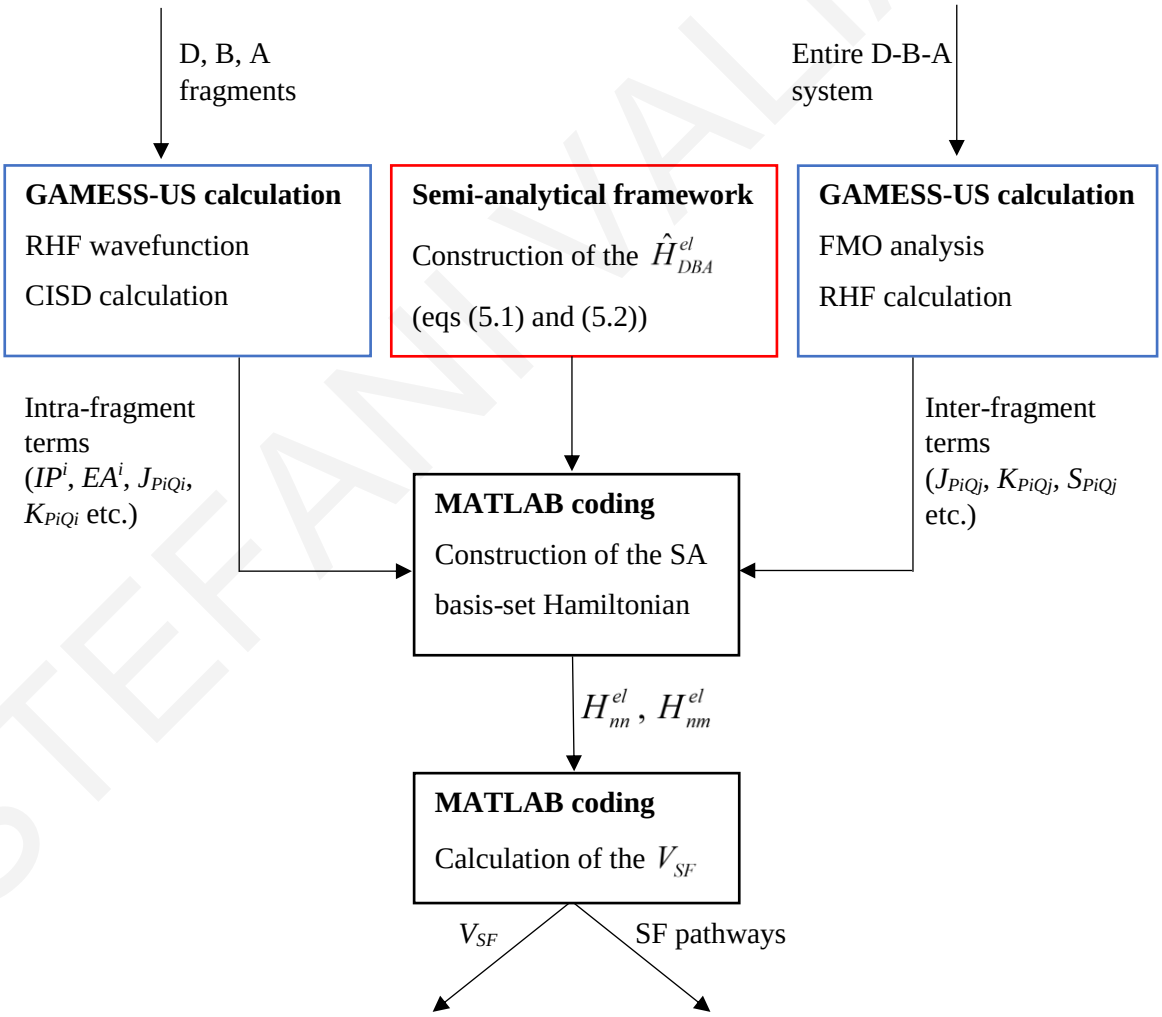

Figure 8.6 Flowchart demonstrating the semi-analytical / computational framework constructed for the analysis described in Chapter 5.

8.4 References

[1] Dupuis, M.; Spangler, D.; Wendolowski, J. J. *National Resource for Computations in Chemistry Software Catalog*; University of California, Berkeley, CA, Program QG01, 1980.

[2] Schmidt, M. W.; Baldridge, K. K.; Boatz, J. A.; Elbert, S. T.; Gordon, M. S.; Jensen, J. H.; Koseki, S.; Matsunaga, N.; Nguyen, K. A.; Shujun, S.; et al. General Atomic and Molecular Electronic Structure System. *J. Comput. Chem.* **1983**, *14 (11)*, 1347-1363.

[3] Advances in electronic structure theory: GAMESS a decade later; Gordon, M. S., Schmidt, M. W., Dykstra, C. E., Frenking, G., Kim, K. S., Scuseria, G. E., Eds.; Theory and Applications of Computational Chemistry: the first forty years; Elsevier, Amsterdam, 2005; pp 1167-1189.

[4] Muller, R. P. PyQuante Quantum Chemistry Program Suite. http://pyquante.sourceforge.net.

[5] Sun, Q.; Berkelbach, T.C.; Blunt, N.S.; Booth, G.H.; Guo, S.; Li, Z.; Liu, J.; McClain, J.; Sayfutyarova, E.R.; Sharma, S.; et al. PySCF: The Python-based Simulations of Chemistry Framework. *Wiley Interdiscip. Rev.: Comput. Mol. Sci.* **2018**, *8*, e1340.

[6] Murphy, K. V.; Turney, J. M.; Schaefer III, H. F. Student-Friendly Guide to Molecular Integrals. *J. Chem. Educ.* **2018**, *95 (9)*, 1572-1578.

[7] Sandoval-Salinas, M. E.; Casanova, D. The Doubly Excited State in Singlet Fission. *ChemPhotoChem.* **2021**, *5*, 282-293.

[8] Casanova, D.; Krylov, A. I. Quantifying local exciton, charge resonance, and multiexciton character in correlated wave functions of multichromophoric systems. *J. Chem. Phys.* **2016**, *144*, 014102.

[9] Luzanov, A. V.; Casanova, D.; Feng, X. et al. Quantifying charge resonance and multiexciton character in coupled chromophores by charge and spin cumulant analysis. *J. Chem. Phys.* **2015**, *142*, 224104.

[10] Szabo, A.; Ostlund, N. S. *Modern Quantum Chemistry: Introduction to Advanced Electronic Structure Theory*; Dover, Mineola, New York, 1996.

[11] Sherrill, C. D. Derivation of the Configuration Interaction Singles (CIS) Method for Various Single Determinant References and Extensions to Include Selected Double Substitutions (XCIS). *Sch. Chem. Biochem*. **1996**, 1-14.

[12] Neese, F.; Wennmohs, F.; Becker, U.; Riplinger, C. The ORCA quantum chemistry program package. *J. Chem. Phys.* **2020**, *152*, 224108.

[13] Basel, B. S. *et al*. Unified model for singlet fission within a non-conjugated covalent pentacene dimer. *Nat Commun.* **2017**, *8*, 15171.

[14] Higham, D. J.; Higham, N. J. *Matlab Guide*; 3rd ed.; SIAM, 2017.

[15] Etter, D. M. *Introduction to MATLAB*; 2nd ed.; Pearson Education Inc, Upper Saddle River, 2011.

CHAPTER 9

Conclusions

This dissertation describes analytical and computational studies of electron transfer (ET) and transport (ETr) in molecules and molecular junctions, as well as singlet fission (SF) in molecular systems. Most of the work is closely related to experiments although its scope is broader than specific experiments. It relates to two published and one submitted research paper, and a review article.

Specifically, in our first two published papers as presented in Chapters 3 and 4, we deal with the field of molecular electronics and junctions. In Chapter 3 we model transport in hybrid metal – ET protein – metal heterojunctions systems. The goal is to explain experimental results on the dependence of current on temperature and bias voltage for Azurin (Az): Holo-Az (Cu-substituted Az), Apo-Az (no metal) and Ni-, Co- and Zn-substituted Az. The experimental results are very interesting because they enable the analysis of transport through the same protein monolayer medium as a function of the metal substitution, the temperature and the voltage. Our results strongly suggest that for Holo-Az the transport mechanism depends on the protein monolayer/heterojunction setup. In one type of heterojunction, transport is dominated by resonant incoherent hopping through the Cu redox site, whereas in the other it is mediated by off-resonant tunneling. For the unsubstituted (Apo-Az) and other metal-substituted Azurins the dominant transport mechanism at low temperatures is off-resonant tunneling, with an average tunneling barrier that depends on the type of metal dopant, and at the highest temperatures it is through-amino acid hopping (Valianti, S.; Cuevas, J. C.; Skourtis, S. S. Charge-Transport Mechanisms in Azurin-Based Monolayer Junctions. *J. Phys. Chem. C* **2019**, *123 (10)*, 5907-5922.).

In Chapter 4, we propose a donor (D) – bridge (B) – acceptor (A) molecular junction, functioning in the incoherent hopping regime, that is suited for establishing direct correlations between the electrode-to-electrode current and the intramolecular donor-to-acceptor electron transfer rate. We suggest that this type of junction may be used to observe the Marcus-inverted-parabola dependence of the intramolecular rate on energy gap, by varying the bias voltage. The realization of such an experiment would enable meaningful comparisons between solution-phase electron transfer rates and molecular-junction currents for the same molecule (Valianti, S.; Skourtis, S. S. Observing Donor-to-Acceptor Electron-

Transfer Rates and the Marcus Inverted Parabola in Molecular Junctions. *J. Phys. Chem. B* **2019**, *123(45)*, 9641-9653.).

In Chapter 5 we describe a semi-analytical / computational framework to explore structure-function relationships for singlet fission in D-B-A molecular architectures. The aim of introducing a bridging linker between the D and A molecules is to tune, by modifying the bridge structure, the electronic pathways that lead to fission and to D-A-separated correlated triplets. We identify different bridge-mediation regimes for the effective singlet-fission coupling in the coherent tunneling limit and derive the dominant fission pathways in each regime. We describe the dependence of these regimes on D-B-A exciton-state energetics and on D-B (A-B) one-electron and two-electron matrix elements. This semi-analytical approach can be used to guide computational and experimental searches for D-B-A systems with tuned singlet fission rates. We use this approach to interpret the bridge-resonance effect of singlet fission that has been observed in recent experiments. We identify bi-excitonic D(A)-B correlated triplet-pair (CTP) states $\left|D^{+-}B^{+-}A\right\rangle_{CTP}$ $\left(\left|D\,B^{+-}A^{+-}\right\rangle_{CTP}\right)$, that act as "bottleneck" states for singlet fission and are responsible for the bridge-resonance effect that leads to the enhancement of the SF rate (Valianti, S.; Skourtis, S. S. The Role of Bridge-state Intermediates for Donor-bridge-acceptor Systems: A Semi-analytical Approach to Bridge-tuning of the Donor-acceptor Fission Coupling. *J. Phys. Chem. Lett*. under review).

In Appendix A we present an extensive review article on vibrational effects in molecular electron transfer reactions (Valianti, S.; Skourtis, S. S. Vibrational control of molecular electron transfer reactions. *Mol. Phys*. **2019**, *117 (19)*, 2618-2631.).

APPENDIX A

Vibrational Control of Molecular Electron Transfer Reactions

Vibrational motions promote molecular electron transfer reactions by bringing electron donor and electron acceptor electronic states to fleeting resonance, and by modulating the donor-to-acceptor electronic coupling. The main experimental signature of molecular motion effects on the electron transfer rate is the temperature dependence of the rate, which gives information about the overall free energy activation barrier for the electron transfer reaction. Another approach to probing the vibrational control of electron transfer rections is to excite specific electron-transfer-active vibrational motions by external infrared fields. This type of experimental probe is potentially more specific than thermal excitation and recent experiments have shown that molecular electron transfer rates can be perturbed by mode-specific infrared driving. We review the theory and experiments of vibrational control of electron transfer rates, and discuss future challenges that need to be tackled in order to achieve the mode-specific tuning of rates.

Molecular electron transfer and energy transfer reactions are ubiquitous in chemistry and biology. [1-8] Molecular motions are critical in determining the electron transfer (ET) rates by modulating the relative energies of electron donating and accepting states and the electronic couplings between these states ([9,10] and [8,11-15] for reviews). An interesting approach to probing the vibrational control of ET rates experimentally is to identify vibrational modes that influence the transport rate ("ET-active" modes), and to perturb these vibrations selectively by infrared (IR) excitation. [13-17] This type of experiment can reveal ET mechanism and potentially offer reversible mode-specific control of the reaction rate, since the influence of the IR excitation on the molecule is non-destructive and reversible. We first review the theory of molecular ET rates with an emphasis on the roles of ET-active vibrations. Then we discuss the theory of IR-perturbed ET and the experimental advances in this new and exciting field.

A.1 ET rate regimes: the roles of vibrational motions

The central roles of molecular vibrations in mediating chemical reactions is known since the development of transition state theory (TST). [9,18] Traditional ET rate theory of molecular donor-to-acceptor ET reactions is largely based on transition state TST. [9-11] Thus, the important "ET-active" vibrations are those which bring electron-donor and electron-acceptor states to quasi-resonance. Here we consider the simplest case of an electron that is initially localized in a donor (D) molecular electronic state (Fig. A.1). The electron may transfer to a final acceptor (A) electronic state by tunneling through a connecting molecular bridge (B). [19] The bridge-mediated D-A electronic coupling is denoted V .

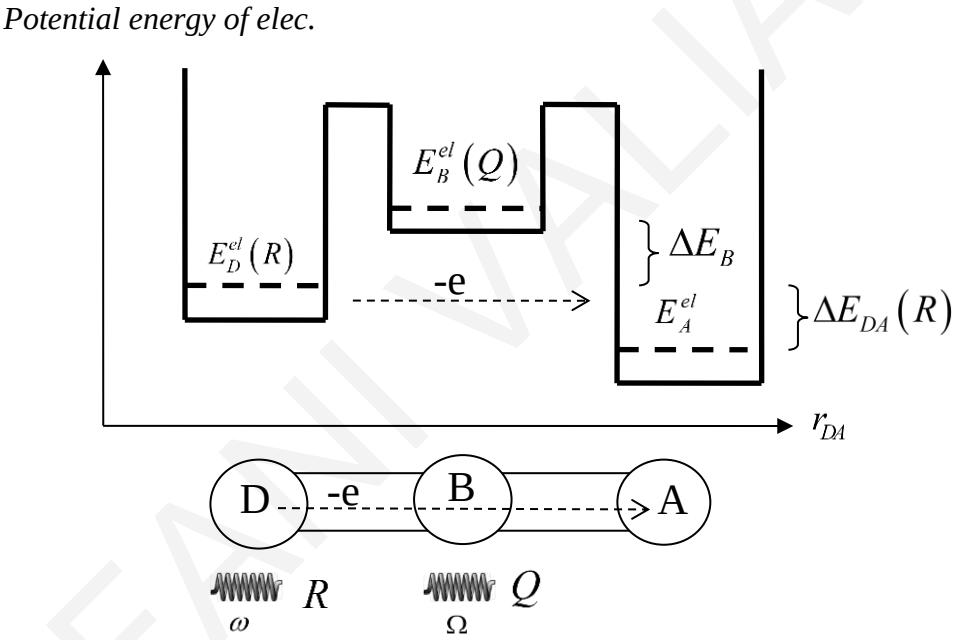

Figure A.1 Bridge-mediated donor-to-acceptor electron transfer (ET). The energy difference between donor (D) and acceptor (A) electronic states, ΔE_{DA}, is modulated by vibrations (accepting modes) that bring D and A to resonance. In the diagram one accepting mode R is assumed to modulate the D-state energy. When the B electronic state energy (E_B^{el}) is off-resonant to the donor and acceptor energies (E_D^{el} , E_A^{el}), the bridge acts as a tunnelling barrier for the transferring electron. The bridge-mediated tunnelling matrix element between D and A is denoted V . Bridge vibrations that modulate E_B^{el} cause fluctuations in V (promoting modes). The diagram shows a single promoting mode Q . If $E_B^{el}(Q)$ fluctuations

are large enough to bring the B state to D (A) resonance, ET may take place by a flickering resonance or a hopping mechanism, rather than tunnelling.

The D and A state energies are modulated by some vibration (described by a normal mode coordinate R). This type of ET-active vibration is often called an accepting mode. For some value $R = R_{res}$, D and A states become resonant, ($E_D^{el}(R_{res}) = E_A^{el}(R_{res})$), and the probability of ET from D-to-A is enhanced. In our simple model we will also include a vibrational mode Q that modulates the D-A coupling, $V(Q)$. This vibration may modulate the tunneling barrier width (eg. D-A distance modulation) or the tunneling barrier height (e.g., a bridge electronic-level modulation, Fig. A.1). Such an an ET-active vibration is often called a promoting or inducing mode. The Born-Oppenheimer Hamiltonian of the model is described by eq. 1 and is illustrated in Fig. A.2

$$\hat{H}^{BO} = E_D^{BO}(R)|D\rangle\langle D| + E_A^{BO}(R)|A\rangle\langle A| + V(Q)\left(|D\rangle\langle A| + h.c.\right). \qquad \text{(A.1)}$$

$E_D^{BO}(R)$ ($E_A^{BO}(R)$) are the diabatic Born-Oppenheimer (BO) surfaces for the D and A states. In Fig. A.2 they are assumed to be harmonic of frequency ω, i.e., $E_D^{BO}(R) = E_{D(\min)}^{BO} + m\omega^2(R - R_D)^2/2$ and $E_A^{BO}(R) = E_{A(\min)}^{BO} + m\omega^2(R - R_A)^2/2$. The accepting mode coordinate R sees the diabatic potential energy surface $E_D^{BO}(R)$ ($E_A^{BO}(R)$) when the electron is at the D (A) state. For the coordinate value $R = R_{res}$, the D and A diabatic BO surfaces cross, i.e., $E_D^{BO}(R_{res}) = E_A^{BO}(R_{res})$ in Fig. A.2. This crossing defines the center of the resonance region (see below). We assume that the promoting mode coordinate Q which modulates the coupling $V(Q)$ also sees a harmonic potential energy surface that is independent of whether the electron is in the D or A state. For bridge-mediated ET, this independence would be largely true for a bridge-localized vibration. We denote the promoting mode potential energy surface $E_B(Q) = \mu\Omega^2(Q - Q_{eq})^2/2$.

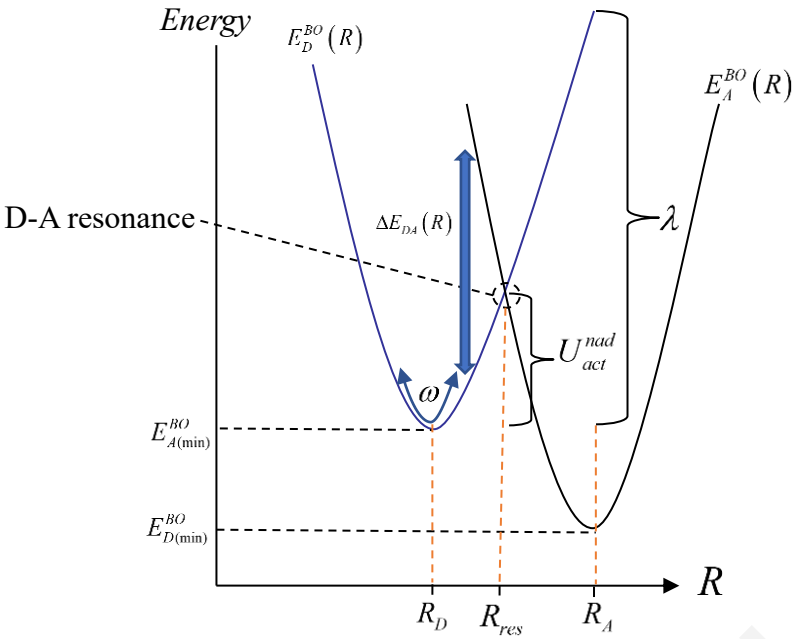

Figure A.2 The dynamics of the accepting mode R in Fig. A.1 depend on the transferring electron's state. When the electron is initially localized at the donor (D) state, the accepting mode R "sees" the potential energy surface $E_D^{BO}(R)$ (diabatic BO surface) with equilibrium value R_D. When the electron has transferred to the acceptor (A) state the dynamics of R is governed by $E_A^{BO}(R)$ with equilibrium value R_A. With the electron initially at D, and assuming that R is a classical vibration, the oscillations of R around R_D lead to D-A energy gap fluctuations $\Delta E_{DA}(R)$. Whenever crosses R_{res}, D an A states become resonant and ET takes place with high probability due to the coupling V, with a probability equal to the Landau-Zener probability $P_{D\to A}^{LZ}$. In the nonadiabatic limit, the coupling is weak $P_{D\to A}^{LZ} \ll 1$, and many crossings of R_{res} are required to change electronic state from D to A (i.e., for ET to take place). Thus, the diabatic BO surfaces (diagonal part of the Hamiltonian in eq. (A.1)), give the correct electronic-state-dependent dynamics of R.

In the following, the above model is used to describe different ET regimes and the roles of ET-active vibrations in determining the rate in each regime. [1,3,4,9-11] We distinguish between classical and quantum vibrational effects. Traditional ET theory relates only to accepting-mode dynamics so we first assume that the D-A coupling in eq. (A.1) does not fluctuate ($V(Q) = V$, a constant).

A.2 Classical accepting modes

The accepting mode may be treated as a classical vibration at a given temperature T if $k_B T >> \hbar\omega$. In this situation the dynamics of R is described by classical trajectories $R(t)$ on the D (or A) BO surfaces. To distinguish between the different limiting regimes of ET (weak versus strong electronic coupling V), we use the Landau-Zener D-to-A transition probability $P_{D\to A}^{LZ} = 1 - \exp(-\gamma_{LZ})$ where $\gamma_{LZ}(V)$ is the Landau-Zener parameter (e.g., [10,11]). Suppose the electron is originally in the D state and R is far from the resonance value R_{res}. The potential energy surface that determines the dynamics of R is the diabatic $E_D^{BO}(R)$ (Fig. A.2). Since $E_D^{BO}(R)$ is harmonic, any mode trajectory $R(t)$ with the electron in the D state will oscillate around the $E_D^{BO}(R)$ equilibrium value R_D and the D-A energy gap will be time-dependent, i.e., $\Delta E_{DA}(t) = E_A^{BO}(R(t)) - E_D^{BO}(R(t))$ in Fig. A.2. A mode resonance-crossing event takes place every time (denoted t_{res}) the trajectory $R(t)$ attains the D-A resonance value $R(t_{res}) = R_{res}$ for which $\Delta E_{DA}(R(t_{res})) = 0$ and the D and A electronic states become resonant i.e., $E_D^{el}(R_{res}) = E_A^{el}(R_{res})$. For each such crossing event the probability of D-to-A ET is given by the Landau-Zener probability $P_{D\to A}^{LZ} = 1 - \exp(-\gamma_{LZ})$. The parameter γ_{LZ} may be interpreted as the ratio between the Landau –Zener time and the Rabi time, i.e., $\gamma_{LZ} \approx \tau_{LZ}/\tau_{Rabi}$ (e.g., [20]). The Landau-Zener time is a measure of the time D and A states remain in the resonance region per crossing event, where the resonance region is defined by all values of t around t_{res} (or of $R(t)$ around R_{res}) such that $|\Delta E_{DA}(t)| < |V|$. Thus $\tau_{LZ} \approx V / \langle |d_t \Delta E_{DA}(t_{res})| \rangle_{eq}$ where $\langle ... \rangle_{eq}$ denotes thermal (equilibrium) average and $d_t \equiv d/dt$. The Rabi time, $\tau_{Rabi} \approx h/V$, is a measure of the period of oscillations of the transition probability $P_{D\to A}(t)$ if the D and A states remain in resonance. A more exact analysis in terms of the simple model in Fig. A.2 gives

$$\gamma_{LZ} = \frac{\pi^{3/2} V^2}{\hbar\omega\sqrt{\lambda k_B T}} \ , \qquad \text{(A.2)}$$

where $\lambda = m\omega^2 (R_A - R_D)^2/2$ is the reorganization energy (Fig. A.2). [11] The term $\omega\sqrt{\lambda k_B T}$

is obtained from $\left\langle \left| d_t \Delta E_{DA}(t_{res}) \right| \right\rangle$ by writing it in terms of the mean mean velocity of the oscillator at the resonance crossing, i.e., $\left\langle \left| d_t \Delta E_{DA}(t_{res}) \right| \right\rangle_q = \left\langle \left| dR(t_{res})/dt \right| \right\rangle_{eq} \times \left| d\Delta E_{DA} / dR \right|$.

A.2.1 Nonadiabatic weak-coupling regime

This regime applies to weak D-A coupling V such that $\gamma_{LZ} << 1$ and $\tau_{Rabi} >> \tau_{LZ}$. In this nonadiabatic limit, the probability of ET for each resonance crossing is very small and is given by $P_{D\to A}^{LZ} \approx \gamma_{LZ}$. The rate is given by

$$k_{ET}^{nad(eq)} = \frac{2\pi}{\hbar} V^2 \rho_{FC}^{cl(eq)}, \qquad \rho_{FC} = \frac{1}{\sqrt{4\pi\lambda k_B T}} \exp\left(-\frac{U_{act}^{nad}}{k_B T} \right) \tag{A.3}$$

where $\rho_{FC}^{cl(eq)}$ is the classical thermal Franck Condon factor. U_{act}^{nad} is the activation energy of the reaction and given by,

$$U_{act}^{nad} = \frac{(\Delta E + \lambda)^2}{4\lambda} \tag{A.4}$$

where $\Delta E = E_{A(\min)}^{BO} - E_{D(\min)}^{BO}$ is the energy gap between BO surface minima (Fig. A.2). In the nonadiabatic limit, the ET is rate-limited by the activation event to the crossing region ($\propto \exp\left(-U_{act}^{nad}/k_B T\right)$) and by the D-A coupling ($\propto V^2$). The ET-active mode enables the activation to resonance and its frequency also determines the amount of time D and A remain in resonance (the latter appears in the Landau-Zener parameter).

A more general form of eq. (A.5) replaces the activation energy by an activation free energy. This generalization applies to the realistic case where several independent accepting vibrational modes $\{R_i\}$ modulate the D-A energy gap, i.e., $\Delta E_{DA}(\{R_i\}) = E_A^{BO}(\{R_i\}) - E_D^{BO}(\{R_i\})$. In this situation many different sets of resonance configurations $\{R_i\}_{res}$ are possible (for which $\Delta E_{DA}(\{R_i\}_{res}) = 0$). Thus, there is an entropy $k_B \ln(\mathrm{N})$ associated with the number N of all such sets with $\Delta E_{DA} = 0$, and the activation energy should be replaced by an activation free energy which includes this entropy.

A.2.2 Adiabatic strong-coupling regime

This regime is characterized by strong coupling V such that $\gamma_{LZ} \geq 1$ and $\tau_{Rabi} \leq \tau_{LZ}$. In the adiabatic limit the probability of ET for each resonance crossing is near-unity $P_{D\to A}^{LZ} \approx 1$ (complete D-to-A ET per resonance crossing). The rate is given by

$$k_{ET}^{ad(eq)} \approx \frac{\omega}{2\pi} \exp\left(-\frac{U_{act}^{ad}}{k_B T} \right) \tag{A.5}$$

with activation energy $U_{act}^{ad} \approx U_{act}^{nad} - |V|$ that is lower than the nonadiabatic activation energy. This lowering is due to the broadening of the Landau-Zener region (Fig. A.3).

The adiabatic rate is rate-limited by the activation event to the adiabatic crossing region ($\propto \exp\left(-U_{act}^{ad(eq)} / k_B T\right)$) but not by the electronic coupling. Rather, the rate is proportional to the oscillation frequency of the ET-active vibration (which is the TST attempt-frequency). As in the nonadiabatic case, the ET-active mode enables D-A resonance.

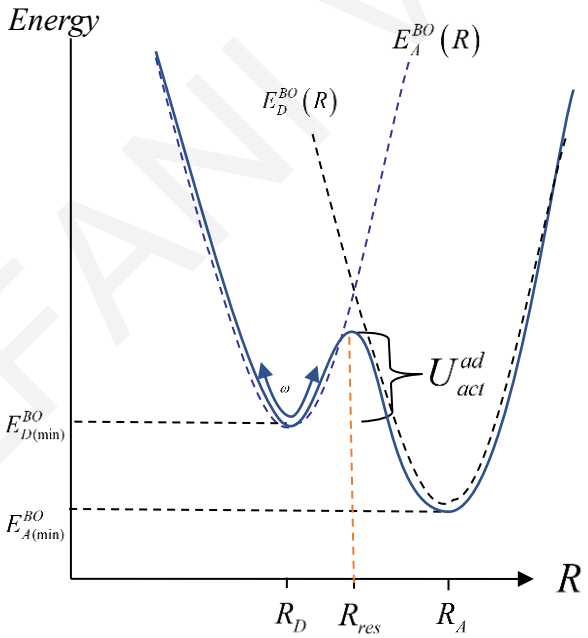

Figure A.3 In the adiabatic limit (strong D-A coupling V) the dynamics of the promoting mode R is best described by an adiabatic BO surface (lowest eigenstate of the Hamiltonian in eq. (A.1)). Due to the large value of V, D and A states are quasi-resonant in a wider region of R around R_{res}. Assuming that R is a classical coordinate, D-to-A ET takes place with

near-unity probability every time R enters this quasi-resonance region, $P_{D\to A}^{LZ}\approx 1$. Thus, as a function of R, the potential energy surface that determines the dynamics in the resonance region is due to the lowest adiabatic BO state which is a linear combination of diabatic D and A BO states of Fig. A.2.

A.3 Quantum accepting modes

The accepting mode may be treated as quantum at a given temperature T if $k_B T << \hbar\omega$. In this situation the dynamics of R is described by vibrational wavefunctions and the state of the ET system is described by products of electronic and vibrational states $|el;vi\rangle = |el\rangle \otimes |vi\rangle$ (vibronic states).

A.3.1 Nonadiabatic weak-coupling regime

For a quantum accepting mode the full Hamiltonian of the ET system is written as $\hat{H} = |D\rangle\langle D| \otimes \hat{H}_D^{vib} + |A\rangle\langle A| \otimes \hat{H}_A^{vib} + V\left(|D\rangle\langle A| + h.c.\right) \otimes \hat{I}^{vib}$, where $\hat{H}_D^{vib} = \hat{P}^2/2m + E_D^{BO}\left(\hat{R}\right)$, and $\hat{H}_A^{vib} = \hat{P}^2/2m + E_A^{BO}\left(\hat{R}\right)$. The vibrational states $|n_D\rangle$ and $|n_A\rangle$ denote harmonic oscillator eigenstates of $\hat{H}_D^{vib}$ and $\hat{H}_A^{vib}$, respectively, with eigenenergies $E_{D(\min)}^{BO} + \varepsilon_{n_D}$ and $E_{A(\min)}^{BO} + \varepsilon_{n_A}$ (Fig. A.4), where $\varepsilon_{n_D} = \hbar\omega\left(n_D + 1/2\right)$ and $\varepsilon_{n_A} = \hbar\omega\left(n_A + 1/2\right)$. The ET rate can be expressed as a thermally weighted sum of Fermi-Golden Rule rates $k_{D,n_D\to A,n_A}^{nad}$ between initial $|D;n_D\rangle = |D\rangle|n_D\rangle$ and final $|A;n_A\rangle = |A\rangle|n_A\rangle$ vibronic states (Fig A.4). Each rate $k_{D,n_D\to A,n_A}^{nad}$ is induced by the coupling $\langle D;n_D|\hat{H}|A;n_A\rangle = V \times \langle n_D|n_A\rangle$ (where $\langle n_D|n_A\rangle$ is the vibrational-state overlap). Thus, the thermally averaged nonadiabatic ET rate is given by

$$\tilde{k}_{ET}^{nad(eq)} = \sum_{n_D} p_{n_D}^{eq} \sum_{n_A} \tilde{k}_{D,n_D\to A,n_A}^{nad}, \tag{A.6a}$$

where

$$\tilde{k}_{D,n_D\to A,n_A}^{nad} = \frac{2\pi}{\hbar}|V|^2 \left|\langle n_D|n_A\rangle\right|^2 \delta\left[\left\{E_{D(\min)}^{BO} + \varepsilon_{n_D}\right\} - \left\{E_{A(\min)}^{BO} + \varepsilon_{n_A}\right\}\right]. \tag{A.6b}$$

The tilde notation denotes quantum-mode, (to distinguish from the classical-mode rate in eq. (A.3)). The double sum in eq. (A.6a) is between initial ($|n_D\rangle$) and final ($|n_A\rangle$) vibrational states, where $p_{n_D}^{eq} = e^{-\varepsilon_{n_D}/k_BT} \Big/ \sum_{n_D} e^{-\varepsilon_{n_D}/k_BT}$ is the thermal equilibrium probability of each initial vibrational state ($\left|\langle n_D | n_A\rangle\right|^2$ is the $|n_D\rangle$ to $|n_A\rangle$ Franck-Condon factor). Equations (A.6a) and (A.6b) can be cast in a more familiar form analogous to eq. (A.3), i.e.,

$$\begin{aligned} \tilde{k}_{ET}^{nad(eq)} &= (2\pi/\hbar)V^2 \rho_{FC}^{qu(eq)}, \\ \rho_{FC}^{qu(eq)} &= \sum_{n_D} p_{n_D}^{eq} \sum_{n_A} \left|\langle n_D | n_A\rangle\right|^2 \delta\left[\left\{E_{D(\min)}^{BO} + \varepsilon_{n_D}\right\} - \left\{E_{A(\min)}^{BO} + \varepsilon_{n_A}\right\}\right]. \end{aligned} \tag{A.7}$$

$\rho_{FC}^{qu(eq)}$ is the quantum thermally-weighted Franck-Condon factor. Since the initial and final vibrational states have finite lifetimes due to vibrational relaxation, their energies are homogeneously broadened. Thus, each of the delta functions should be thought of as a Lorentzian $(\hbar\Gamma/\pi)\left[\left(\left\{E_{D(\min)}^{BO} + \varepsilon_{n_D}\right\} - \left\{E_{A(\min)}^{BO} + \varepsilon_{n_A}\right\}\right)^2 + (\hbar\Gamma)^2\right]^{-1}$ whose width is determined by the vibrational relaxation rates Γ_{n_D}, Γ_{n_A} of the initial and final vibrational states, i.e., where $\Gamma = \Gamma_{n_D} + \Gamma_{n_A}$ (Fig. A.4).

Equations (A.6a), (A.6b) or (A.7) describe the nonadiabatic rate in the Condon approximation. This approximation is explained below when we consider coupling fluctuations. The weak-coupling (nonadiabatic) regime is valid when $\left|V \times \langle n_D | n_A\rangle\right| << \hbar\Gamma$, in which case there are no coherent oscillations in the transition probabilities between initial and final vibronic states. Thus, the time evolution of the transition probabilities can be described by rates $k_{D,n_D \to A,n_A}^{nad}$ proportional to $\left|V \times \langle n_D | n_A\rangle\right|^2$.

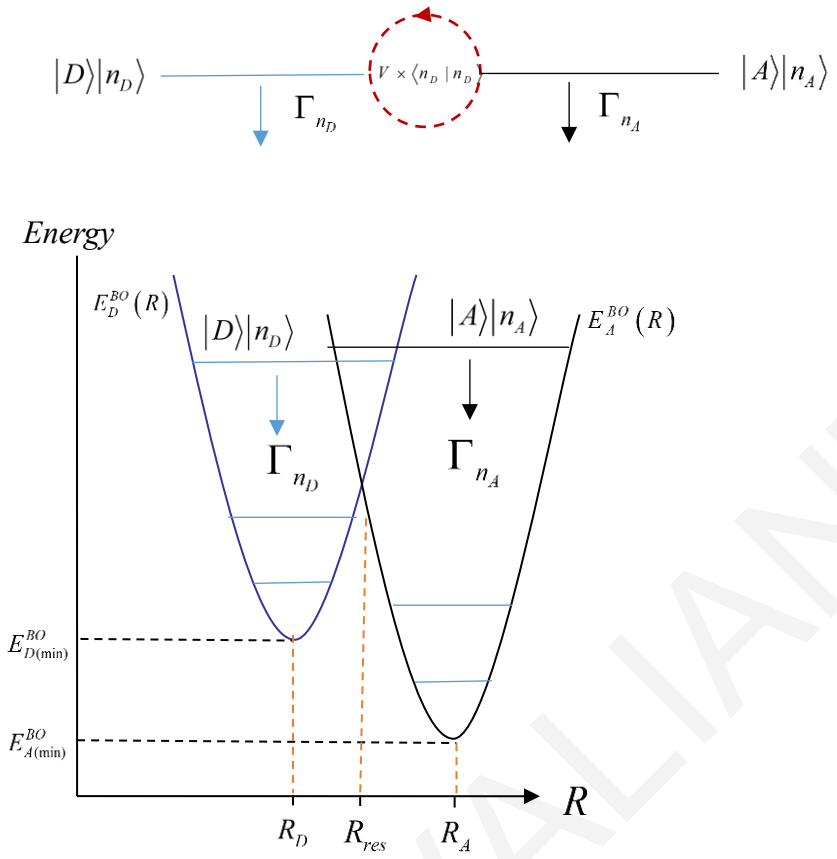

Figure A.4 Vibronic picture of the nonadiabatic ET rate for a quantum accepting mode. The average rate is a thermally weighted sum of vibronic rates $k^{nad}_{D,n_D\to A,n_A}$ between initial $|D;n_D\rangle=|D\rangle|n_D\rangle$ and final $|A;n_A\rangle=|A\rangle|n_A\rangle$ vibronic states. Each transition is induced by the vibronic coupling $V\times\langle n_D|n_A\rangle$. $|n_D\rangle$ and $|n_A\rangle$ denote harmonic oscillator eigenstates of the $E_D^{BO}(R)$ and $E_A^{BO}(R)$, respectively. Γ_{n_D} and Γ_{n_A} are the vibrational relaxation rates of the initial and final vibrational states ($\Gamma=\Gamma_{n_D}+\Gamma_{n_A}$). The quantum nonadiabatic regime is valid when $|V\times\langle n_D|n_A\rangle|<\hbar\Gamma$. In the quantum adiabatic regime, $|V\times\langle n_D|n_A\rangle|\geq\hbar\Gamma$, and coherent oscillations between quasi-resonant $|D\rangle|n_D\rangle$ and $|A\rangle|n_A\rangle$ vibronic states may be important. The ET transition is not fully described by simple rate equations.

A.3.2 Adiabatic strong-coupling regime

When $|V\times\langle n_D|n_A\rangle|\geq\hbar\Gamma$ (see Fig. A.4) coherent oscillations between quasi-resonant $|D\rangle|n_D\rangle$ and $|A\rangle|n_A\rangle$ vibronic states may be observed and, in this case, the ET reaction cannot be described by simple rate equations. The time evolution of the transition probability

from D-to-A should be described by density matrix equations of the relevant vibronic states which incorporate the vibronic-state coupling to the bath degrees of freedom. This methodology is briefly described in the discussion of eq. (A.18).

A.4 Rates in terms of vibrational-coordinate and energy-gap probability densities

To show explicitly the role of vibrational fluctuations on ET rates, we consider as an example the nonadiabatic rate in eq. (A.3) for a classical accepting-mode R, and show how to express this rate in terms of the canonical probability density of R. This density is given by $p_D^{eq}(R) = \int dP\ \rho_{can}(P,R)$, where

$$\rho_{can}(P,R) = \exp\left[-\left(P^2/2m + E_D^{BO}(R)\right)/k_BT\right] \Big/ \iint dPdR \exp\left[-\left(P^2/2m + E_D^{BO}(R)\right)/k_BT\right]. \tag{A.8}$$

The nonadiabatic rate is an equilibrium thermal average $\langle ... \rangle_{eq(D)}$ with respect to R of $R-$dependent ET rates derived from Fermi's golden rule:

$$k_{ET}^{nad(eq)} = \left\langle k_{ET}^{nad}(R)\right\rangle_{eq(D)} = \int dR\ \ p_D^{eq}(R)\ \ \frac{2\pi}{\hbar} V^2 \delta\left(\Delta E_{DA}(R)\right). \tag{A.9}$$

For the harmonic energy surface in Fig. A.2, $E_D^{BO}(R) = E_{D(\min)}^{BO} + m\omega^2 (R-R_D)^2/2$, and the equilibrium density is Gaussian,

$$p_D^{eq}(R) = \frac{1}{\sqrt{2\pi\sigma_R^2}} \exp\left(-(R-R_D)^2/2\sigma_R^2\right), \qquad \sigma_R^2 = k_BT/m\omega^2\ . \tag{A.10}$$

Equation (A.3) is obtained from eqs (A.8) and (A.9) by assuming harmonic BO surfaces for $\Delta E_{DA}(R) = E_A^{BO}(R) - E_D^{BO}(R)$ such that, in the delta-function, $\Delta E_{DA}(R) \approx \Delta E_{DA}^{harm}(R)$ where $\Delta E_{DA}^{harm}(R) = \left(E_{A(\min)}^{BO} - E_{D(\min)}^{BO}\right) + \lambda - \left(2\lambda/\left(R_A - R_D\right)\right)R$.

Alternatively, the nonadiabatic rate can be written in terms of the energy gap $\Delta E_{DA}(R)$ fluctuations caused by the R vibration. This approach is more natural for the realistic case of many accepting modes, where the D-A energy gap arising from all modes is the relevant ET rate reaction coordinate rather than the individual mode coordinates. In our simple example, the equilibrium probability density for the energy gap is given by

$\rho_D^{eq}\left(\Delta E_{DA}\right) = \int dR\ \ p_D^{eq}\left(R\right)\ \delta\left(\Delta E_{DA} - \Delta E_{DA}\left(R\right)\right)$, where ΔE_{DA} denotes a specific energy-gap value. From eq. (A.8) and from the expression for $\Delta E_{DA}^{harm}\left(R\right)$, it can be shown that

$$\rho_D^{eq}\left(\Delta E_{DA}\right) = \frac{1}{\sqrt{2\pi\sigma_{\Delta E_{AD}}^2}} \exp\left(-\left(\Delta E_{DA} - \left\langle \Delta E_{DA}\right\rangle\right)^2 \Big/ 2\sigma_{\Delta E_{DA}}^2\right), \tag{A.11}$$

where, $\sigma_{\Delta E_{DA}}^2 = 2\lambda k_B T$ and $\left\langle \Delta E_{DA}\right\rangle = E_{D(\min)}^{BO} - E_{A(\min)}^{BO} + \lambda$. The nonadiabatic rate in eq. (A.3) is a thermal average over ΔE_{DA} values of Fermi' s golden rule rates:

$$\begin{aligned} & k_{ET}^{nad(eq)} = \left\langle k_{ET}^{nad}\left(\Delta E_{DA}\right)\right\rangle_{eq} = \\ & \int d\Delta E_{DA}\ \ \rho_D^{eq}\left(\Delta E_{DA}\right)\ \frac{2\pi}{\hbar} V^2 \delta\left(\Delta E_{DA}\right) = \frac{2\pi}{\hbar}\ V^2\ \underbrace{\rho_D^{eq}\left(\Delta E_{DA} = 0\right)}_{\rho_{FC}^{cl(eq)}} \end{aligned} \tag{A.12}$$

The adiabatic rate in eq. (A.5) may also be derived from the probability density of the classical accepting mode coordinate. This approach to deriving the adiabatic rate is identical to analogous derivations of TST rates which involve thermal activation over a simple barrier.[9,18,21-22] A formulation of the quantum-nonadiabatic rate (eqs (A.6a) and (A.6b)) in terms of the accepting-mode-coordinate probability distributions requires the use of semi-classical formulations of the ET rate (e.g., [22] for a review).

A.5 Coupling fluctuation effects and promoting modes

Up to this point we have assumed that the D-A electronic coupling V in eq. (A.1) does not fluctuate. If we allow for coupling fluctuations in addition to energy-gap fluctuations we can obtain a simple generalization of the nonadiabatic rate expressions ([12,14] for reviews). Consider, for example, a bridge mode Q of frequency Ω (Fig. A.1) which modulates the tunnelling barrier between D and A such that the bridge-mediated D-A coupling depends on the mode coordinate, $V = V\left(Q\right)$. Q is denoted a promoting mode and it may be considered a classical oscillator if $\hbar\Omega << k_B T$, and a quantum oscillator in the opposite limit.

A.5.1 Classical promoting mode

For a classical promoting mode, the equilibrium probability density of Q is given $p_B^{eq}(Q) = \left(2\pi\sigma_Q^2\right)^{-1/2} \exp\left(-(Q-\langle Q\rangle)^2/2\sigma_Q^2\right)$ (as in eq. (A.10)) where B denotes bridge. The equilibrium probability density for the D-A coupling is given by $\rho_V^{eq}(V) = \int dQ\ p_B^{eq}(Q)\ \delta\left(V - V(Q)\right)$. The nonadiabatic ET rate in eq. (A.3), which is an equilibrium average over accepting mode fluctuations, must now also be averaged over promoting mode fluctuations, i.e.,

$$\left\langle k_{ET}^{nad}(Q)\right\rangle_{eq} = \int dQ\ p_B^{eq}(Q)\frac{2\pi}{\hbar}\ V(Q)^2\ \rho_{FC}^{eq} = \int dV \rho_B^{eq}(V)\frac{2\pi}{\hbar}V^2\rho_{FC} = \frac{2\pi}{\hbar}\left\langle V^2\right\rangle_{eq}\rho_{FC}^{cl(eq)} \tag{A.13}$$

Defining an average rate as in eq. (A.13) assumes the typical slowest timescale of coupling fluctuations is fast compared to the typical ET time (inverse ET rate). If the coupling fluctuation timescale is slower than the ET time, then the ET kinetics will be distributed and such kinetics cannot be described by a single (average-rate) value (see e.g., [23] for a discussion of this regime in ET).

In summary, the simplest effect of coupling fluctuations in eq. (A.2) is the replacement of V^2 by a thermally averaged $\left\langle V^2\right\rangle_{eq}$. Equation (A.13) generalizes the classical nonadiabatic rate in the Franck-Condon approximation by incorporating "static" effects of coupling fluctuations via the average $\left\langle V^2\right\rangle_{eq} = \langle V\rangle_{eq}^2 + \sigma_V^2$. It is useful for the discussion in the following sections to express the rate in eq. (A.13) as a double average over promoting and accepting mode fluctuations or, equivalently, coupling and energy gap fluctuations

$$\begin{aligned} k_{ET}^{nad(eq)} &= \int dQ\ p_B^{eq}(Q)\int dR\ p_R^{eq}(Q)\ \frac{2\pi}{\hbar}V(Q)^2\ \delta\left(\Delta E_{DA}(R)\right) \\ &= \int dQ\ \rho_B^{eq}(V)\int d\Delta E_{DA}\ \rho_D^{eq}\left(\Delta E_{DA}\right)\ \frac{2\pi}{\hbar}V^2\delta\left(\Delta E_{DA}\right). \end{aligned} \tag{A.14}$$

A.5.2 Quantum promoting modes and the breakdown of the Condon approximation

The quantum nonadiabatic ET rate in eqs (A.6) or (A.7) is a thermally-weighted sum of nonadiabatic rates between initial and final vibronic states (eq. (A.6a)). To incorporate the effects of a quantum accepting mode in the nonadiabatic rate, the vibronic states of the system must now include the promoting mode eigenstates. [24] Therefore, initial and final vibronic states of the ET reaction are written as $\left|D,n_D,\nu_{in}\right\rangle=\left|D\right\rangle\left|n_D\right\rangle\left|\nu_{in}\right\rangle$ and $\left|A,n_A,\nu_{fi}\right\rangle=\left|A\right\rangle\left|n_A\right\rangle\left|\nu_{fi}\right\rangle$, where $\left|\nu_{in}\right\rangle$ and $\left|\nu_{fi}\right\rangle$ are initial and final promoting mode eigenstates, respectively, with energies $\varepsilon_{\nu_{in}}=\hbar\Omega\left(\nu_{in}+1/2\right)$ and $\varepsilon_{\nu_{fi}}=\hbar\Omega\left(\nu_{fi}+1/2\right)$. By analogy to eqs (A.6a) and (A.6b),

$$\tilde{k}_{ET}^{nad(eq)}=\sum_{\nu_{in}}p_{\nu_{in}}^{eq}\sum_{n_D}p_{n_D}^{eq}\sum_{\nu_{fi}}\sum_{n_A}\tilde{k}_{D,n_D,\nu_{in}\to A,n_A,\nu_{fi}}^{nad}\,, \tag{A.15}$$

where $k_{D,n_D,\nu_{in}\to A,n_A,\nu_{fi}}^{nad}$ is the Fermi-Golden Rule rate between $\left|D,n_D,\nu_{in}\right\rangle$ and $\left|A,n_A,\nu_{fi}\right\rangle$,

$$k_{D,n_D,\nu_{in}\to A,n_A,\nu_{fi}}^{nad}= \frac{2\pi}{\hbar}\left|\left\langle D,n_D,\nu_{in}\left|\hat{V}\right|A,n_A,\nu_{fi}\right\rangle\right|^2\delta\left[\left\{E_{D(\min)}^{BO}+\varepsilon_{n_D}+\varepsilon_{\nu_{in}}\right\}-\left\{E_{A(\min)}^{BO}+\varepsilon_{n_A}+\varepsilon_{\nu_{fi}}\right\}\right]. \tag{A.16}$$

The average in eq. (A.15) is over accepting and promoting mode equilibrium distributions. $p_{n_D}^{eq}=e^{-\varepsilon_{n_D}/k_BT}\Big/\sum_{n_D}e^{-\varepsilon_{n_D}/k_BT}$, $p_{\nu_{in}}^{eq}=e^{-\varepsilon_{\nu_{in}}/k_BT}\Big/\sum_{n_D}e^{-\varepsilon_{\nu_{in}}/k_BT}$. The coupling in eq. (A.16) is given by $\left\langle D,n_D,\nu_{in}\left|\hat{V}\right|A,n_A,\nu_{fi}\right\rangle=\left\langle D,\nu_{in}\left|V(Q)\right|A,\nu_{fi}\right\rangle\left\langle n_D\,|\,n_A\right\rangle$, where $\hat{V}=V\left(Q\right)\left(\left|D\right\rangle\left\langle A\right|+h.c.\right)$. To compute the matrix elements $\left\langle D,\nu_{in}\left|V(Q)\right|A,\nu_{fi}\right\rangle$, $V(Q)$ can be expanded as $V\left(Q\right)=V\left(Q_0\right)+\frac{1}{2}\left[\frac{d^2V}{dQ^2}\right]_{Q_0}\left(Q-Q_0\right)^2+\textit{higher order}$. The golden-rule limit is valid when $\left|V\times\left\langle n_D\,|\,n_A\right\rangle\times\left\langle\nu_{in}\left|\nu_{fi}\right\rangle\right|<<\hbar\Gamma$, where $\Gamma=\Gamma_{n_D}+\Gamma_{n_A}+\Gamma_{\nu_{in}}+\Gamma_{\nu_{fi}}$ is a total vibrational relaxation rate for the initial and final vibrational states.

The expression in eqs (A.15) and (A.16) can be cast into a time-domain form ([12,14] and references therein). It is the time Fourier transform of the product of two equilibrium correlation functions (eq. (A.17)), where the transform is evaluated at the frequency of the $E_{D(\min)}^{BO}-E_{A(\min)}^{BO}$ gap (Fig. A.2):

$$\tilde{k}_{ET}^{nad(eq)} = \frac{1}{\hbar^2}\int_{-\infty}^{+\infty} dt\; e^{i\left(E_{D(\min)}^{BO}-E_{A(\min)}^{BO}\right)t/\hbar}\; \left\langle \hat{C}_V(t)\right\rangle_{eq(B)}\; \left\langle \hat{C}_{FC}(t)\right\rangle_{eq(D)}. \qquad \text{(A.17)}$$

$\left\langle \hat{C}_V(t)\right\rangle_{eq(B)} = \left\langle \hat{V}(t)\hat{V}(0)\right\rangle_{eq(B)}$ is the time-dependent coupling correlation function where $\hat{V}(t) = \exp\left(it\hat{H}_B^{vib}/\hbar\right)\hat{V}(0)\exp\left(-it\hat{H}_B^{vib}/\hbar\right)$ is evolved in time using the vibrational Hamiltonian $\hat{H}_B^{vib}$ for the promoting mode. The averaging is over the promoting mode equilibrium distribution, $\langle ...\rangle_{eq(B)} = \sum_{\nu_{in}} p_{\nu_{in}}^{eq}\langle \nu_{in}|...|\nu_{in}\rangle$. $\left\langle \hat{C}_{FC}(t)\right\rangle_{eq(D)}$ is the Franck-Condon correlation function, where $\hat{C}_{FC}(t) = \exp\left(it\hat{H}_D^{vib}/\hbar\right)\exp\left(-it\hat{H}_A^{vib}/\hbar\right)$ and $\hat{H}_D^{vib}$ and $\hat{H}_A^{vib}$ are the accepting-mode vibrational Hamiltonians for the D and A BO surfaces of Fig. A.2. The equilibrium average involves the D vibrational equilibrium distribution $\langle ...\rangle_{eq(D)} = \sum_{n_D} p_{n_D}^{eq}\langle n_D|...|n_D\rangle$.

Equation (A.17) is convenient for computations involving molecular dynamics simulations, where the correlation-function averages can be evaluated in the semi-classical approximation. It is also the starting point for deriving the Condon approximation and its dynamical corrections. If coupling fluctuations are very slow with respect to energy gap fluctuations then, in eq. (A.17), $\left\langle \hat{C}_V(t)\right\rangle_{eq(B)}$ can be replaced by $\left\langle \hat{C}_V(t=0)\right\rangle_{eq(B)} = \left\langle \hat{V}^2\right\rangle_{eq(B)}$ and taken out of the Fourier integral. This leads to the most-general expression for the quantum nonadiabatic rate in the Condon approximation, $\tilde{k}_{ET}^{nad(eq)} = 2\pi/\hbar\left\langle \hat{V}^2\right\rangle_{eq(B)}\rho_{FC}^{qu(cl)}$, which is a generalization of eq. (A.7) for fluctuating coupling. The classical limit of this expression leads to eqs (A.13) or (A.14). Dynamical non-Condon effects are important when the coupling and energy-gap fluctuations are of similar magnitudes and timescales. Dynamical non-Condon corrections to the Condon rate can be computed by expanding $\left\langle \hat{C}_V(t)\right\rangle_{eq(B)}$ in a Taylor series with respect to time and keeping successive terms $\left(t^n/n!\right)\times\frac{d^n}{dt^n}\left\langle \hat{C}_V(t=0)\right\rangle_{eq(B)}$ in the Fourier integral of eq. (A.17). [24]

The nonadiabatic rate equations can be further generalized to include several promoting and accepting modes, mixed classical and quantum modes within the same molecular system, and interdependent promoting and accepting modes, i.e., $V = V(Q,R)$. Although the nonadiabatic-rate limit is not always valid (see below), we will use eqs (A.13)-(A.15) in

much of our discussion of non-equilibrium vibrational effects because these rate equations are easily generalized to describe non-equilibrium vibrational distributions of the ET-active modes.

A.5.3 Adiabatic strong-coupling regime

Introducing a classical accepting mode for the adiabatic rate in eq. (A.5) means that the mode will modulate the adiabatic activation energy (Fig. A.3) through the coupling, i.e., $U_{act}^{ad} \approx U_{act}^{nad} - |V| \rightarrow U_{act}^{ad}(Q) \approx U_{act}^{ad} - |V(Q)|$. Thus, the averaging of the adiabatic rate over accepting and promoting mode fluctuations maps to problems of stochastic resonance which involve rate averaging over fluctuating barriers. [21]

In the quantum adiabatic regime, $\left|V \times \langle n_D | n_A \rangle \times \langle \nu_{in} | \nu_{fi} \rangle\right| \geq \hbar\Gamma$, where $\Gamma = \Gamma_{n_D} + \Gamma_{n_A} + \Gamma_{\nu_{in}} + \Gamma_{\nu_{fi}}$ is a total vibrational relaxation rate for the initial and final vibrational states. As already discussed, simple rate equations are not appropriate in this limit and the time evolution of the transition probability from D-to-A may be partially oscillatory. The ET transition should be described by density matrix equations involving the relevant accepting and promoting vibronic states and the system's coupling to bath degrees of freedom. Namely, the D-B-A system Hamiltonian is written in the basis of the $|D, n_D, \nu_{in}\rangle$ and $|A, n_A, \nu_{fi}\rangle$ states as $\hat{H}_S = \hat{H}_D + \hat{H}_B + \hat{H}_A + \hat{H}_{DB} + \hat{H}_{AB}$ where $\hat{H}_D$, $\hat{H}_B$ and $\hat{H}_A$ are vibronic Hamiltonians for the D, B and A moieties, while $\hat{H}_{DB}$ and $\hat{H}_{AB}$ are vibronic Hamiltonians for the D-B and A-B interactions. Each $\hat{H}_K$ is of the form $\hat{H}_K = \hat{H}_K^{el} + \hat{H}_K^{vi} + \hat{H}_K^{el-vi}$ where "el" denotes electronic, "vi" vibrational and "el-vi" electronic-vibrational-coupling. The time evolution of the system's vibronic populations and coherences is described by a stochastic Liouville equation for the reduced (system) density matrix $\hat{\sigma}(t)$, given by:

$$i\hbar \frac{d\hat{\sigma}(t)}{dt} = \left[\hat{H}_S, \hat{\sigma}(t)\right] + \hat{L}^{diss}\hat{\sigma}(t). \qquad \text{(A.18)}$$

$\left[\hat{H}_S, \hat{\sigma}(t)\right]$ is the coherent part and $\hat{L}^{diss}(t)\hat{\sigma}(t)$ is the dissipative part which describes the interaction of the system's vibronic states with the bath and which contains vibronic coherence and population decay rates Γ_i. [9,10]

A.6 Examples of energy-level and coupling fluctuations in electron transfer reactions

Numerous computational studies have examined the fluctuation dependence of the bridge-mediated D-A coupling for long-distance ET in systems where the transfer mechanism is tunneling ([12,14] for reviews). The general conclusion of these studies is that the Condon approximation expression for the nonadiabatic rate, $k_{ET} = 2\pi/\hbar \left\langle V^2 \right\rangle_{eq(B)} \rho_{FC}$, describes the rates quite accurately. These studies show that coupling fluctuations are important in determining the rate, especially for metal-to-metal protein ET which involves extended and floppy protein bridge structures. Writing $\left\langle V^2 \right\rangle_{eq} = \left\langle V \right\rangle_{eq}^2 + \sigma_V^2$, it is found that $\sigma_V^2 \gg \left\langle V \right\rangle^2$ for D-A distances greater than 6-7 Angstrom. [25] In this regime of large coupling fluctuations, thermal fluctuations of the D-B-A structure access molecular conformations with tunnelling matrix elements that are order-of-magnitude larger than the average-structure matrix element.

Energy-level fluctuations are particularly important in low-gap D-B-A systems where, at thermal equilibrium, there exist molecular conformations for which bridge electronic states are quasi-resonant with the donor and acceptor electronic states. [6,15] Molecular dynamics simulations combined with electronic structure computations on DNA hole-transfer systems show that, in many cases, the fluctuations in the D(A)-to-B energy gap is of the order of the average gap, i.e., $\left\langle \Delta E_{DB} \right\rangle \approx \sigma^2_{\Delta E_{DB}}$ (the bridge states are usually the highest occupied molecular orbitals of the bases). [26-29] In such systems, different transport mechanisms may coexist at the ensemble level, with contributions from tunnelling, thermally activated hopping and flickering resonance ET channels. [6,8,30] The multiplicity of mechanisms makes the phenomenology of the D-to-A ET rate complex. An open question is how to deconvolute the experimentally the different channels.

For the primary reactions in photosynthesis, [31,32] where excited state ET is ultrafast (picosecond timescale), there is experimental evidence of vibrational enhancement of the primary ET rate. [33] For example, in the Photosystem II reaction center, there exist vibrational modes with phonon energies that are resonant to the energy gap between the primary electron donor and the first charge-transfer exciton states. Two-dimensional electronic spectroscopy and modelling in the spirit of eq. (A.18), (where the system is described in a vibronic basis that includes the relevant modes), suggests that the primary ET reaction rate is enhanced and controlled by the vibronic resonances involving these resonant vibrations ([33] and references therein).

A very interesting aspect of fluctuation dynamics in ET is non-ergodic and gated dynamics. For example, when accepting mode vibrational timescales are much slower than the ET timescale, the DA energy gap fluctuations caused by these slow modes are frozen on the ET (experimental) timescale. Such an ET system is denoted non-ergodic with respect to these slow vibrations because, on the timescale of ET, these vibrations do not explore their entire phase space so as to contribute to ET activation. Thus, the canonical distributions in eqs (A.8) and (A.10)-(A.11) cannot be applied to these vibrations. Gated dynamics describe the situation when different interconverting stable conformations of the ET system (structural and/or solvent polarization) lead to different ET rates. When the interconversion rates are comparable or slower than the ET rates, the ET dynamics is said to be gated by these interconversion events. These regimes have been studied in reaction-rate and ET theory for some time, e.g., in the context of solvent-controlled ET ([3,8,14] for reviews of the extensive literature). The experimental phenomenology of the above-mentioned regimes includes non-exponential ET rate kinetics and the non-Arrhenius temperature dependence of the rate. The non-ergodic regime may also imply non-Gaussian fluctuations for the D-A energy gaps (i.e., eq. (A.11) does not apply). [34-36] Non-ergodic energy gap fluctuations were shown to be relevant in some biological ET systems and it has been suggested that they improve the efficiency of some biological ET reactions. [8,37-39]

A.7 Tuning electron transfer rates by driving vibrations with external fields

Given the importance of energy-level and coupling fluctuations in molecular ET reactions, it has been proposed to control these fluctuations by using external infra-red (IR) fields. [40-44] The goal is to perturb the ET reaction rate in a mode-specific way and also to probe ET mechanism. [12-14,16,17] The suggested approach involves either targeting with IR existing IR-active groups in the molecular ET system, or substituting IR-active groups in the molecule which could transfer their excitation energy (imparted by the IR pulse) to molecular ET-active vibrations. Further, isotopic substitutions of IR-active groups in specific locations in the molecule could enable the selective perturbation of donor, bridge or acceptor vibrations. [40-42] Due the transient effect of the IR pulse on the ET rate, a large IR-induced perturbation of the ET reaction yield is expected in systems with multiple reactions which compete with ET. [44] Indeed, many of the successful IR-perturbed ET experiments described below involve competing reaction systems.

IR-driving may enhance or reduce the ET rate by creating transient IR-perturbed molecular ensembles with non-equilibrium probability distributions for the ET-active mode coordinates (and thus, non-equilibrium probabilities for the energy-gap or coupling). The simplest expression for the IR-perturbed nonadiabatic rate in the case of classical mode excitations is given by

$$\begin{aligned} k_{ET}^{nad(IR)}(t) &= \int dQ\; p_B^{(IR)}(Q,t) \int dR\; p_R^{(IR)}(Q,t)\; \frac{2\pi}{\hbar} V(Q)^2\, \delta\left(\Delta E_{DA}(R)\right) \\ &= \int dQ\; \rho_B^{(IR)}(V,t) \int d\Delta E_{DA}\; \rho_D^{(IR)}(\Delta E_{DA},t)\; \frac{2\pi}{\hbar} V(Q)^2\, \delta\left(\Delta E_{DA}\right). \end{aligned} \tag{A.19}$$

(to be compared to the equilibrium rate in eq. (A.14)). The nonadiabatic rate is an average over Q (promoting mode) and R (accepting mode) of (Q,R) – dependent golden rule ET rates. In contrast to the equilibrium eq. (A.14), the averaging is with respect to time-dependent (non-equilibrium) distributions of the promoting and the accepting modes. In the second line of the equation the integral over the accepting mode coordinate is converted to an integral over the DA energy gap. Similarly, for quantum mode excitations, the simplest IR-perturbed nonadiabatic rate expression is

$$\tilde{k}_{ET}^{nad(neq)}(t) = \sum_{\nu_{in}} p_{\nu_{in}}^{(IR)}(t) \sum_{n_D} p_{n_D}^{(IR)}(t) \sum_{\nu_{fi}} \sum_{n_A} \tilde{k}_{D,n_D,\nu_{in}\to A,n_A,\nu_{fi}}^{nad} \tag{A.20}$$

(replacing the rate in eq. (A.15)). In the equations above $\rho^{(IR)}(t)$ and $p_i^{(IR)}(t)$ denote time-dependent (non-equilibrium) probability densities or distributions. The equations assume that both the accepting and the promoting modes have been targeted and driven out of equilibrium by IR.

These equations indicate that the effect of IR driving on the ET rate is transient and it is expected to vanish sometime after the application of the IR pulse and on a timescale that is related to the intra-molecular vibrational energy redistribution (IVR) times of the molecule-solvent ET system (denoted τ_{IVR}). Thus, setting as $t=0$ the time right after the application of the IR pulse, we expect the IR-perturbed mode probability distributions to decay to the equilibrium distributions for $t > \tau_{IVR}$, i.e., $\rho^{(IR)}(t) \xrightarrow{\tau_{IVR}} \rho^{(eq)}$ in eq. (A.19) (and $p_i^{(IR)}(t) \xrightarrow{\tau_{IVR}} p_i^{(eq)}$ in eq. (A.20)). A large IR-induced effect on the nonadiabatic ET rate would require that, for the time period between the application of the IR pulse and τ_{IVR}, $k_{ET}^{nad(IR)}(t) \ll k_{ET}^{nad(eq)}$ or $k_{ET}^{nad(IR)}(t) >> k_{ET}^{nad(eq)}$.

The transient nature of the time-dependent IR perturbation on the ET rate suggests that permanent effects of the perturbation, such as changing the ET reaction yield, can be achieved in systems where secondary reactions compete with ET. [44] For example, ET systems with a single donor and multiple acceptor units connected by independent bridges, (A_L-B_L-D-B_R-A_R), are good candidates for using pulsed-IR excitation to change the relative populations and yields of $(A_L)^-$ and $(A_R)^-$ ET products (Fig. A.5). An isotopic substitution of an IR-sensitive group in one of the bridge units allows the selective IR-perturbation of one of the ET reactions, thus influencing the relative L/R yields. [44] An example of a related recent experiment is described in the following section.

Equation (A.19) implies that the classical nonadiabatic rate may be accelerated by the IR excitation of an accepting mode if the resulting non-equilibrium probability density for the energy gap enhances the probability of D-A resonance as compared to the equilibrium density, i.e., $\rho_D^{(IR)}\left(\Delta E_{DA}=0,t\right) >> \rho_D^{(eq)}\left(\Delta E_{DA}=0,t\right)$ (the opposite condition applies for a significant reduction of the ET rate). The excitation of promoting modes may have a significant effect on the Condon rate ($\propto \left\langle V^2 \right\rangle$), if $\rho_B^{(IR)}\left(V,t\right)$ is sufficiently different from $\rho_B^{(eq)}\left(V\right)$ such that, for $0 \le t \le \tau_{IVR}$, $\left(\left\langle V^2 \right\rangle_{neq(B)} - \left\langle V^2 \right\rangle_{eq(B)}\right) \Big/ \left\langle V^2 \right\rangle_{eq(B)}$ is large ("neq" denotes the non-equilibrium ensemble average which is time-dependent).

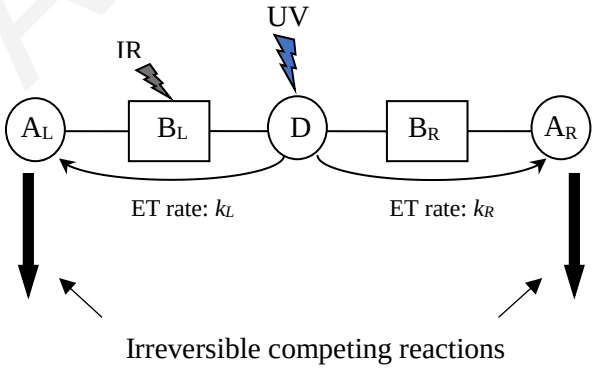

Figure A.5 A D moiety connected via left (L) and right (R) B units to distinct A moieties. Upon photo-excitation of D by UV, irreversible ET is initiated to A_L and to A_R simultaneously (with ET rates k_L and k_R). The IR excitation of one B unit which trasiently affects the corresponding ET rate, can irreversibly affect the the L to R reaction yield of the competing ET reactions and thus tune the directionality of ET.

Similar considerations apply for the quantum nonadiabatic rate of eq. (A.20). The IR excitation effects on the ET rate will be observable if the IR pulse causes large changes in the probabilities $p_i^{(eq)} \to p_i^{(IR)}(t)$ of those initial accepting-mode ($|n_D\rangle$) or promoting-mode ($|\nu_{in}\rangle$) states which have significant transfer rates $\tilde{k}^{nad}_{D,n_D,\nu_{in}\to A,n_A,\nu_{fi}}$. The excitation of a quantum promoting mode may also enhance inelastic tunnelling and switch on an otherwise symmetry forbidden transition. In a molecule with alternative through-bridge tunnelling paths, [19] the isotopic substitution of an IR-sensitive group in one of the paths could be used to realize a which-way molecular interferometer. The IR pulse targeting this group selects the electron's tunneling path by causing a path-specific vibration to exchange a quantum of vibrational energy with the electron traversing the path. [41-43]

However, some words of caution about oversimplified interpretations of IR-perturbation effects are in place. First, IR-perturbations could enhance non-Condon effects within the nonadiabatic regime. For example, the excitation of high frequency promoting modes could speed up the timescale of coupling fluctuations, [45] thus inducing the breakdown of the Condon approximation ([14] for a review). In this case, the equilibrium coupling correlation function $\left\langle \hat{C}_V(t) \right\rangle_{eq(B)}$ in eq. (A.17) should be replaced by a non-equilibrium $\left\langle \hat{C}_V(t) \right\rangle_{neq(B)}$, where $\langle .... \rangle_{neq(B)} = \sum_{\nu_{in}} p^{(IR)}_{\nu_{in}}(t) \langle \nu_{in} | ..... | \nu_{in} \rangle$. If the IR-induced fluctuations of $\left\langle \hat{C}_V(t) \right\rangle_{neq(B)}$ are of comparable timescales as the decay time of the Franck-Condon correlation function $\left\langle \hat{C}_{FC}(t) \right\rangle_{eq(B)}$, then the IR-perturbed rate should not be interpreted in terms of the Condon equation $\tilde{k}^{nad(neq)}_{ET} = (2\pi/\hbar) \left\langle \hat{V}^2 \right\rangle_{neq(B)} \rho_{FC}$, but rather in terms of the non-equilibrium eq. (A.17) where $\left\langle \hat{C}_V(t) \right\rangle_{neq(B)}$ is retained inside the time integral.

Second, eqs (A.19) and (A.20) are often too simple to be used for the prediction or the interpretation of IR-perturbation effects on nonadiabatic rates. The equations assume only two ET-active modes (one accepting and one promoting) which are either both classical (eq. (A.19)) or both quantum (eq. (A.20)). In many ET systems there are several classical and quantum promoting and accepting modes affecting ET. Therefore, more general multi-mode expressions should be used which incorporate several quantum- and classical-mode ET channels. This means that the initial and final vibrational states in the double sum of eq. (A.20) should be replaced by sums over initial and final multi-mode (product) states of accepting and promoting vibrations; i.e., $|n_D\rangle|\nu_{in}\rangle \to |vibr_{in}\rangle$ and $|n_A\rangle|\nu_{fi}\rangle \to |vibr_{fi}\rangle$, where

$|vibr_{in}\rangle = \prod_i |n_{D(i)}\rangle \prod_j |\nu_{in(j)}\rangle$ and $|vibr_{fi}\rangle = \prod_l |n_{A(l)}\rangle \prod_m |\nu_{fi(m)}\rangle$. Further, the corresponding vibronic rates $\tilde{k}^{nad}_{D,vibr_{in}\to A,vibr_{fi}}$ in the multi-mode sum become functions of several classical accepting and promoting mode coordinates $\{R_k\},\{Q_n\}$, i.e., $\tilde{k}^{nad}_{D,vibr_{in}\to A,vibr_{fi}}(\{R_k\},\{Q_n\})$. Thus, the overall quantum-classical nonadiabatic rate involves both a quantum average over initial vibronic states with probabilities $\prod_i p_{n_{D(i)}} \prod_j p_{\nu_{in(j)}}$ (where only the probabilities of modes perturbed by IR and are non-equilibrium), and a classical average over the classical mode probability densities $\rho_D(\{R_k\},t)\rho_\nu(\{Q_l\},t)$. When there are several ET-active modes contributing to the energy gap and to the coupling fluctuations, the IR-perturbation of a few of these modes may not have a substantial effect on the ET rate.

Timescales of IVR in molecules range between tens of femtoseconds to tens of picoseconds. Therefore, ET systems with ET times much greater than tens of picoseconds are too slow to be perturbed effectively by IR fields. In such systems the vibrational perturbation imparted by the IR pulse will be lost to the solvent by the time ET takes place. This ET-time limitation imposed by the IVR timescales implies that IR-perturbations of ET are likely to be large for fast ET reactions with transfer times (τ_{ET}) up to tens of picoseconds. However, reactions with ultrafast timescales (picoseconds or less) are not in the nonadiabatic limit and the interpretation of IR-perturbation effects of such ultrafast ET rates should not be based on nonadiabatic rate theory (eqs (A.19) and (A.20) and their quantum-classical multimode generalizations). Instead, the more general vibronic-density-matrix approach should be used (eq. (A.18)), where the effect of the IR-pulse field ($E^{IR}_{pulse}(t)$) is included as a perturbation of the system Hamiltonian, i.e., $\hat{H}_S \to \hat{H}_S + \hat{V}_{IR}(t)$ in eq. (A.17). [44] For example, for a perturbation of the accepting mode R, $\hat{V}_{IR}(t) = -(\partial\hat{\mu}/\partial R) R E^{IR}_{pulse}(t)$ where $\hat{\mu}$ is the dipole operator in the vibronic basis. For such ultrafast reactions the effects of the IR perturbation may be system specific and the ET probability can show vibronic coherences which are affected by the IR pulse. [44]

For systems with low tunnelling barriers (Fig. A.1), the IR perturbation may bring bridge electronic states to flickering resonance with donor and acceptor states. [6,30,45] In this situation, two-state donor-acceptor Hamiltonians as in eq. (A.1), which incorporate the effect of the bridge through a bridge-mediated tunnelling matrix element V, are not appropriate for the description of the IR-perturbed ET reaction at the ensemble level. The Hamiltonian

in eq. (A.1) can only describe through-bridge tunnelling ET (via off-resonant virtual bridge electronic states). For a D-B-A system with low-lying bridge electronic states, the IR-perturbed ensemble will contain a sub-ensemble where the B states are resonant to D and A, and where ET takes place by a resonant tunnelling mechanism. For this sub-ensemble the transferring electron will proceed through real bridge intermediate states. This process can only be described by at least three-state D-B-A Hamiltonians which incorporate the B state intermediate on an equal footing as the D and A states. [46-51] Indeed, it has been shown that the IR perturbation of the bridge will have the largest effects on the donor-to-acceptor ET rate if the B electronic state becomes quasi-resonant to D and A. [44] It should be noted that much of the above discussion applies to photoinduced ultrafast ET reaction systems, where the vibrational excitation is not caused by an IR field but rather by the electronic absorption which initiates ET. The ground-to-excited electronic state transition creates non-equilibrium vibrational probability distributions on the excited donor energy surface. [52]

A.8 Experiments of IR-perturbed electron transfer

The first experimental attempt to perturb molecular ET rates by IR pulses was a UV (pump) – IR (pump) –Vis (probe) experiment on an anthracene/dimethylaniline (DMA-GC-Anth) structure bridged by a guanosine-cytidine (GC) hydrogen-bonded pair (Fig. A.6). [16,53] Photoexcitation of anthracene by the UV pump induces an ET reaction from DMA to the photo-excited anthracene on a timescale of tens of picoseconds. The experiment found that the IR pulse, targeted to excite the bridge hydrogen-bond vibrations, causes ET rate slowing of about 67% per excited molecule. Very recently, a similar UV(pump)-IR(pump)-Vis(probe) experiment on the same molecule (targeting by IR the hydrogen bond vibrations) demonstrated that the reverse charge recombination reaction is accelerated by IR by 3.5-fold per molecule. [54]

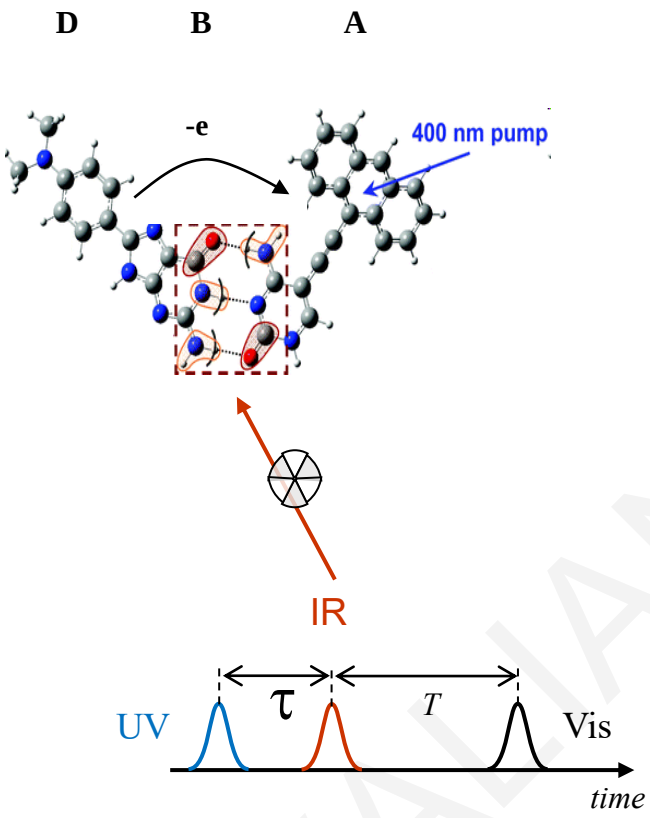

Figure A.6 UV(pump)–IR(pump)-Vis(probe) experiment on an anthracene/dimethylaniline (DMA-GC-Anth) structure bridged by a guanosine-cytidine (GC) hydrogen-bonded pair. Photoexcitation of anthracene by the UV pump induces an ET reaction from DMA to the photo-excited anthracene on a timescale of tens of picoseconds. The experiment found that the IR pulse exciting bridge hydrogen-bond vibrations causes the ET rate slowing about 67% per excited molecule. A more recent experiment showed that the IR excitation accelerates the recombination rate by 3.5-fold per molecule. [54]

A series of UV(pump)-IR(pump)-IR(probe) experiments were performed on ET D-B-A molecules with phenothiazine (PTZ) donors, a naphthalene monoimide (NAP) acceptor, and a platinum(II)-trans-acetylide bridge (Fig. A.7a). [17,55-57] In these experiments a 400nm UV-pump was used to prepare a DB^+A^- charge transfer (CT) state. This state can undergo three different competing reactions: DB^+A^- to DBA (charge-recombination), DB^+A^- to ^3A (formation of a triplet excited state that is acceptor-localized), and DB^+A^- to $^3D^+BA^-$ (forward ET reaction). This ET reaction takes place on ultrafast timescales (sub-picoseconds to tens of picoseconds). In the experiments, a narrow band IR (pump) pulse was used to excite the acetylide bridge -C≡C- stretching modes. For a PTZ-CH_2 donor the result of the IR-perturbation was 100% suppression of the DB^+A^- to $^3D^+BA^-$ ET reaction, and a concomitant

increase of the DB^+A^- to ^3A reaction yield. For PTZ and MeO-PTZ donors, the IR suppression of the DB^+A^- to $^3D^+BA^-$ ET reaction was 50% and no suppression, respectively.

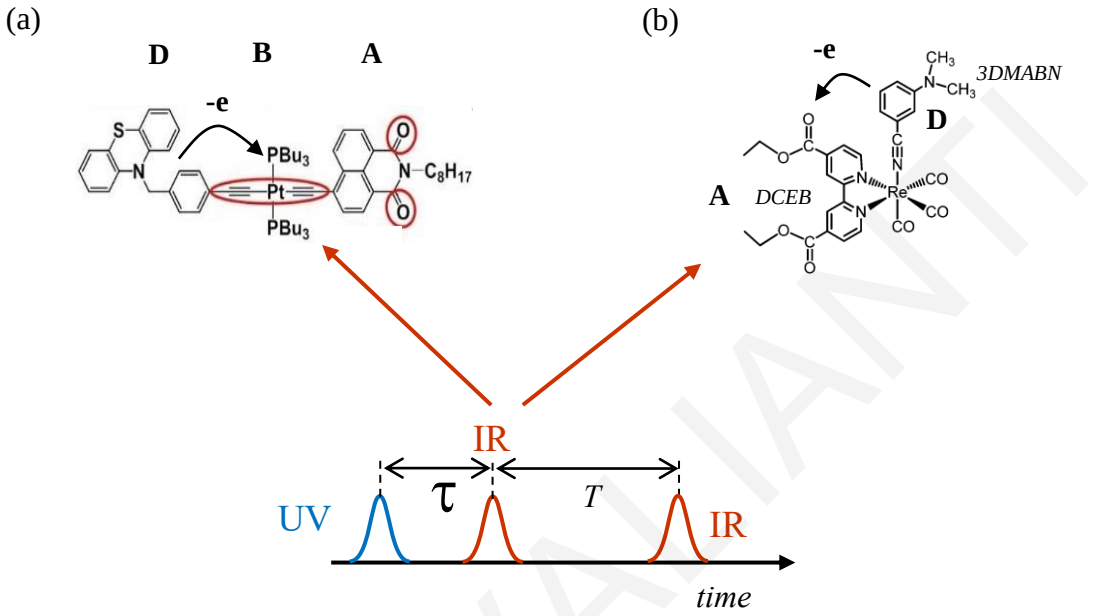

Figure A.7 (a) UV(pump)-IR(pump)-IR(probe) experiments on ET molecules with phenothiazine (PTZ) donors, a naphthalene monoimide (NAP) acceptor, and a platinum(II)-trans-acetylide bridge. A 400nm UV-pump prepares a DB^+A^- charge transfer (CT) state. Following the UV excitation a DB^+A^- to $^3D^+BA^-$ ET reaction takes place on timescales of up to tens of picoseconds. The IR excitation of the acetylide bridge -C≡C- stretching modes can fully suppress this reaction. (b) Experiments with fac-[$Re^I(CO)_3$(DCEB)(3-DMABN)] (ReEBA) complexes where 3DMABN is 3-dimethylaminobenzonitrile and DCEB is 4,4′-(dicarboxyethyl)-2,2-bipyridine. Photo-excitation by UV creates a triplet metal-to-ligand charge transfer (^{3}MLCT) excited state where the electron is localized in 3-DMABN. This state then converts to a triplet ligand-to-ligand charge transfer (^{3}LLCT) state through a ~10 picosecond ET reaction from 3-DMABN to DCEB. The IR (pump) excitation which targets the electron-acceptor (DCEB) ring-stretching modes accelerates the ET rate by ~28%.

Another UV(pump)- IR(pump)-IR(probe) experiment used forked D_L-B-A-B_{is}-D_R ET systems (the subscripts L, R denote left and right) with a central acceptor (($CO_2Et)_2$bpy) connected to two independent bridge-donor (acetylide-PTZ) units through a central Pt atom (the reverse architecture of Fig. A.5). [58] One of the -C≡C- units was replaced by the isotopic substitute -^{13}C≡^{13}C- (B_{isot}) such that it could be targeted independently from the other by the

IR pump pulse. Initial UV excitation at 400nm creates within a few picoseconds a metal-to-ligand (Pt-to-bpy) charge transfer state (MLCT). This state can decay in approximately 10 picoseconds to L and R charge-separated states (A^--B-D_L^+ and A^--B_{is}-D_R^+), following ET from D_L and D_R. After the UV excitation, the selective IR excitation of the B_{isot} stretching modes reduced the rate of A^--B_{is}-D_R^+ formation by ~70% and increased the rate of A^--B-D_L^+ formation by ~40%. Approximately the reverse behavior was seen when the other bridge (B) was targeted by the IR pump.

The fourth type of ET system used for UV(pump)-IR(pump)-IR(probe) experiments involves fac-[$Re^I(CO)_3$(DCEB)(3-DMABN)] (ReEBA) complexes (Fig. A.7b), where 3DMABN is 3-dimethylaminobenzonitrile and DCEB is 4,4′-(dicarboxyethyl)-2,2-bipyridine. In these experiments [59,60] the initial state formed upon photo-excitation by UV is a triplet metal-to-ligand charge transfer (^{3}MLCT) excited state where the electron is localized in 3-DMABN. This state then converts to a triplet ligand-to-ligand charge transfer (^{3}LLCT) state through a ~10 picosecond ET reaction from 3-DMABN to DCEB. In the experiments the IR pump excitation targeted the electron-acceptor (DCEB) ring-stretching modes and the ET rate accelerated by ~28%.

The above experiments clearly demonstrate that the mode-specific IR perturbation of an ET reaction can have significant effects on the reaction rate if the ET time is up to a few tens of picoseconds (i.e., not much greater than IVR times). The detailed interpretation of these IR-perturbation effects can be quite challenging. For the PTZ-bridge-NAP systems in Fig. A.7, the authors suggest that IR excitation modifies the D-A energy gap and the D-A coupling. [17,55,56] Recent computational studies based on a vibronic model build from ab-initio excited-state computations indicate that the IR excitation increases the D-A coupling. [57] For the system in Fig. A.7b, the ET rate acceleration was interpreted using TD-DFT computations of the triplet excited electronic state energies as a function of the bipyridine-ring-stretching normal-mode coordinates (targeted by the IR excitation). These computations suggest that the IR excitation brings the donor and acceptor electronic states (^{3}MLCT and ^{3}LLCT) to near degeneracy. [59,60] For the case of the DMA-GC-Anth structure (Fig. A.6), the IR-induced deceleration of the forward ET reaction and the acceleration of the recombination reaction were analysed theoretically and computationally and explained in [54,61]. It was found that the forward reaction is near-activationless (the crossing between the D and A BO surfaces in Fig. A.2 is near the minimum of the D BO surface). The IR perturbation depletes vibrational population from the minimum of the (initial) D BO surface, which slows down the forward reaction since this minimum is the D-to-A crossing region. The reverse ET

reaction is necessarily activated and the IR perturbation, which adds vibrational energy on the A BO surface, increases the vibrational population at the crossing region, thus accelerating the reaction. [54]

A.9 Conclusions

Theoretical studies of IR-pulse control of ET rates [40-44] inspired experiments on D-B-A ET systems which demonstrated the feasibility of ET rate modulation up to 100% by targeting specific bridge ET-active modes. [16,17,53-60] The ET rates in these experiments are fast (up to tens of picoseconds) and the magnitudes of the IR-induced modulations vary depending on the system. The central challenges in this field are to identify the general parameter regimes determining the magnitudes of the IR-perturbation effects, and to predict and simulate these effects for particular molecular systems and pulse sequences using the tools of computational quantum chemistry and molecular dynamics.

The design of an experiment that produces a significant IR modulation of an ET rate will depend critically on the details of D-B-A molecular structure. Given the right molecular structure, a successful experiment should first be able to excite the most important ET-active modes, either directly by IR or indirectly (i.e., the ET-active modes should be sinks for the excess energy supplied to the system by the IR excitation). Second, the excess energy supplied to these modes should be maintained on a timescale comparable to the ET timescale. Third, since the vibrational perturbation is transient, a permanent effect on the ET reaction yield can be achieved if the ET reaction competes with other reactions. [44]

Given the above constraints, it is essential to develop computational tools that can identify the ET-active modes which modulate the ET energy gaps and couplings, and can also simulate simultaneously the pulse excitation events, the time-dependent IVR pathways following the excitation events, and the time-dependent ET pathways. Vibrational energy redistribution (and dephasing) is likely to have the most significant influence on the level of IR-perturbation of the ET rate.

The mode-specific driving of ET reactions can be a very useful experimental tool for probing ET mechanism, with the potential of modifying the mechanism in D-B-A systems with low bridge energy gaps (where IR driving may switch between through-bridge hopping or flickering-resonance channels and through-bridge tunneling). For the IR control of ET reactions at the ensemble level, (rather than the single molecule level), a major obstacle is

the low IR absorption intensity of molecular vibrations. To augment the level of vibrational excitation it is possible to use surface enhanced IR absorption methods. [44] Another path would be to damp vibrational energy to the D-B-A system via electronic absorption by attaching to the system heating molecules such as azobenene. Such molecules undergo rapid internal conversion when excited electronically and could damp the excess vibrational energy to the D-B-A system. Finally, advances in producing intense psec-wide Terahertz (THz) pulses suggest that THz driving of ET-active modes will be possible in the near future. THz pulses would target low-frequency "classical" vibrations (not accessed directly by IR) which are often the most important in gating ET reactions. [45]

The specific research work presented in this Chapter has been published during the doctoral program (see ref. [61]).

A.10 References

[1] Marcus, R.A; Sutin, N. Electron transfers in chemistry and biology. *Biochim. Biophys. Acta.* **1985**, *811*, 265-322.

[2] Winkler, L.R.; Gray, H.B. Electron Flow through Metalloproteins. *Chem. Rev*. **2014**, *114*, 3369.

[3] Jortner, J.; Bixon, M.; Prigogine, I.; Rice, S.A. *Electron Transfer - from Isolated Molecules to Biomolecules*; John Wiley & Sons, *New York, 1999.*

[4] Balzani, V.; Piotrowiak, P.; Rodgers, M.A.J.; Mattay, J.; Astruc, D.; Gray, H.B.; Wrinkler, J.; Fukuzumi, S.; Mallouk, T.E.; Haas, Y.; et al. *Electron Transfer in Chemistry; I–V ed.;* Weinheim:Wiley-VCH, *2001*.

[5] Beratan, D.N.; Skourtis, S.S. *Electron transfer mechanisms*; Curr. Op. Chem. Biol. 2, 235, *1998*.

[6] Skourtis, S.S. Reviewprobing protein electron transfer mechanisms from the molecular to the cellular scales. *Pept. Sci.* **2012**, *100*, 82.

[7] Mohseni, M.; Omar, Y.; Engel, G.; Plenio, M. *Quantum Effects in Biology*. Cambridge University Press, Cambridge, *2014*.

[8] Blumberger, J. Recent Advances in the Theory and Molecular Simulation of Biological Electron Transfer Reactions. *Chem. Rev*. **2015**, *115*, 11191.

[9] Nitzan, A. *Chemical Dynamics in Condensed Phases*; Oxford University Press, 2006.

[10] May, V.; Kuhn, O. *Charge and Energy Transfer Dynamics in Molecular Systems*; 3rd ed.; Wiley-VCH, Berlin, 2011.

[11] Sumi, S. *Electron Transfer in Chemistry, Vol I,* Wiley-VCH Verlag GmbH: Weinheim, Germany, 65-108, 2001.

[12] Skourtis, S.S.; Lin, J.; Beratan D.N. *Modern Methods for Theoretical Physical Chemistry of Biopolymers,* edited by Starikov, E.B.; Lewis, J.P.; Tanaka, S. Elsevier, Boston, MA, *2006*.

[13] Beratan, D.N.; Skourtis, S.S.; Balabin, I.A.; Balaeff, A.; Keinan, S.; Venkatramani, R.; Xiao, D. Steering Electrons on Moving Pathways. *Acc. Chem. Res*. **2009**, *42*, 1669.

[14] Skourtis, S.S.; Waldeck, D.H.; Beratan, D.N. Fluctuations in biological and bioinspired electron-transfer reactions. *Annu. Rev. Phys. Chem*. **2010**, *61*, 461.

[15] Beratan, D.N.; Liu, C.; Migliore, A.; Polizzi, N.F.; Skourtis, S.S.; Zhang, P.; Zhang, Y. Charge Transfer in Dynamical Biosystems, or The Treachery of (Static) Images. *Acc. Chem. Res.* **2015**, *48*, 474.

[16] Rubtsov, I.V. Shake it off. *Nat. Chem.* **2015**, *7*, 683.

[17] Delor, M.; Sazanovich, I.V.; Towrie, M.; Weinstein, J.A. On the mechanism of vibrational control of light-induces charge transfer in donor-bridge-acceptor assemblies. *Acc. Chem. Res.* **2015**, *48*, 1131-1139.

[18] Hänggi, P.; Talkner, P.; Borkovec, M. Reaction-rate theory: fifty years of Kramers. *Rev. Mod. Phys.* **1990**, *62*, 51.

[19] Skourtis, S.S.; Beratan, D.N. Theories of structure-function relationships for bridge-mediated electron transfer. *Adv. Chem. Phys.* **1999**, *106*, 377.

[20] Kuznetsov, A.M.; Ulstrup, J. *Electron Transfer in Chemistry and Biology: An Introduction to the Theory*. John Wiley & Sons, Chichester, 1999.

[21] Gammaitoni, L.; Hänggi, P.; Jung, P.; Marchesoni, F. Stochastic resonance. *Rev. Mod. Phys*. **1998**, *70*, 23.

[22] Pechukas, P. *Dynamics of Molecular Collisions Part B*. Modern Theoretical Chemistry 2, Springer, New York, *1976*.

[23] Bixon, M.; Jortner, J. Effects of Configurational Fluctuation on Electronic Coupling for Charge Transfer Dynamics. *Russ. J. Electrochem.* **2003,** *39,* 5.

[24] Troisi, A.; Nitzan, A.; Ratner, M.A. A rate constant expression for charge transfer through fluctuating bridges. *J. Chem. Phys.* **2003**, *119,* 5782.

[25] Balabin, I.A.; Beratan, D.N.; Skourtis, S.S. Persistence of Structure Over Fluctuations in Biological Electron-Transfer Reactions. *Phys. Rev. Lett.* **2008**, *201*, 158102.

[26] *Schuster, G.B. Long-Range Charge Transfer in DNA I and II;* Top Curr. Chem, vol. 236-237, Springer, Berlin, 2004.

[27] Voityuk, A.A. Electronic couplings and on-site energies for hole transfer in DNA: Systematic quantum mechanical/molecular dynamic study. *J. Chem. Phys.* **2008**, *128*, 115101.

[28] Kubar, T.; Kleinekathöfer, U.; Elstner, M. Solvent Fluctuations Drive the Hole Transfer in DNA: A Mixed Quantum-Classical Study. *J. Phys. Chem B.* **2009**, *113*, 13107.

[29] Kubar, T.; Elstner, M.; Coarse-Grained Time-Dependent Density Functional Simulation of Charge Transfer in Complex Systems: Application to Hole Transfer in DNA. *J. Phys. Chem. B.* **2010**, *114*, 11221.

[30] Zhang, Y.; Liu, C.; Balaedd, A.; Skourtis, S.S.; Beratan, D.N. Biological charge transfer via flickering resonance. *Proc. Nat. Acad. Sci. U.S.A.* **2014**, *111,* 10049.

[31] Blankenship, R.E. *Molecular Mechanisms of Photosynthesis*, 2nd ed.; Blackwell Science, Oxford, 2002.

[32] Scholes, G.D.; Fleming, G.R.; Olaya-Castro, A.; van Grondelle, R. Lessons from nature about solar light harvesting. *Nature Chem.* **2011**, *3*, 763.

[33] Romero, E.; Novoderezhkin, V.I.; van Grondelle, R. Quantum design of photosynthesis for bio-inspired solar-energy conversion. *Nature.* **2017**, *543*, 355.

[34] Tachiya, M. Relation between the Electron-Transfer Rate and the Free Energy Change of Reaction. *J. Phys. Chem.* **1989**, *93*, 7050.

[35] Tachiya, M. Effect of the dielectric saturation on the rates of electron transfer in polar solvents. *Chem. Phys. Lett.* **1989**, *159,* 505.

[36] Tachiya, M. Generalization of the Marcus Equations for the Electron-Transfer Rate. *J. Phys. Chem.* **1993**, *97*, 5911.

[37] Matyushov, D.V. Energetics of Electron-Transfer Reactions in Soft Condensed Media. *Acc. Chem. Res.* **2007**, *40*, 294.

[38] Waskasi, M.M.; Newton, M.D.; Matyushov, D.V. Impact of Temperature and Non-Gaussian Statistics on Electron Transfer in Donor–Bridge–Acceptor Molecules. *J. Phys. Chem. B.* **2017**, *121*, 2665.

[39] Seyedi, S.; Matyushov, D.V. Dipolar susceptibility of protein hydration shells. *Phys. Chem. Lett.* **2018**, *9*, 2359.

[40] Skourtis, S.S.; Waldeck, D.H.; Beratan, D.N. Inelastic Electron Tunneling Erases Coupling-Pathway Interferences. *J. Phys. Chem. B.* **2004**, *108*, 15511.

[41] Skourtis, S.S.; Beratan, D.N. A Molecular Double Slit Paradigm. *AIP Conf. Proc.* **2007**, *2*, 809.

[42] Xiao, D.Q.; Skourtis, S.S.; Rubtsov, I.V.; Beratan, D.N. Turning Charge Transfer On and Off in a Molecular Interferometer with Vibronic Pathways. Nano Lett. ***2009***, 9, *1818.*

[43] Carias, H.; Beratan, D.N.; Skourtis, S.S. Floquet analysis for vibronically modulated electron tunneling. *J. Phys. Chem. B.* **2011**, *115*, 5510.

[44] Antoniou, P.; Ma, Z.; Zhang, P.; Beratan, D.N.; Skourtis, S.S. Vibrational control of electron-transfer reactions: a feasibility study for the fast coherent transfer regime. *Phys. Chem. Chem. Phys.* **2015**, *17*, 30854.

[45] Skourtis, S.S.; Balabin, I.A.; Kawatsu, T.; Beratan, D.N. Protein dynamics and electron transfer: Electronic decoherence and non-Condon effects. *Proc. Natl. Acad. Sci. U.S.A.* **2005**, *102*, 3552.

[46] Skourtis, S.S; Onuchic, J.N. Effective two-state systems in bridge-mediated electron transfer. A Green function analysis. *Chem. Phys. Lett.* **1993**, *209*, 171.

[47] Skourtis, S.S.; Beratan, D.N.; Onuchic, J.N. The two-state reduction for electron and hole transfer in bridge-mediated electron-transfer reactions. *Chem. Phys.* **1993**, *176*, 501.

[48] Skourtis, S.S.; Mukamel, S. Superexchange versus sequential long range electron transfer; density matrix pathways in Liouville space. *Chem. Phys.* **1995**, *197*, 367.

[49] Xie, Q.; Archontis, G.; Skourtis, S.S. Protein electron transfer: a numerical study of tunneling through fluctuating bridges. *Chem. Phys. Lett.* **1999**, *312*, 237.

[50] Skourtis, S.S.; Archontis, G.; Xie, Q. Electron transfer through fluctuating bridges: On the validity of the superexchange mechanism and time-dependent tunneling matrix elements. *J. Chem. Phys.* **2001**, *115*, 9444.

[51] Teklos, A.; Skourtis, S.S. Electron transfer through time dependent bridges: Differences between Franck–Condon and Born–Oppenheimer breakdown. *Chem. Phys.* **2005**, *319*, 52.

[52] Feskov, S.V.; Mikhailova, V.A.; Ivanov, I.A.I. Non-equilibrium effects in ultrafast photoinduced charge transfer kinetics. J. *Photochem. Photobiol. C.* **2016**, *29*, 48.

[53] Lin, Z.W.; Lawrence, C.M.; Xiao, D.Q.; Kireev, V.V.; Skourtis, S.S.; Sessler, J.L.; Beratan, D.N.; Rubtsov, I.V. Modulating unimolecular charge transfer by exciting bridge vibrations. *J. Am. Chem. Soc.* **2009**, *131*, 18060.

[54] Ma, Z.; Lin, Z.; Lawrence, C.M.; Rubtsov, I.V.; Antoniou, P.; Skourtis, S.S.; Zhang, P.; Beratan, D.N. How can infra-red excitation both accelerate and slow charge transfer in the same molecule?. *Chem. Sci.* **2018**, *9*, 6395.

[55] Delor, M.; Keane, T.; Scattergood, P.A.; Sazanovich, I.V.; Greetham, G.M.; Towrie, M.; Meijer, A.J.H.M; Weinstein, J.A. On the mechanism of vibrational control of light-induced charge transfer in donor–bridge–acceptor assemblies. *Nat. Chem.* **2015**, *7*, 689.

[56] Delor, M.; Scattergood, P.A.; Sazanovich, I.V.; Parker, A.W.; Greetham, G.M.; Meijer, A.J.H.M; Towrie, M.; Weinstein, J.A. Toward control of electron transfer in donor-acceptor molecules by bond-specific infrared excitation. *Science.* **2014**, *346*, 1492.

[57] Yang, X.; Keane, T.; Delor, M.; Meijer, A.J.H.M.; Weinstein, J.A.; Bittner, E.R. Identifying electron transfer coordinates in donor-bridge-acceptor systems using mode projection analysis. *Nat. Commun.* **2017**, *8*, 14554.

[58] Delor, M.; Archer, S.A.; Keane, T.; Meijer, A.J.H.M.; Sazanovich, I.V.; Greetham, G.M.; Towrie, M.; Weinstein, J.A. Directing the path of light-induced electron transfer at a molecular fork using vibrational excitation. Nat. Chem. ***2017***, 9, *1099.*

[59] Yue, Y.; Grusenmeyer, T.; Ma, Z.; Zhang, P.; Schmehl, R.H.; Beratan, D.N.; Rubtsov, I.V. Electron transfer rate modulation in a compact Re(I) donor–acceptor complex. *Dalton Trans.* **2015**, *44*, 8609.

[60] Yue, Y.; Grusenmeyer, T.; Ma, Z.; Zhang, P.; Schmehl, R.H.; Beratan, D.N.; Rubtsov, I.V. Full-electron ligand-to-ligand charge transfer in a compact Re (I) complex. J. Phys. Chem. A. **2014**, 118, 10407.

[61] Valianti, S.; Skourtis, S. S. Vibrational control of molecular electron transfer reactions. *Mol. Phys.* **2019**, *117 (19)*, 2618-2631.

APPENDIX B

Energies of the many-electron basis states of the D-B-A systems as a function of the HOMO-LUMO exciton energies and of the differences between the IPs of D(A) and B

In Chapter 5 we studied the role of bridge-state intermediates in Singlet Fission (SF) for donor (D) - bridge (B) - acceptor (A) systems. For this purpose, we constructed a semi-analytical / computational framework to explore structure-function relationships for SF in D-B-A molecular architectures. Through this semi-analytical approach we expressed the energies of the basis-states used to represent the CISD Hamiltonian, as functions of the exciton energies of D(A) and B and of the energy difference between the ionization potentials (IPs) of D(A) and B, through the parameters X, Y and z, respectively (see approximate excitation energies on Table 5.1 and analytical exact expressions on Table 7.1),

$$X \equiv x - J_{H_{D(A)}L_{D(A)}} + 2K_{H_{D(A)}L_{D(A)}}\ ,\ \ Y \equiv y - J_{H_BL_B} + 2K_{H_BL_B}\ ,\ z = IP^{D(A)} - IP^B \qquad \text{(B.1)}$$

where

$$x = IP^{D(A)} - EA^{D(A)},\ y = IP^B - EA^B. \qquad \text{(B.2)}$$

Below we present 3D graphs showing this dependence for the four different reference molecular systems we studied (pi-stacking pentacene trimer, non-pi-stacking pentacene trimer, pentacene-tetracene-pentacene and NC1 molecular systems in Fig. 5.3).

(a)

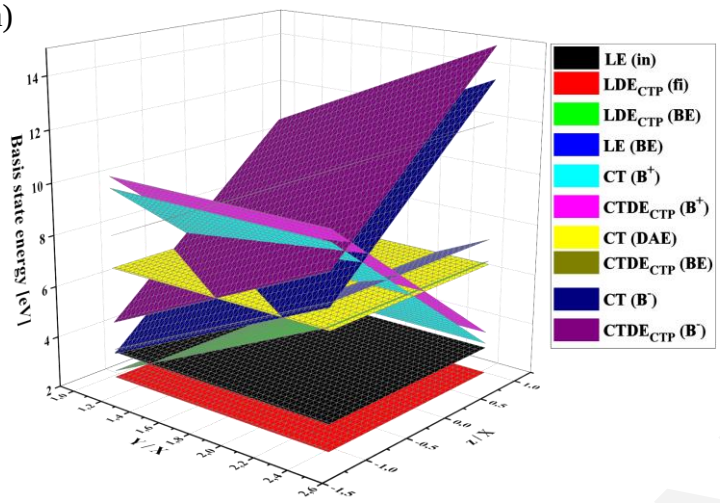

(b)

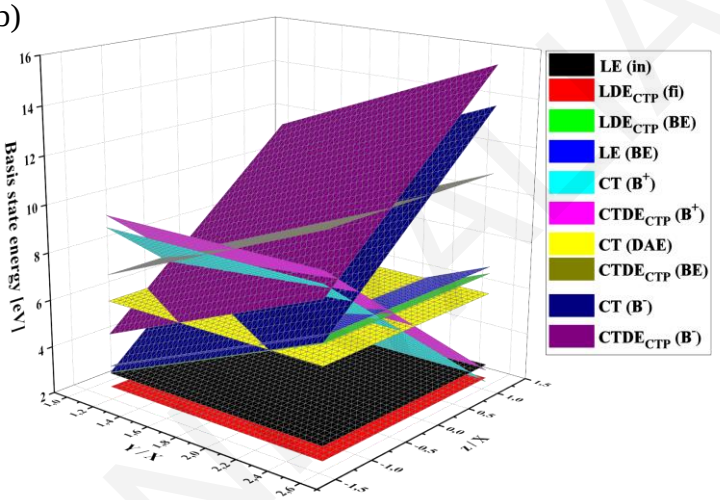

(c)

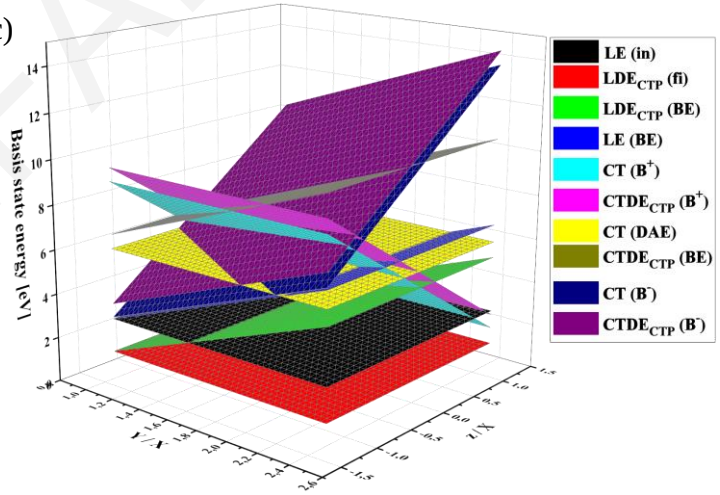

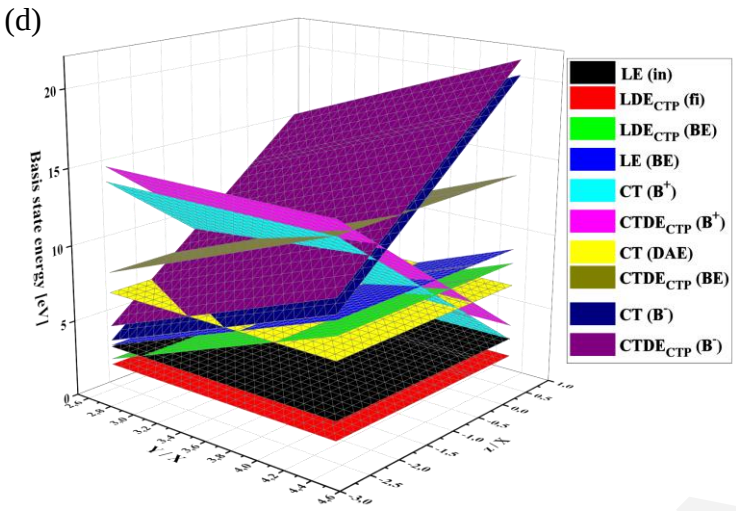

Figure B.1 Basis States energies as a function of Y/X and z/X parameters for: (a) the pi-stacking tri-pentacene conformation shown in Fig. 5.3a, (b) the non-pi-stacking tri-pentacene conformation shown in Fig. 5.3b, (c) the pentacene-tetracene-pentacene molecular system of Fig. 5.3c, and (d) the NC1 molecular system of Fig. 5.3d.